PACIFIC EARTHQUAKE ENGINEERING
RESEARCH CENTER

NGA-East: Ground-Motion Standard Deviation Models for Central and Eastern North America

Linda Al Atik

Linda Alatik Consulting
San Francisco, California

PEER Report No. 2015/07
Pacific Earthquake Engineering Research Center
Headquarters at the University of California, Berkeley

June 2015

PEER 2015/07
JUNE 2015

NGA-East: Ground-Motion Standard Deviation Models for Central and Eastern North America

Linda Al Atik

Linda Alatik Consulting
San Francisco, California

PEER Report 2015/07
Pacific Earthquake Engineering Research Center
Headquarters at the University of California, Berkeley

June 2015

ABSTRACT

Empirical ground-motion data from Central and Eastern North America (CENA) are used to analyze the components of ground-motion variability in CENA. Trends of ground-motion variability with parameters such as magnitude, distance, and V_{S30} are analyzed and compared to trends of ground-motion variability in other regions, particularly the Western United States (WUS) using the NGA-West2 dataset.

The CENA dataset is limited in magnitude range to small-to-moderate magnitudes and in frequency content to frequencies between 1 and 10 Hz due to the bandwidth limitations of the recordings. Therefore, standard deviation models developed using the CENA ground-motion data cannot be reliably extrapolated to large magnitudes and to frequencies outside of 1 to 10 Hz. As a result, standard deviation models from other regions such as WUS and Japan are used to inform the extrapolation of CENA standard deviations and overcome data limitations. Candidate models for between-event standard deviation (τ), single-station within-event standard deviation (ϕ_{SS}), and site-to-site variability (ϕ_{S2S}) are developed for CENA. In turn, these models are combined to develop single-station sigma (σ_{SS}) and ergodic sigma models for CENA.

ACKNOWLEDGMENTS

This study was sponsored by the Pacific Earthquake Engineering Research center (PEER), as part of the NGA-East research project, and was funded by the U.S. Nuclear Regulatory Commission (NRC), the U.S. Department of Energy (DOE), and the Electric Power Research Institute (EPRI), with the participation of the U.S. Geological Survey (USGS). Any opinions, findings, and conclusions or recommendations expressed in this material are those of the authors and do not necessarily reflect those of the sponsoring agencies.

The author acknowledges Justin Hollenback for his help in providing CENA ground-motion residuals for use in this study. The author also acknowledges the numerous NGA-East Project participants who provided feedback on the analysis and the model development presented in this report, with a very special attention to the members of the NGA-East Sigma Working Group (Jack Baker, Adrian Rodriguez-Marek, Brian Chiou, Ellen Rathje, Ken Campbell, and Melanie Walling). The author acknowledges Yousef Bozorgnia for his leadership throughout the project and the PEER staff for their editing and project support.

CONTENTS

ABSTRACT .... **iii**

ACKNOWLEDGMENTS .... **v**

TABLE OF CONTENTS .... **vii**

LIST OF ABBREVIATIONS AND SYMBOLS .... **ix**

LIST OF TABLES .... **xi**

LIST OF FIGURES .... **xiii**

1 INTRODUCTION **1**

1.1 Scope **1**

1.2 Background on Ground-motion variability and its Components **2**

1.3 Approach **4**

1.4 Past Studies **4**

1.4.1 Ergodic σ for CENA 4

1.4.2 Single-Station σ 5

2 DATASETS **9**

2.1 NGA-East **9**

2.2 NGA-West2 .... **17**

3 GMPE FUNCTIONAL FORM AND RESIDUAL PLOTS **23**

4 ANALYSIS OF THE COMPONENTS OF GROUND-MOTION VARIABILITY **49**

4.1 Methodology **49**

4.2 τ **51**

4.3 ϕ **57**

4.4 ϕ_{SS} **71**

4.5 ϕ_{S2S} **86**

4.6 Other Effects **96**

4.6.1 Regression Approach 96

4.6.2 Regional Effects 98

5 CENA STANDARD DEVIATION MODELS **101**

5.1 General Framework **101**

5.1.1 χ-Square Distribution 101

5.2 τ 102

5.2.1 Candidate Models 102

5.2.1.1 Global τ Model... 102

5.2.1.2 CENA Constant τ Model 109

5.2.1.3 CENA Magnitude-Dependent τ Model.. 110

5.2.2 Comparison to Existing Models...114

5.3 σ_{SS} 116

5.3.1 Candidate Models 116

5.3.1.1 Global ϕ_{SS} Model 116

5.3.1.2 CENA Constant ϕ_{SS} Model.. 124

5.3.1.3 CENA Magnitude-Dependent ϕ_{SS} Model 126

5.3.2 Comparison to Existing Models...132

5.4 ϕ_{S2S} 137

5.5 ϕ...140

5.6 Single-Station σ...149

5.7 Ergodic σ..158

5.8 Other Considerations..170

5.8.1 Application to Potentially Induced Earthquakes.....................................170

5.8.2 Application to Gulf Region...173

6 CONCLUSIONS 177

REFERENCES..179

LIST OF ABBREVIATIONS AND SYMBOLS

ASK14	Abrahamson et al. (2014)
BSSA14	Boore et al. (2014)
CB14	Campbell and Bozorgnia (2014)
CDF	Cumulative density function
CENA	Central and Eastern North America
CEUS	Central and Eastern US
CV	Coefficient of variation
CY14	Chiou and Youngs (2014)
DCPP	Diablo Canyon Power Plant
ENA	Eastern and North America
F	Frequency (Hz)
GMM	Ground-motion model
GMPE	Ground-motion prediction equation
H_{dep}	Hypocentral depth (km)
$\mathbf{M}$	Moment magnitude
NGA-East	Next generation attenuation relationships for Central and Eastern North America
NGA-West1	Next generation attenuation relationships for Western US
NGA-West2	Enhancement of next generation attenuation relationships for Western US
PGA	Peak ground acceleration
PGV	Peak ground velocity
Phi, ϕ	Within-event standard deviation
PhiSS, ϕ_{SS}	Single-station within-event standard deviation
$\phi_{SS,S}$	Single-station within-event standard deviation estimated at an individual station
PhiS2S, ϕ_{S2S}	Site-to-site variability
PIE	Potentially-induced events
PRP	PEGASOS Refinement Project
PSA	Pseudo-spectral acceleration response spectral ordinate
PSHA	Probabilistic seismic hazard analysis
PVNGS	Palo Verde Nuclear Generating Station
R_{JB}	Joyner-Boore distance
R_{RUP}	Rupture distance

SD	Standard deviation
SSHAC	Senior Seismic Hazard Analysis Committee
SWUS	Southwestern United States Ground-Motion Characterization Level 3 SSHAC Project
T	Spectral period (sec)
Tau, τ	Between-event standard deviation
TNSP	Thyspunt Nuclear Siting Project
Var	Variance
V_{S30}	Time-averaged shear-wave velocity to a depth of 30 m
WNA	Western North America
WUS	Western U.S.

LIST OF TABLES

Table 1.1 Summary of terminology for residual components and standard deviations (*SD* denotes standard deviation). 3

Table 2.1 Number of recordings, earthquakes and stations at $F = 4$ Hz used in the within-event and between-event residuals analysis. 10

Table 2.2 Number of recordings, earthquakes and stations used in the single-station analysis at $F = 4$ Hz. 15

Table 2.3 Number of recordings, earthquakes, and stations in the NGA-West2 datasets used in the single-station analysis. 17

Table 5.1 Mean and standard deviation of the coefficients of the global τ model. 109

Table 5.2 Mean and standard deviation of the CENA constant τ model. 110

Table 5.3 Mean and standard deviation of the coefficients of the CENA magnitude-dependent τ model. 111

Table 5.4 Coefficients of the global τ model. 115

Table 5.5 Coefficients of the CENA constant τ model. 116

Table 5.6 Coefficients of the CENA magnitude-dependent τ model. 116

Table 5.7 Standard deviation of $\phi_{SS,S}$ using the ASK14 residuals at PGA and periods of 0.1 and 1 sec for a minimum number of recordings per station (Nmin) of 5 to 25 121

Table 5.8 Mean and standard deviation of the coefficients of the global magnitude-dependent ϕ_{SS} model. 124

Table 5.9 Mean and standard deviation of the CENA constant ϕ_{SS} model. 126

Table 5.10 Mean and standard deviation of the coefficients of the CENA magnitude-dependent ϕ_{SS} model. 132

Table 5.11 Coefficients of the global ϕ_{SS} model. 133

Table 5.12 Coefficients of the CENA constant ϕ_{SS} model. 134

Table 5.13 Coefficients of the CENA magnitude-dependent ϕ_{SS} model. 134

Table 5.14 Mean and standard deviation of the CENA ϕ_{S2S} model. 139

Table 5.15 Central, high, and low values of the CENA ϕ_{S2S} model. 140

Table 5.16 Coefficients of the global ϕ model. 142

Table 5.17 Coefficients of the CENA magnitude-dependent ϕ model. 143

Table 5.18 Coefficients of the CENA constant ϕ model. 144

Table 5.19 Coefficients of the global single-station σ model resulting from combining the global ϕ_{SS} model and the global τ model. 151

Table 5.20 Coefficients of the CENA single-station σ model-1 resulting from combining the CENA constant ϕ_{SS} model and the global τ model. 152

Table 5.21 Coefficients of the CENA single-station σ model-2 resulting from combining the CENA magnitude-dependent ϕ_{SS} model and the global τ model....153
Table 5.22 Coefficients of the global ergodic σ model resulting from combining the global ϕ_{SS} model, the global τ model, and the CENA ϕ_{S2S} model....160
Table 5.23 Coefficients of the CENA ergodic σ model-1 resulting from combining the CENA constant ϕ_{SS} model, the global τ model, and the CENA ϕ_{S2S} model....161
Table 5.24 Coefficients of the CENA ergodic σ model-2 resulting from combining the CENA magnitude-dependent ϕ_{SS} model, the global τ model, and the CENA ϕ_{S2S} model....162
Table 5.25 *P*-values from the *F*-test of equality of τ^2 for PIE and the tectonic events for CENA....172
Table 5.26 *P*-values from the *F*-test of equality of ϕ_{SS}^2 for PIE and the tectonic events for CENA....172
Table 5.27 *P*-values from the *F*-test of equality of τ^2 for tectonic events in the Gulf region and the rest of CENA. Values in red indicate cases where the equality of τ^2 is rejected at 5% significance level....174
Table 5.28 *P*-values from the *F*-test of equality of ϕ_{SS}^2 for tectonic events in the Gulf region and the rest of CENA....174
Table 5.29 *P*-values from the *F*-test of equality of ϕ_{S2S}^2 for tectonic events in the Gulf region and the rest of CENA. Values in red indicate cases where the equality of ϕ_{S2S}^2 is rejected at 5% significance level....174

LIST OF FIGURES

Figure 2.1 Magnitude and distance distribution of the CENA ground-motion data used in the between-event and within-event residuals analysis at F = 4 Hz..........11

Figure 2.2 Magnitude and distance distribution of the CENA ground-motion data by region used in the between-event and within-event residuals analysis at F = 4 Hz..........11

Figure 2.3 Magnitude and hypocentral depth distribution of the CENA earthquakes used in the between-event and within-event residuals analysis at F = 4 Hz..........12

Figure 2.4 Histogram of the number of stations in the V_{S30} bins for the dataset used in the between-event and within-event residuals analysis at F = 4 Hz. 12

Figure 2.5 Number of stations and recordings with different assigned V_{S30} codes used in the between-event and within-event residuals analysis at F = 4 Hz. 13

Figure 2.6 Number of recordings versus spectral period for the dataset used in the between-event and within-event residuals analysis. 14

Figure 2.7 Histogram of the number of stations versus bins of the number of recordings per station for the dataset used in the between-event and within-event residuals analysis at F = 4 Hz. 14

Figure 2.8 Magnitude and distance distribution of the CENA ground-motion data used in the single-station analysis at F = 4 Hz. 15

Figure 2.9 Histogram of the number of stations in different V_{S30} bins for the dataset used in the single-station analysis at F = 4 Hz. 16

Figure 2.10 Number of recordings versus spectral period for the dataset used in the single-station analysis. 16

Figure 2.11 Data distribution (magnitude-distance plot, V_{S30} histogram, and number of recordings histogram) for the ASK14 dataset used in the single-station analysis..........18

Figure 2.12 Data distribution (magnitude-distance plot, V_{S30} histogram, and number of recordings histogram) for the BSSA14 dataset used in the single-station analysis..........19

Figure 2.13 Data distribution (magnitude-distance plot, V_{S30} histogram, and number of recordings histogram) for the CB14 dataset used in the single-station analysis..........20

Figure 2.14 Data distribution (magnitude-distance plot, V_{S30} histogram, and number of recordings histogram) for the CY14 dataset used in the single-station analysis..........21

Figure 3.1 Event terms versus magnitude for F = 10 Hz. 25

Figure 3.2 Event terms versus magnitude for F = 4 Hz. 26

Figure 3.3 Event terms versus magnitude for F = 2 Hz. 27

Figure 3.4 Event terms versus magnitude for F = 1.33 Hz. 28

Figure 3.5 Event terms versus magnitude for F = 1 Hz. 29

Figure 3.6 Event terms versus magnitude for F = 0.5 Hz. 30

Figure 3.7 Within-event residuals versus R_{RUP} for F = 10 Hz. 31
Figure 3.8 Within-event residuals versus R_{RUP} for F = 4 Hz. 32
Figure 3.9 Within-event residuals versus R_{RUP} for F = 2 Hz. 33
Figure 3.10 Within-event residuals versus R_{RUP} for F = 1.33 Hz. 34
Figure 3.11 Within-event residuals versus R_{RUP} for F = 1 Hz 35
Figure 3.12 Within-event residuals versus R_{RUP} for F = 0.5 Hz. 36
Figure 3.13 Within-event residuals versus V_{S30} for F = 10 Hz. 37
Figure 3.14 Within-event residuals versus V_{S30} for F = 4 Hz. 38
Figure 3.15 Within-event residuals versus V_{S30} for F = 2 Hz. 39
Figure 3.16 Within-event residuals versus V_{S30} for F = 1.33 Hz. 40
Figure 3.17 Within-event residuals versus V_{S30} for F = 1 Hz. 41
Figure 3.18 Within-event residuals versus V_{S30} for F = 0.5 Hz. 42
Figure 3.19 Within-event residuals (LN units) versus R_{RUP} by region for F = 10 Hz. 43
Figure 3.20 Within-event residuals (LN units) versus R_{RUP} by region for F = 4 Hz. 44
Figure 3.21 Within-event residuals (LN units) versus R_{RUP} by region for F = 2 Hz. 45
Figure 3.22 Within-event residuals (LN units) versus R_{RUP} by region for F = 1.33 Hz. 46
Figure 3.23 Within-event residuals (LN units) versus R_{RUP} by region for F = 1 Hz. 47
Figure 3.24 Within-event residuals (LN units) versus R_{RUP} by region for F = 0.5 Hz. 48

Figure 4.1 τ versus frequency for different minimum number of recordings per earthquake (NRE) used in the regression. 51
Figure 4.2 τ versus frequency for PIE, tectonic and all earthquakes for minimum number (Nmin) of three recordings per earthquake and all magnitudes (left) and for earthquakes with a minimum M of 3.0 (right). 52
Figure 4.3 Comparison of CENA τ to NGA-West2 τ using all CENA earthquakes (left) and earthquakes with a minimum **M** of 3.0 (right). 52
Figure 4.4 τ versus magnitude for CENA compared to WUS τ predicted by NGA-West2 models (left) and computed from NGA-West2 event terms (right) at F = 10 Hz. 53
Figure 4.5 τ versus magnitude for CENA compared to WUS τ predicted by NGA-West2 models (left) and computed from NGA-West2 event terms (right) at F = 4, 2, and 1.33 Hz. 54
Figure 4.6 τ versus magnitude for CENA compared to WUS τ predicted by NGA-West2 models (left) and computed from NGA-West2 event terms (right) at F = 1 and 0.5 Hz. 55
Figure 4.7 τ versus hypocentral depth for CENA at F = 10, 4, 2, 1.33, 1, and 0.5 Hz. 56
Figure 4.8 ϕ versus frequency for different minimum number of recordings per earthquake (NRE) used in the regression. 57
Figure 4.9 ϕ versus frequency for PIE, tectonic and all earthquakes for minimum number (Nmin) of three recordings per earthquake and all magnitudes (left) and for earthquakes with a minimum **M** of 3.0 (right). 58

Figure 4.10 Comparison of CENA ϕ to NGA-West2 ϕ using all CENA recordings (left) and recordings with a minimum **M** of 3.0 (right). 58
Figure 4.11 CENA ϕ by region using all recordings (left) and recordings with a minimum **M** of 3.0 (right)...59
Figure 4.12 ϕ versus magnitude for CENA compared to WUS ϕ predicted by NGA-West2 models (left); and computed from NGA-West2 residuals (right) at $F = 10$, 4, and 2 Hz. 60
Figure 4.13 ϕ versus magnitude for CENA compared to WUS ϕ predicted by NGA-West2 models (left) and computed from NGA-West2 residuals (right) at $F = 1.33$, 1, and 0.5 Hz...61
Figure 4.14 ϕ versus distance for CENA compared to WUS ϕ at $F = 10$, 4, 2, 1.33, 1, and 0.5 Hz. 62
Figure 4.15 CENA ϕ versus distance in three magnitude bins compared to WUS ϕ at $F = 10$ Hz...64
Figure 4.16 CENA ϕ versus distance in three magnitude bins compared to WUS ϕ at $F = 4$ Hz...65
Figure 4.17 CENA ϕ versus distance in three magnitude bins compared to WUS ϕ at $F = 2$ Hz...66
Figure 4.18 CENA ϕ versus distance in three magnitude bins compared to WUS ϕ at $F = 1.33$ Hz...67
Figure 4.19 CENA ϕ versus distance in three magnitude bins compared to WUS ϕ at $F = 1$ Hz...68
Figure 4.20 CENA ϕ versus distance in three magnitude bins compared to WUS ϕ at $F = 0.5$ Hz...69
Figure 4.21 CENA ϕ versus V_{S30} at $F = 10$, 4, 2, 1.33, 1, and 0.5 Hz. 70
Figure 4.22 CENA ϕ versus frequency for the different V_{S30} codes. 71
Figure 4.23 ϕ_{SS} versus frequency for different minimum number of recordings per station (NRS) used in the regression...72
Figure 4.24 ϕ_{SS} versus frequency for PIE, tectonic, and all earthquakes for minimum number (Nmin) of three recordings per station and all magnitudes (left) and for earthquakes with a minimum **M** of 3.0 (right). 72
Figure 4.25 CENA ϕ_{SS} by region using all recordings (left) and recordings with a minimum **M** of 3.0 (right)...73
Figure 4.26 Comparison of CENA and NGA-West2 ϕ_{SS} versus frequency for the datasets with $\mathbf{M} \geq 3.0$ and all distances (left) and **M** between 3.0 and 6.0 and R_{RUP} distance up to 300 km (right)...73
Figure 4.27 ϕ_{SS} versus magnitude for CENA at $F = 10$, 4, 2, 1.33, 1, and 0.5 Hz. 75
Figure 4.28 Comparison of CENA and WUS ϕ_{SS} versus magnitude for R_{RUP} distance up to 500 km (left) and 300 km (right) at $F = 10$, 4, and 2 Hz. 76
Figure 4.29 Comparison of CENA and WUS ϕ_{SS} versus magnitude for R_{RUP} distance up to 500 km (left) and 300 km (right) at $F = 1.33$, 1, and 0.5 Hz. 77
Figure 4.30 ϕ_{SS} versus R_{RUP} distance for CENA at $F = 10$, 4, 2, 1.33, 1, and 0.5 Hz. 78

Figure 4.31 Comparison of CENA and WUS ϕ_{SS} versus R_{rup} for **M** greater than 3.0 (left) and **M** between 3.0 and 6.0 (right) at F = 10, 4, and 2 Hz. 79
Figure 4.32 Comparison of CENA and WUS ϕ_{SS} versus R_{RUP} for **M** greater than 3.0 (left) and **M** between 3.0 and 6.0 (right) at F = 1.33, 1, and 0.5 Hz. 80
Figure 4.33 Comparison of CENA and WUS ϕ_{SS} versus distance in three magnitude bins at F = 10 and 4 Hz. 81
Figure 4.34 Comparison of CENA and WUS ϕ_{SS} versus distance in three magnitude bins at F = 2 and 1.33 Hz. 82
Figure 4.35 Comparison of CENA and WUS ϕ_{SS} versus distance in three magnitude bins at F = 1 and 0.5 Hz. 83
Figure 4.36 ϕ_{SS} versus V_{S30} for CENA at F = 10, 4, 2, 1.33, 1, and 0.5 Hz. 84
Figure 4.37 Comparison of CENA and WUS ϕ_{SS} versus V_{S30} at F = 10, 4, 2, 1.33, 1, and 0.5 Hz. 85
Figure 4.38 CENA ϕ_{S2S} versus frequency for different minimum number of recordings per station (NRS) used in the regression. 87
Figure 4.39 CENA site terms as a function of V_{S30} for F = 10, 4, and 2 Hz. 88
Figure 4.40 CENA site terms as a function of V_{S30} for F = 1.33, 1, and 0.5 Hz. 89
Figure 4.41 CENA ϕ_{S2S} versus frequency for the different V_{S30} codes. 90
Figure 4.42 Comparison of ϕ_{S2S} for CENA stations with measured versus inferred V_{S30}. 90
Figure 4.43 Comparison of CENA ϕ_{S2S} for PIE and tectonic events. 91
Figure 4.44 Comparison of CENA ϕ_{S2S} versus V_{S30} for tectonic, PIE, and all earthquakes at F = 10, 4, 2, 1.33, 1, and 0.5 Hz. 92
Figure 4.45 Location of the stations that recorded PIEs (red) and tectonic events (blue) for F = 4 Hz. 93
Figure 4.46 Comparison of ϕ_{S2S} for CENA, NGA-West2, and Japan. 93
Figure 4.47 Metadata for Japan single-station sigma study. M_w and R_{RUP} obtained from the F-net catalog (blue crosses) and previously published finite fault source models (red circles) (see Dawood and Rodriguez-Marek [2015]). 94
Figure 4.48 Comparison of CENA and WUS ϕ_{S2S} versus V_{S30} at F = 10, 4, 2, 1.33, 1, and 0.5 Hz. 95
Figure 4.49 CENA τ, ϕ, ϕ_{SS}, and ϕ_{S2S} using three recordings per earthquake for τ and ϕ, and three recordings per station for ϕ_{SS} and ϕ_{S2S}. 97
Figure 4.50 Comparison of CENA ϕ (left) and τ (right) using the two-regression, iterative, and Bayesian regression approaches. 97
Figure 4.51 Geographical distribution of event terms at F = 4 Hz. 98
Figure 4.52 Geographical distribution of site terms at F = 4 Hz. 99
Figure 4.53 Geographical distribution of earthquakes and stations. 99
Figure 4.54 Comparison of ϕ (left) and τ (right) for all tectonic earthquakes and two subsets of tectonic earthquakes in the smaller regions. 100

Figure 5.1 Global τ model versus magnitude at PGV and F = 100, 10, 5, 2, and 1 Hz. 104
Figure 5.2 Global τ model versus magnitude at F = 0.33, 0.2, 0.13, and 0.1 Hz. 105

Figure 5.3 Coefficients of the global τ model versus frequency as derived (solid lines) and smoothed (dashed lines). 106
Figure 5.4 Standard deviations computed using point-source stochastic simulations with random κ values [Coppersmith et al. 2014]. 106
Figure 5.5 Standard deviations computed using point-source stochastic simulations with correlated κ values [Coppersmith et al. 2014]. 107
Figure 5.6 Between-model variability of global τ^2. 108
Figure 5.7 Within-model variability of global τ^2. 108
Figure 5.8 Total variability of global τ^2. 109
Figure 5.9 Constant CENA τ model. 111
Figure 5.10 Variability in constant CENA τ^2 model. 112
Figure 5.11 Coefficients of the CENA magnitude-dependent τ model. 112
Figure 5.12 Variability in CENA magnitude-dependent τ^2 model compared to the global model. 113
Figure 5.13 Comparison of candidate τ models for CENA. Dashed lines represent the 5th and 95th percentiles of the models. 113
Figure 5.14 Comparison of the candidate τ models for CENA to SWUS τ model. Dashed lines represent the 5th and 95th percentiles of the models. 114
Figure 5.15 Comparison of the candidate τ models for CENA to the Hanford τ model at M5.0, 6.0, and 7.0. Dashed lines represent the 5th and 95th percentiles of the models. 115
Figure 5.16 Global ϕ_{SS} model versus magnitude at PGV and F = 100, 10, 5, 2, and 1 Hz. 118
Figure 5.17 Global ϕ_{SS} model versus magnitude at PGV and F = 0.33, 0.2, and 0.1 Hz. 119
Figure 5.18 Coefficients of the global ϕ_{SS} model versus frequency. 120
Figure 5.19 Coefficient of variation (CV) of ϕ_{SS} at the stations in the ASK14 dataset for different number of recordings per station (N). The blue line represents the CV from a simulated ground-motion dataset where ϕ_{SS} at all stations are equal, hence the blue line represents pure sampling error. 122
Figure 5.20 Coefficient of variation (CV) for the ASK14 dataset for different number of recordings per station (N). The blue lines represent the CV of the realizations (N) of simulated datasets with different assigned CV. 122
Figure 5.21 Variability in the global ϕ_{SS}^2 model at **M** = 5.0 (coefficient *a*). 123
Figure 5.22 Variability in the global ϕ_{SS}^2 model at **M** = 6.5 (coefficient *b*). 123
Figure 5.24 Variability in constant CENA ϕ_{SS}^2 model. 125
Figure 5.25 Coefficients of magnitude-dependent CENA ϕ_{SS} model. 127
Figure 5.26 Variability in the magnitude-dependent CENA ϕ_{SS}^2 at **M** = 5.0 (coefficient *a*). 128
Figure 5.27 Variability in the magnitude-dependent CENA ϕ_{SS}^2 model at **M** = 6.5 (coefficient *b*). 128

Figure 5.28 Comparison of candidate ϕ_{SS} models for CENA versus magnitude at PGV and F = 100, 10, 5, 1, and 1 Hz. Dashed lines represent the 5th and 95th percentiles of the models. 129
Figure 5.29 Comparison of candidate ϕ_{SS} models for CENA versus magnitude at F = 0.33, 0.2, and 0.1 Hz. Dashed lines represent the 5th and 95th percentiles of the models. 130
Figure 5.30 Comparison of candidate ϕ_{SS} models for CENA versus frequency for **M** = 5.0, 6.0, and 7.0. Dashed lines represent the 5th and 95th percentiles of the models. 131
Figure 5.31 Comparison of the CENA ϕ_{SS} models to the Hanford model at F = 100 and 1 Hz. Dashed lines represent the 5th and 95th percentiles of the models. 135
Figure 5.32 Comparison of the CENA ϕ_{SS} models to one the SWUS magnitude-dependent ϕ_{SS} models derived from California data at F = 100 and 1 Hz. Dashed lines represent the 5th and 95th percentiles of the models. 136
Figure 5.33 ϕ_{S2S} mean model for CENA. 138
Figure 5.34 Variability of CENA ϕ_{S2S}^2. 138
Figure 5.35 Comparison of ϕ models for CENA versus magnitude at PGV and F = 100, 10, 5, 2, and 1 Hz. Dashed lines represent the 5th and 95th percentiles of the models. 145
Figure 5.36 Comparison of ϕ models for CENA versus magnitude at F = 0.33, 0.2, and 0.1 Hz. Dashed lines represent the 5th and 95th percentiles of the models. 146
Figure 5.37 Comparison of ϕ models for CENA versus frequency for **M** = 5.0, 6.0, and 7.0. Dashed lines represent the 5th and 95th percentiles of the models. 147
Figure 5.38 Comparison of ϕ models for CENA and NGA-West2 versus frequency for **M** = 5.0, 6.0, and 7.0. Dashed lines represent the 5th and 95th percentiles of the CENA models. 148
Figure 5.39 Comparison of three candidate single-station σ models for CENA versus magnitude at PGV and F = 100, 10, 5, 2, and 1 Hz. Dashed lines represent the 5th and 95th percentiles of the models. 154
Figure 5.40 Comparison of three candidate single-station σ models for CENA versus magnitude at PGV and F = 0.33, 0.2, and 0.1 Hz. Dashed lines represent the 5th and 95th percentiles of the models. 155
Figure 5.41 Comparison of three candidate single-station σ models for CENA versus frequency for **M** = 5.0, 6.0, and 7.0. Dashed lines represent the 5th and 95th percentiles of the models. 156
Figure 5.42 Comparison of three candidate single-station σ models for CENA and Hanford versus frequency for **M** = 5.0, 6.0, and 7.0. Dashed lines represent the 5th and 95th percentiles of the models. 157
Figure 5.43 Comparison of three candidate ergodic σ models for CENA versus magnitude at PGV and F = 100, 10, 5, 2, and 1 Hz. Dashed lines represent the 5th and 95th percentiles of the models. 163
Figure 5.44 Comparison of three candidate ergodic σ models for CENA versus magnitude at PGV and F = 0.33, 0.2, and 0.1 Hz. Dashed lines represent the 5th and 95th percentiles of the models. 164

Figure 5.45 Comparison of three candidate ergodic σ models for CENA versus frequency for **M** = 5.0, 6.0, and 7.0. Dashed lines represent the 5th and 95th percentiles of the models. 165
Figure 5.46 Comparison of three candidate ergodic global σ models for CENA and NGA-West2 models versus frequency for **M** = 5.0, 6.0, and 7.0. Dashed lines represent the 5th and 95th percentiles of the CENA global model. 166
Figure 5.47 Comparison of three candidate ergodic CENA σ model-1 and NGA-West2 models versus frequency for **M** = 5.0, 6.0, and 7.0. Dashed lines represent the 5th and 95th percentiles of CENA model-1. 167
Figure 5.48 Comparison of three candidate ergodic CENA σ model-2 and NGA-West2 models versus frequency for **M** = 5.0, 6.0, and 7.0. Dashed lines represent the 5th and 95th percentiles of CENA model-2. 168
Figure 5.49 Comparison of three candidate ergodic σ models for CENA to the EPRI 2013 and Atkinson et al. [2012] σ models versus frequency for **M** = 5.0, 6.0, and 7.0. Dashed lines represent the 5th and 95th percentiles of the CENA models. 169
Figure 5.50 Comparison of τ values obtained from mixed effects regressions using all CENA earthquakes, PIE-only and tectonic-only events. Only earthquakes with minimum **M** of 3.0 were used....................171
Figure 5.51 Comparison of ϕ_{SS} values obtained from mixed effects regressions using all CENA earthquakes, PIE-only and tectonic-only events. Only earthquakes with minimum **M** of 3.0 were used....................171
Figure 5.52 Comparison of ϕ_{S2S} values obtained from mixed effects regressions using all CENA earthquakes, PIE-only and tectonic-only events. Earthquakes with **M** greater than 2.0 were used....................172
Figure 5.53 Magnitude and distance distribution of the Gulf region data at F = 4 Hz. 175
Figure 5.54 Comparison of CENA τ models at **M**5.0 to τ values for the Gulf region. Dashed lines represent the 5th and 95th percentiles of the CENA models............175
Figure 5.55 Comparison of CENA ϕ_{SS} models at M5.0 to ϕ_{SS} values for the Gulf region. Dashed lines represent the 5th and 95th percentiles of the CENA models. 176
Figure 5.56 Comparison of CENA ϕ_{S2S} model to ϕ_{S2S} values for the Gulf region. Dashed lines represent the 5th and 95th percentiles of the CENA ϕ_{S2S} model....................176

1 Introduction

1.1 SCOPE

Ground-motion models (GMMs) or ground-motion prediction equations (GMPEs) usually describe the distribution of ground motion in terms of a median and a logarithmic standard deviation for the average horizontal component of peak ground acceleration (PGA), peak ground velocity (PGV), and 5%-damped elastic pseudo-spectral acceleration response spectral ordinates (PSA) for a wide range of oscillator periods (e.g., often from 0.01 to 10 sec). The standard deviation models developed using a broad range of earthquakes, sites, and regions are typically used to analyze the hazard at a single site from a relatively small source region. Such practice is referred to as the ergodic assumption [Anderson and Brune 1999] and assumes that the ground-motion variability at a single site-source combination is the same as the ground-motion variability observed in a global dataset.

In recent years, the availability of well-recorded ground motions at single sites from multiple occurrences of earthquakes allowed researchers and practitioners to partially remove the ergodic assumption by estimating the repeatable site effects and removing them from the ground-motion variability. This leads to a reduction in the aleatory ground-motion variability but requires using a site-specific median ground-motion model with increased epistemic uncertainty. This epistemic uncertainty is typically manifested by additional branches in the ground-motion logic tree. Models for single-station standard deviations have been developed and used on large projects such as the PEGASOS Refinement Project (PRP) [Renault et al. 2010]., BC Hydro Probabilistic Seismic Hazard Assessment Project [BC Hydro 2011], Thyspunt Nuclear Siting Project [Bommer et al. 2013], the Hanford Probabilistic Seismic Hazard Analysis Project [Coppersmith et al. 2014], and the Southwestern United States Ground-Motion Characterization Level 3 SSHAC Project [GeoPentech 2015].

A database of the ground motion recorded in Central and Eastern North America (CENA) was collected and processed by the NGA-East project [Goulet et al. 2014]. This database was used to analyze the different components of ground-motion variability in CENA. Moreover, the NGA-West2 project collected and processed the largest ground-motion database to date with repeatable recordings per earthquake and per station [Ancheta et al. 2014]. This study makes use of the NGA-West2 dataset to gain insight on the behavior of the ground-motion variability in magnitude, distance, and frequency ranges that are not well populated in the NGA-East database. Candidate models for ergodic σ and single-station σ are proposed for use in CENA and discussed herein. These models are applicable for magnitude 4.0 to 8.2, distance up to 1000 km, and for PGA, PGV, and PSA at periods of 0.01 to 10 sec (frequencies of 0.1 to 100 Hz).

1.2 BACKGROUND ON GROUND-MOTION VARIABILITY AND ITS COMPONENTS

Probabilistic seismic hazard analyses (PSHA) typically aim to evaluate the hazard at a single-site from a relatively small source region. This requires characterizing the ground motion (median and variability) at a particular site due to the future occurrence of different earthquakes. Because repeated recordings at the site of interest are usually not available, the ergodic assumption [Anderson and Brune 1999] is adopted whereby the ground-motion variability over different sites and source regions is assumed applicable to an individual site. The availability of repeated recordings at individual stations in recent ground-motion databases allowed for the estimation of the site-to-site variability and for removing it from the ground-motion aleatory variability. This leads to a reduced aleatory variability, as observed in previous studies (e.g., Chen and Tsai [2002]; Atkinson [2006]; Morikawa et al. [2008]; Lin et al. [2011]; Rodriguez-Marek et al. [2011]; Chen and Faccioli [2013]; Rodriguez-Marek et al. [2013]; and Luzi et al. [2014]). Partially removing the ergodic assumption requires adjusting the median ground-motion models to be site-specific and the proper accounting for the increased epistemic uncertainty resulting from the limited knowledge of the site-specific adjustment factors.

The use of single-station σ allows for proper identification of the various components of ground-motion variability, where some of the apparent randomness can be transformed to epistemic uncertainty. With the acquisition of additional data, this epistemic uncertainty can—in theory—be removed or decreased. Moreover, the use of single-station σ has the advantage of avoiding double counting of the uncertainty in cases where the site-to-site variability is part of the total σ, and where site-specific response analyses are carried out and the uncertainty in the site amplification factors is properly captured. The components of ground-motion variability are described in Al Atik et al. [2010] and a brief review of the components and notations relevant to this study is provided here. Table 1.1 summarizes the adopted notation following Al Atik et al. [2010] for the components of the ground-motion residuals and their respective standard deviations.

The ground-motion residual (Δ_{es}) represents the difference (in natural log units) between observed ground motion and the median predicted by GMPEs. Total residuals can be separated into between-event residuals (δB_e) and within-event residuals (δW_{es}):

$$\Delta_{es} = \delta B_e + \delta W_{es} \tag{1.1}$$

where subscripts e and s refer to earthquake and station, respectively. The between-event and within-event residuals have standard deviations denoted as τ and ϕ, respectively, and are assumed to be uncorrelated. As a result, the total ergodic standard deviation σ can be written as:

$$\sigma = \sqrt{\phi^2 + \tau^2} \tag{1.2}$$

In turn, the within-event residual can be separated into the site-to-site term $\delta S2S_s$ and the single-station within-event residual δWS_{es}:

$$\delta W_{es} = \delta S2S_s + \delta WS_{es} \tag{1.3}$$

where $\delta S2S_s$ represents the systematic deviation of the ground motion at site s from the median event-corrected ground motion predicted by the GMPE. δWS_{es} is the site-corrected and event-corrected residual referred to as single-station within-event residual. The site-to-site term and the single-station within-event residuals have standard deviations denoted as ϕ_{S2S} and ϕ_{SS}, respectively. The total single-station standard deviation (single-station sigma, σ_{SS}), sometimes referred to as the partially non-ergodic sigma and the ergodic standard deviation (σ), can be written as:

$$\sigma_{SS} = \sqrt{\phi_{SS}^2 + \tau^2} \tag{1.4}$$

$$\sigma = \sqrt{\phi_{S2S}^2 + \phi_{SS}^2 + \tau^2}. \tag{1.5}$$

The use of single-station sigma in PSHA requires the estimation of the median site term ($\delta S2S_s$) and its associated epistemic uncertainty. This is typically done through site response analyses or through the analysis of ground-motion data recorded at the site, if available. When ground-motion recordings are used to estimate the site term, epistemic uncertainty arises from the limited number of recordings available. As the number of recordings increases, the epistemic uncertainty on the value of the site term typically decreases. On the other hand, site response analyses have inherent uncertainties both in the input parameters and the modeling processes, and these lead to epistemic uncertainty in the estimated site term. Another requirement for the application of partially non-ergodic σ is that the epistemic uncertainty in the single-station within-event standard deviation is estimated and accounted for in the ground-motion logic tree. This requirement arises from observations that there is non-negligible variability in the standard deviation of site- and event-corrected residuals at a single station ($\phi_{SS,S}$) compared to the average ϕ_{SS} estimated over all the stations in the database [Rodriguez-Marek et al. 2013]. This uncertainty could be due to site-specific features such as topography or subsurface layering.

Table 1.1 Summary of terminology for residual components and standard deviations (*SD* denotes standard deviation).

Residual Component	Residual Notation	Standard Deviation Component	Standard Deviation Notation
Total residual	Δ_{es}	Total or ergodic standard deviation	σ
Between-event residual (event term)	δB_e	Between-event (inter-event) standard deviation (τ)	$\tau = SD(\delta B_e)$
Within-event residual (intra-event residual; event-corrected residual)	δW_{es}	Within-event (intra-event) standard deviation (ϕ)	$\phi = SD(\delta W_{es})$
Site-to-site residual (site term)	$\delta S2S_s$	Site-to-site variability	$\phi_{S2S} = SD(\delta S2S_s)$
Single-station within-event residual (site- and event-corrected residual)	δWS_{es}	Single-station within-event standard deviation (single-station ϕ)	$\phi_{SS} = SD(\delta WS_{es})$

1.3 APPROACH

The goal of this study is to analyze the components of ground-motion variability in CENA and develop candidate standard deviation models applicable for the ground motion in CENA. The adopted approach consists of evaluating the individual components of ground-motion variability (τ, ϕ, ϕ_{SS}, and ϕ_{S2S}) in CENA and comparing them to the observed variability in other regions, particularly active tectonic regions, making use of the abundant NGA-West2 dataset. Comparing the ground-motion variability in CENA to the variability in other regions is necessary to inform the extrapolation of the standard deviation models for CENA beyond the magnitude range available in the NGA-East dataset, where the largest recorded magnitude is 6.8.

Dividing the variability into its components allows a better understanding of the sources of variability. Moreover, such breakdown allows the use of single-station σ for sites where site-specific analyses are performed or ground-motion recordings are available, thus avoiding double-counting of the site-to-site variability. Another advantage of this approach is that the value of the single-station within-event standard deviation (ϕ_{SS}) has been observed to be relatively constant across different regions and tectonic environments [Rodriguez-Marek et al. 2013]. The observed lack of regional dependence in ϕ_{SS} allows the use of global datasets for estimating CENA ϕ_{SS}, thus bypassing the data limitations in the NGA-East dataset.

This report presents the results of the analysis of between-event, within-event, single-station within-event, and site-to-site standard deviations for CENA, and compares them to the corresponding components of variability observed in the NGA-West2 dataset. Candidate models for τ, ϕ_{SS}, and ϕ_{S2S} are developed and presented.

1.4 PAST STUDIES

1.4.1 Ergodic σ for CENA

Previous CENA ground-motion studies developed ergodic standard deviation models. Aleatory variability models associated with exiting CENA GMPEs range from values of 0.55 to 0.62 natural log units proposed by Atkinson and Boore [1995] based on empirical data to values of 0.75 to 0.95 proposed by Silva et al. [2002] based on parametric variability and model misfit to empirical data. Toro et al. [1997] evaluated the modeling and parametric components of the aleatory variability based on the predictions of the stochastic ground-motion model, and their sigma values are magnitude, distance, and frequency-dependent ranging from around 0.53 to 0.88 natural log units. The EPRI [2004] study developed a model for aleatory variability based on evaluating the range of σ associated with the GMPEs available at the time of the study. An additional component of variability was added at small distances for the GMPEs using the R_{JB} distance measure due to the range in the possible rupture distances for a given value of R_{JB}. Atkinson and Boore [2006] evaluated the aleatory variability of ground motion based on the uncertainty in the simulation parameters to be equal to 0.3 in log10 units at all frequencies, magnitudes, and distances.

Other ground-motion models for Eastern and North America (ENA) based their aleatory variability models on those of active tectonic regions. Campbell [2003] evaluated the aleatory variability of ground motion in ENA using the hybrid empirical approach. His σ model is based on the aleatory variability of GMPEs in active tectonic regions, with a small additional component to account for the fact that some of the host GMPE parameters are treated as random variables. His σ values were magnitude- and frequency-dependent, ranging in values from 0.41 in natural log units for magnitudes greater than 7.16 to 0.80 for magnitude 4.0. Tavakoli and Pezeshk [2005] based their aleatory variability model for ENA on an average of aleatory variability values from Western U.S. (WUS) GMPEs. Pezeshk et al. [2011] used an average of the aleatory variability published in NGA-West1 models to represent the aleatory variability in ENA ground motions.

In 2006, EPRI performed an extensive evaluation of the between-event and the within-event components of the aleatory variability in the Central and Eastern U.S. (CEUS) using a variety of datasets [EPRI 2006]. Their study concluded that the between-event variability for CEUS earthquakes is slightly larger than that for earthquakes in active tectonic regions; therefore, they increased τ by 0.03 natural log units. In addition, they found that the within-event variability for CEUS earthquakes is similar to or slightly smaller than that of earthquakes in active tectonic regions. Two branches were adopted to model ϕ: (1) a favored model with weight of 0.7 whereby ϕ in CEUS is similar to that in active tectonic regions; and (2) a ϕ model with a weight of 0.3 based on ϕ in active tectonic regions decreased by 0.03 natural log units. EPRI used the variability at 10 Hz for active tectonic regions to represent the variability in CEUS ground motion between 10 and 25 Hz based on the fact that CEUS ground motions have larger high-frequency energy than in the WUS. Finally, EPRI found no strong basis for increasing ϕ at small distances when the R_{JB} distance measure is used. Their preferred model did not include an increase in ϕ at small R_{RUP} values; however, two alternative models with combined weight of 0.4 included additional variability for R_{JB} values less than or equal to 10 km [EPRI 2006].

Based on the conclusion of the 2006 EPRI study that the aleatory variability of ground motions in CEUS is similar to that in active tectonic regions, in 2013 EPRI based their aleatory variability model on the average of preliminary aleatory variability values of four NGA-West2 models (not including Idriss [2014]) [EPRI 2013]. This aleatory variability model has magnitude breaks in the magnitude dependence at **M** at 5.0, 6.0, and 7.0. Similar to the 2006 study, the 2013 study increased τ by 0.03 natural log units to adjust the values derived for active tectonic regions for application in CEUS. In addition, the values of τ and ϕ between 10 Hz and PGA were set equal to the value at 10 Hz to account for the increase in high-frequency content of the CEUS ground motions. The 2013 study favored model (weight 0.6) shows no increase in the aleatory variability at small values of R_{JB}; an alternative model includes an additional aleatory component with a maximum of 0.16 for R_{JB} values less than 10 km.

Recently, Atkinson [2013] evaluated empirical ground-motion data and also concluded that aleatory variability in CENA ground motions should be similar to that in active tectonic regions. Atkinson et al. [2012] have implemented this concept in proposed ground-motion models for use in updating the seismic hazard maps for Canada.

1.4.2 Single-Station σ

The development and use of single-station aleatory variability models has not been common practice in CEUS primarily due to data limitations and the insufficient number of repeated recordings at individual stations. Atkinson [2013] used ground-motion data from small-to-moderate magnitude earthquakes recorded at six stations in the Charlevoix region of Canada to evaluate the aleatory variability in ENA ground motions. Atkinson [2013] estimated single-station σ to be in the range of 0.23–0.28 in log10 units and concluded that single-station σ in ENA is similar to that observed in California [Atkinson 2006].

Since single-station within-event standard deviation (ϕ_{SS}) models have been observed to be stable across regions and tectonic environment, it is worthwhile to summarize the existing ϕ_{SS} models outside of CENA. The concept of partially non-ergodic PSHA and the associated single-station σ was first formulated by Anderson and Brune [1999]. A recent increase in repeated ground-motion recordings at individual stations allowed the estimation of the site terms and removing them from the ground-motion variability, leading to the development of single-station σ models (e.g., Chen and Tsai [2002]; Atkinson [2006]; Morikawa et al. [2008]; Lin et al. [2011]; Rodriguez-Marek et al. [2011]; Chen and Faccioli [2013]; Rodriguez-Marek et al. [2013]; and Luzi et al. [2014]). This review focuses on the recent ϕ_{SS} models that were developed from large datasets.

Rodriguez-Marek et al. [2013] developed ϕ_{SS} models derived from a global dataset with $\mathbf{M} \geq 4.5$ and $R_{RUP} \leq 200$ km compiled as part of the PEGASOS Refinement Project (PRP) [Renault et al. 2010]. The PRP dataset consisted of residuals of ground-motion data from California (Chiou et al. [2010] model for small magnitude events and the Abrahamson and Silva [2008] model for larger magnitude events), Taiwan (Lin et al. [2011] data), Switzerland (Edwards and Fäh [2013]), Japan (Rodriguez-Marek et al. [2011]), and Turkey (Akkar et al. [2010]). A minimum of five recordings per earthquake and per station was imposed on the dataset for the residuals analysis.

Rodriguez-Marek et al. [2013] observed that the value of ϕ_{SS} appears to be largely region-independent. Moreover, ϕ_{SS} values obtained from this study were comparable to ϕ_{SS} values estimated in Lin et al. [2011] study using ground-motion data from Taiwan and Abrahamson et al. [2014b] using global data from subduction regions. Rodriguez-Marek et al. [2013] observed that an average ϕ_{SS} value of 0.45 (natural log units) seems to be a good fit to their results across all periods. Rodriguez-Marek et al. [2013] also observed that ϕ_{SS} shows a magnitude-dependent trend with values decreasing from a maximum at **M**5.0 to a minimum at **M**7.0, and a distance-dependence for small magnitude events. As a result, three candidate models were adopted in the PRP (referred to as PRP models): constant ϕ_{SS} model (magnitude- and distance-independent; homoscedastic), distance-dependent ϕ_{SS} model, and magnitude- and distance-dependent ϕ_{SS} model.

The Thyspunt Nuclear Siting Project (TNSP) in South Africa [Bommer et al. 2013; Rodriguez-Marek et al. 2014] developed ϕ_{SS} models based on the PRP data with $\mathbf{M} \geq 5.0$ (data from California, Japan, and Taiwan). The TNSP adopted two ϕ_{SS} models: a homoscedastic model with ϕ_{SS} = 0.45 and a magnitude-dependent model. The Hanford Probabilistic Seismic Hazard Analysis Project, referred to herein as the Hanford Project [Coppersmith et al. 2014], developed ϕ_{SS} models for crustal and subduction earthquakes. For crustal earthquakes, the Hanford Project used the PRP data with $\mathbf{M} \geq 5.0$ to develop a magnitude-dependent ϕ_{SS} model. For subduction earthquakes, the Hanford project used a global dataset of interface and intra-slab earthquakes (BC Hydro dataset augmented with data from Japan, Chile, and Central America) to develop a homoscedastic ϕ_{SS} model with ϕ_{SS} = 0.45 at all periods.

The Southwestern United States Ground-Motion Characterization Level 3 SSHAC Project (SWUS) [GeoPentech 2015] used a global dataset consisting of the NGA-West2 data

[Ancheta et al. 2014] supplemented with the Lin et al. [2011] data from Taiwan as well as the European dataset of Akkar et al. [2014] to develop ϕ_{SS} models for the Diablo Canyon Power Plant (DCPP) and the Palo Verde Nuclear Generating Station (PVNGS) sites. A minimum of three recordings per station was used in the analysis of the within-event residuals. Five ϕ_{SS} models were developed for the SWUS project focusing on magnitude and distance ranges of importance to the hazard at DCPP and PVNGS. Two ϕ_{SS} models were developed using the global dataset (NGA-West2 and additional Taiwanese data). These global ϕ_{SS} models are homoscedastic and were derived using data with $\mathbf{M} \geq 5.0$ and R_{RUP} less than 50 km and with $\mathbf{M} \geq 5.5$ and R_{RUP} between 200 and 400 km, respectively. Two magnitude-dependent ϕ_{SS} models were derived using California NGA-West2 ground-motion data with R_{RUP} less than 50 km. These models have magnitude breaks at **M**5.0 and 7.0, and **M**5.0 and 5.5, respectively. A homoscedastic ϕ_{SS} model was developed using the European dataset of Akkar et al. [2014] with $\mathbf{M} \geq 5.0$ and distance less than 50 km.

2 Datasets

2.1 NGA-EAST

The CENA dataset compiled and processed by the NGA-East project was used to evaluate ground-motion residuals and the components τ, ϕ, ϕ_{SS}, and ϕ_{S2S} of ground-motion variability in CENA [Goulet et al. 2014]. Recordings were excluded from the analysis if they satisfied one of the following criteria:

- Recordings flagged for having data issues known to impact ground motions;
- Recordings flagged for having residuals with respect to Atkinson and Boore [2006 and 2011] that fall outside of +/-4σ at PGA, PGV, and PSA (0.05 sec);
- Recordings flagged for having the station, earthquake or both located outside of the CENA defined regions with the exception of the three recordings from the Nahanni earthquake kept for being the only event in the CENA flatfile with magnitude greater than 6.0; and
- Ground-motion recordings from the Gulf Coast and Mississippi Embayment Region (GC).

While the maximum distance in the NGA-East dataset is on the order of 3000 km, only ground-motion data with maximum distance of 500 km were considered reliable for use in this analysis. Earthquakes with a minimum of three recordings each were used to compute the within-event and between-event residuals at each spectral period. The analysis was performed for spectral periods of 0.03, 0.04, 0.05, 0.075, 0.1, 0.15, 0.2, 0.25, 0.3, 0.4, 0.5, 0.75, 1.0, 1.5, 2.0, 3.0, 4.0, 5.0, 7.5, and 10.0 sec (frequencies of 30.33, 25, 20, 13.33, 10, 6.67, 5, 4, 3.33, 2.5, 2, 1.33, 1, 0.67, 0.5, 0.33, 0.25, 0.2, 0.13, and 0.1 Hz), and PGV taking into the account the useable frequency bandwidth of the recordings. Note that the analysis could not be performed for frequencies greater than 30.33 Hz due to insufficient data at high frequencies resulting from the limited frequency bandwidth of the recordings.

The magnitude and distance distribution of the ground-motion data used in the within-event and between-event residuals analysis is shown in Figure 2.1 at a frequency F = 4 Hz. Figure 2.1 shows that CENA earthquakes range in magnitude from 2.57 to 6.76. The dataset consists of tectonic earthquakes and potentially-induced earthquakes (PIEs), as classified by the USGS. Table 2.1 lists the number of PIE and tectonic recordings, earthquakes, and stations in the dataset at F = 4 Hz. Figure 2.2 shows the magnitude and distance distribution of the CENA data by region whereby the regions are defined based on the source-to-site paths location as follows:

- Region 2 consists of paths contained within Central North America and has 1521 recordings at $F = 4$ Hz;
- Region 3 consists of paths contained within the Appalachian Province and has 117 recordings at $F = 4$ Hz;
- Region 4 consists of paths contained within the Atlantic Coastal Plain and has 13 recordings at $F = 4$ Hz;
- Region 5 consists of paths crossing at least two of the regions defined above and has 191 recordings at $F = 4$ Hz.

The magnitude and hypocentral depth distribution of the 62 CENA earthquakes used in the between-event and within-event residuals analysis is shown in Figure 2.3, with PIE having shallower average depth than the tectonic events. The CENA stations have V_{S30} ranging from 144 to 2000 m/sec. Figure 2.4 shows the number of stations in different V_{S30} bins, and indicates that most of the stations in the dataset have V_{S30} ranging between 250 and 750 m/sec. A relatively small number of stations in the dataset (53 stations at $F = 4$ Hz) had measured V_{S30}, and other proxies were used to assign V_{S30} at the station locations where measurements were unavailable. Codes were given to the stations to indicate the method used to assign "preferred" V_{S30} as follows (Chapter 5 of [Goulet et al. 2014]):

- Code 0: V_{S30} is based on measurements;
- Code 1: V_{S30} is based on known site conditions and geology based on measurements at a different location with the same geological condition. This assignment is only used based on a recommendation or site visit from a geologist;
- Code 2: V_{S30} is based on the *P*-wave seismogram method [Kim et al. 2014] and only used for sites with estimated $V_{S30} \geq 760$ m/sec;
- Code 3: V_{S30} is based on hybrid slope-geology method [Thompson and Silva 2013]; only used for sites with estimated $V_{S30} \geq 760$ m/sec;
- Code 4: V_{S30} is weighted average of estimates from all available proxies; and
- Code 5: V_{S30} is weighted average of estimates from all available proxies when estimates from the *P*-wave seismogram method are not available.

Table 2.1 Number of recordings, earthquakes and stations at *F* = 4 Hz used in the within-event and between-event residuals analysis.

	No. of Recordings	No. of Earthquakes	No. of Stations
Tectonic	1122	53	345
PIE	720	9	181
Total	1842	62	447

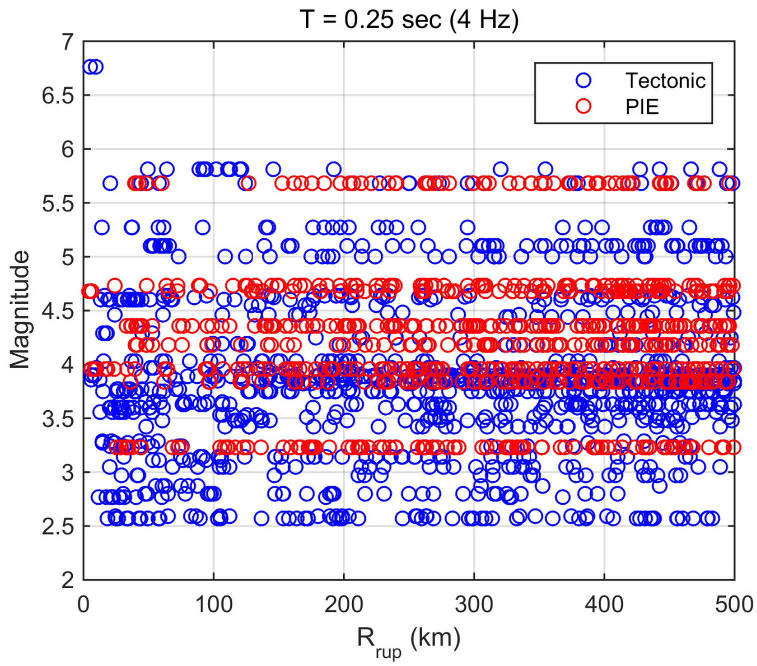

Figure 2.1 Magnitude and distance distribution of the CENA ground-motion data used in the between-event and within-event residuals analysis at *F* = 4 Hz.

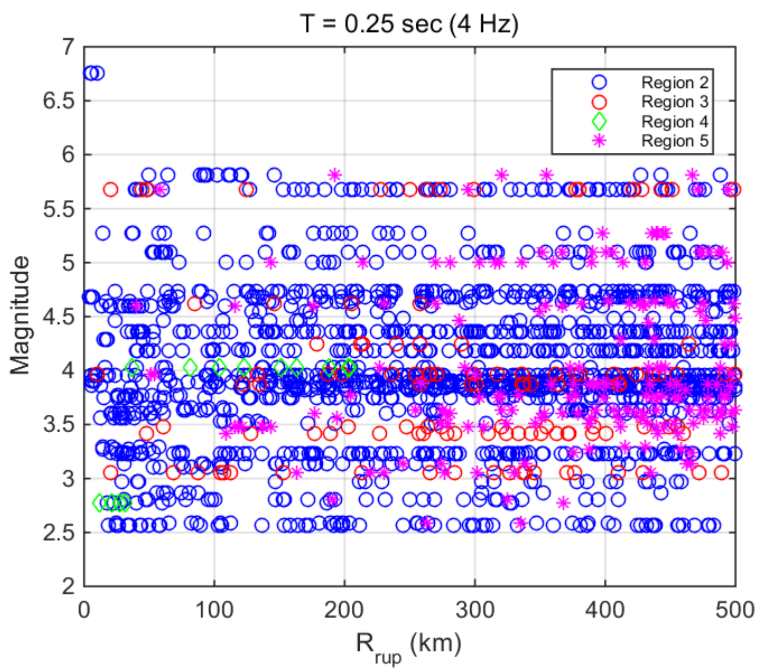

Figure 2.2 Magnitude and distance distribution of the CENA ground-motion data by region used in the between-event and within-event residuals analysis at *F* = 4 Hz.

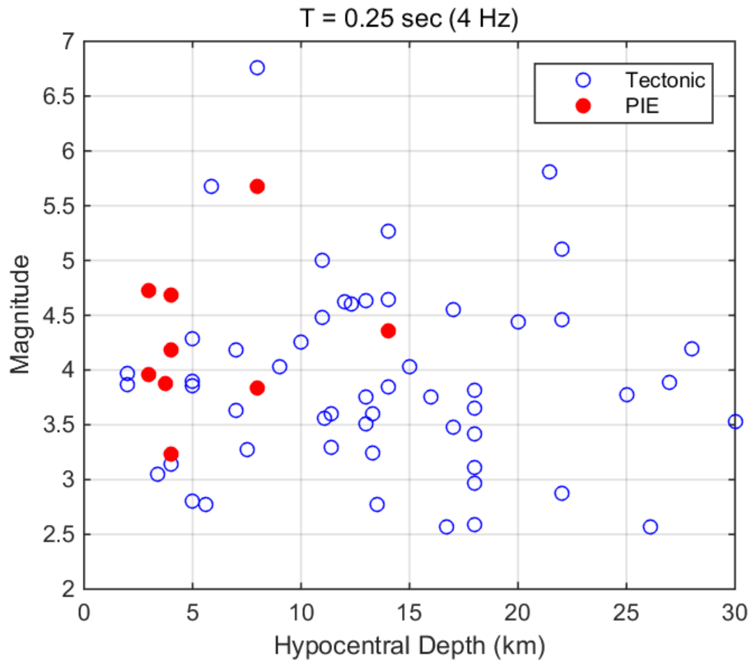

Figure 2.3 **Magnitude and hypocentral depth distribution of the CENA earthquakes used in the between-event and within-event residuals analysis at *F* = 4 Hz.**

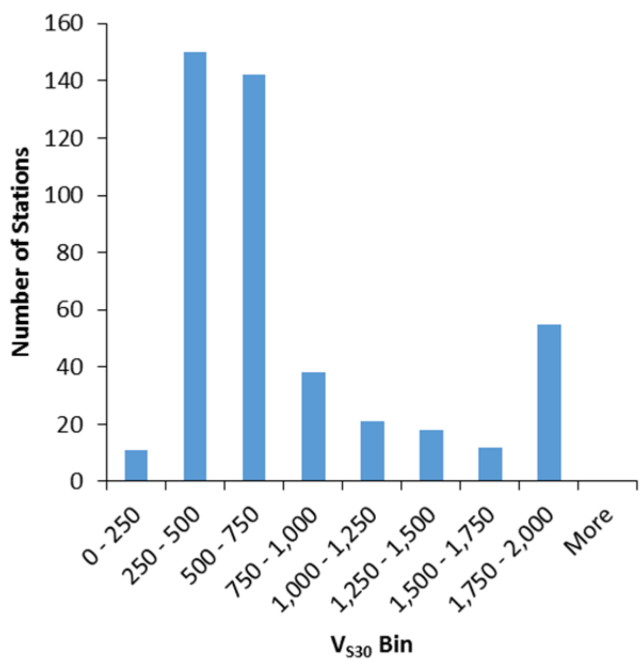

Figure 2.4 **Histogram of the number of stations in the V_{S30} bins for the dataset used in the between-event and within-event residuals analysis at *F* = 4 Hz.**

Figure 2.5 shows the number of stations and recordings in the dataset for the different V_{S30} codes at F = 4 Hz, indicating that only 53 stations have measured V_{S30} values and most of the stations are assigned to Code 5. Figure 2.6 shows the total number of recordings versus spectral periods, indicating that spectral periods outside 0.075 to 2.0 sec (frequency between 0.5 and 13.33 Hz) cannot be reliably used to evaluate ground-motion variability due to the limited useable frequency bandwidth of the recordings. Figure 2.7 shows a histogram of the number of stations versus bins of number of recordings, indicating that the majority of the stations recorded less than three earthquakes each.

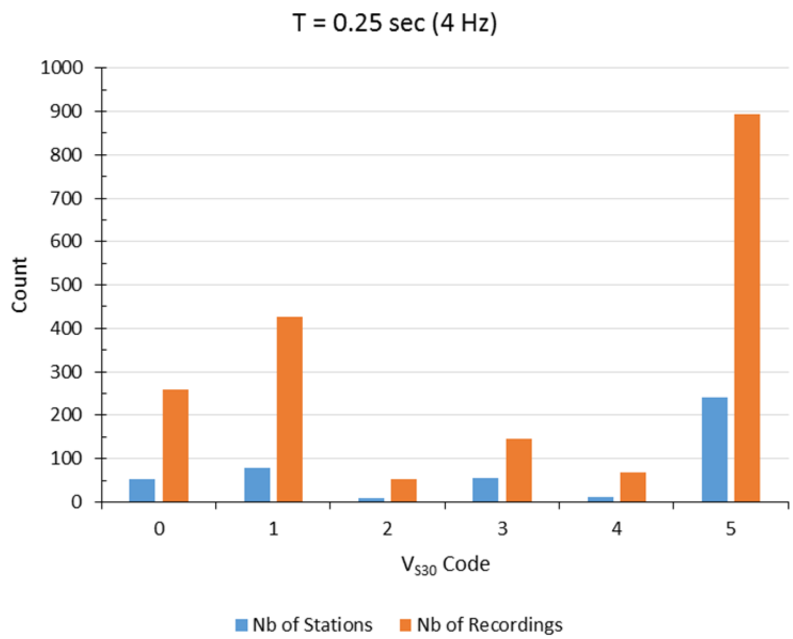

Figure 2.5 **Number of stations and recordings with different assigned V_{S30} codes used in the between-event and within-event residuals analysis at F = 4 Hz.**

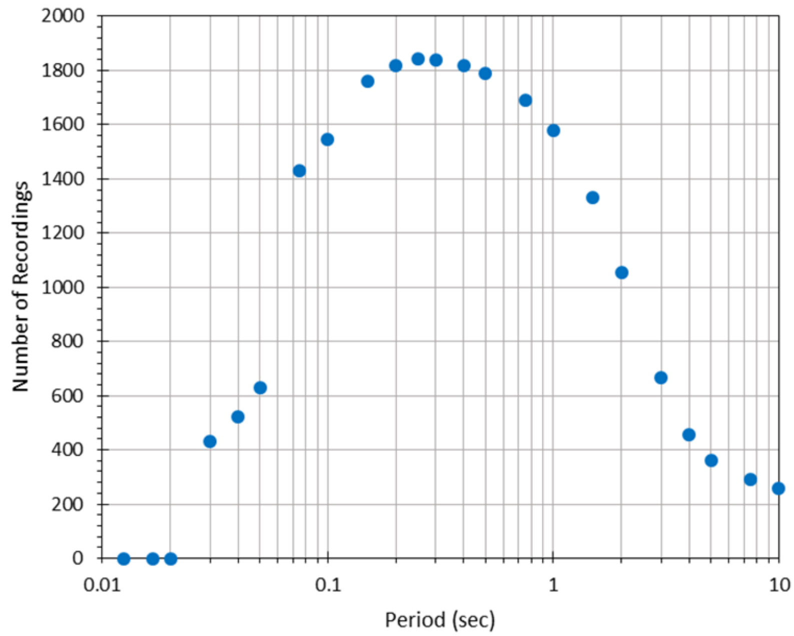

Figure 2.6 **Number of recordings versus spectral period for the dataset used in the between-event and within-event residuals analysis.**

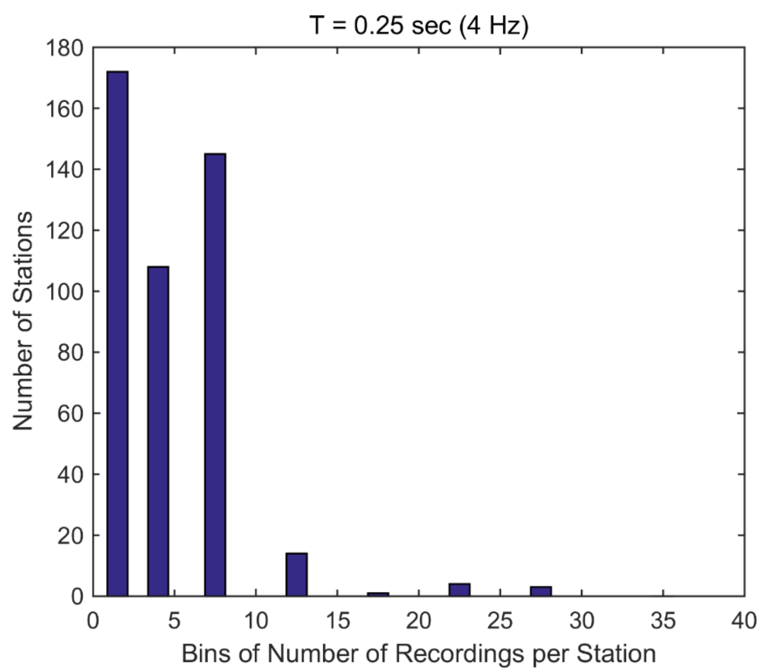

Figure 2.7 **Histogram of the number of stations versus bins of the number of recordings per station for the dataset used in the between-event and within-event residuals analysis at *F* = 4 Hz.**

The single-station analysis was performed using a subset of the CENA dataset consisting of stations that recorded a minimum of three earthquakes each. This criterion was applied to obtain a reliable estimate of the site terms. Figure 2.8 shows the magnitude and distance distribution of the recordings, and Table 2.2 summarizes the number of recordings, earthquakes, and stations used in this analysis. Figure 2.9 shows the number of stations in different V_{S30} bins, indicating that most of the stations have V_{S30} values ranging from 250 to 750 m/sec. Figure 2.10 shows the number of recordings versus spectral period used in the single-station analysis, indicating that spectral periods outside 0.075 to 2.0 sec (frequency between 0.5 and 13.33 Hz) cannot be reliably used to evaluate ϕ_{SS} and ϕ_{S2S} due to the frequency bandwidth limitations of the recordings.

Table 2.2 Number of recordings, earthquakes and stations used in the single-station analysis at *F* = 4 Hz.

	No. of Recordings	No. of Earthquakes	No. of Stations
Tectonic	927	51	189
PIE	691	9	161
Total	1618	60	275

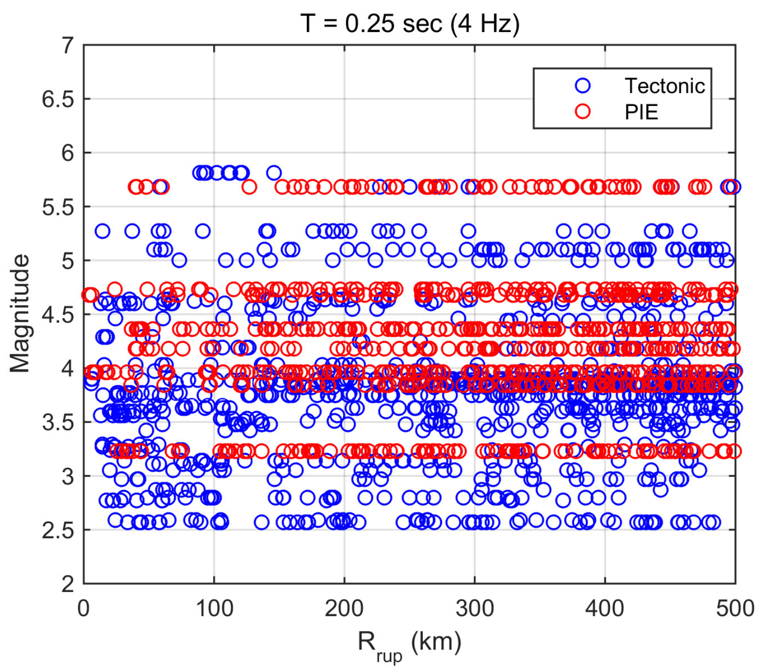

Figure 2.8 Magnitude and distance distribution of the CENA ground-motion data used in the single-station analysis at *F* = 4 Hz.

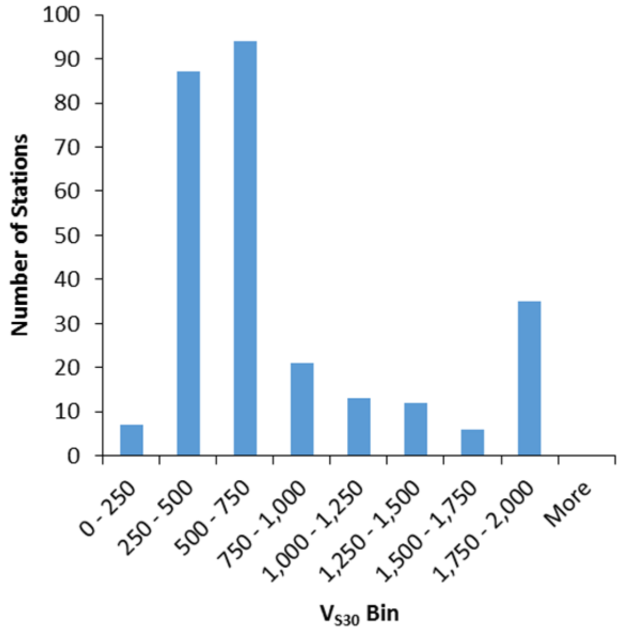

Figure 2.9 **Histogram of the number of stations in different V_{S30} bins for the dataset used in the single-station analysis at F = 4 Hz.**

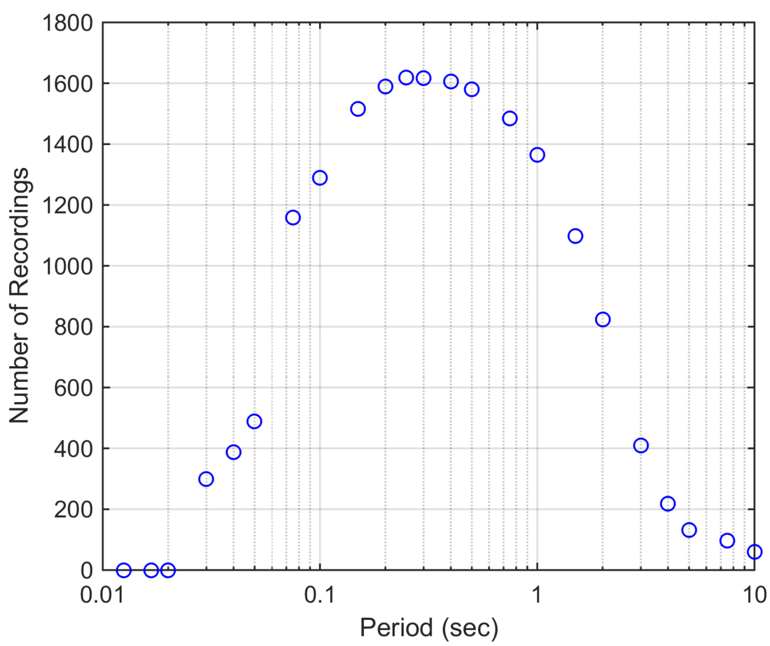

Figure 2.10 **Number of recordings versus spectral period for the dataset used in the single-station analysis.**

2.2 NGA-WEST2

This study relies on comparisons of the components of ground-motion variability in CENA to those observed in WUS to inform the extrapolation of the aleatory variability in CENA to magnitude, distance, and frequency ranges not well covered in the CENA dataset. Four sets of NGA-West2 GMPE within-event and between-event residuals were used in this analysis: Abrahamson et al. [2014a] (ASK14), Boore et al. [2014] (BSSA14), Campbell and Bozorgnia [2014] (CB14), and Chiou and Youngs [2014] (CY14). Idriss [2014] residuals were not used because within-event and between-event residuals were not provided for this GMPE. These datasets consist of ground-motion data recorded primarily in California, with additional data from Taiwan, Japan, Italy, China, and other active tectonic regions. The data distributions of the four sets of NGA-West2 residuals are discussed in the *Earthquake Spectra* Special Issue on the NGA-West2 Project (see references for each of the models). Provided herein is an overview of the subsets of the four NGA-West2 datasets used in the single-station analysis.

The NGA-West2 single-station analysis was performed using stations that recorded a minimum of three earthquakes each. Plots of the magnitude-distance distribution, V_{S30} histograms, and number of recordings histograms are provided in Figures 2.11 to 2.14 for the four sets of residuals with stations with a minimum of three recordings each. A summary of the number of recordings, earthquakes, and stations is listed in Table 2.3 for the four GMPEs. Figures 2.11 to 2.15 show that the four NGA-West2 datasets consist of recordings with magnitude 3.0 to 8.0 and distances up to 400 km. CB14 performed their regression on ground-motion data with distance less than 80 km and then applied an additional distance scaling term for distance greater than 80 km. Most of the recording stations have V_{S30} that fall in the range of 200 to 600 m/sec.

Table 2.3 Number of recordings, earthquakes, and stations in the NGA-West2 datasets used in the single-station analysis.

	No. of Recordings	No. of Earthquakes	No. of Stations
ASK14	13,020	297	1227
BSSA14	15,466	377	1344
CB14	5285	244	535
CY14	9197	269	798

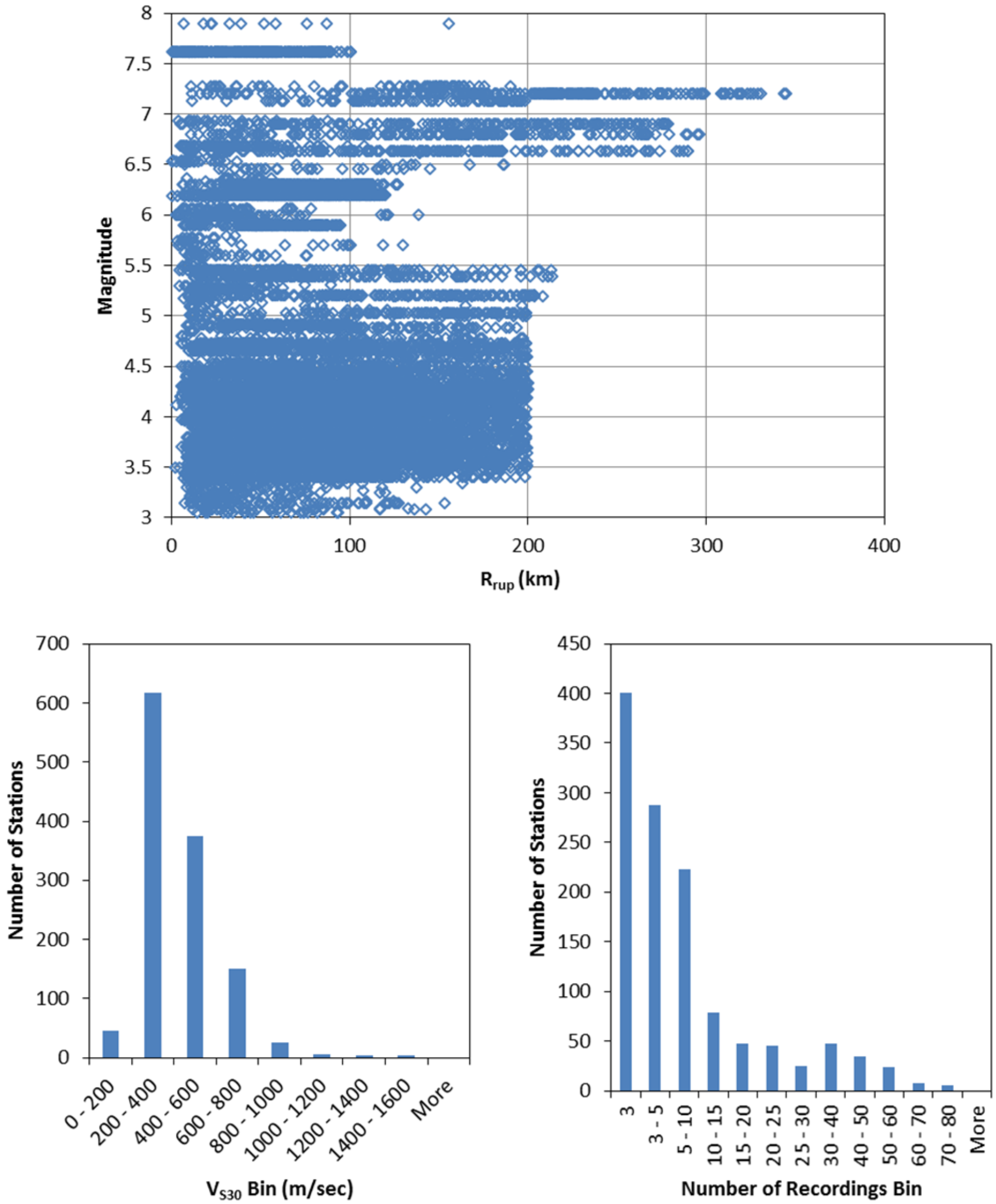

Figure 2.11 **Data distribution (magnitude-distance plot, V_{S30} histogram, and number of recordings histogram) for the ASK14 dataset used in the single-station analysis.**

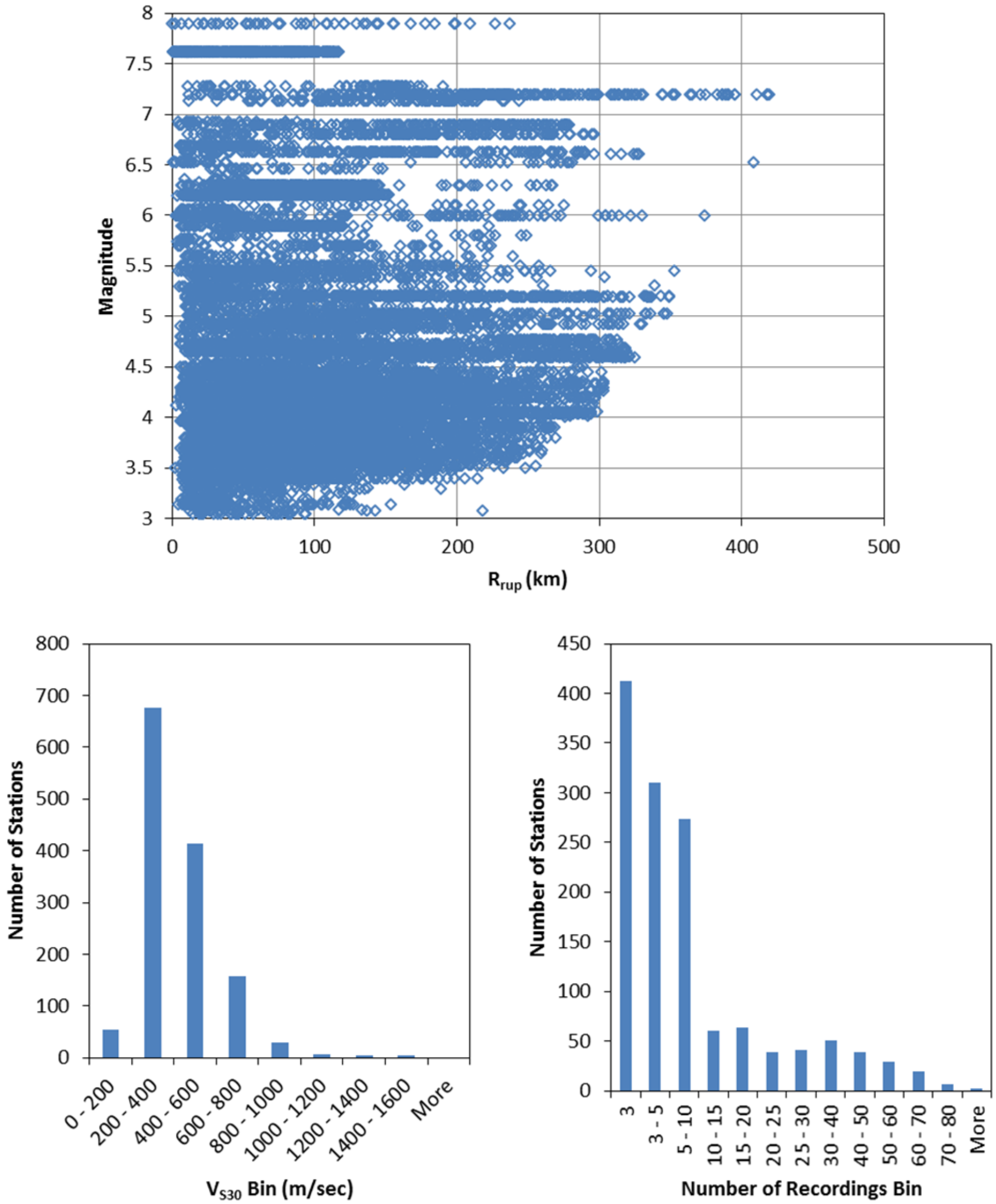

Figure 2.12 **Data distribution (magnitude-distance plot, V_{S30} histogram, and number of recordings histogram) for the BSSA14 dataset used in the single-station analysis.**

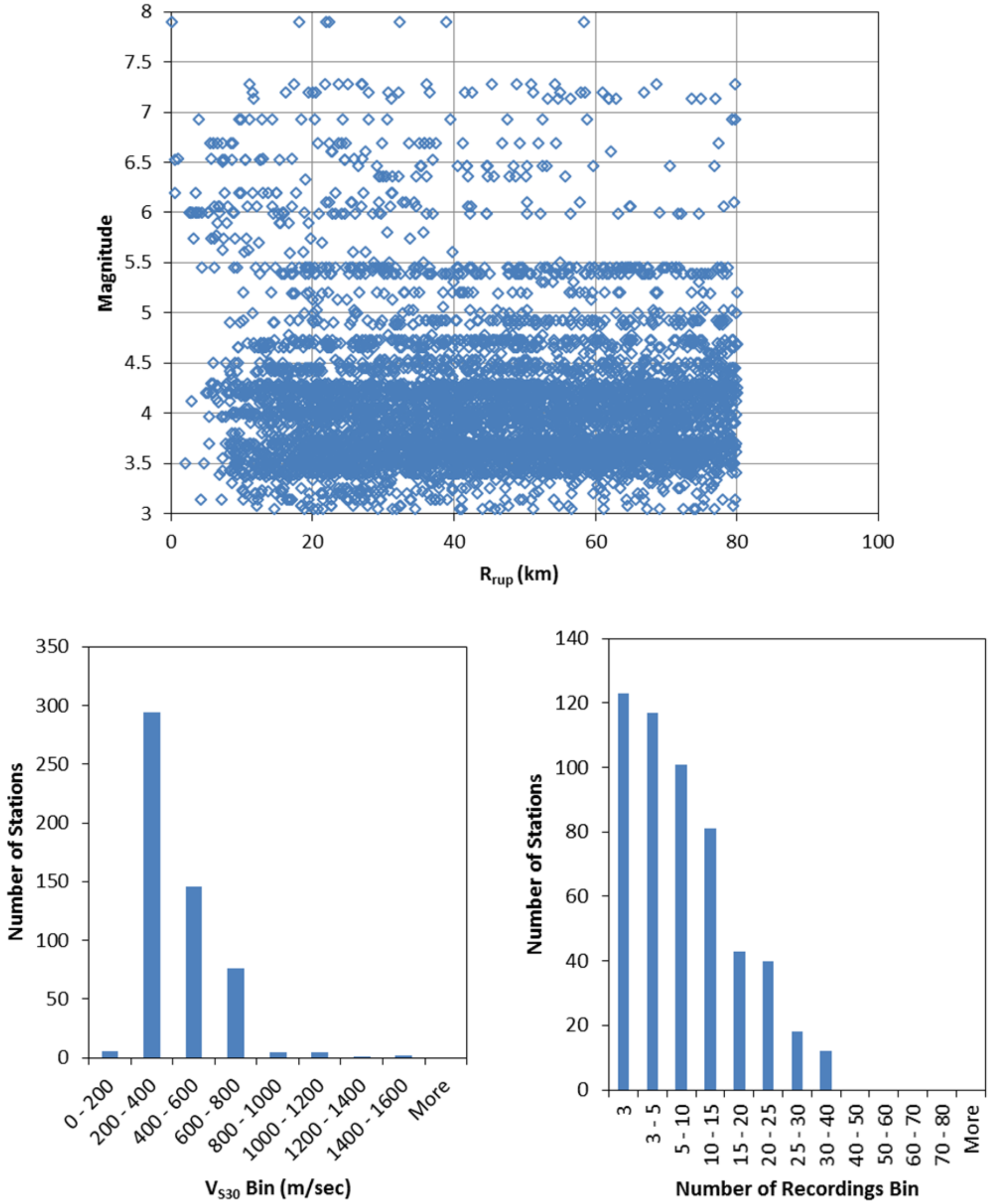

Figure 2.13 Data distribution (magnitude-distance plot, V_{S30} histogram, and number of recordings histogram) for the CB14 dataset used in the single-station analysis.

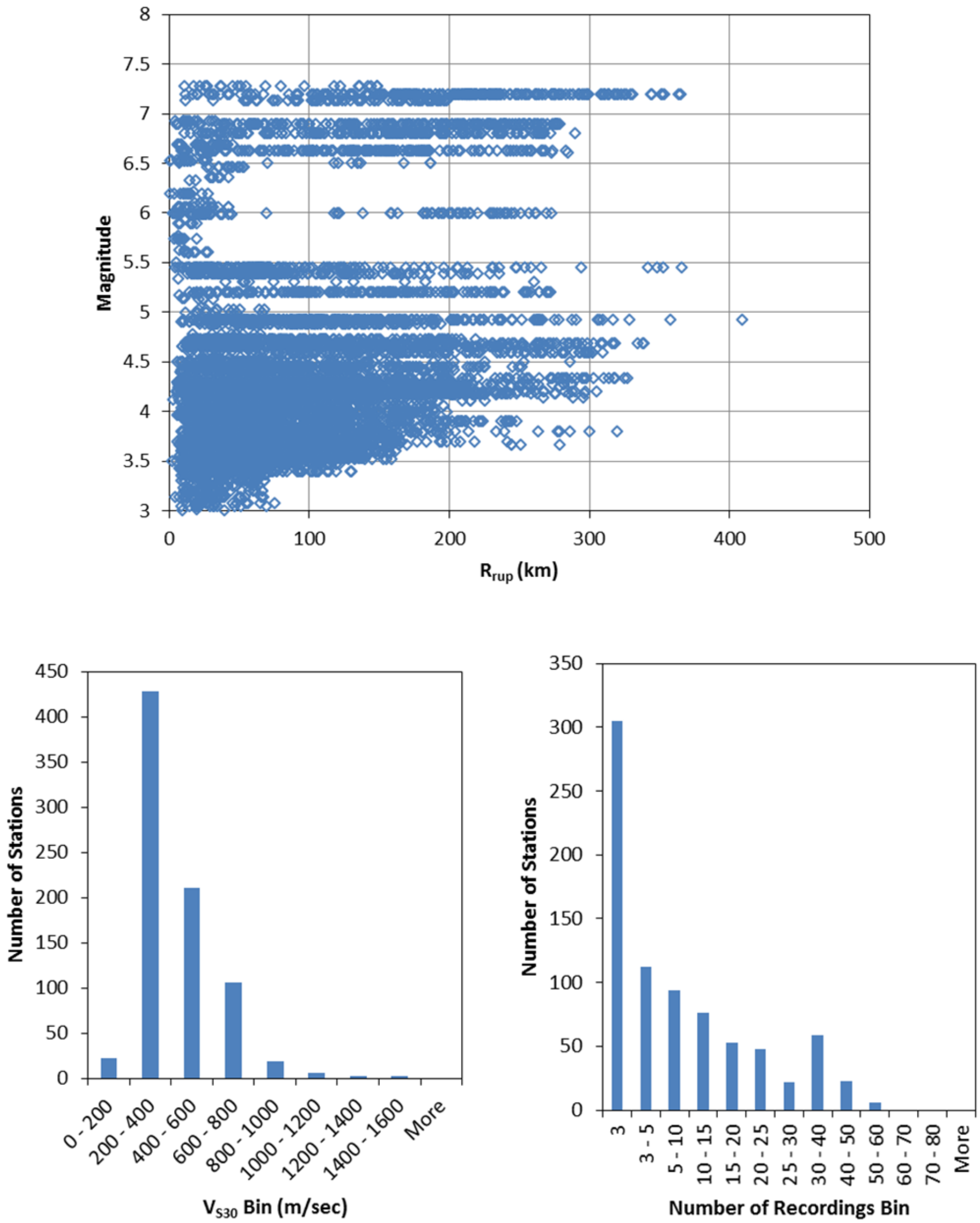

Figure 2.14 Data distribution (magnitude-distance plot, V_{S30} histogram, and number of recordings histogram) for the CY14 dataset used in the single-station analysis.

3 GMPE Functional Form and Residual Plots

As described in Section 2.1, CENA ground-motion data were used to derive an empirical GMPE for CENA. This model was derived for the purpose of analyzing ground-motion variability and deriving standard deviation models for CENA; therefore, it is not intended for use in median ground-motion predictions. The functional form and modeling assumptions are closely related to those of the PEER Ground-motion model (GMM) documented in Chapter 11 of the *PEER Report No. 2014/04* [2015a]. The model for the median ground motion has the following functional form:

$$
\begin{aligned}
&ln(y) = \\
&\begin{cases}
c_1 + c_2\mathbf{M} + c_3\mathbf{M}^2 + c_4 ln\left(\sqrt{R_{RUP}^2 + c_6^2}\right) + c_7\sqrt{R_{RUP}^2 + c_6^2} & \\
\quad +c_8 ln(V_{S30}) + c_9\left(\frac{H_{dep}}{20}\right) & for\ R_{RUP} < 50\ km \\
c_1 + c_2\mathbf{M} + c_3\mathbf{M}^2 + (c_4 - c_{4h}) ln\left(\sqrt{50^2 + c_6^2}\right) + c_{4h} ln\left(\sqrt{R_{RUP}^2 + c_6^2}\right) & \\
\quad +c_7\sqrt{R_{RUP}^2 + c_6^2} + c_8 ln(V_{S30}) + c_9\left(\frac{H_{dep}}{20}\right) & for\ R_{RUP} \geq 50\ km
\end{cases}
\end{aligned}
\tag{3.1}
$$

where H_{dep} is hypocentral depth (km). The geometrical spreading term hinges at an R_{RUP} distance of 50 km and its coefficient for distances greater than 50 km (c_{4h}) is period-dependent determined based on SMSIM simulations [Boore 2005]. Coefficients of geometrical spreading within 50 km and anelastic attenuation, c_4 and c_7, distinguish between PIE and tectonic events, and have different values for earthquakes located in the Oklahoma-Arkansas region (mostly consisting of PIEs). Coefficient c_6, commonly referred to as “fictitious depth,” was fixed to the same form used in ASK14:

$$
c_6 = \begin{cases} 1 & for\ \mathbf{M} \leq 4.0 \\ 3.5\mathbf{M} - 13 & for\ 4.0 < \mathbf{M} \leq 5.0 \\ 4.5 & for\ \mathbf{M} > 5.0 \end{cases}
\tag{3.2}
$$

The mixed-effects algorithm described in Abrahamson and Youngs [1992] was used for the regression analysis and the separation of the total residuals into between-event and within-event residuals at each period assuming homoscedastic ϕ and τ (ϕ and τ are period-dependent). Coefficients c_1, c_2, c_3, c_4, c_7, c_8, and c_9 were determined from the regression. Residuals from the regression analysis are plotted as function of the independent model parameters to allow an evaluation of the model. Residual plots are shown for spectral periods of 0.1, 0.25, 0.5, 0.75, 1, and 2 sec (frequencies of 10, 4, 2, 1.33, 1, and 0.5 Hz). Plots are not shown for periods outside of 0.1 to 2 sec due to the frequency bandwidth limitations of the recordings and the limited data available at periods outside of 0.1 to 2 sec leading to unreliable results (Figure 2.6).

Between-event residuals are plotted as a function of magnitude and hypocentral depth and shown in Figures 3.1 to 3.6 for spectral periods of 0.1, 0.25, 0.5, 0.75, 1, and 2 sec, respectively. Potentially induced earthquakes and tectonic events are distinguished in the between-event residual plots. Figures 3.1 to 3.6 generally show no trend in the event terms with magnitude or hypocentral depth for the tectonic events. Within-event residuals are plotted as a function of R_{RUP} for the PIE and tectonic events as shown in Figures 3.7 to 3.12 for spectral periods of 0.1, 0.25, 0.5, 0.75, 1, and 2 sec, respectively. Averages of the within-event residuals are shown in different R_{RUP} bins with edges of 0, 50, 100, 200, 300, 400, and 500 km. No trend is generally observed in the within-event residuals versus distance for the PIE and tectonic events. Within-event residuals are plotted as a function of V_{S30} for the PIE and tectonic events, as shown in Figures 3.13 to 3.18 for spectral periods of 0.1, 0.25, 0.5, 0.75, 1, and 2 sec, respectively. Average within-event residuals in V_{S30} bins of unit width equal to 250 m/sec are shown in Figures 3.13 to 3.18; in general, they show no trend in the within-event residuals with V_{S30} in the bins with numerous recordings. Finally, within-event residuals are plotted as a function of R_{RUP} by region as shown in Figure 3.19 to 3.24.

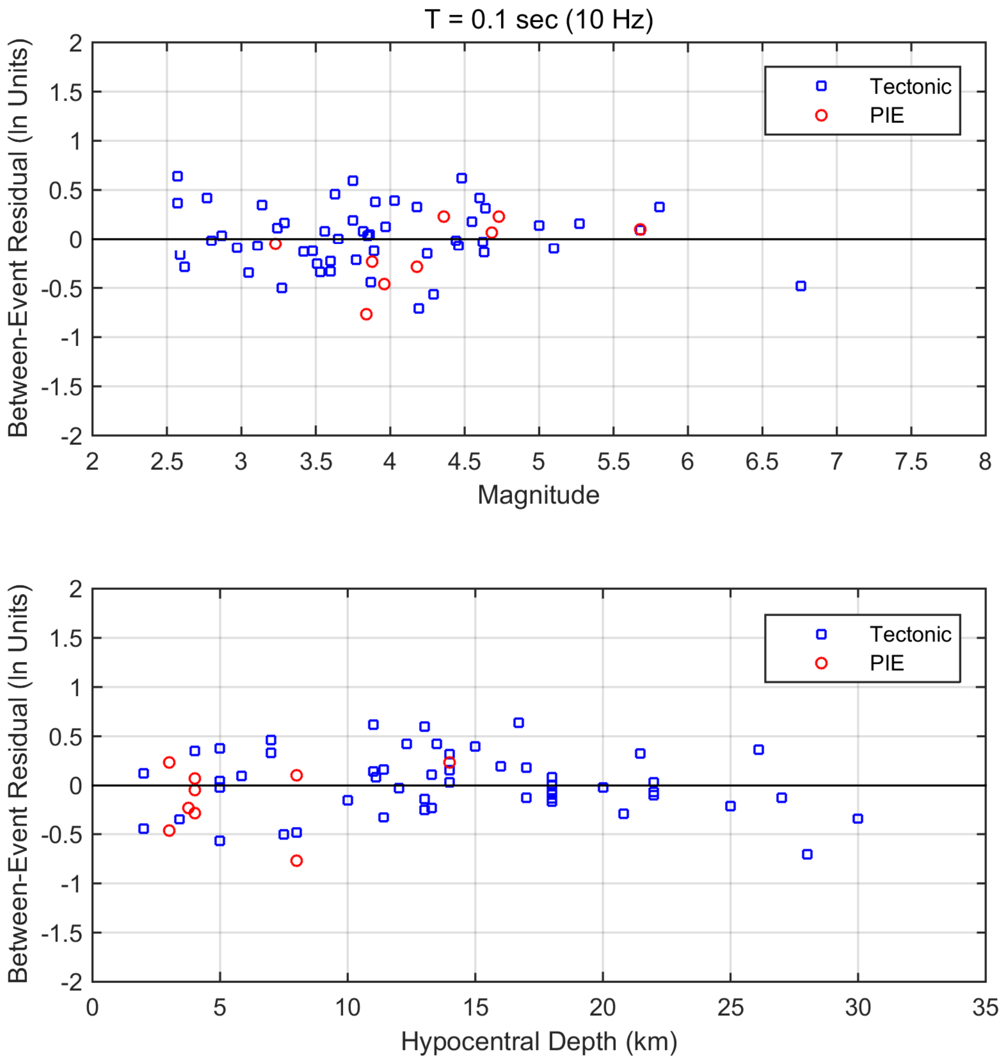

Figure 3.1 Event terms versus magnitude for *F* = 10 Hz.

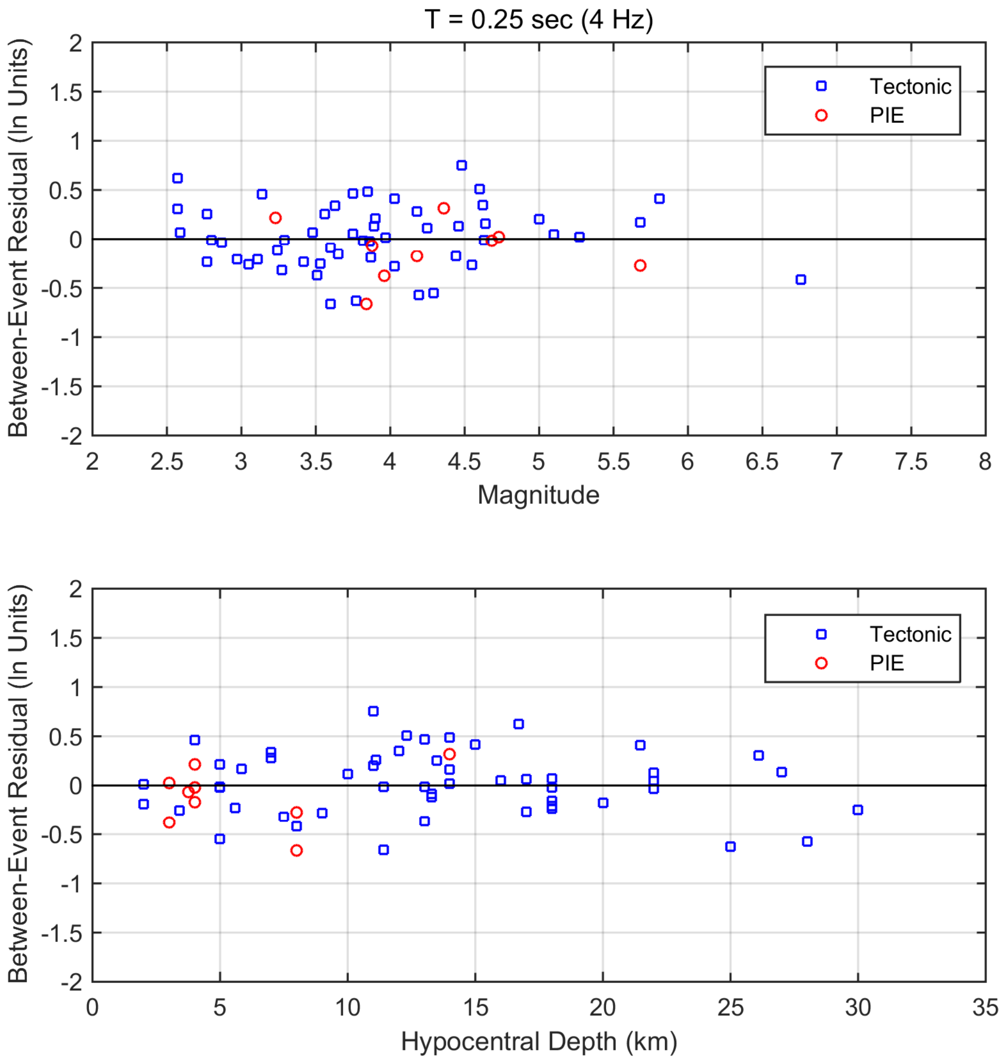

Figure 3.2 Event terms versus magnitude for *F* = 4 Hz.

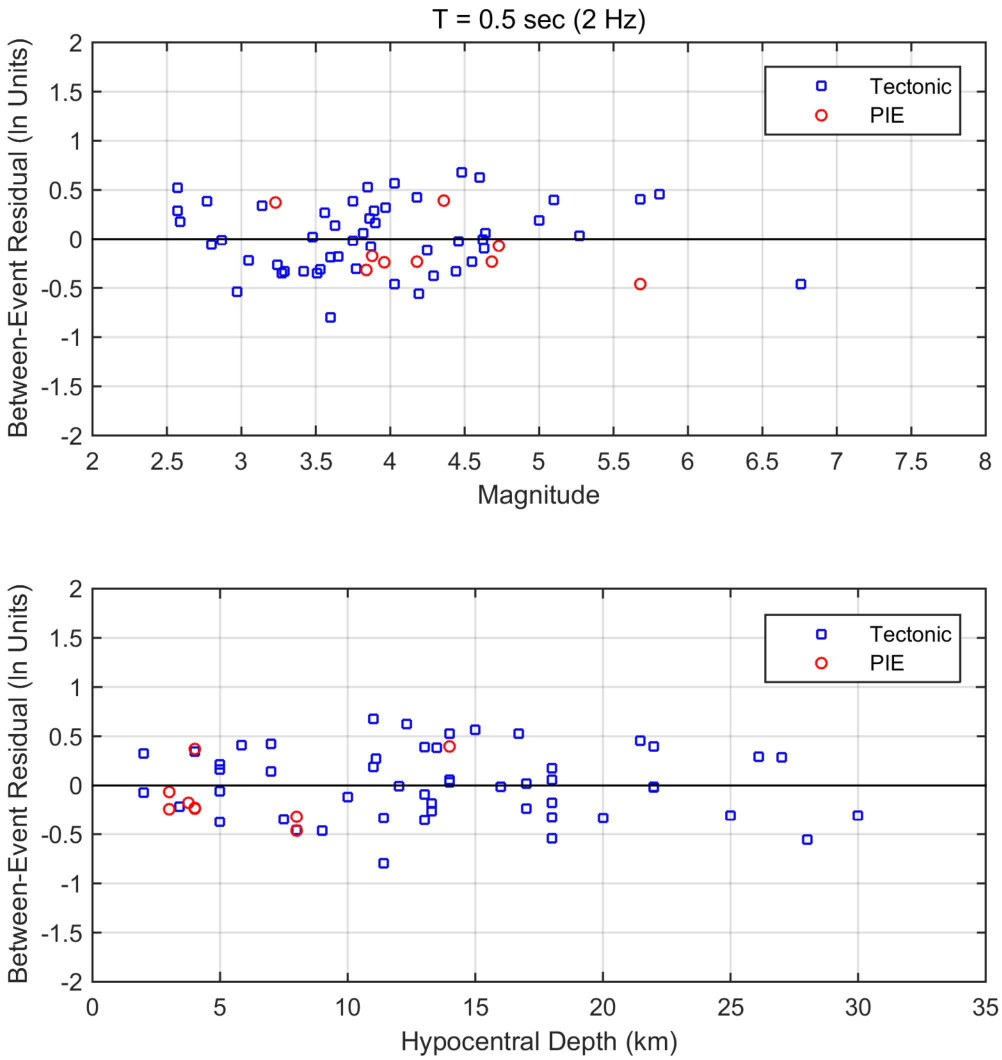

Figure 3.3 Event terms versus magnitude for *F* = 2 Hz.

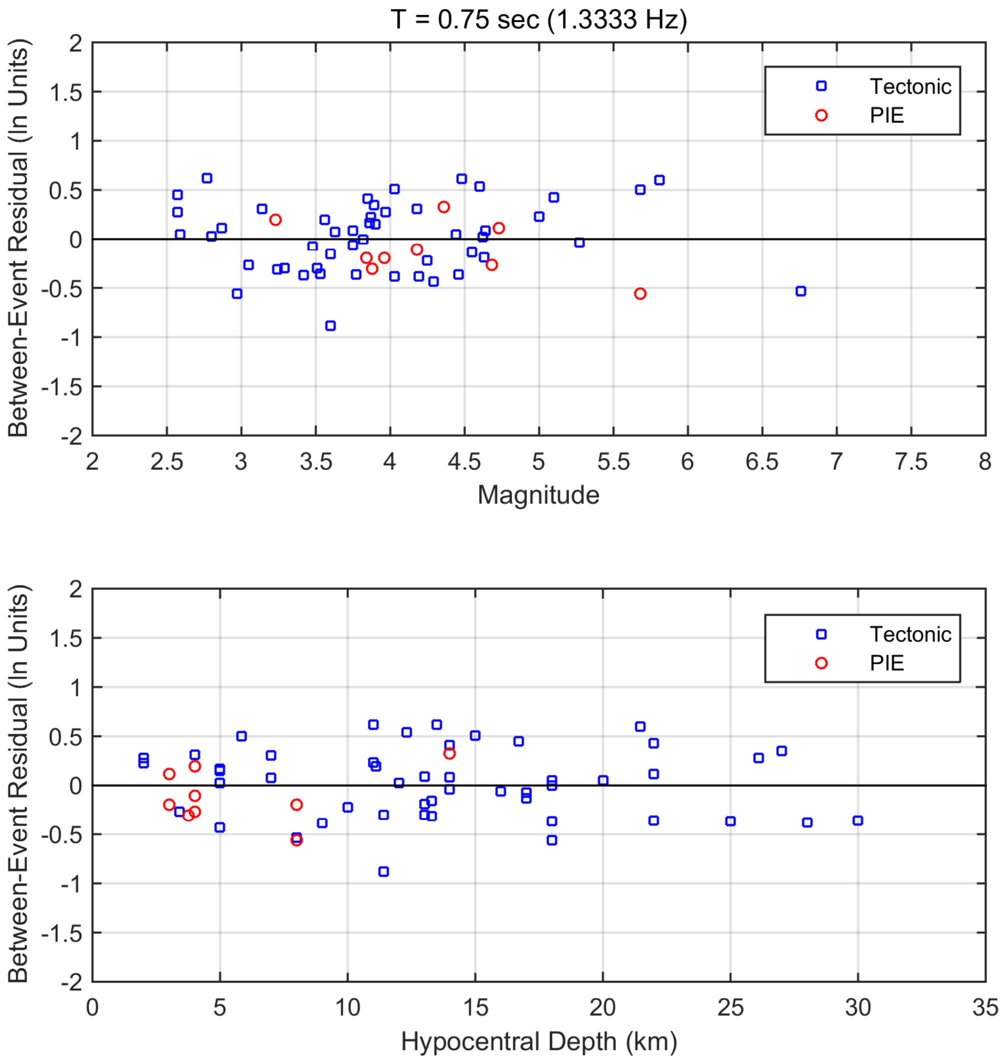

Figure 3.4 Event terms versus magnitude for *F* = 1.33 Hz.

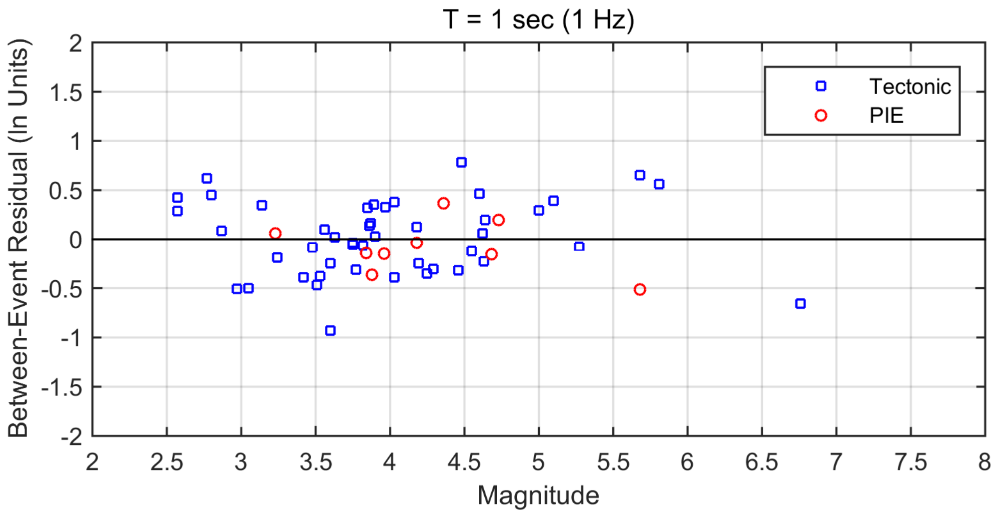

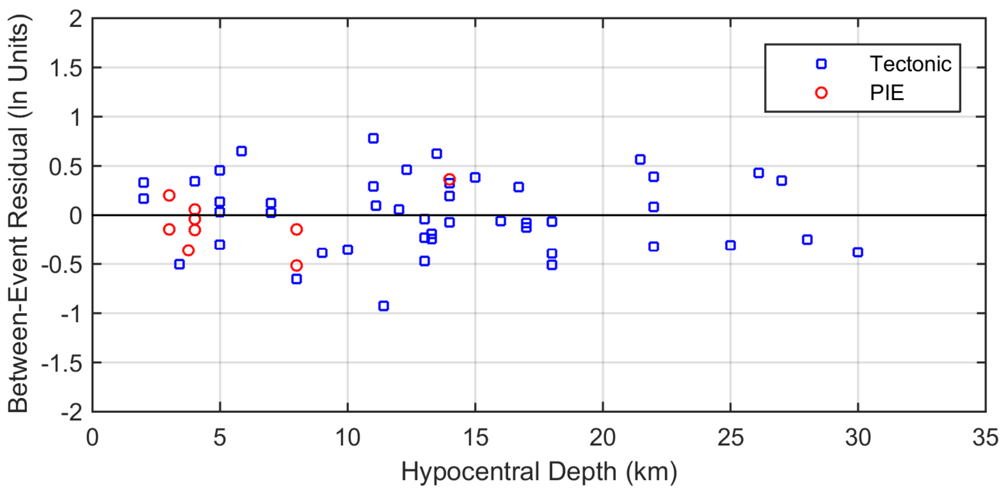

Figure 3.5 Event terms versus magnitude for *F* = 1 Hz.

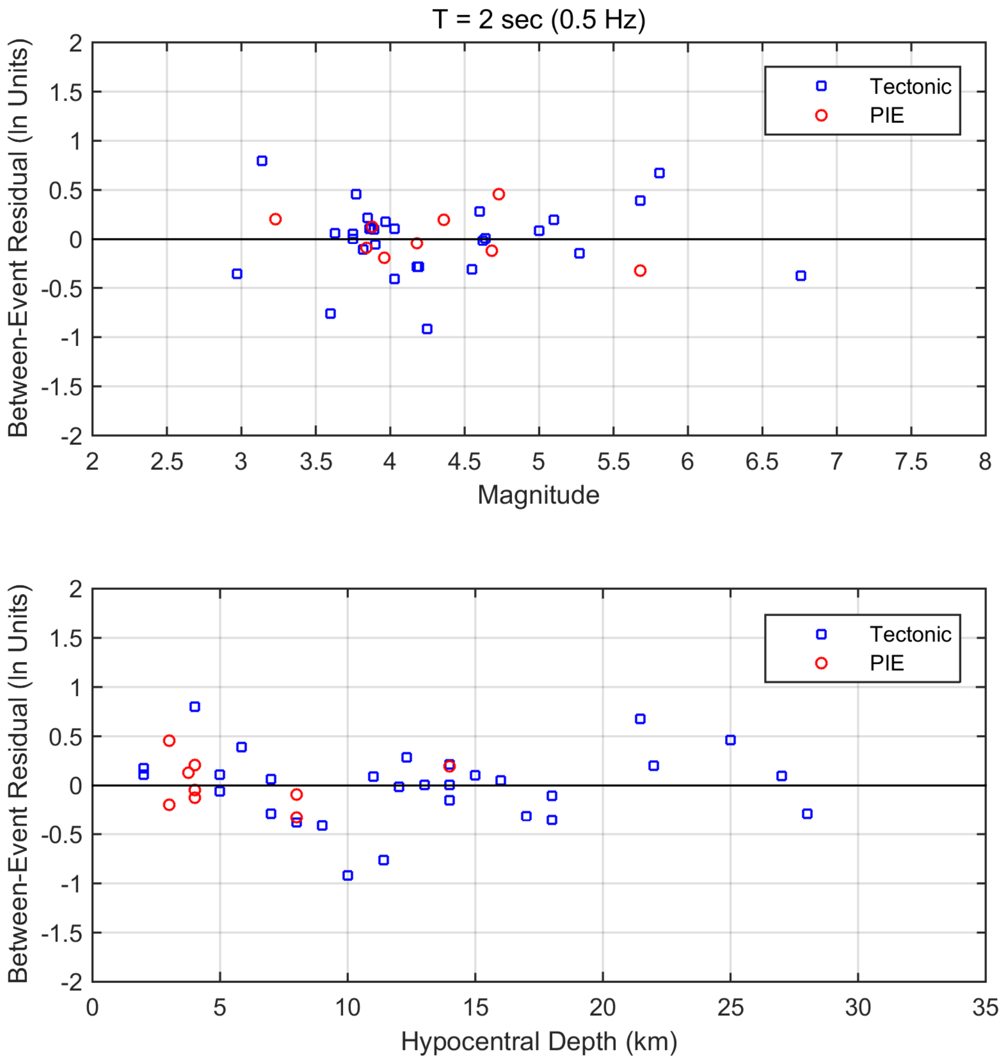

Figure 3.6 Event terms versus magnitude for *F* = 0.5 Hz.

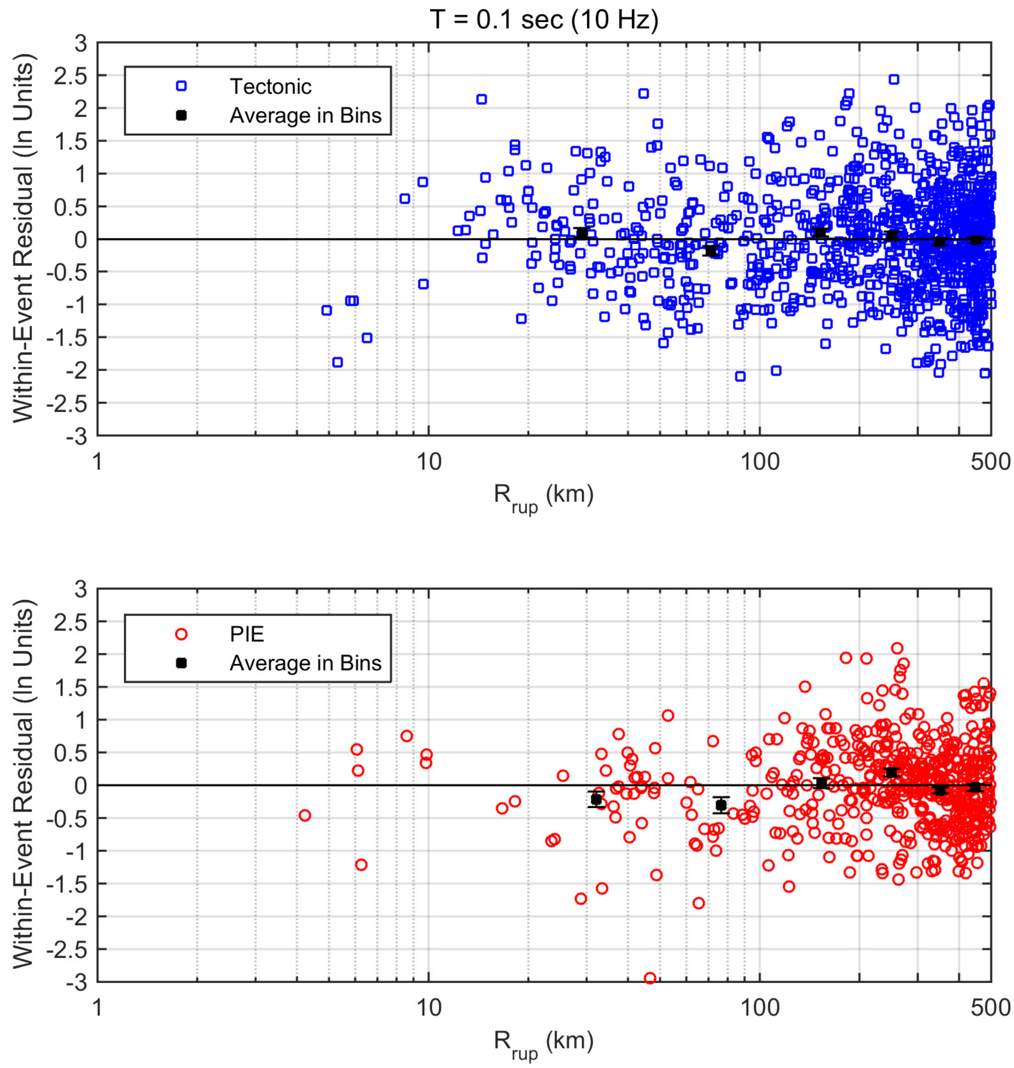

Figure 3.7 Within-event residuals versus R_{RUP} for F = 10 Hz.

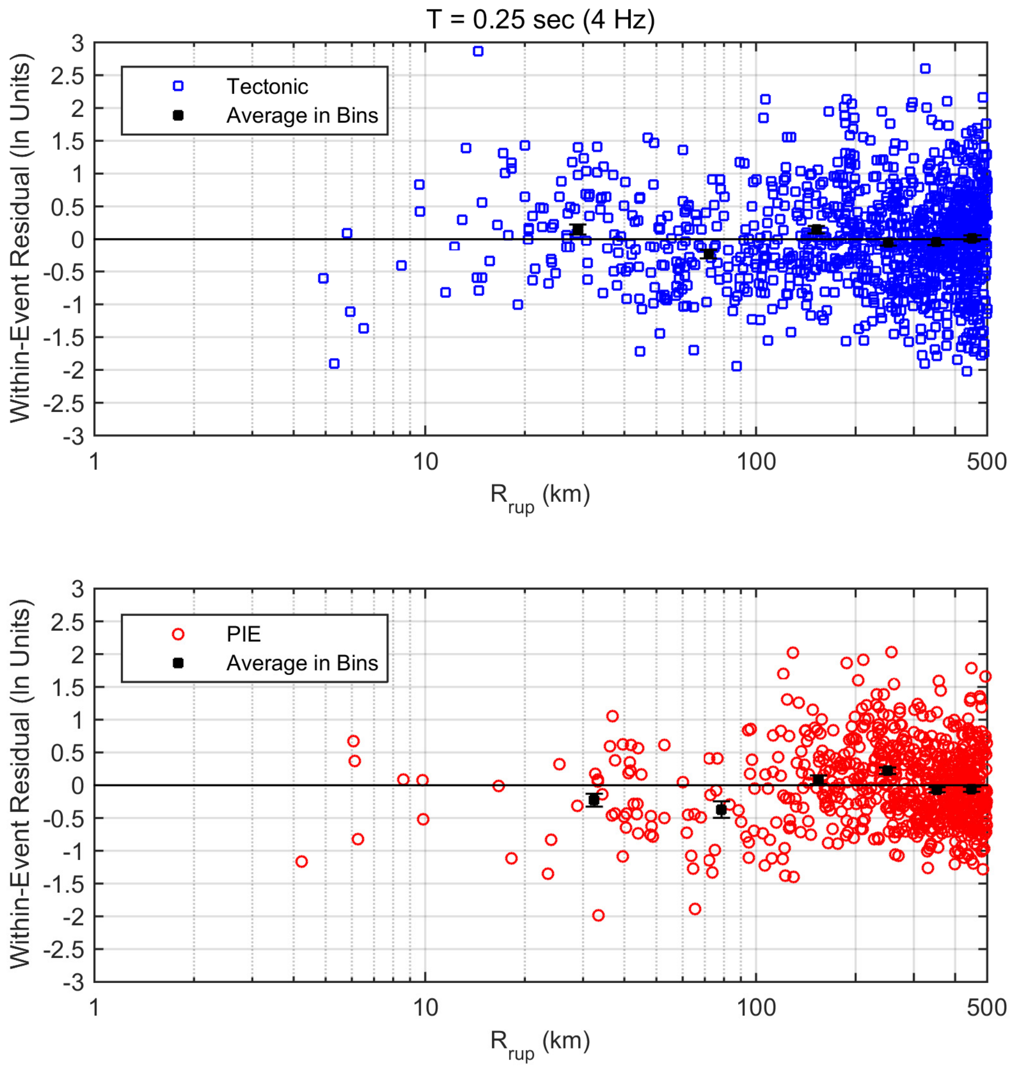

Figure 3.8 Within-event residuals versus R_{RUP} for F = 4 Hz.

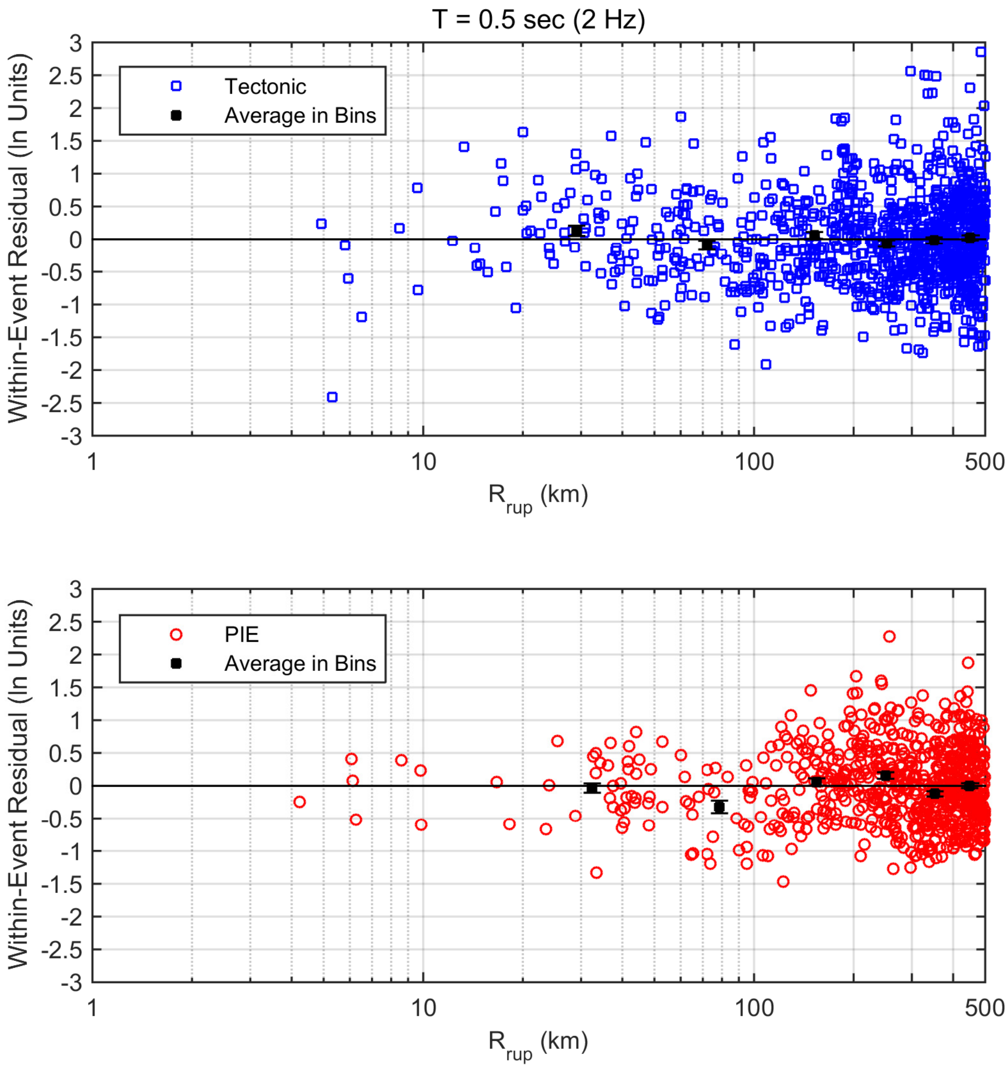

Figure 3.9 Within-event residuals versus R_{RUP} for F = 2 Hz.

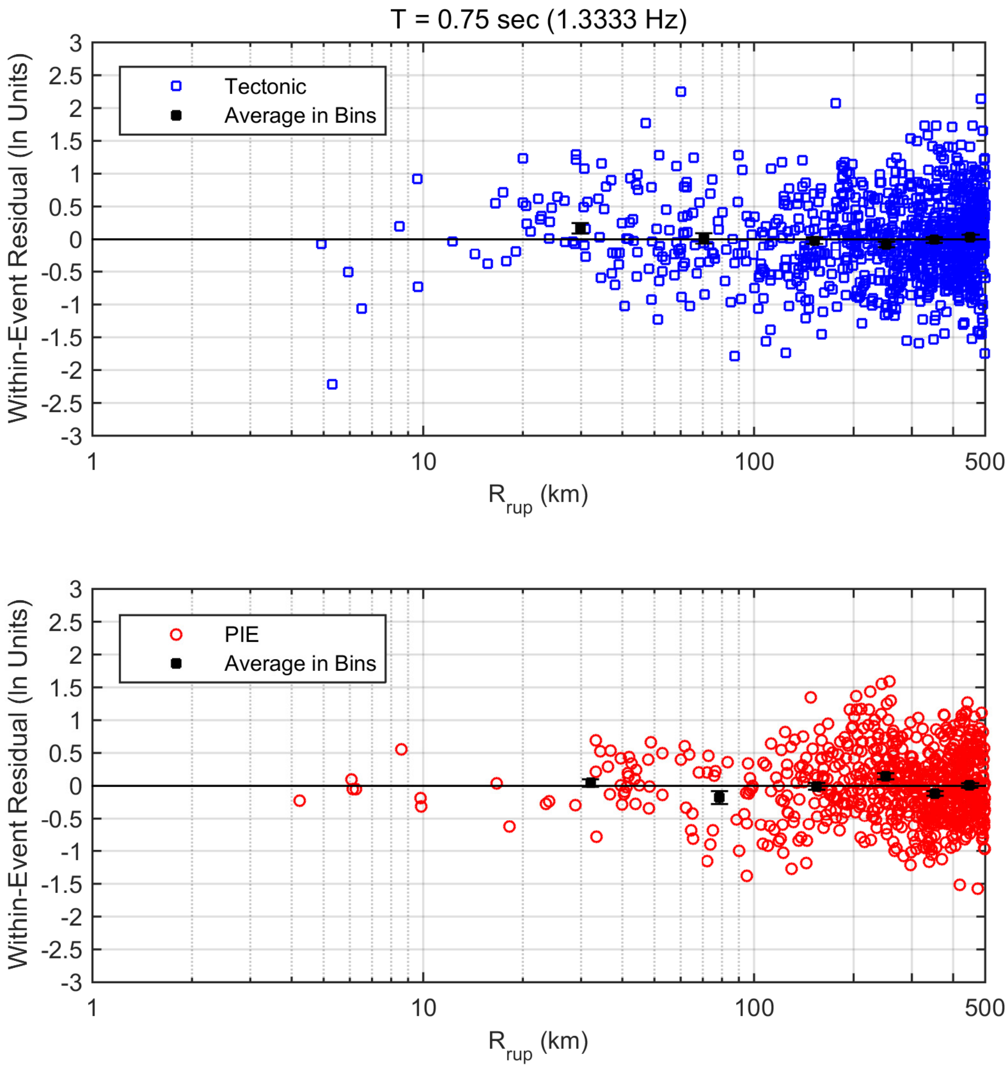

Figure 3.10 Within-event residuals versus R_{RUP} for F = 1.33 Hz.

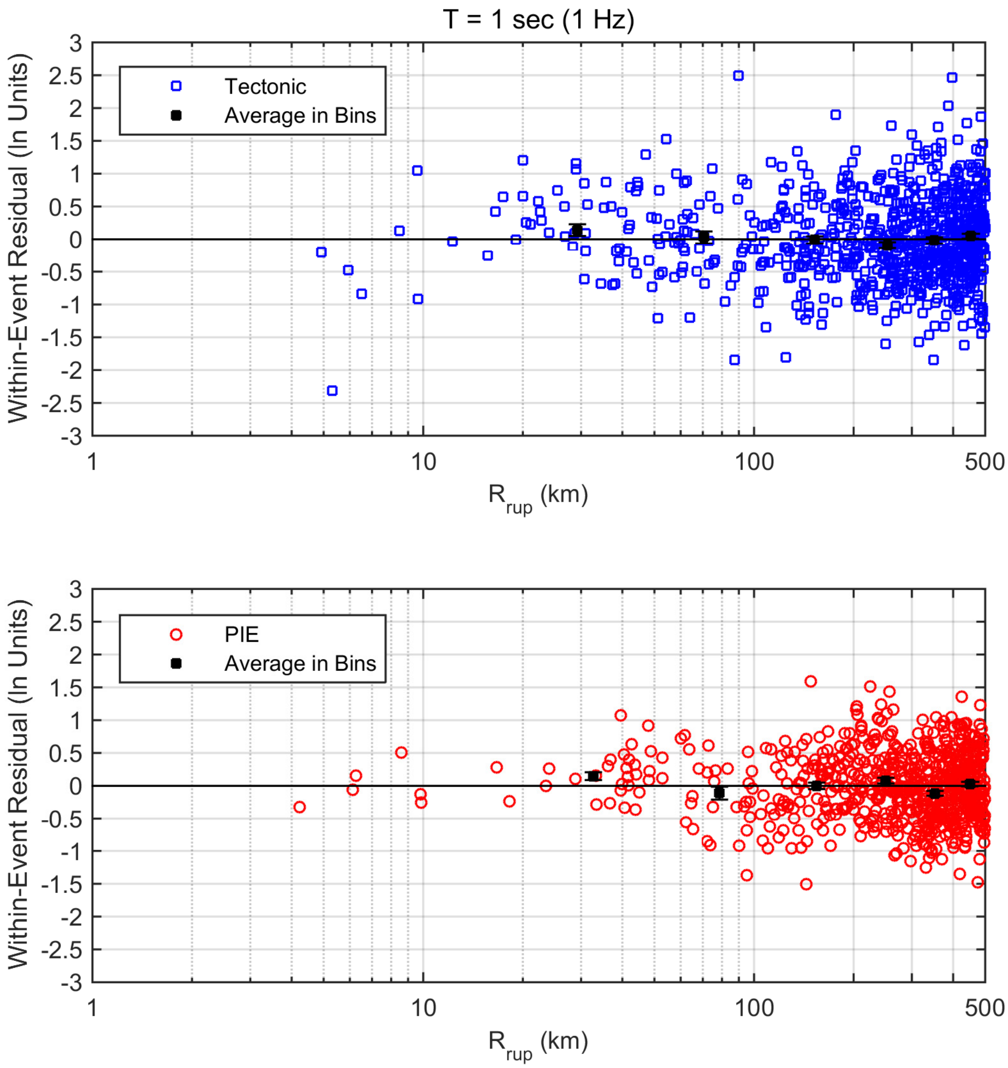

Figure 3.11 Within-event residuals versus R_{RUP} for F = 1 Hz.

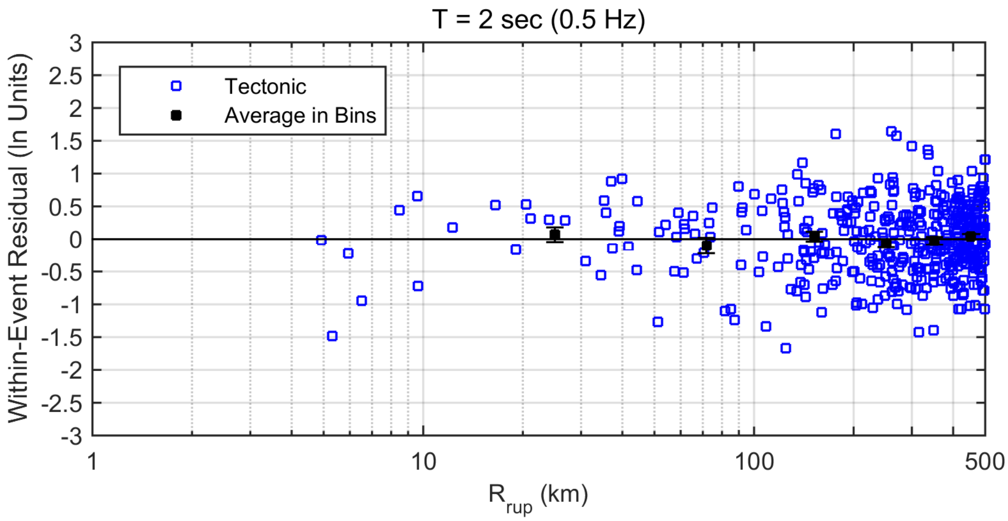

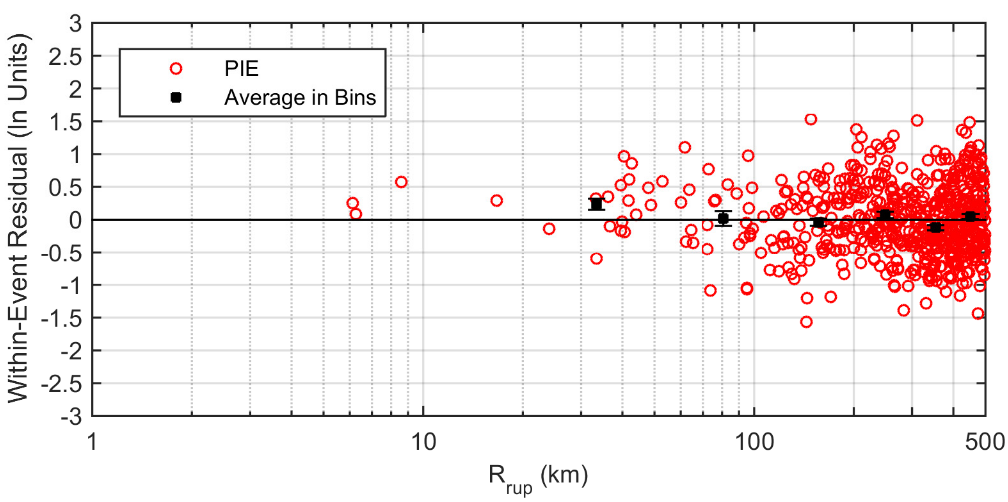

Figure 3.12 Within-event residuals versus R_{RUP} for F = 0.5 Hz.

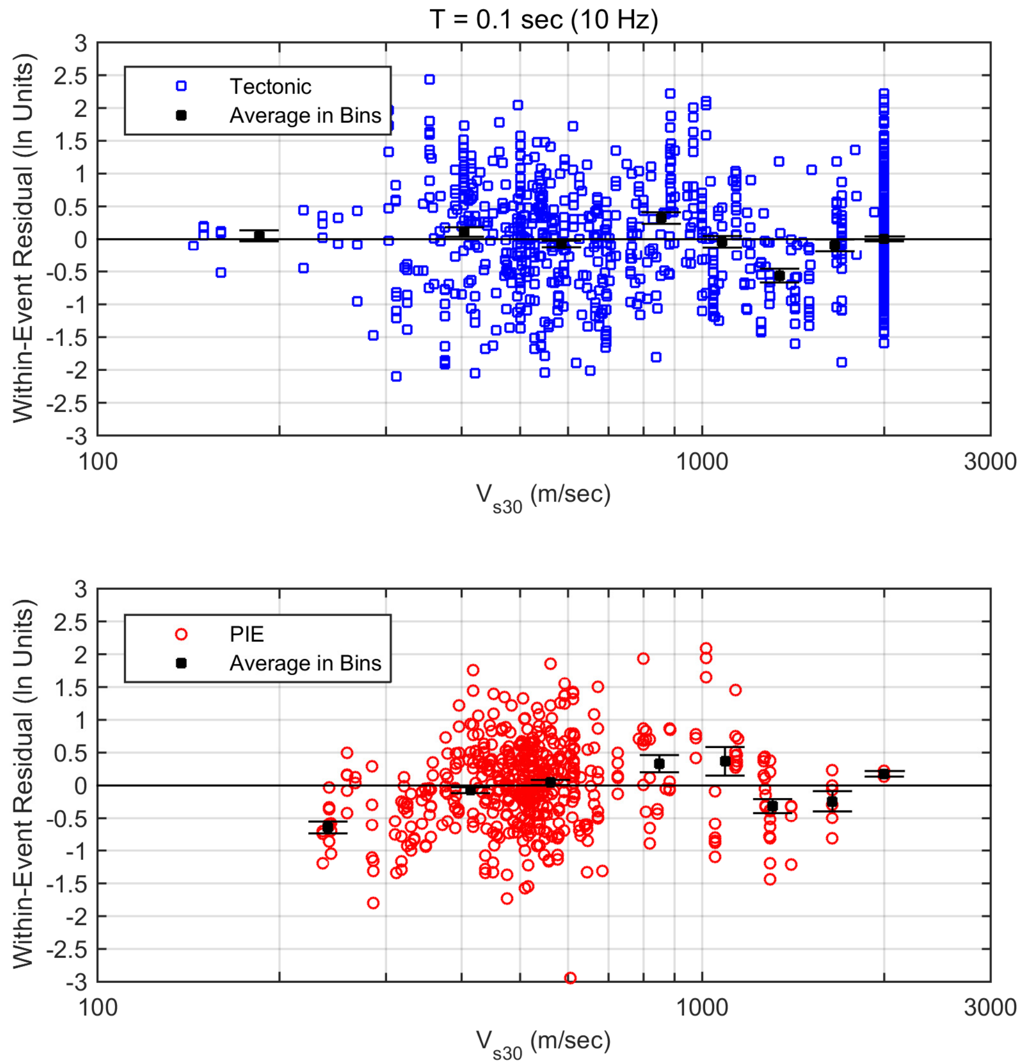

Figure 3.13 Within-event residuals versus V_{S30} for F = 10 Hz.

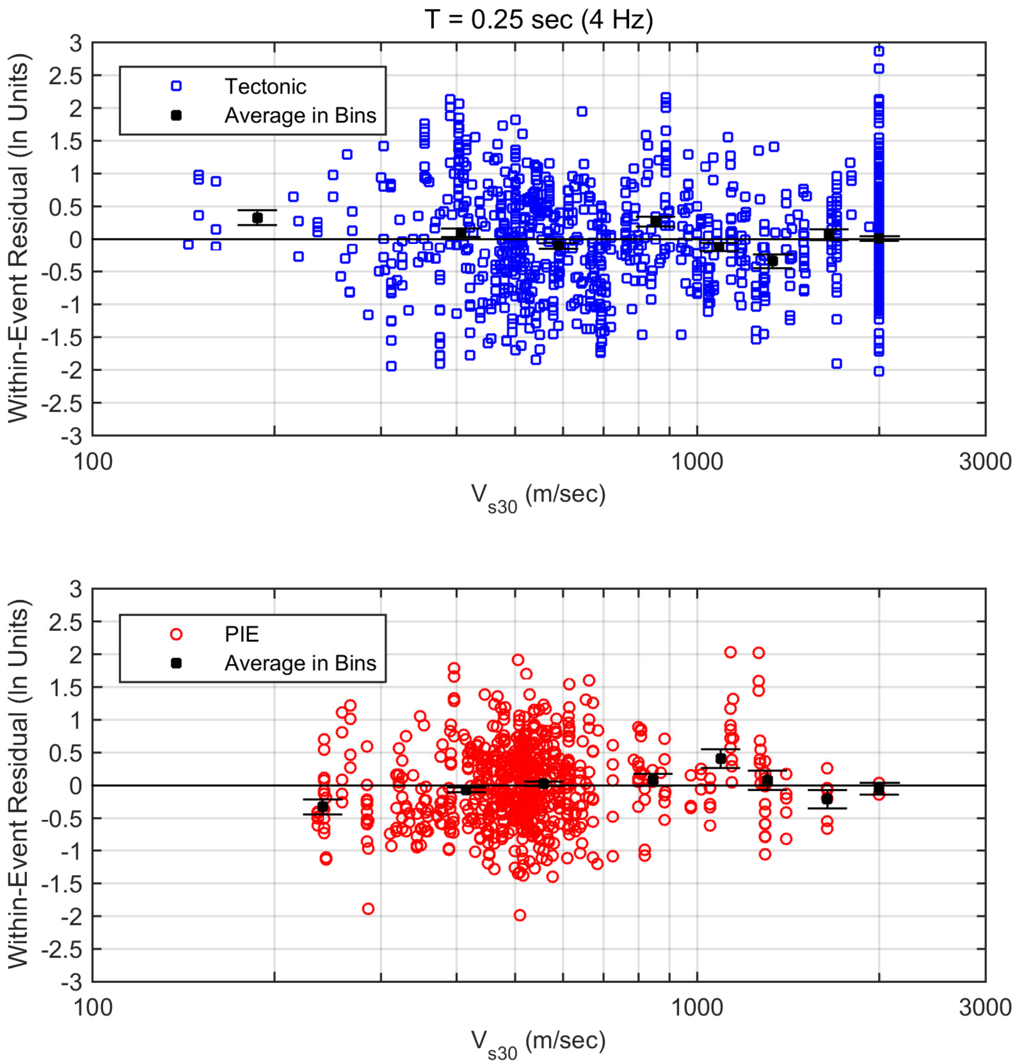

Figure 3.14 **Within-event residuals versus V_{S30} for F = 4 Hz.**

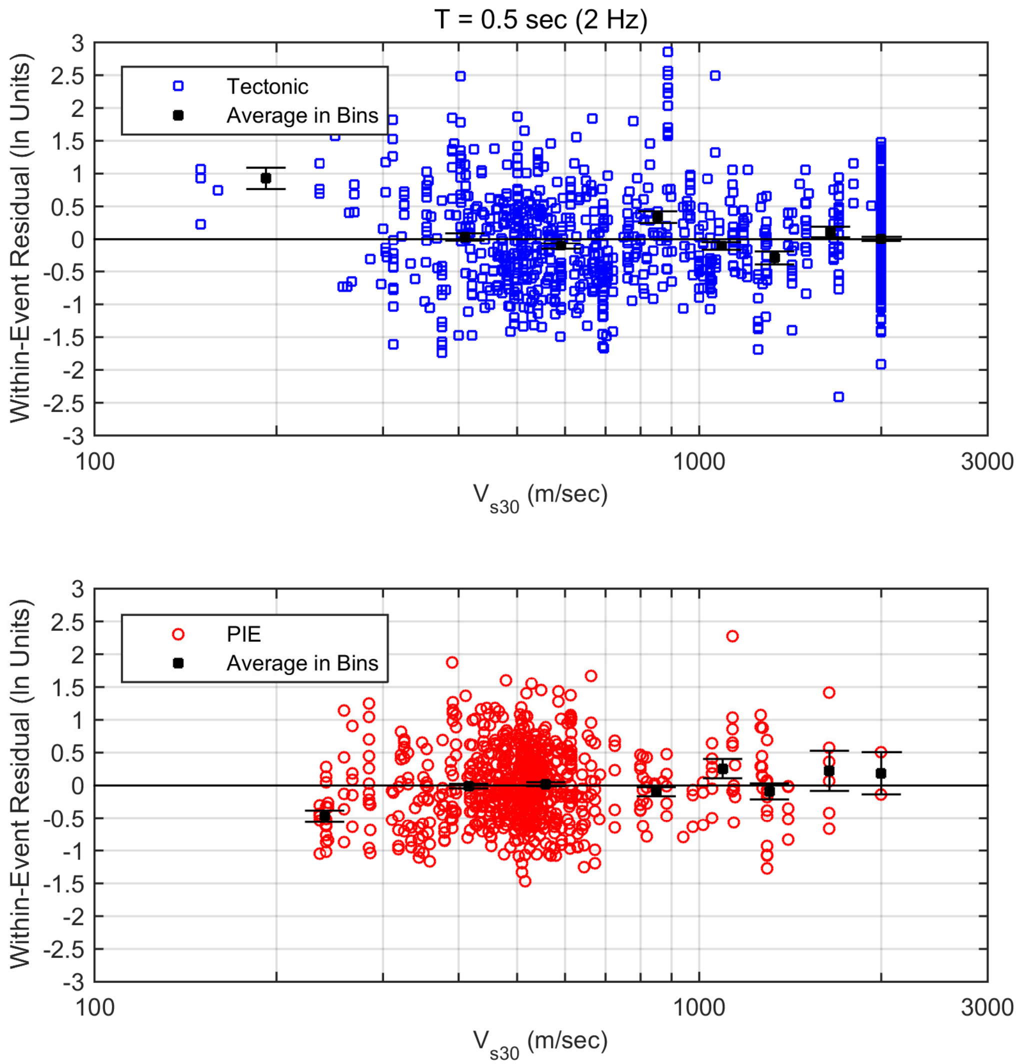

Figure 3.15 Within-event residuals versus V_{S30} for F = 2 Hz.

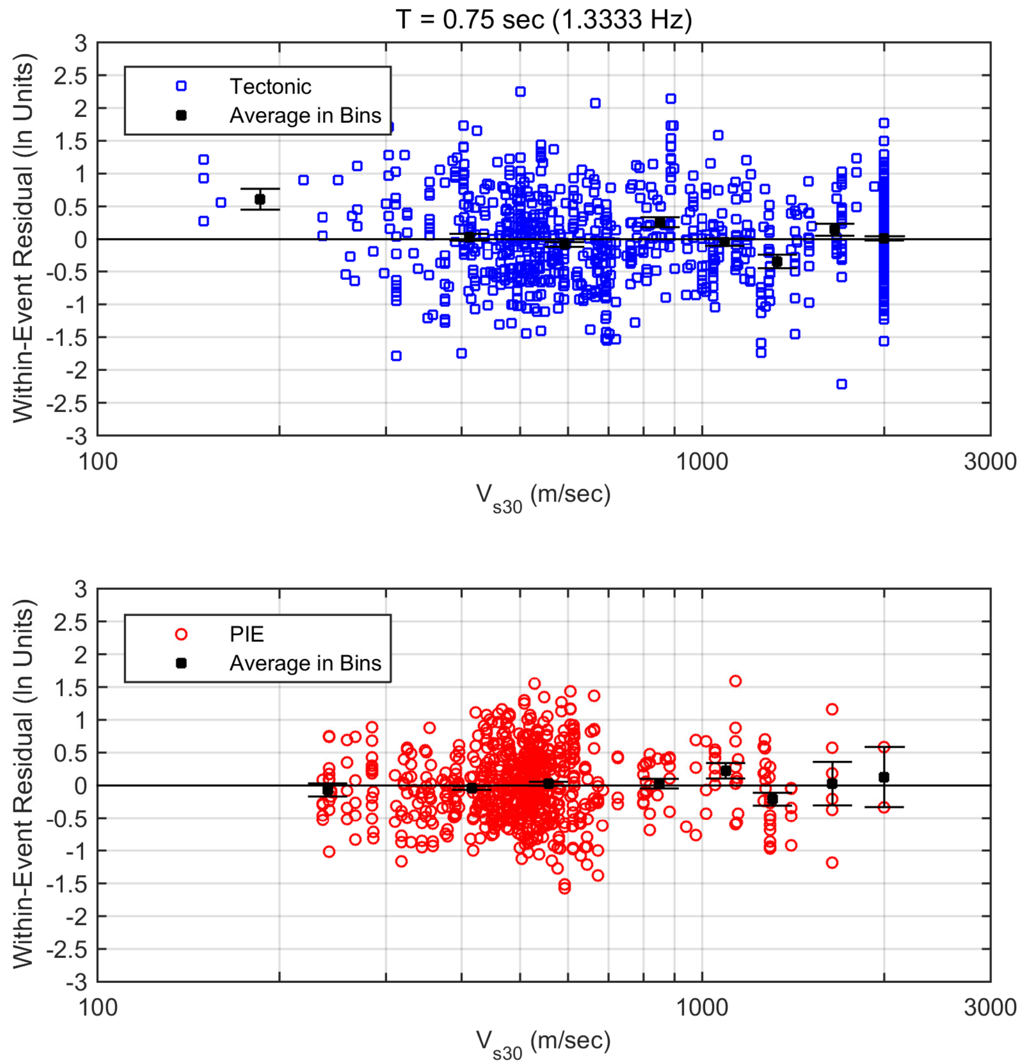

Figure 3.16 Within-event residuals versus V_{S30} for F = 1.33 Hz.

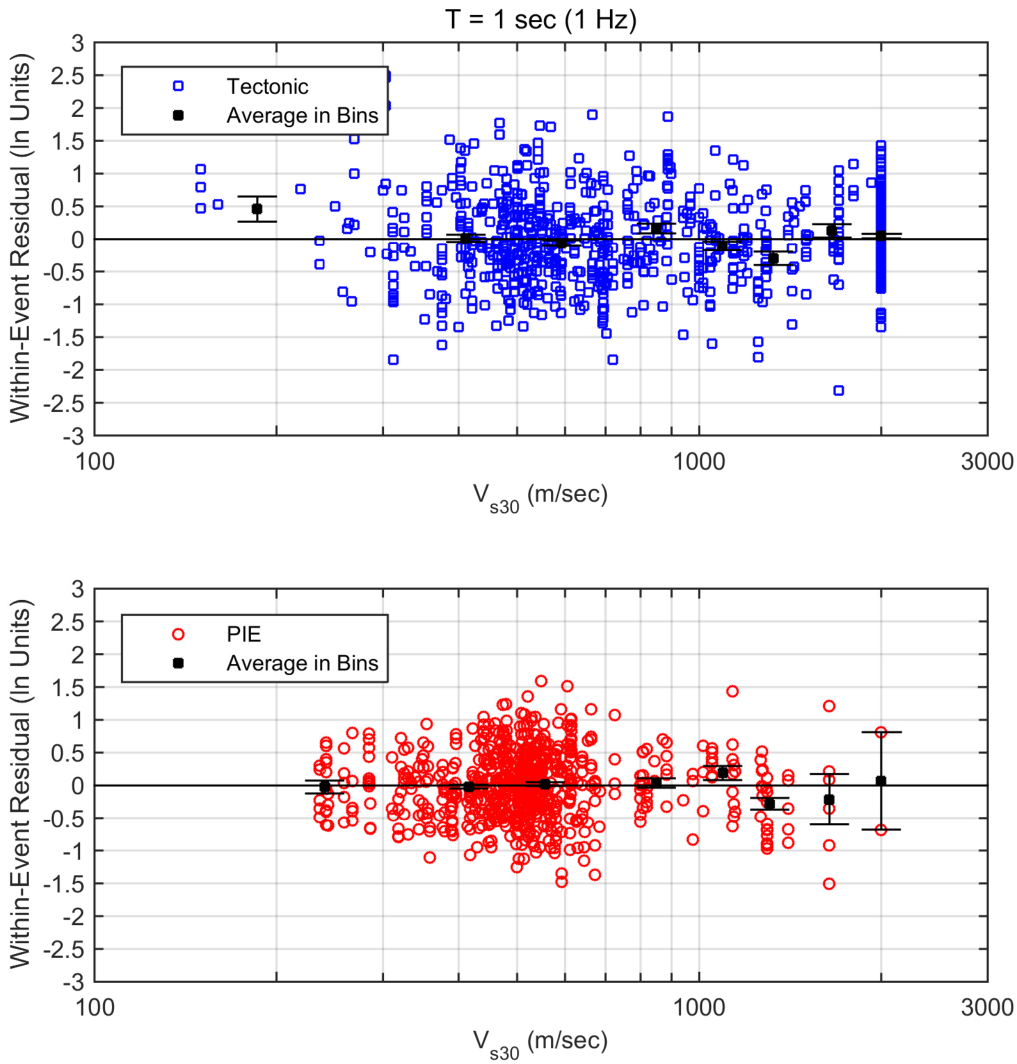

Figure 3.17 Within-event residuals versus V_{S30} for F = 1 Hz.

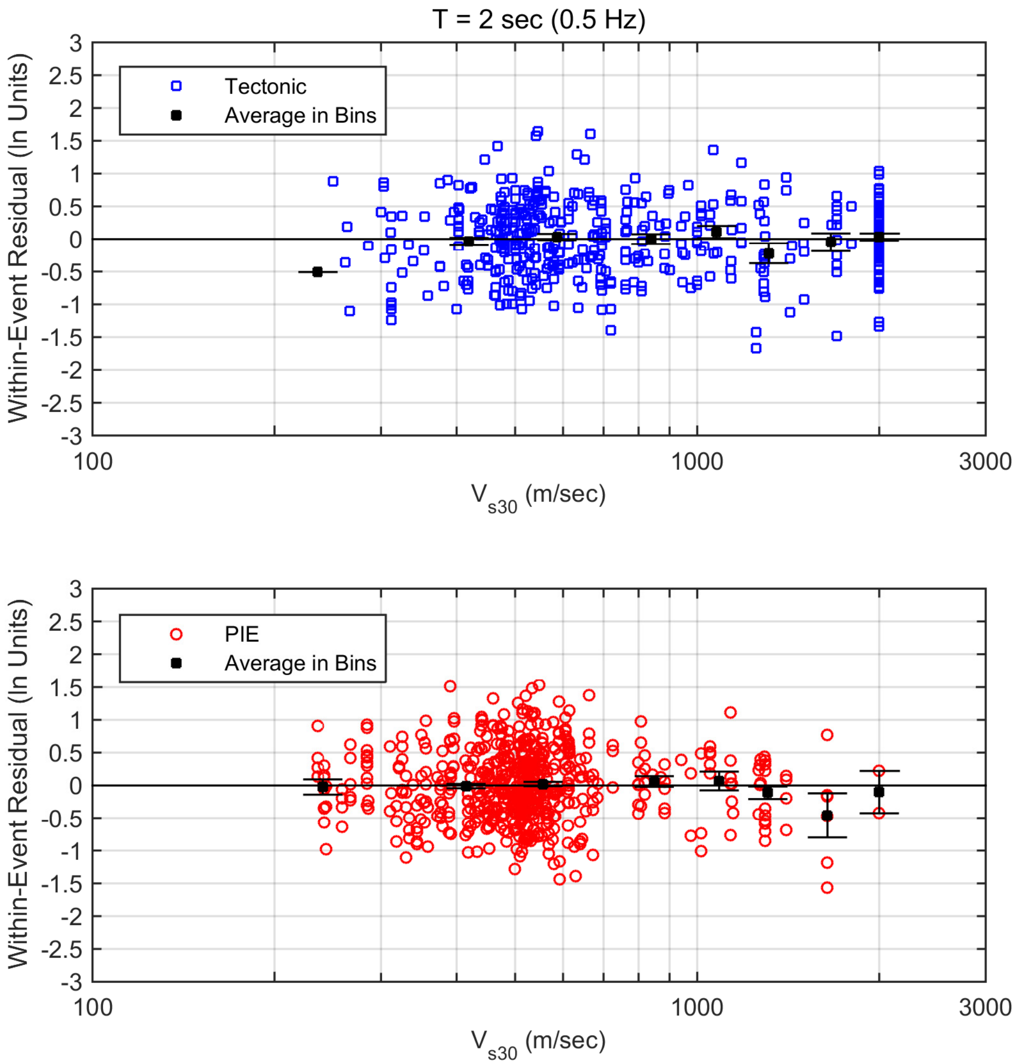

Figure 3.18 Within-event residuals versus V_{S30} for F = 0.5 Hz.

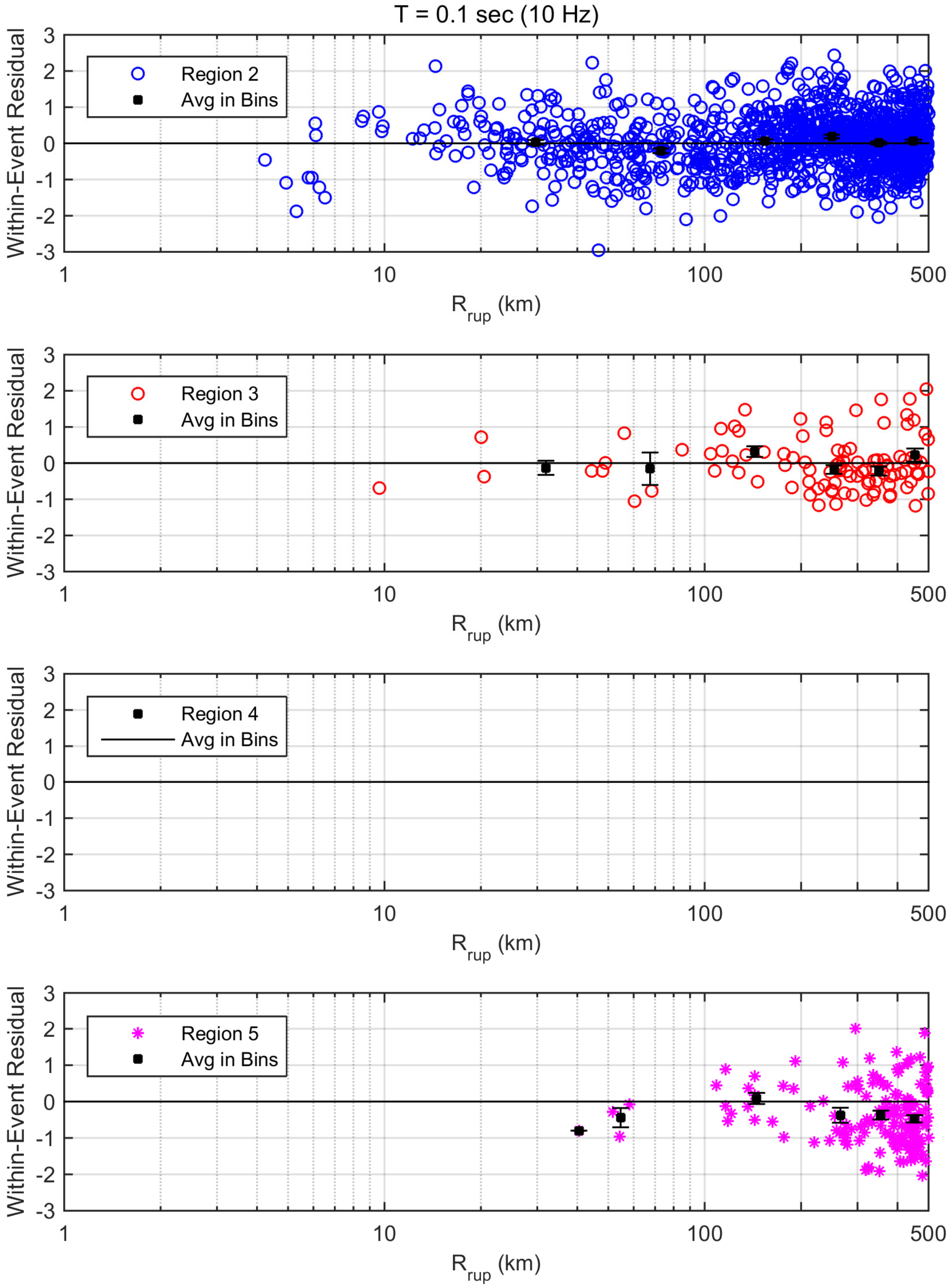

Figure 3.19 Within-event residuals (LN units) versus R_{RUP} by region for F = 10 Hz.

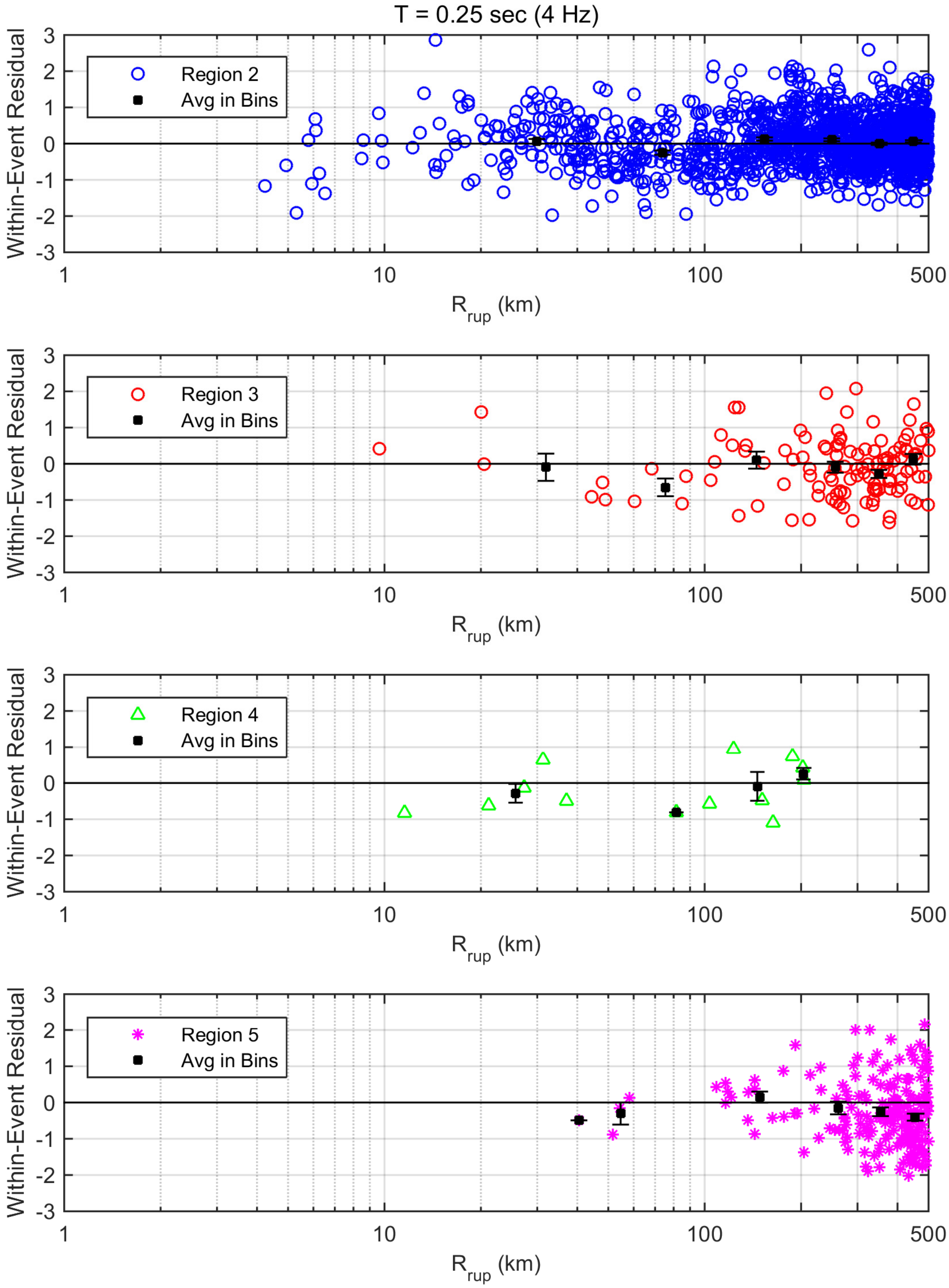

Figure 3.20 Within-event residuals (LN units) versus R_{RUP} by region for F = 4 Hz.

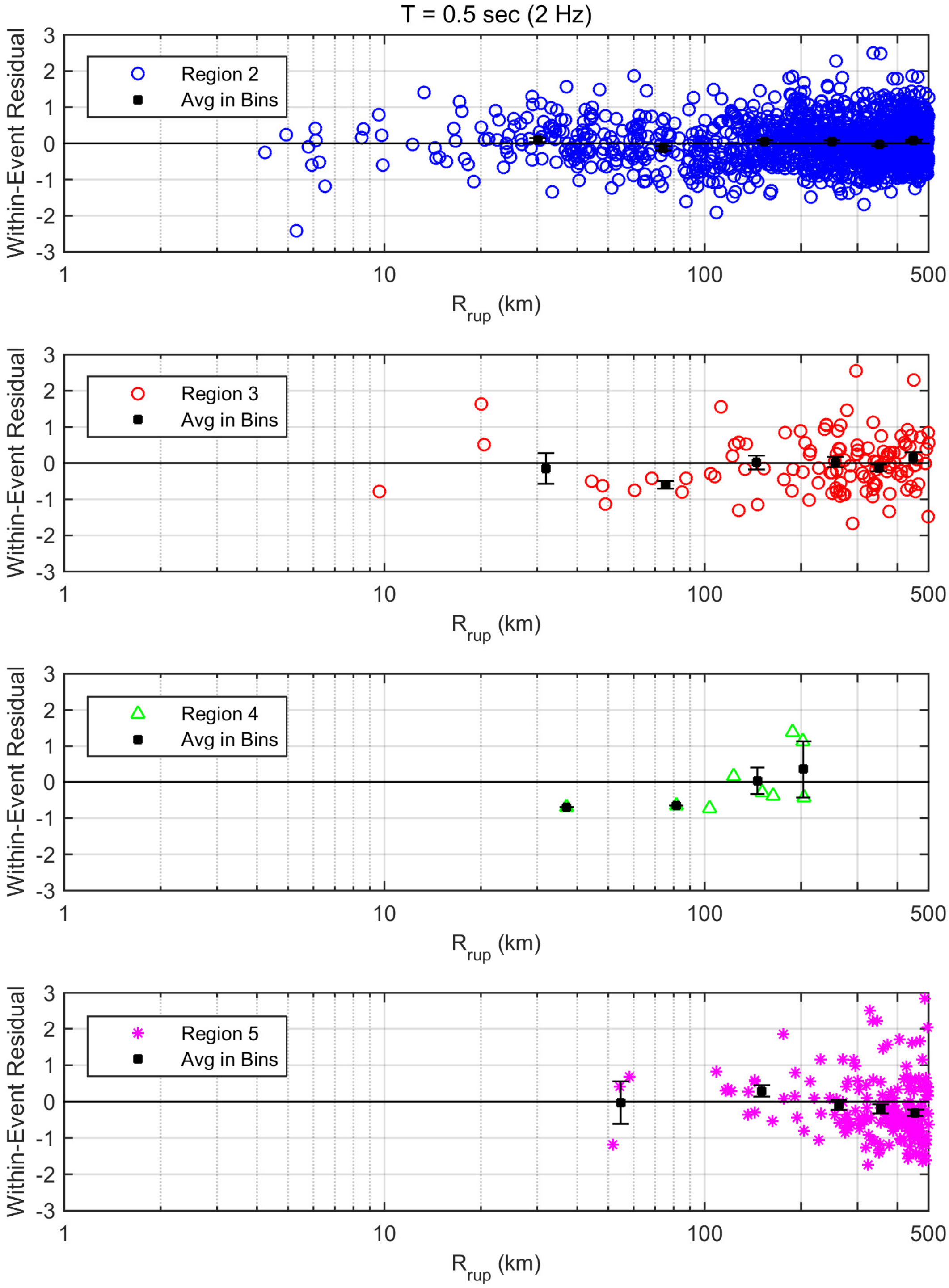

Figure 3.21 Within-event residuals (LN units) versus R_{RUP} by region for F = 2 Hz.

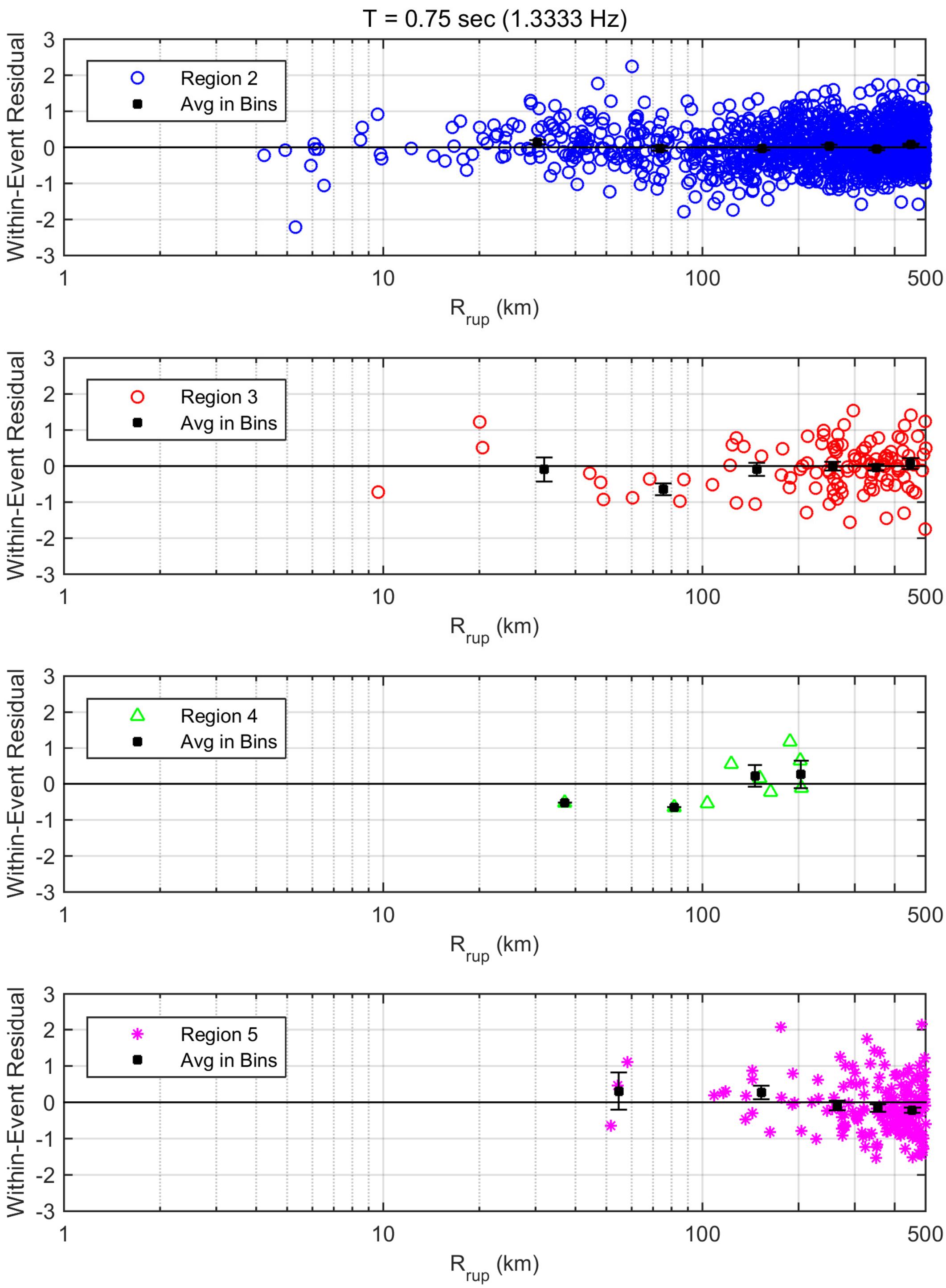

Figure 3.22 **Within-event residuals (LN units) versus R_{RUP} by region for F = 1.33 Hz.**

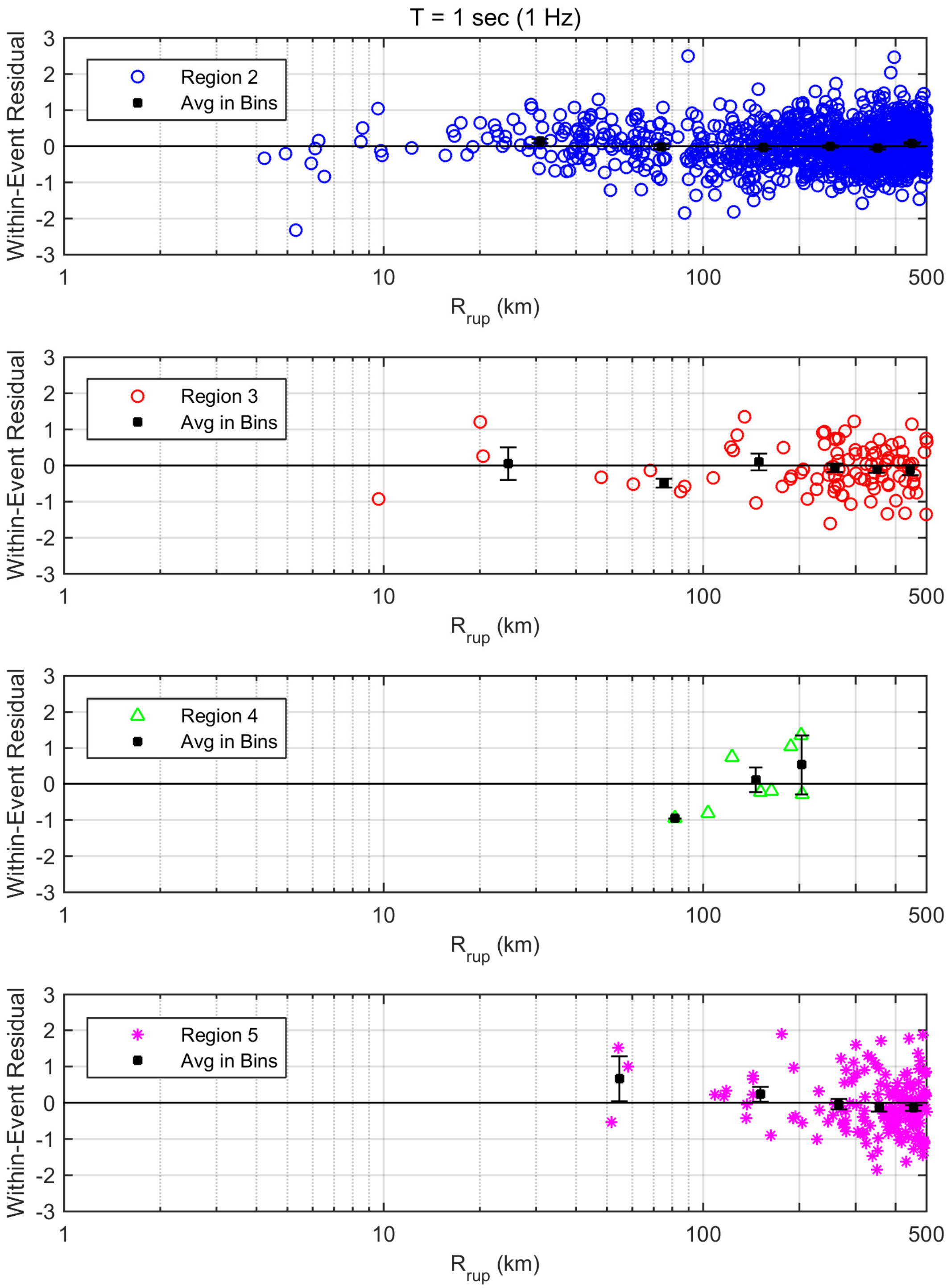

Figure 3.23 Within-event residuals (LN units) versus R_{RUP} by region for F = 1 Hz.

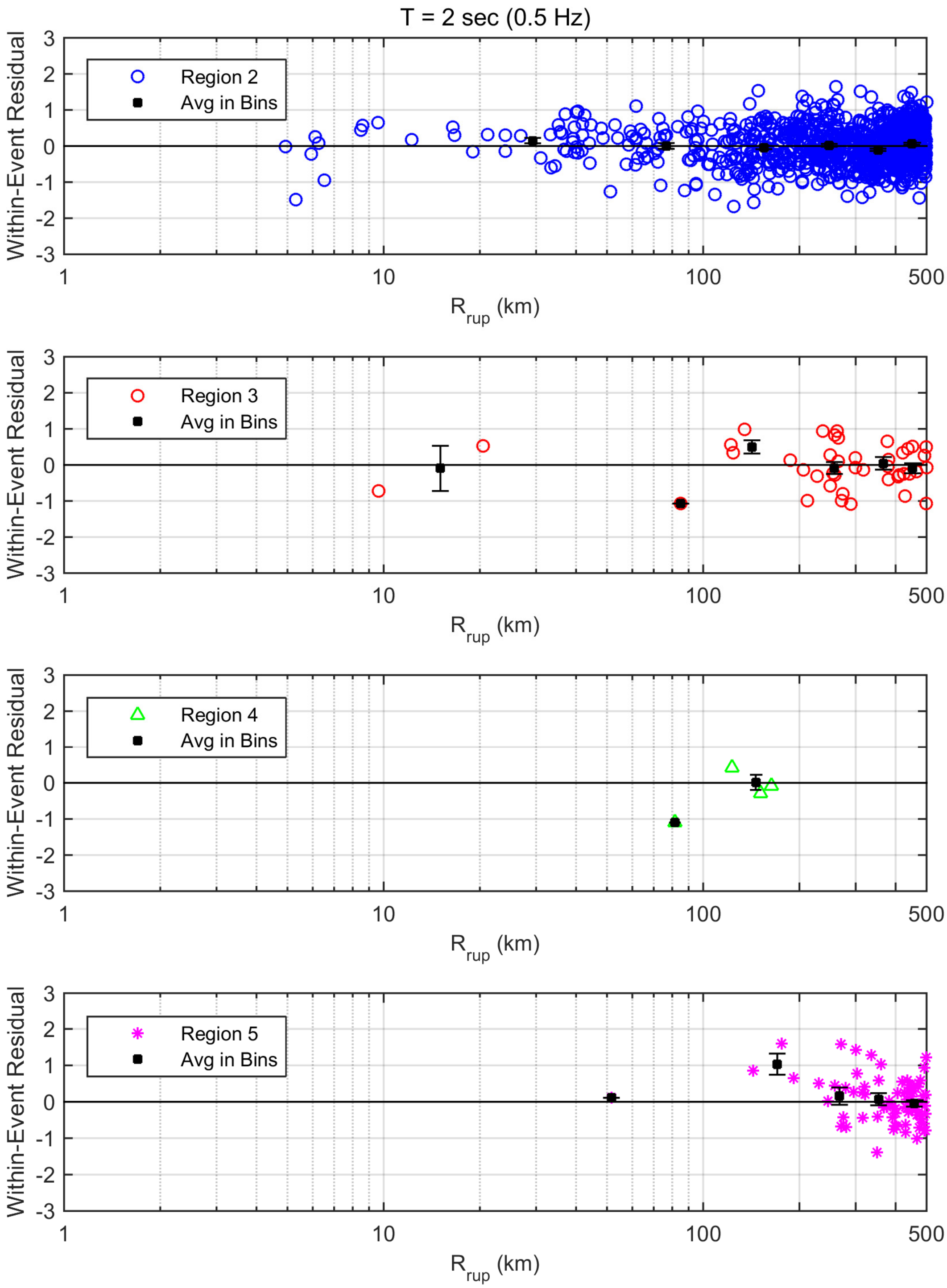

Figure 3.24 Within-event residuals (LN units) versus R_{RUP} by region for F = 0.5 Hz.

4 Analysis of the Components of Ground-Motion Variability

4.1 METHODOLOGY

Between-event and within-event residuals obtained from the regression of the CENA data with respect to the GMPE described in Section 3 are used to analyze trends in the between-event and within-event standard deviations, τ and ϕ. Trends of CENA τ with magnitude and hypocentral depth are evaluated. Similarly, trends of CENA ϕ with magnitude, distance, and V_{S30} are evaluated. Dependence of the ϕ and τ results on the minimum number of recordings per earthquake used in the regression analysis is investigated. Results are presented separately for PIE and tectonic events. The CENA τ and ϕ results are then compared to WUS τ and ϕ obtained from the NGA-West2 models. The WUS τ and ϕ values used in the comparisons are either based on the predictions of the NGA-West2 standard deviation models or computed using the event terms and the within-event residuals of the four NGA-West2 models (ASK14, BSSA14, CB14, and CY14) in different magnitude and/or distance bins. Average τ in different magnitude and hypocentral depth bins is calculated as shown in the equation below.

$$\tau\left(M_i, H_{dep_j}\right) = \sqrt{\frac{\sum_{e=1}^{NofEqk} E_{ije}\delta B_e^2}{\left(\sum_{e=1}^{NofEqk} E_{ije}\right)-1}} \tag{4.1}$$

where $NofEqk$ is the number of earthquakes in the dataset, and E_{ije} is a dummy variable with a value of 1 if earthquake e falls into magnitude bin i and hypocentral distance bin j, and 0 otherwise. Note that calculating τ in a magnitude bin only is done by setting the hypocentral depth bin to encompass all the earthquake depths in the dataset. Similarly, the equation used for calculating average ϕ in different magnitude, distance, and V_{S30} bins is shown below.

$$\phi\left(M_i, R_{rup_j}, V_{S30_k}\right) = \sqrt{\frac{\sum_{e=1}^{NofEqk}\sum_{s=1}^{NofSta_e} E_{ijkes}\delta W_{es}^2}{\left(\sum_{e=1}^{NofEqk}\sum_{s=1}^{NofSta_e} E_{ijkes}\right)-1}} \tag{4.2}$$

where $NofSta_e$ is the number of recordings from earthquake e, and E_{ijkes} is a dummy variable with a value of 1 if the recording at station s from earthquake e falls into magnitude bin i, R_{RUP} distance bin j, and V_{S30} bin k, and equal to 0 otherwise. The standard errors of τ and ϕ in different bins are computed as shown in Equations (4.3) and (4.4) below.

$$SE\left[\tau\left(M_i, H_{dep_j}\right)\right] = \frac{\tau\left(M_i, H_{dep_j}\right)}{\sqrt{2\left(\left(\sum_{e=1}^{NofEqk} E_{ije}\right)-1\right)}}, \tag{4.3}$$

$$SE\left[\phi\left(M_i, R_{rup_j}, V_{S30_k}\right)\right] = \frac{\phi\left(M_i, R_{rup_j}, V_{S30_k}\right)}{\sqrt{2\left(\left(\sum_{e=1}^{NofEqk}\sum_{s=1}^{NofSta_e} E_{ijkes}\right)-1\right)}}. \tag{4.4}$$

The mixed-effects algorithm described in Abrahamson and Youngs [1992] was used for the separation of the within-event residuals into site-to-site residuals and single-station within-event residuals assuming constant standard deviations (homoscedastic). Single-station within-event residuals are binned in different magnitude, distance, and V_{S30} bins to evaluate the trend in ϕ_{SS} with magnitude, distance, and V_{S30}. These trends are evaluated for PIE and tectonic events separately. Similarly, site terms are grouped in different V_{S30} bins to evaluate the dependence of ϕ_{S2S} on site conditions. Other factors such as the dependence of the results on the minimum number of recordings per station used in the regression analysis are evaluated. CENA ϕ_{SS} and ϕ_{S2S} results are compared to WUS ϕ_{SS} and ϕ_{S2S} obtained for the four NGA-West2 models. The WUS single-station sigma analysis was performed on the within-event residuals of the four NGA-West2 models using the same methodology used for the CENA single-station analysis. The average ϕ_{SS} in different bins is calculated in Equation (4.5):

$$\phi_{SS}\left(M_i, R_{rup_j}, V_{S30_k}\right) = \sqrt{\frac{\sum_{s=1}^{NofSta}\sum_{e=1}^{NofEqk_s} E_{ijkes}\delta WS_{es}^2}{\left(\sum_{s=1}^{NofSta}\sum_{e=1}^{NofEqk_s} E_{ijkes}\right)-1}} \tag{4.5}$$

where *NofSta* is the number of stations in the dataset that satisfy the minimum of recordings per station criterion used in the regression. E_{ijkes} is a dummy variable with a value of 1 if the recording at station *s* from earthquake *e* falls into magnitude bin *i*, R_{RUP} distance bin *j*, and V_{S30} bin *k*, and equal to 0 otherwise. The standard error of ϕ_{SS} in different bins is calculated as shown below in Equation (4.6):

$$SE\left[\phi_{SS}\left(M_i, R_{RUP_j}, V_{S30_k}\right)\right] = \frac{\phi_{SS}\left(M_i, R_{RUP_j}, V_{S30_k}\right)}{\sqrt{2\left(\left(\sum_{s=1}^{NofSta}\sum_{e=1}^{NofEqk_s} E_{ijkes}\right)-1\right)}}. \tag{4.6}$$

Similarly, ϕ_{S2S} and its standard error are calculated in different V_{S30} bins as follows, in Equation (4.7a) and (4.7b).

$$\phi_{S2S}\left(V_{S30_k}\right) = \sqrt{\frac{\sum_{s=1}^{NofSta} E_{ks}\delta S2S_s^2}{\left(\sum_{S=1}^{NofSta} E_{ks}\right)-1}} \tag{4.7a}$$

$$SE\left[\left(V_{S30_k}\right)\right] = \frac{\left(V_{S30_k}\right)}{\sqrt{2\left(\left(\sum_{S=1}^{NofSta} E_{ks}\right)-1\right)}} \tag{4.7b}$$

where E_{ks} is a dummy variable equal to 1 if stations falls into V_{S30} bin *k*.

4.2 τ

Figure 4.1 shows τ versus frequency for different minimum number of recordings per earthquake (1, 3, 5, and 10) used in the mixed effects regression. These τ values are the result of the regression that includes all earthquakes in the CENA dataset (PIE and tectonic for all magnitudes). Lines are added at 1 and 10 Hz in Figure 4.1 to show the frequency range with reliable results between 1 and 10 Hz resulting from bandwidth limitations of the recordings. Figure 4.1 show that τ values are generally similar between 1 and 10 Hz for a minimum of 1, 3, and 5 recordings per earthquake. For a minimum of 10 recordings per earthquake, τ appears to be smaller. Note that these criteria results in a total of 47, 59, 62, and 66 earthquakes for the minimum of 10, 5, 3, and 1 recordings per earthquake used in the regression at a frequency of 4 Hz, respectively. For the rest of analysis, residuals obtained with a minimum of three recordings per earthquake are used in order to ensure a large enough dataset while obtaining reliable event terms.

Figure 4.2 shows τ versus frequency for the PIE and tectonic earthquakes for all magnitudes as well as events with magnitude greater than or equal to 3.0. Figure 4.2 shows a difference in τ values for PIEs versus tectonic events with PIEs having smaller τ values. Figure 4.3 shows a comparison of CENA τ to WUS τ values as predicted by the 4 NGA-West2 GMPEs (ASK14, BSSA14, CB14, and CY14) for an earthquake with magnitude 3.95 (average magnitude of all earthquakes in the CENA dataset) and magnitude 4.1 (average magnitude of the CENA earthquakes with **M** greater than or equal to 3.0). Figure 4.3 indicates than CENA τ appears to be smaller than average NGA-West2 τ in the frequency range of 1 to 10 Hz.

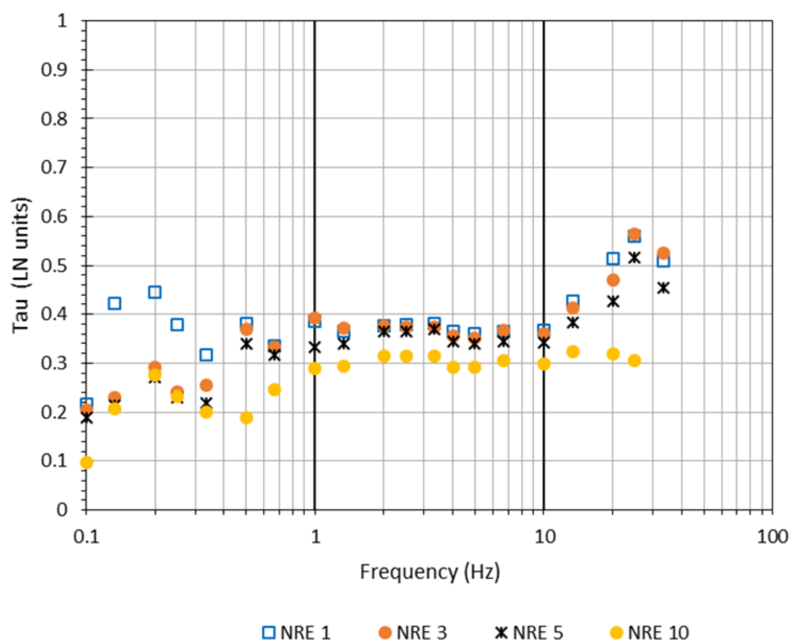

Figure 4.1 **τ versus frequency for different minimum number of recordings per earthquake (NRE) used in the regression.**

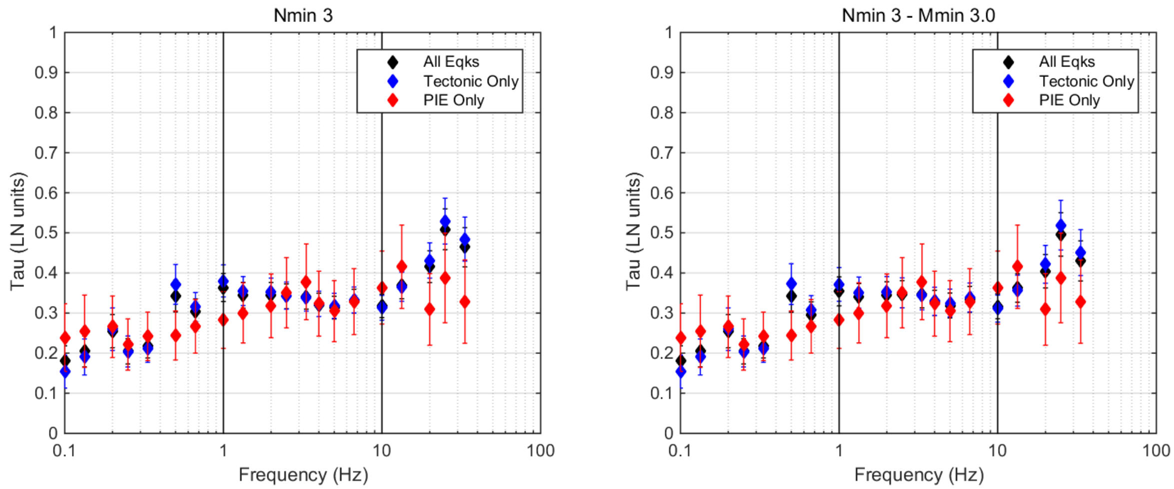

Figure 4.2 τ **versus frequency for PIE, tectonic and all earthquakes for minimum number (Nmin) of three recordings per earthquake and all magnitudes (left) and for earthquakes with a minimum M of 3.0 (right).**

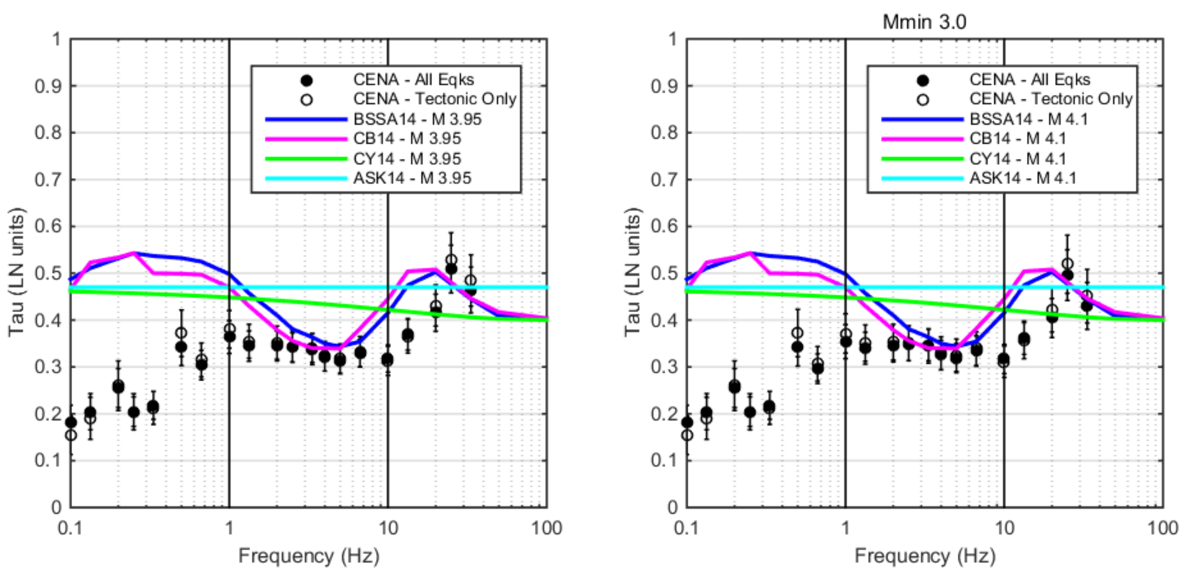

Figure 4.3 **Comparison of CENA** τ **to NGA-West2** τ **using all CENA earthquakes (left) and earthquakes with a minimum M of 3.0 (right).**

The CENA event terms were binned in magnitude bins of 0.5 unit width, and τ was computed in each magnitude bin to evaluate its magnitude dependence. Figures 4.4 to 4.6 show τ as a function of magnitude for spectral periods of 0.1, 0.25, 0.5, 0.75, 1, and 2 sec, respectively, compared to WUS τ. For WUS, τ values are shown as predicted by the four NGA-West2 standard deviation models as well as calculated from the models' event terms binned by magnitude, similar to the approach used for CENA. Figures 4.4 to 4.6 indicate that CENA data show no clear magnitude-dependence trend due to scarcity of data (large error bars), particularly for magnitude greater than 5.0. Moreover, these plots show that CENA τ appears to be generally smaller than WUS τ for magnitude 3.0 to 5.0 for both the predicted NGA-West2 τ as well as τ computed from the event terms of the NGA-West2 models.

Figure 4.7 shows CENA τ values computed from event terms binned in hypocentral depth bins of width equal to 5 km for all earthquakes as well as tectonic only earthquakes in the CENA dataset for spectral periods of 0.1, 0.25, 0.5, 0.75, 1, and 2 sec. These plots generally show no dependence of τ on hypocentral depth for both PIE and tectonic events.

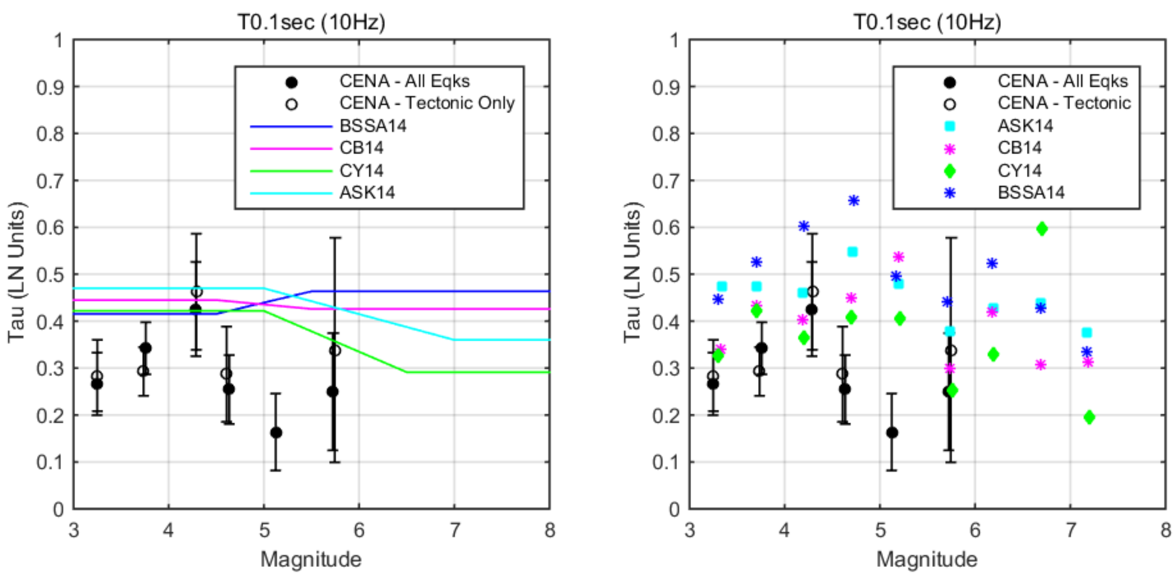

Figure 4.4 τ **versus magnitude for CENA compared to WUS** τ **predicted by NGA-West2 models (left) and computed from NGA-West2 event terms (right) at** ***F*** **= 10 Hz.**

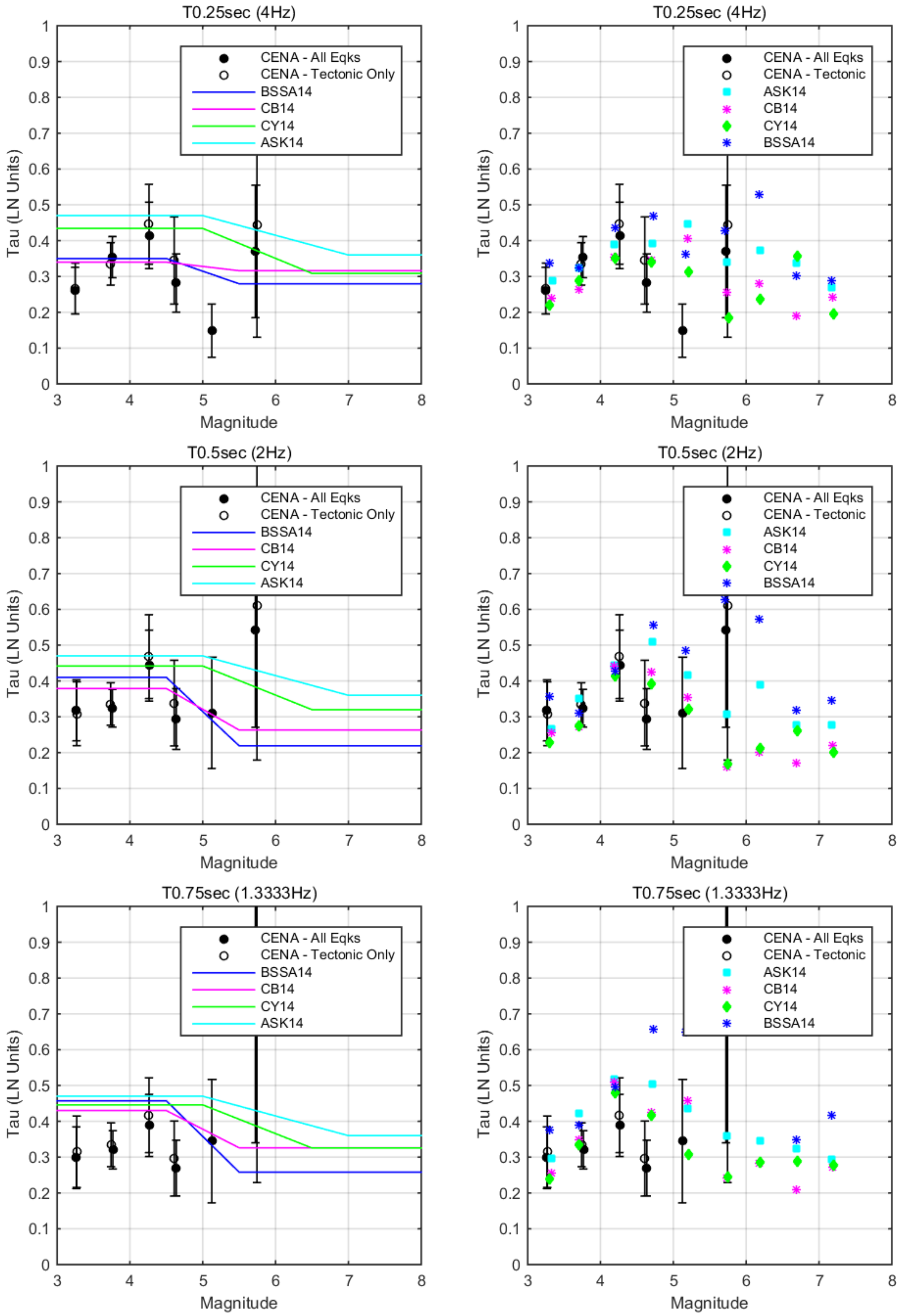

Figure 4.5 τ versus magnitude for CENA compared to WUS τ predicted by NGA-West2 models (left) and computed from NGA-West2 event terms (right) at F = 4, 2, and 1.33 Hz.

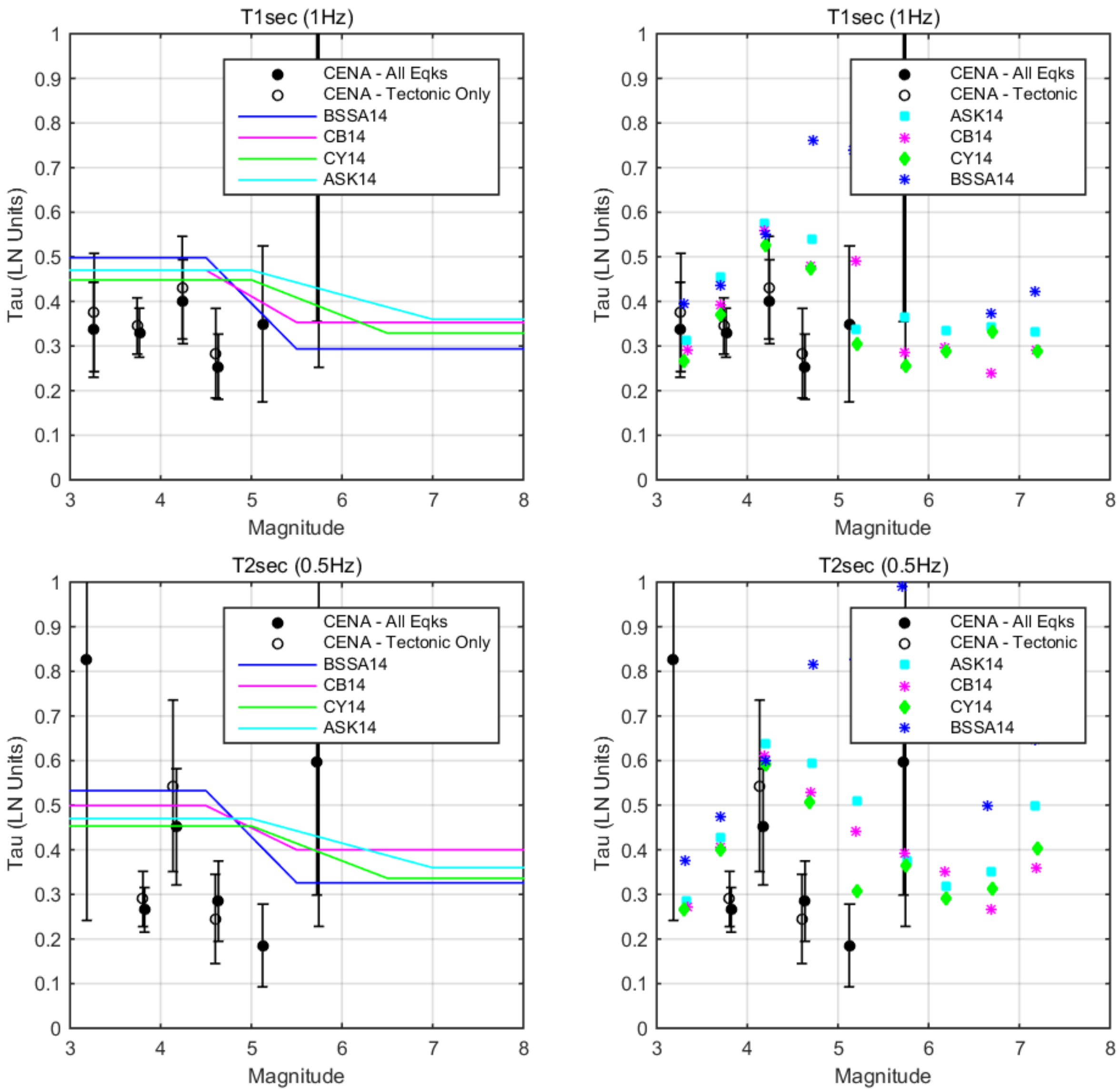

Figure 4.6 τ **versus magnitude for CENA compared to WUS** τ **predicted by NGA-West2 models (left) and computed from NGA-West2 event terms (right) at** F **= 1 and 0.5 Hz.**

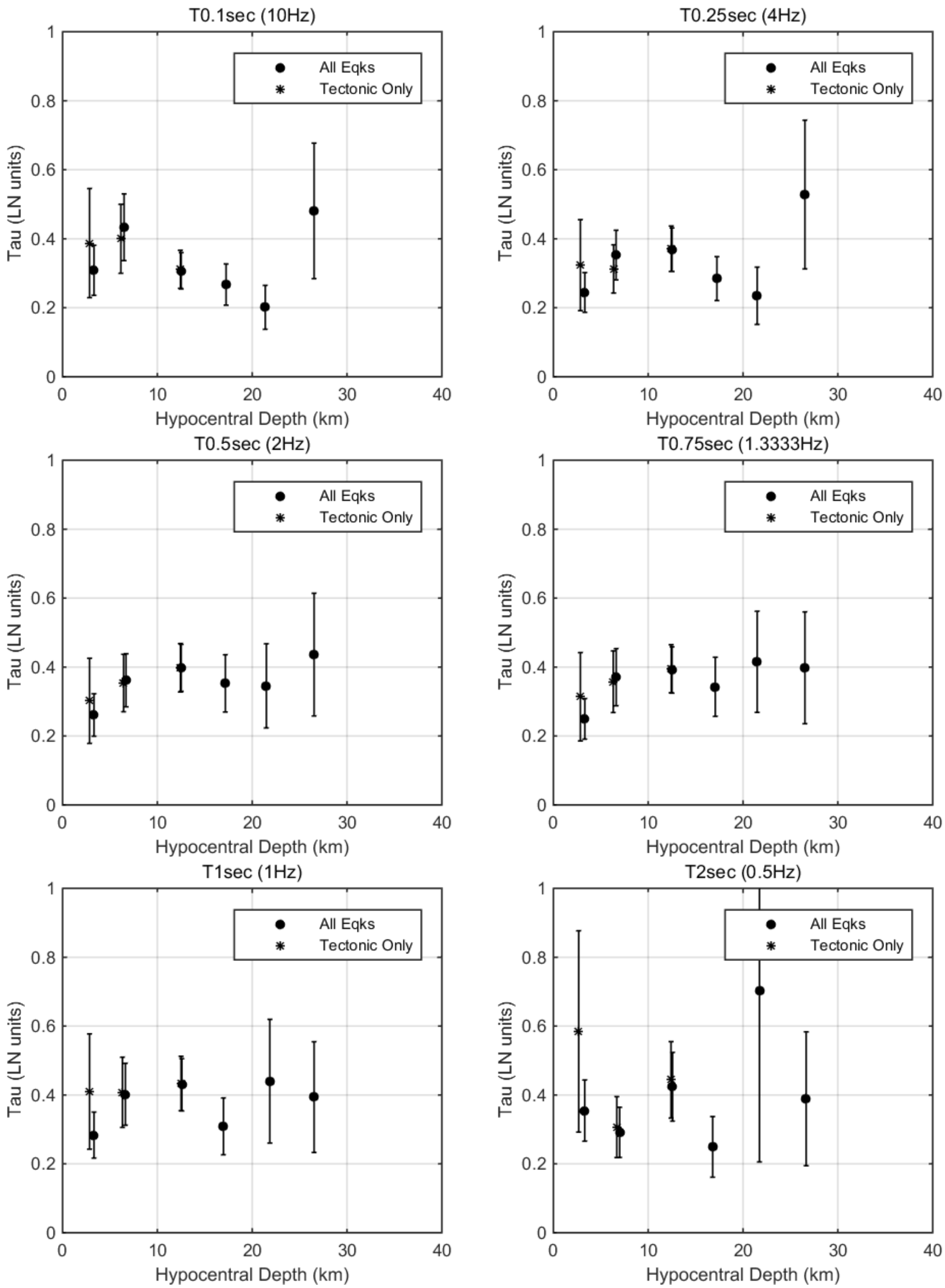

Figure 4.7 τ **versus hypocentral depth for CENA at** ***F*** **= 10, 4, 2, 1.33, 1, and 0.5 Hz.**

4.3 ϕ

Figure 4.8 shows CENA ϕ as a function of frequency for different minimum number of recordings per earthquake (1, 3, 5, and 10) used in the mixed effects regression. These ϕ values are the result of the regression that includes all earthquakes in the CENA dataset (PIE and tectonic for all magnitudes). The total number of recordings used in the regression at $F = 4$ Hz is 1848, 1842, 1831, and 1749 for a minimum of 1, 3, 5, and 10 recordings per earthquake, respectively. Figure 4.8 shows no significant difference in the resulting ϕ values. For the rest of analysis, within-event residuals obtained with a minimum of three recordings per earthquake are used. Figure 4.9 shows ϕ as a function of frequency for the PIE versus tectonic earthquakes for all magnitudes as well as earthquakes with magnitude greater than or equal to 3.0. Figure 4.9 shows a significant difference in ϕ between the PIE and tectonic events. ϕ for tectonic events is slightly larger for magnitudes greater than 3.0 than for all magnitudes in the dataset (**M** greater than 2.0).

Figure 4.10 shows a comparison of CENA ϕ to WUS ϕ values as predicted by the four NGA-West2 GMPEs (ASK14, BSSA14, CB14, and CY14) for an earthquake with magnitude 4.0 (average magnitude of all recordings in the CENA dataset) and magnitude 4.14 (average magnitude of the CENA recordings with **M** greater than or equal to 3.0). Figure 4.10 shows that CENA ϕ for tectonic events is larger than average NGA-West2 ϕ in the frequency range of 1 to 10 Hz. Figure 4.11 shows CENA ϕ for Regions 2, 3, and 5. Region 4 has only few recordings (13 recordings at $F = 4$ Hz); therefore, ϕ is not shown for this region. Figure 4.11 shows that Region 2 defined as having paths contained within Central North America has smaller ϕ values than Regions 3 (paths contained within the Appalachian Province) and 5 (paths crossing at least two of the defined regions). Note that the error bars on the ϕ values for Regions 3 and 5 are large due to the relatively small subsets of data in these regions compared to Region 2.

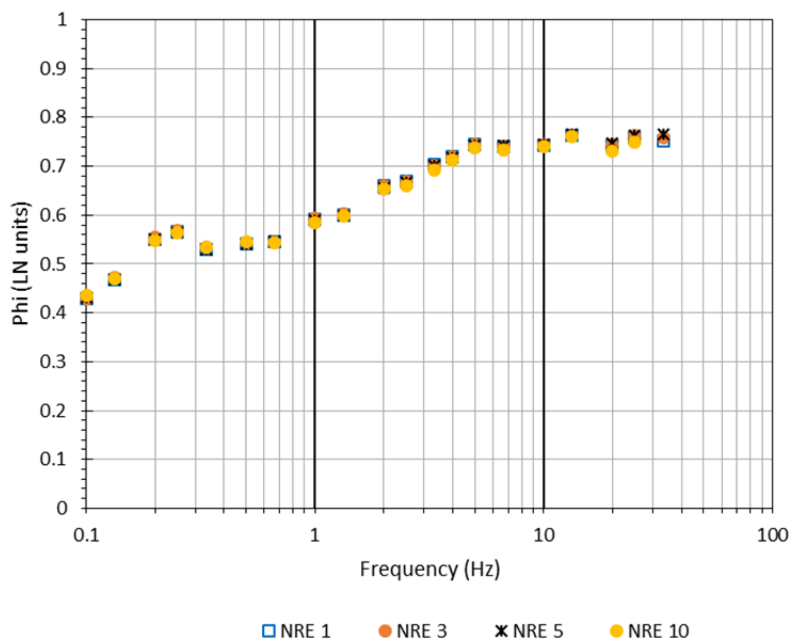

Figure 4.8 **ϕ versus frequency for different minimum number of recordings per earthquake (NRE) used in the regression.**

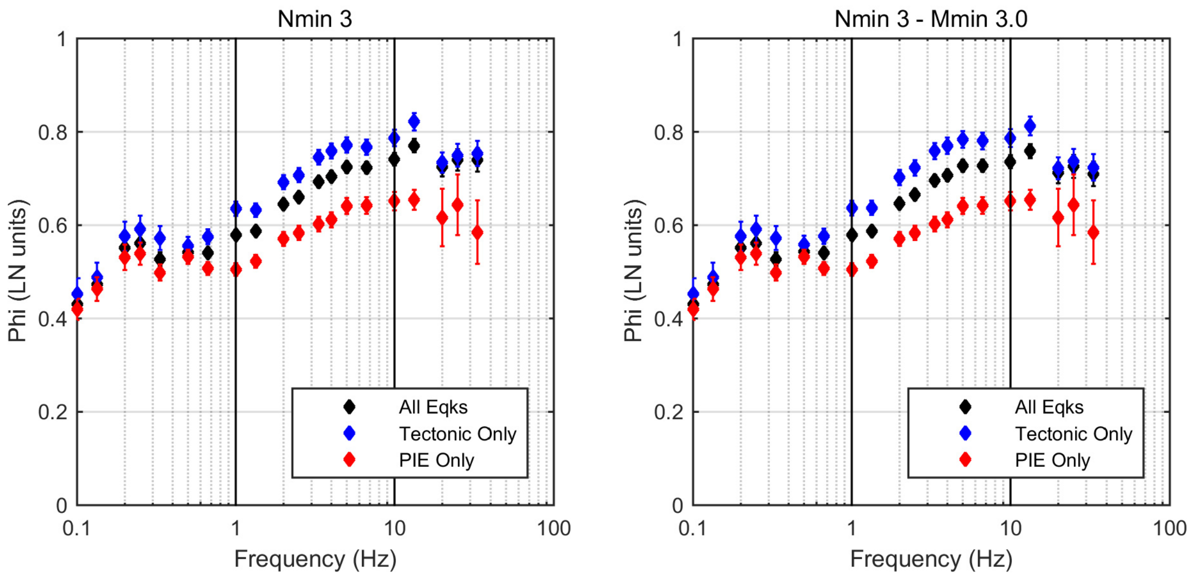

Figure 4.9 **ϕ versus frequency for PIE, tectonic and all earthquakes for minimum number (Nmin) of three recordings per earthquake and all magnitudes (left) and for earthquakes with a minimum M of 3.0 (right).**

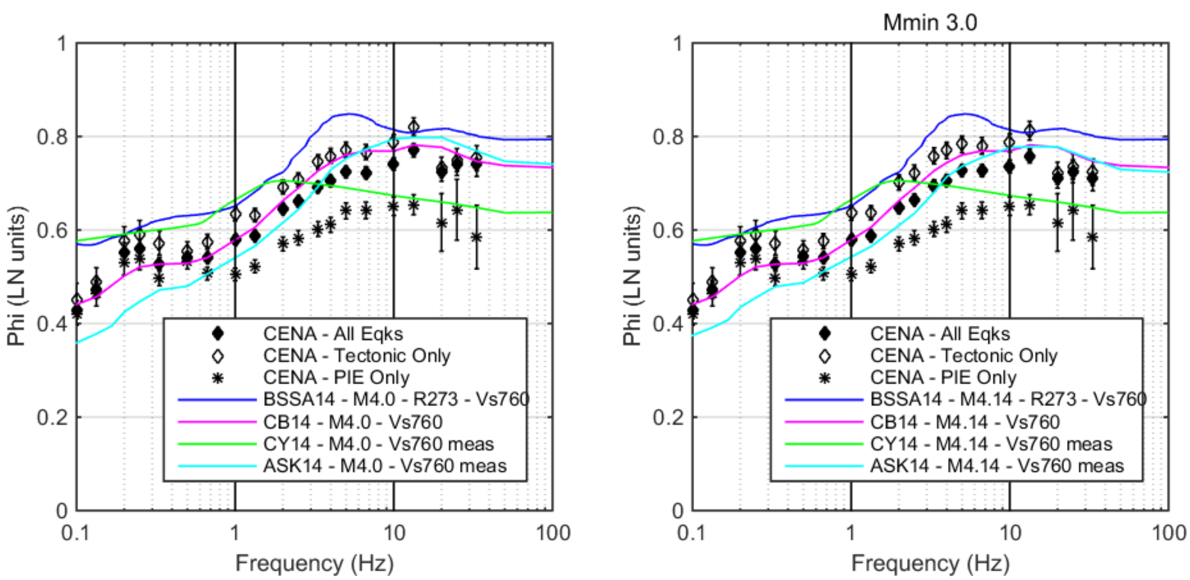

Figure 4.10 **Comparison of CENA ϕ to NGA-West2 ϕ using all CENA recordings (left) and recordings with a minimum M of 3.0 (right).**

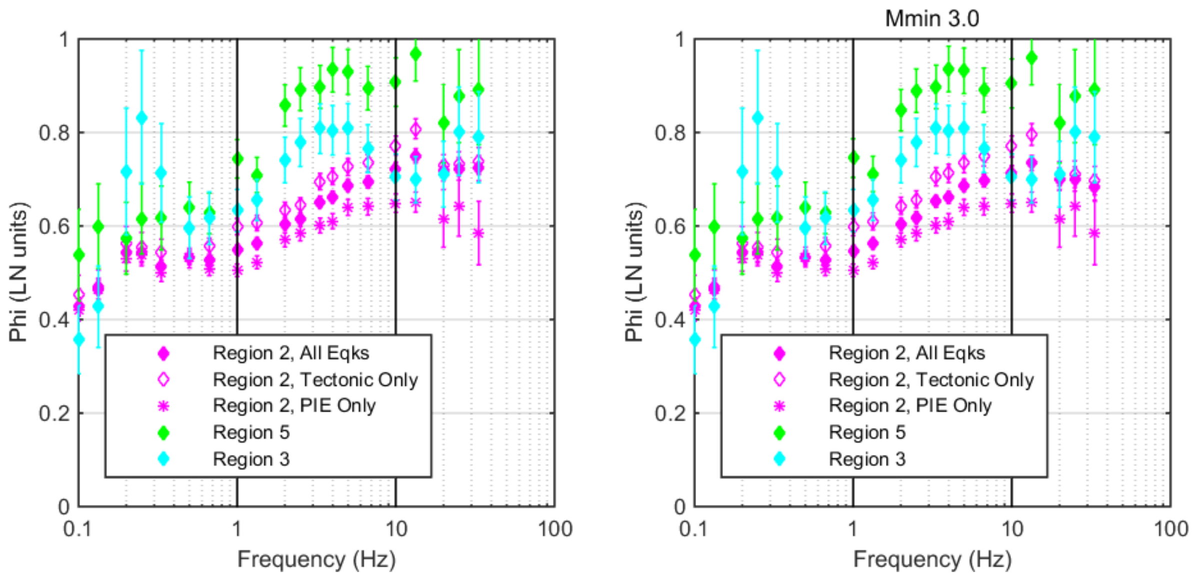

Figure 4.11 **CENA ϕ by region using all recordings (left) and recordings with a minimum M of 3.0 (right).**

The CENA within-event residuals were binned in magnitude bins of 0.5 unit width and ϕ was computed in each magnitude bin to evaluate its magnitude dependence. Figures 4.12 and 4.13 show ϕ as a function of magnitude for spectral periods of 0.1, 0.25, 0.5, 0.75, 1, and 2 sec, respectively, compared to WUS ϕ. For WUS, ϕ values are shown as predicted by the four NGA-West2 standard deviation models as well as calculated from the models' within-event residuals binned by magnitude similar to the approach used for CENA. The plots on the right of Figures 4.12 and 4.13 show CENA ϕ calculated using residuals from recordings with a similar distance range to the WUS data (R_{RUP} less than or equal to 350 km). Figures 4.12 and 4.13 show some trend of ϕ with magnitude similar to the one observed for the NGA-West2 ϕ values for similar distance ranges (plots on the right). However, these trends are difficult to extrapolate for magnitude greater than 5.0 due to limited number of recordings at large magnitudes. These figures also show that CENA ϕ for tectonic events appear to be generally larger than average WUS ϕ.

The CENA within-event residuals were binned in R_{RUP} distance bins of 50 km width and ϕ was calculated for each distance bin. Similarly, within-event residuals of the four NGA-West2 models were binned by distance, and their resulting ϕ was compared to CENA ϕ in the same distance bins. Data with magnitude 3.0 to 6.0 were used to bin CENA and WUS residuals, and calculate their resulting ϕ values in order to have a comparable magnitude range for the WUS and CENA data. Figure 4.14 shows CENA ϕ as a function of R_{RUP} for spectral periods of 0.1, 0.25, 0.5, 0.75, 1, and 2 sec compared to WUS ϕ. Figure 4.14 does not show a clear trend of CENA ϕ with distance similar to WUS ϕ.

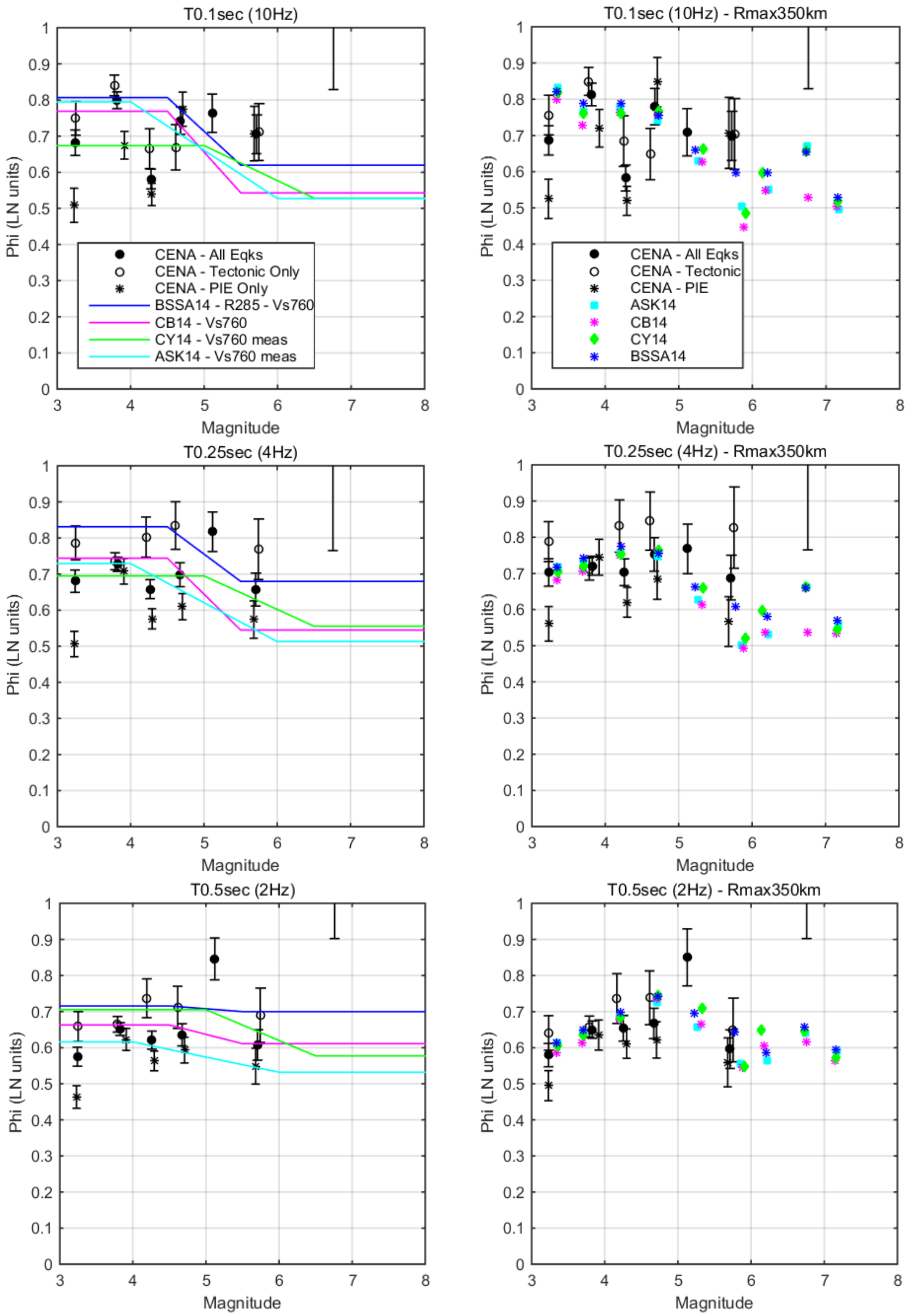

Figure 4.12 ϕ versus magnitude for CENA compared to WUS ϕ predicted by NGA-West2 models (left); and computed from NGA-West2 residuals (right) at *F* = 10, 4, and 2 Hz.

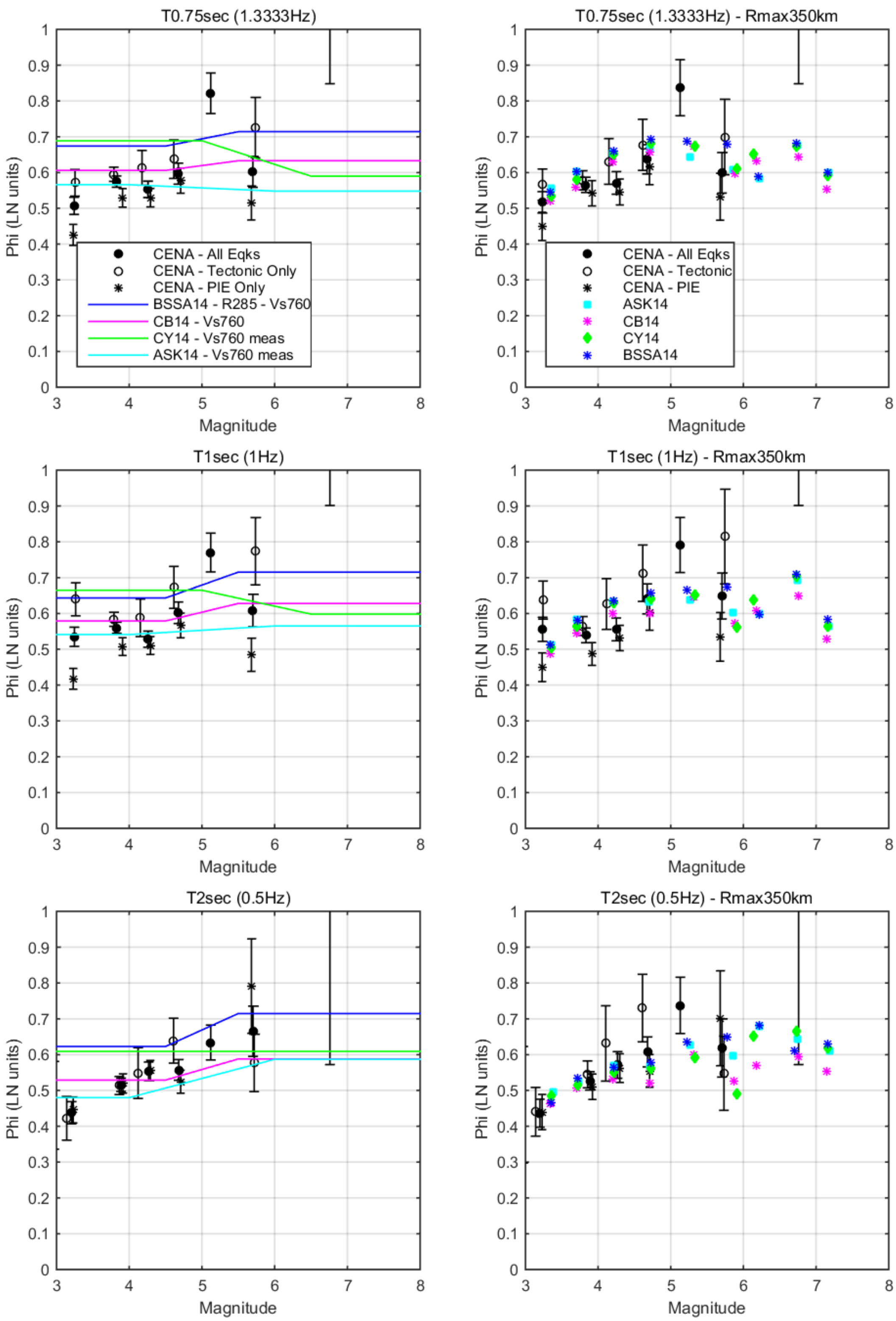

Figure 4.13 ϕ versus magnitude for CENA compared to WUS ϕ predicted by NGA-West2 models (left) and computed from NGA-West2 residuals (right) at F = 1.33, 1, and 0.5 Hz.

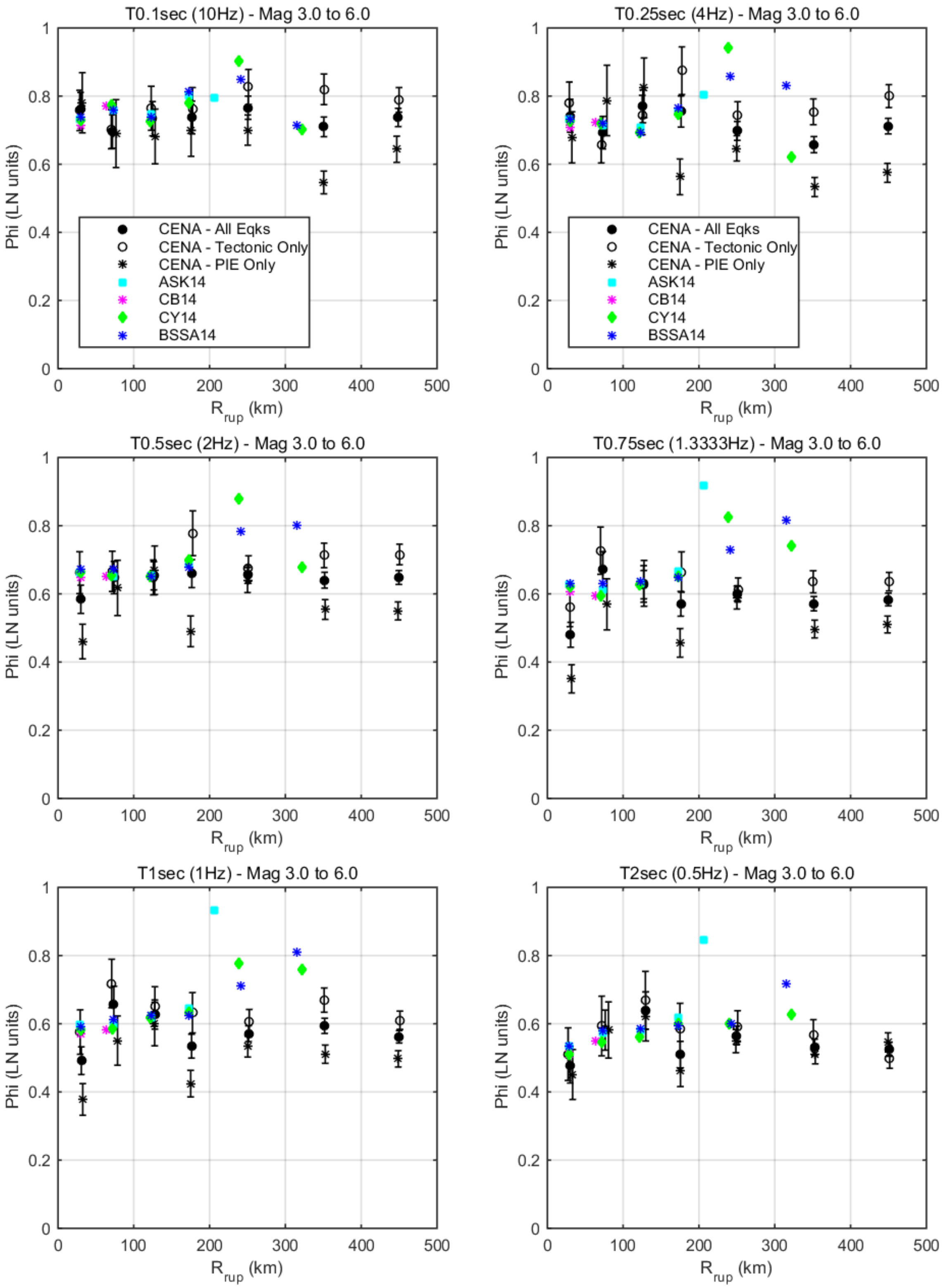

Figure 4.14 ϕ **versus distance for CENA compared to WUS** ϕ **at** F **= 10, 4, 2, 1.33, 1, and 0.5 Hz.**

The CENA and NGA-West2 within-event residuals were binned by magnitude (3.0 to 4.0, 4.0 to 5.0, and 5.0 to 6.0) and in R_{RUP} distance bins of 50 km width to compute ϕ and evaluate its magnitude and distance dependence. Figures 4.15 to 4.20 show CENA and WUS ϕ as a function of distance in the three magnitude bins for spectral periods of 0.1, 0.25, 0.5, 0.75, 1, and 2 sec, respectively. Figures 4.15 to 4.20 do not show clear trends of the CENA ϕ primarily due to relatively small dataset available for magnitudes greater than 4.0.

Figure 4.21 shows CENA ϕ as a function of V_{S30} computed by binning the within-event residuals in V_{S30} bins of 250 m/sec width. Figure 4.21 generally shows no clear trend of ϕ with V_{S30}. CENA within-event residuals were binned by V_{S30} code in order to compare resulting ϕ values for the different V_{S30} codes (0 to 5) in the dataset. Figure 4.22 shows CENA ϕ as a function of frequency for the different V_{S30} codes, indicating that ϕ values calculated for the recordings with measured V_{S30} are not smaller than those calculated for recordings with V_{S30} estimated based on different proxies. Moreover, ϕ values calculated for V_{S30} code 0 (measured V_{S30}), 1 (known site conditions and geology based on measurements at a different location with the same geological condition) and 5 (V_{S30} based on weighted average of estimates from all available proxies when estimates from the *P*-wave seismogram method are not available) are all comparable. This plot indicates that the relatively large ϕ values observed for CENA are unlikely to be primarily the result of errors in V_{S30} assignment.

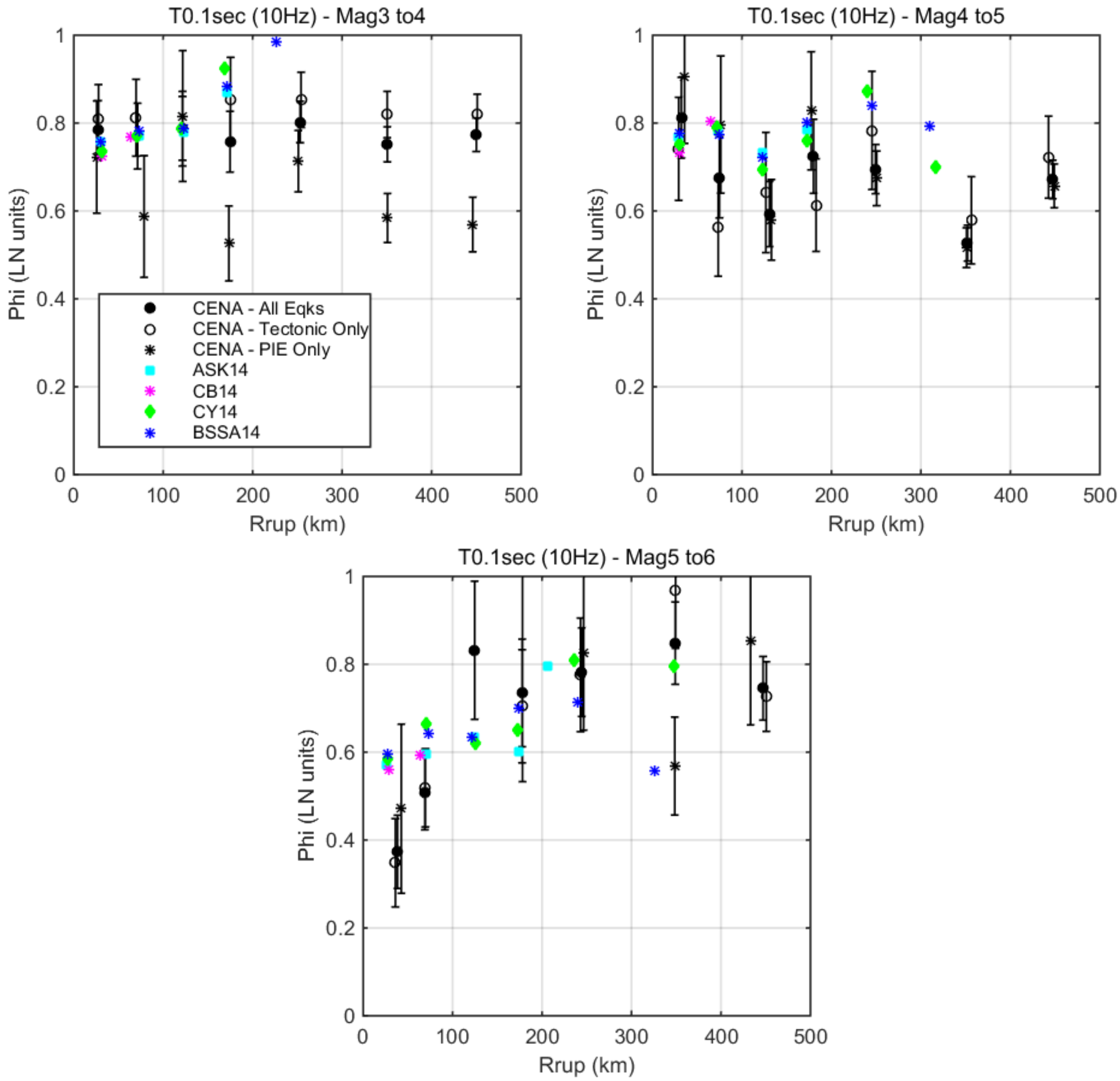

Figure 4.15 **CENA ϕ versus distance in three magnitude bins compared to WUS ϕ at F = 10 Hz.**

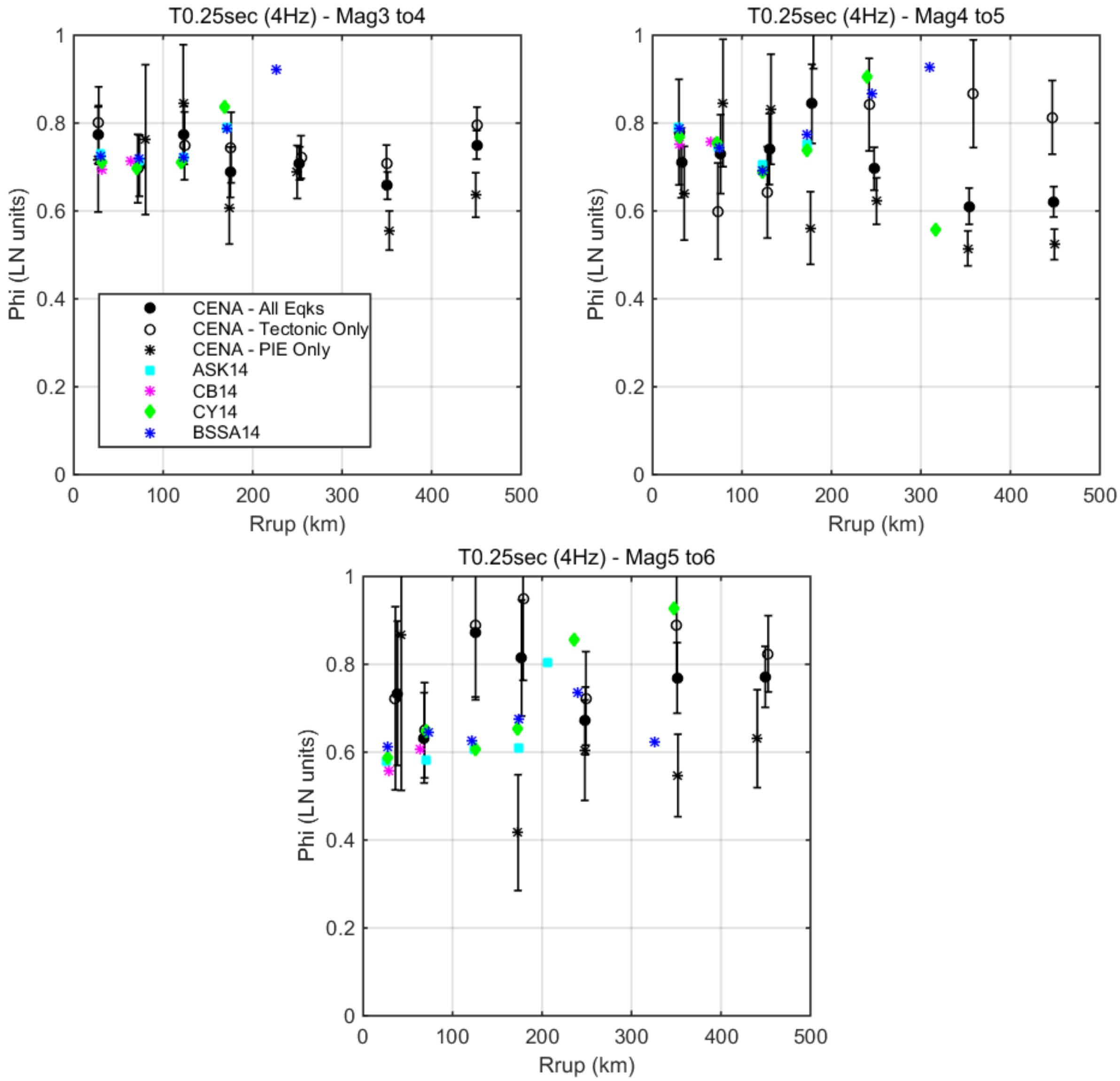

Figure 4.16 CENA ϕ versus distance in three magnitude bins compared to WUS ϕ at F = 4 Hz.

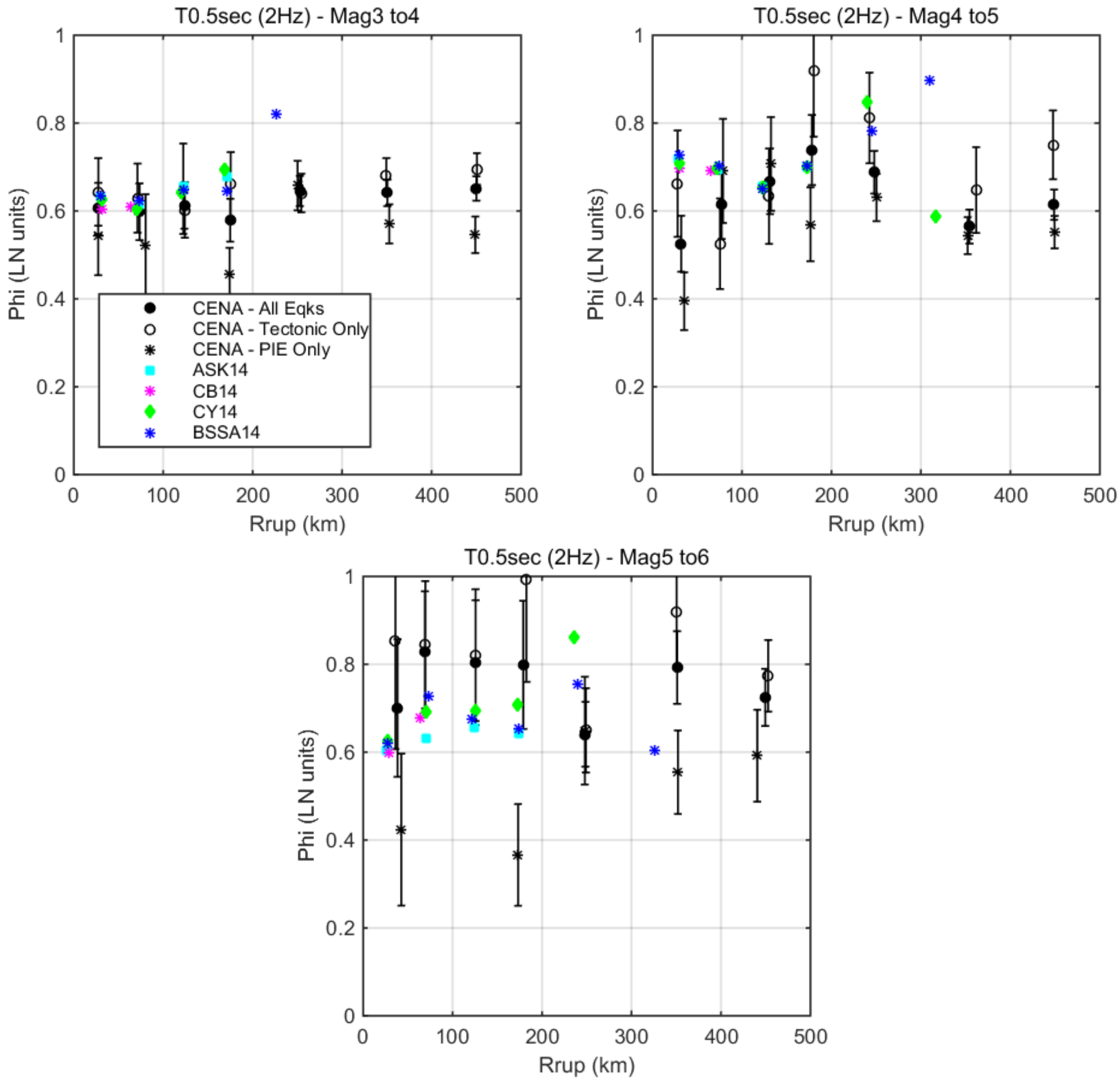

Figure 4.17 **CENA ϕ versus distance in three magnitude bins compared to WUS ϕ at F = 2 Hz.**

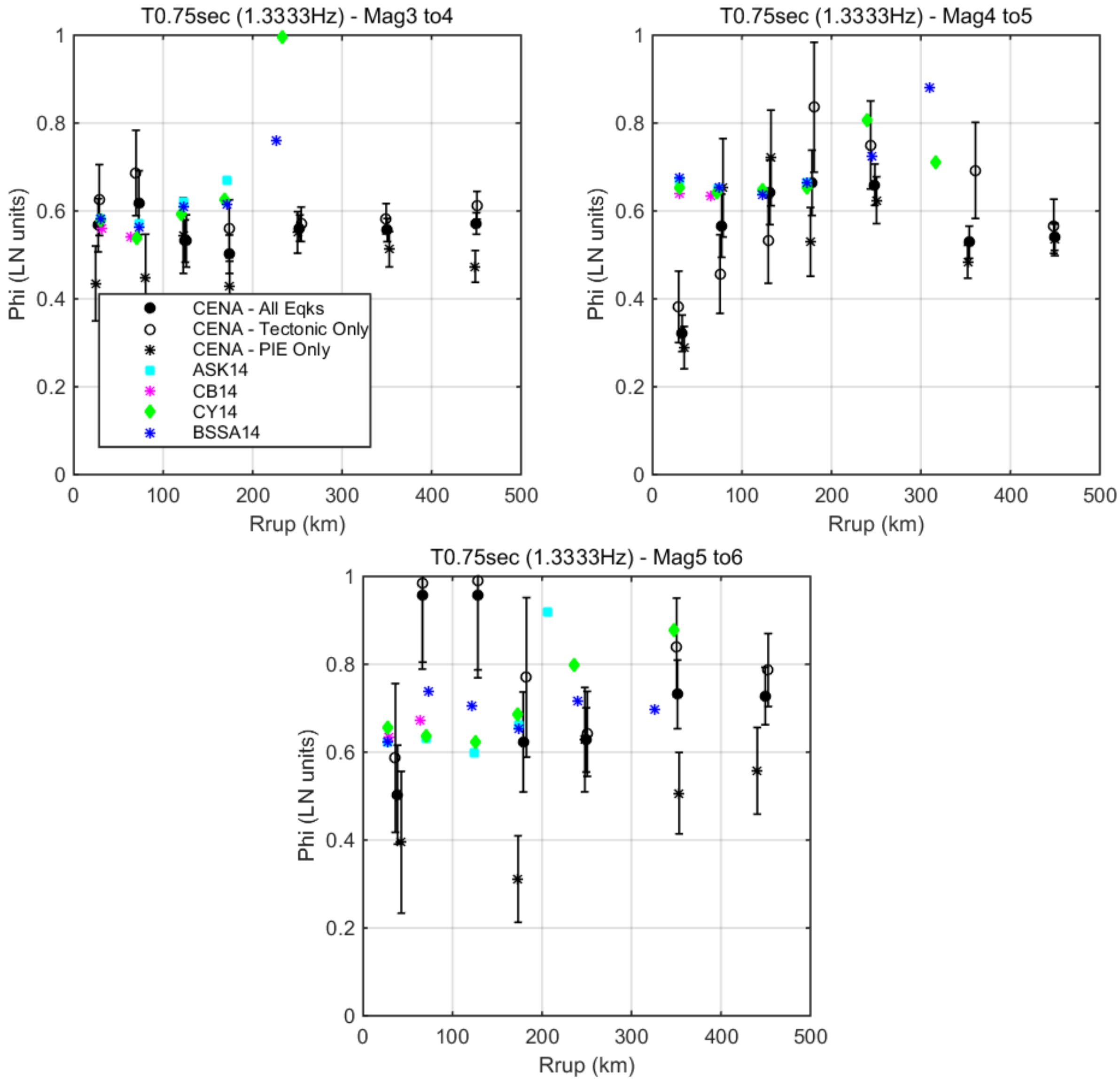

Figure 4.18 CENA ϕ versus distance in three magnitude bins compared to WUS ϕ at F = 1.33 Hz.

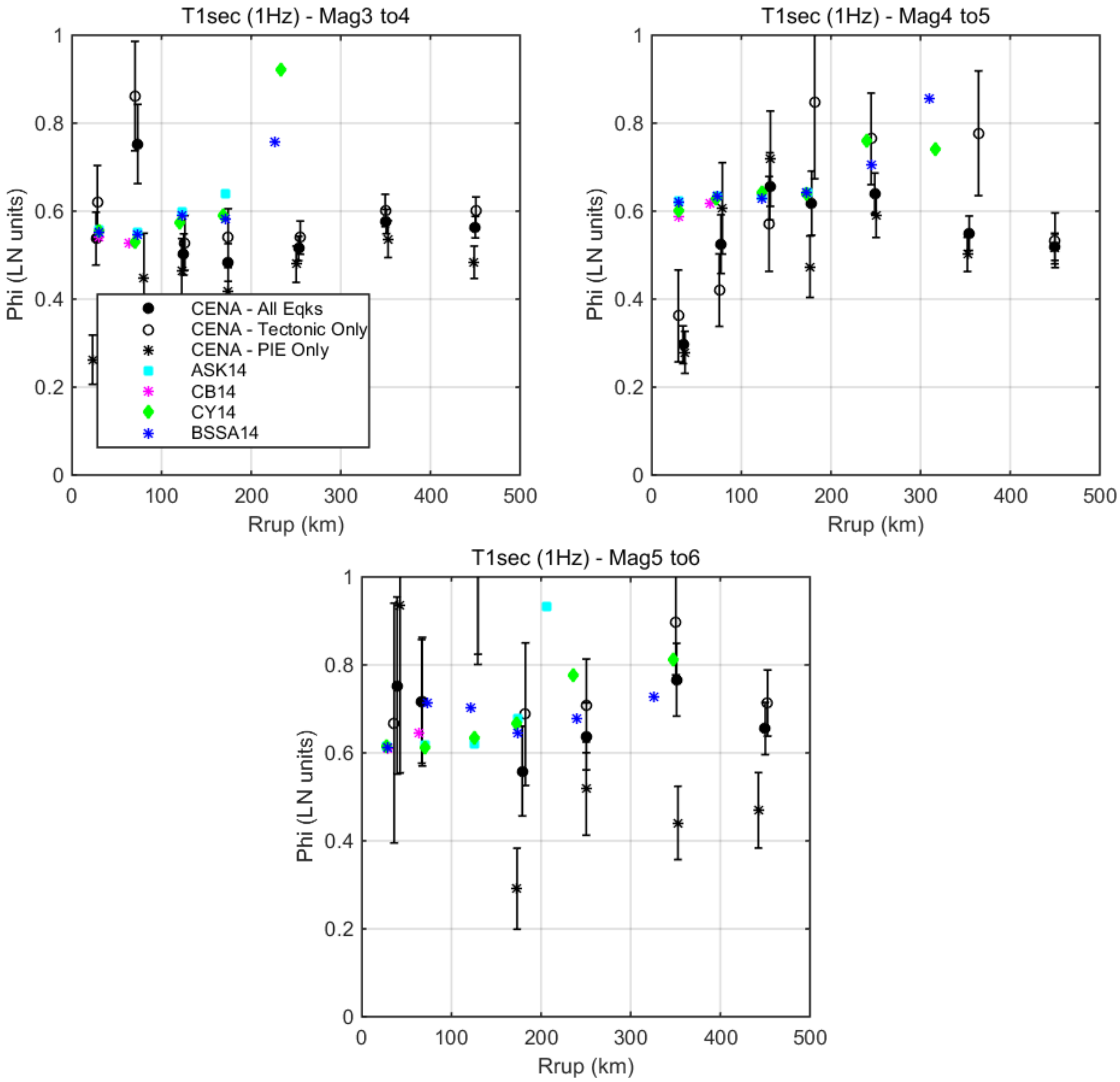

Figure 4.19 CENA ϕ versus distance in three magnitude bins compared to WUS ϕ at F = 1 Hz.

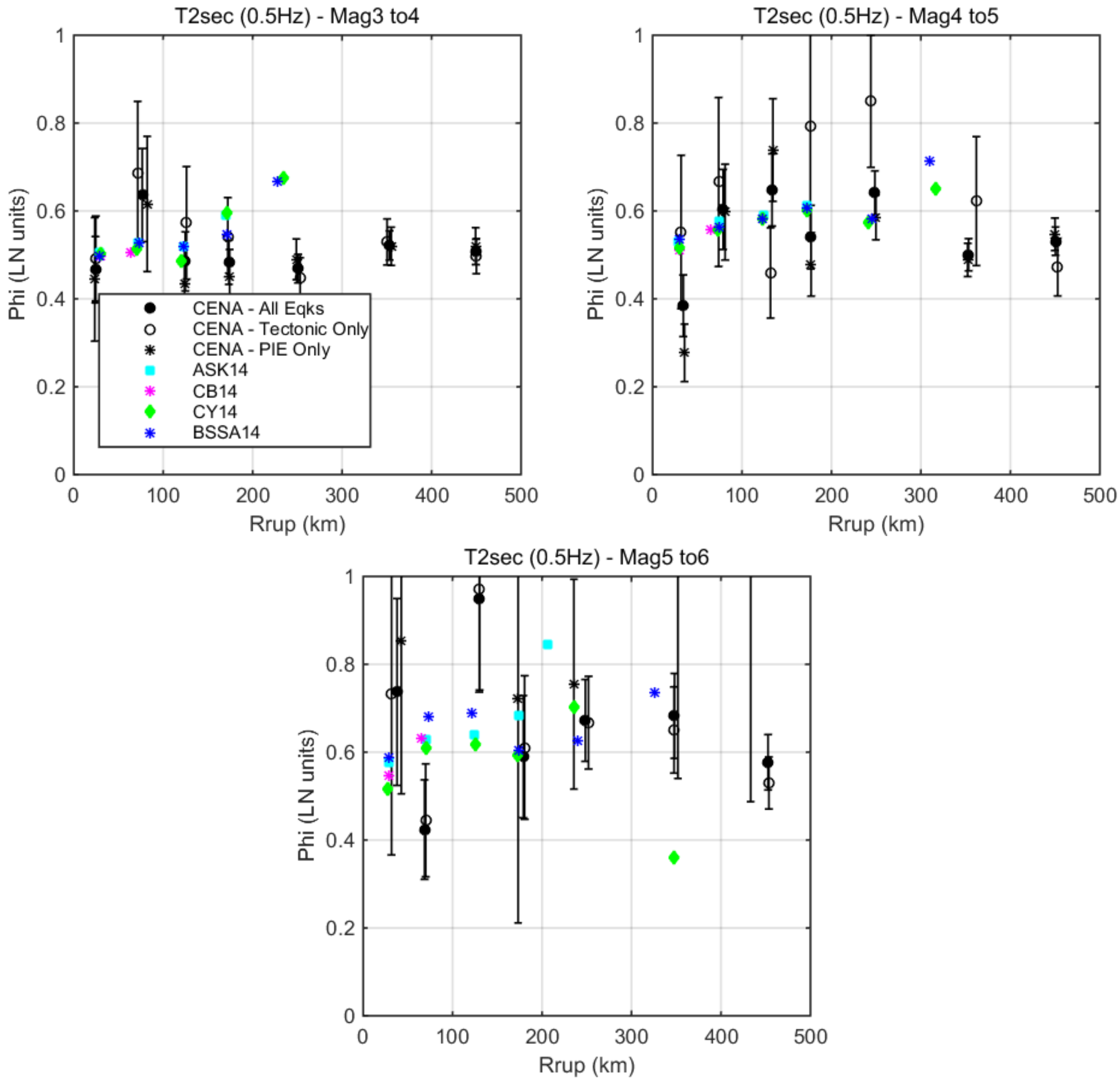

Figure 4.20 **CENA ϕ versus distance in three magnitude bins compared to WUS ϕ at F = 0.5 Hz.**

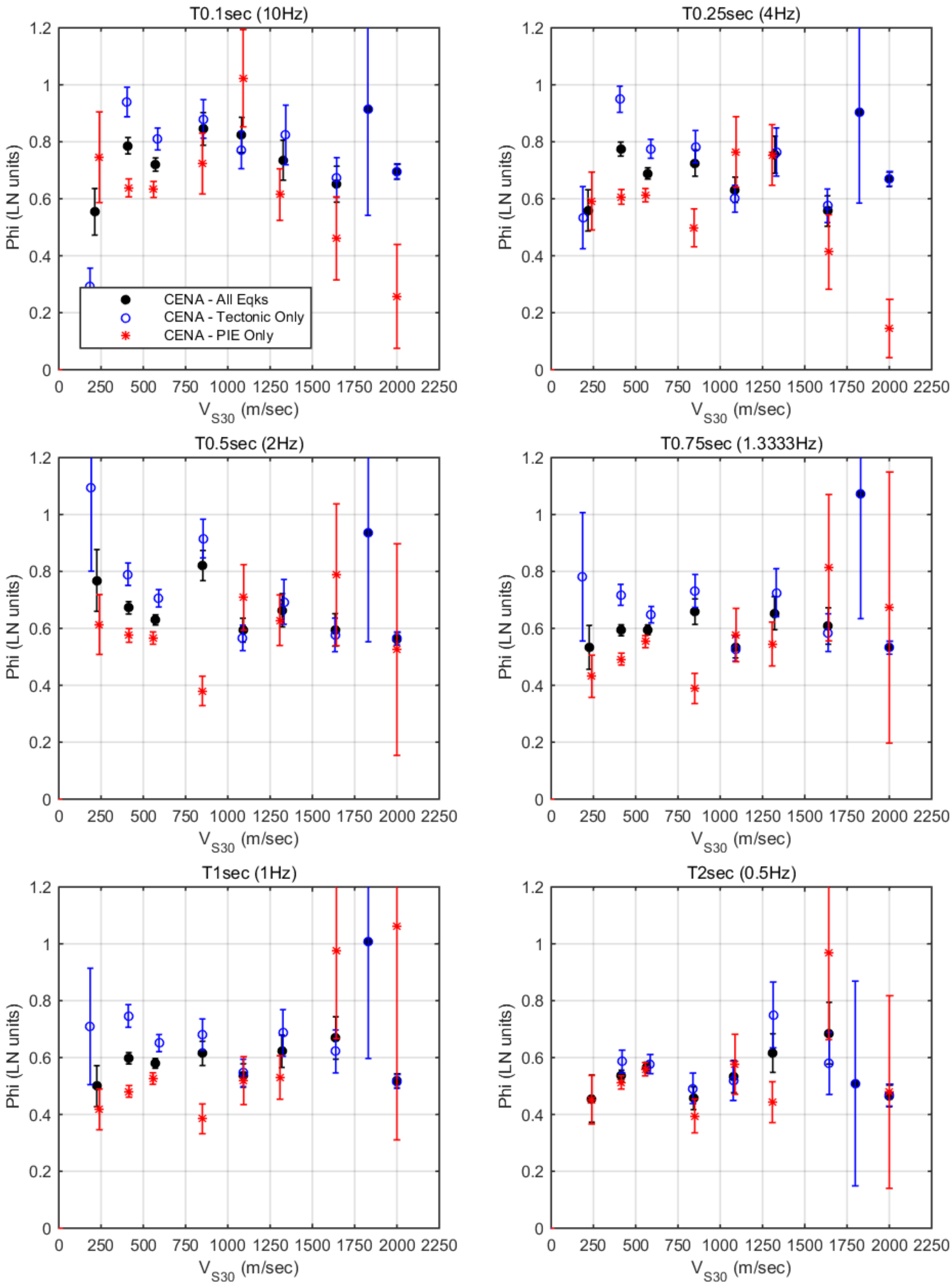

Figure 4.21 CENA ϕ versus V_{S30} at F = 10, 4, 2, 1.33, 1, and 0.5 Hz.

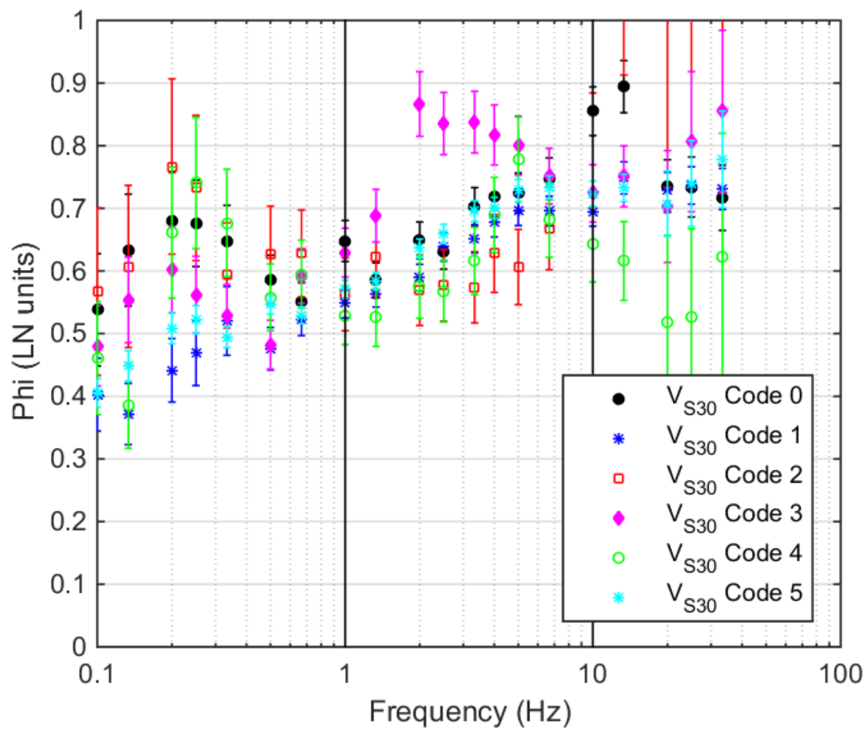

Figure 4.22 CENA ϕ versus frequency for the different V_{S30} codes.

4.4 ϕ_{SS}

Within-event residuals obtained from the CENA dataset with a minimum of three recordings per earthquake were used in the mixed effects regression [Abrahamson and Youngs 1992] to estimate ϕ_{SS} and ϕ_{S2S} and separate the site terms from the single-station within-event residuals. Figure 4.23 shows ϕ_{SS} as a function of frequency for different minimum number of recordings per station (1, 3, 5, and 10) used in the mixed effects regression. These ϕ_{SS} values are the result of the regression that includes all earthquakes in the CENA dataset (PIE and tectonic for all magnitudes). The total number of recordings used in the regression at F = 4 Hz is 1842, 1618, 1245, and 327 for a minimum of 1, 3, 5, and 10 recordings per station, respectively. Figure 4.23 shows that ϕ_{SS} values are comparable between 1 and 10 Hz for a minimum of 1, 3, and 5 recordings per station used in the regression analysis. For a minimum of 10 recordings per station, ϕ_{SS} is higher likely due to the small number of recordings available for the regression. For the rest of the analysis, single-station within-event residuals obtained from the regression with a minimum of three recordings per station are used.

Figure 4.24 shows ϕ_{SS} as a function of frequency for the PIE and tectonic events for all magnitudes as well as events with magnitude greater than or equal to 3.0. Figure 4.24 shows a small difference in ϕ_{SS} values for PIE versus tectonic events with tectonic events having slightly larger ϕ_{SS} values than PIEs. Figure 4.25 shows CENA ϕ_{SS} by region for Regions 2, 3, and 5 for all recordings as well as only those with magnitude greater than or equal to 3.0. Figure 4.25 shows that Region 5 (recordings with paths crossing at least two of the defined regions) has larger ϕ_{SS} values than Regions 2 and 3. Moreover, ϕ_{SS} values calculated using recordings with minimum **M** = 3.0 are similar to those calculated using recordings from all earthquakes in the dataset (minimum **M** = 2.0). Figure 4.26 compares CENA and NGA-West2 ϕ_{SS} as a function of frequency, whereby ϕ_{SS} is calculated using subsets of the CENA and WUS data with minimum **M** = 3.0 and then with **M** between 3.0 and 6.0, and R_{RUP} up to 300 km. Figure 4.26 shows that WUS ϕ_{SS} appears to be slightly larger than CENA ϕ_{SS} in the frequency range of 1 to 10 Hz even for the similar magnitude and distance ranges of the data (**M** between 3.0 and 6.0 and R_{RUP} up to 300 km).

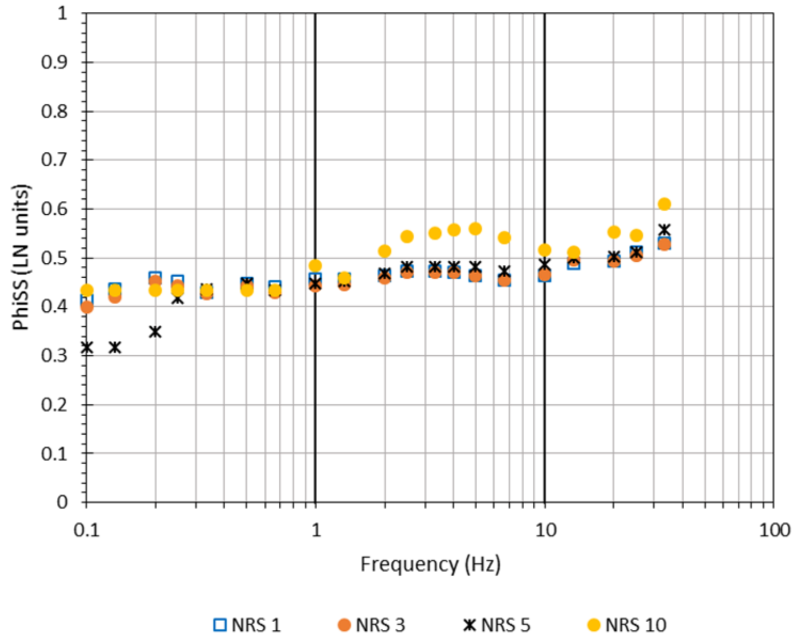

Figure 4.23 **ϕ_{SS} versus frequency for different minimum number of recordings per station (NRS) used in the regression.**

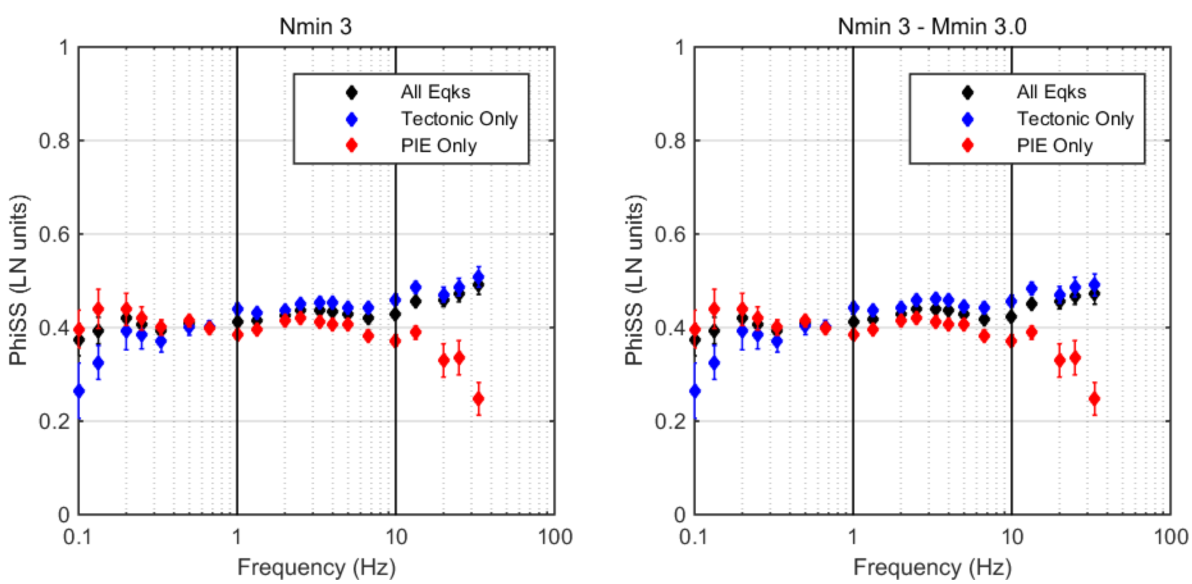

Figure 4.24 **ϕ_{SS} versus frequency for PIE, tectonic, and all earthquakes for minimum number (Nmin) of three recordings per station and all magnitudes (left) and for earthquakes with a minimum M of 3.0 (right).**

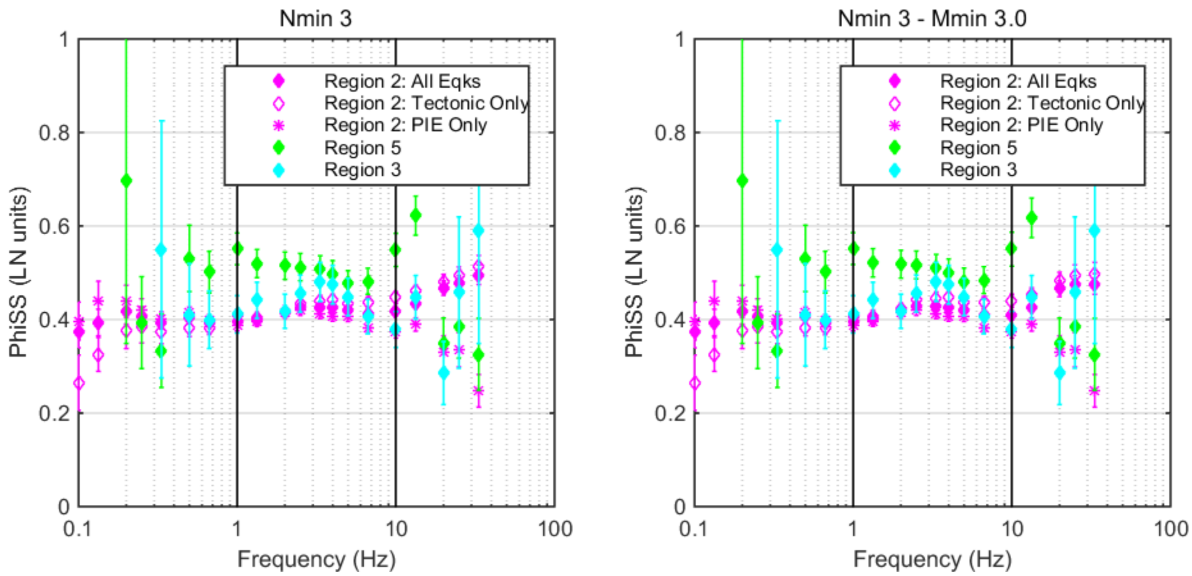

Figure 4.25 **CENA ϕ_{SS} by region using all recordings (left) and recordings with a minimum M of 3.0 (right).**

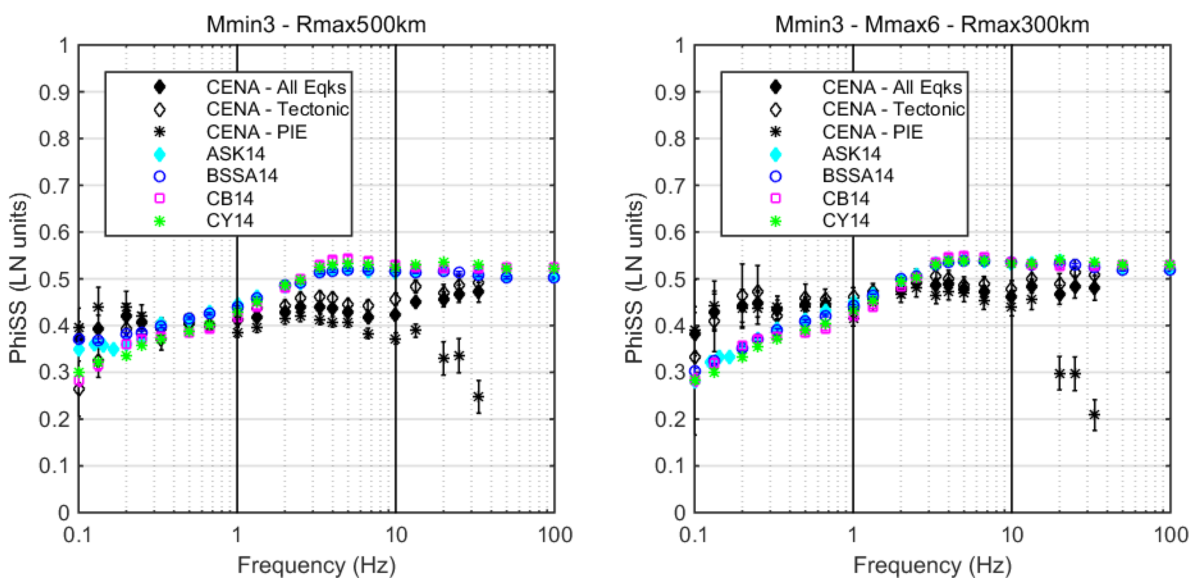

Figure 4.26 **Comparison of CENA and NGA-West2 ϕ_{SS} versus frequency for the datasets with M ≥ 3.0 and all distances (left) and M between 3.0 and 6.0 and R_{RUP} distance up to 300 km (right).**

The CENA single-station within-event residuals were binned by magnitude in bins of 0.5 magnitude unit width, and ϕ_{SS} was calculated in each bin. Figure 4.27 shows the resulting ϕ_{SS} versus magnitude for CENA for PIE, tectonic, and all events in the dataset for spectral periods of 0.1, 0.25, 0.5, 0.75, 1, and 2 sec. Figure 4.27 shows that ϕ_{SS} is relatively constant for magnitude less than 5.0, and that CENA data cannot reliably inform the extrapolation of ϕ_{SS} for **M** < 5.0. Similarly, single-station within-event residuals for the four NGA-West2 GMPEs (ASK14, BSSA14, CB14, and CY14) were binned by magnitude, and the resulting ϕ_{SS} was calculated in each magnitude bin. Figures 4.28 and 4.29 compare CENA and WUS ϕ_{SS} versus magnitude, whereby ϕ_{SS} was calculated using the entire CENA and WUS datasets as well as a subset of data with distance up to 300 km (common distance range in CENA and WUS datasets). Figures 4.28 and 4.29 indicate that WUS ϕ_{SS} shows a trend with magnitude whereby ϕ_{SS} is relatively constant for **M** less than about 5.5 and then decreases as magnitude increases to become constant for **M** greater than about 6.5 or 7.0. For longer periods (*T* greater than 0.75 sec), the magnitude-dependence of WUS ϕ_{SS} becomes less significant. Figures 4.28 and 4.29 also show that CENA ϕ_{SS} is generally comparable to WUS ϕ_{SS} for similar magnitude and distance ranges (R_{RUP} less than 300 km and **M** < 5.5).

The CENA single-station within-event residuals were binned by R_{RUP} distance in bins of 50 km width, and ϕ_{SS} was calculated in each bin. Figure 4.30 shows the resulting ϕ_{SS} versus R_{RUP} distance for CENA for PIE, tectonic, and all events in the dataset for spectral periods of 0.1, 0.25, 0.5, 0.75, 1, and 2 sec. Figure 4.30 shows a trend of CENA ϕ_{SS} with distance whereby ϕ_{SS} decreases as R_{RUP} increases, becoming relatively constant for R_{RUP} larger than about 250 to 300 km; this trend becomes weak at periods greater than 0.75 sec. Similarly, single-station within-event residuals for the four NGA-West2 GMPEs (ASK14, BSSA14, CB14, and CY14) were binned by R_{RUP} distance, and the resulting ϕ_{SS} was calculated in each distance bin. Figures 4.31 and 4.32 compare CENA and WUS ϕ_{SS} as a function of R_{RUP} distance, whereby ϕ_{SS} was calculated using the CENA and WUS datasets with **M** > 3.0 as well as a subset of data with **M** between 3.0 and 6.0 (similar magnitude range in CENA and WUS datasets). Figures 4.31 and 4.32 indicate that WUS ϕ_{SS} appears to be distance-independent for data with **M**3.0 to about 7.9 as well as for **M**3.0 to 6.0.

Figures 4.33 to 4.35 compare CENA and WUS ϕ_{SS} as a function of magnitude and distance for spectral periods of 0.1, 0.25, 0.5, 0.75, 1, and 2 sec. These figures indicate that WUS ϕ_{SS} appears to be generally distance-independent for distance up to 200 to 250 km in the three magnitude bins (**M**3.0 to 4.0, **M**4.0 to 5.0, and **M**5.0 to 6.0). At short periods, CENA ϕ_{SS} generally decreases as R_{RUP} increases for **M** 3.0 to 4.0 and **M** 4.0 to 5.0. Not enough CENA data is available in the **M**5.0 to 6.0 bin. For periods greater than 0.75 sec, the distance-dependence of CENA ϕ_{SS} becomes weak.

The CENA single-station within-event residuals were binned by V_{S30} in bins of 250 m/sec width, and ϕ_{SS} was calculated in each bin. Figure 4.36 shows the resulting ϕ_{SS} as a function of V_{S30} for CENA for PIE, tectonic, and all events in the dataset for spectral periods of 0.1, 0.25, 0.5, 0.75, 1, and 2 sec. Figure 4.36 indicates no clear trend in ϕ_{SS} with V_{S30}, which is expected since site effects have been removed from the calculation of single-station within-event residuals. Figure 4.37 compares ϕ_{SS} as a function of V_{S30} for CENA and WUS. Similarly, WUS ϕ_{SS} shows no clear trend with V_{S30}.

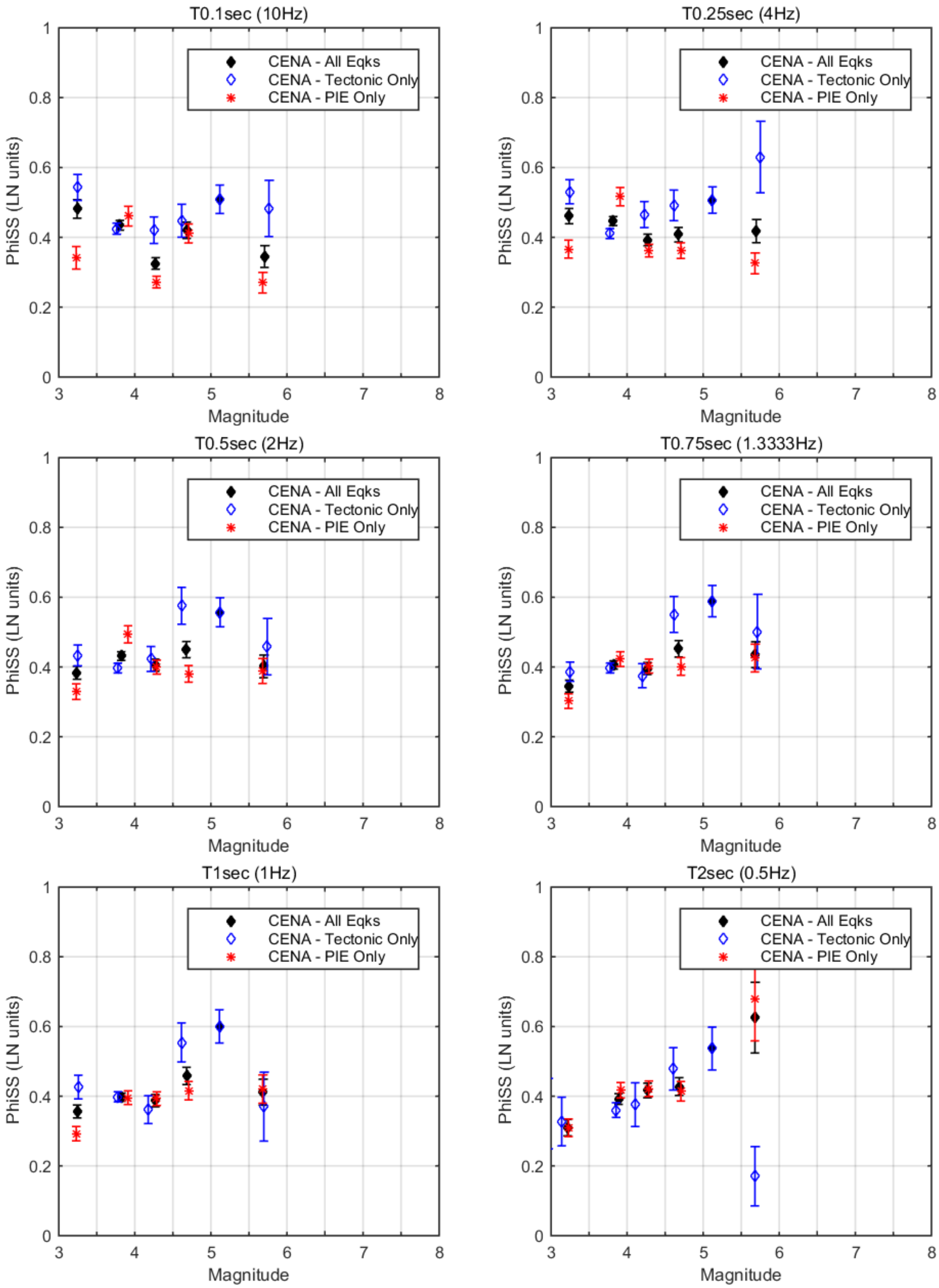

Figure 4.27 ϕ_{SS} **versus magnitude for CENA at** F **= 10, 4, 2, 1.33, 1, and 0.5 Hz.**

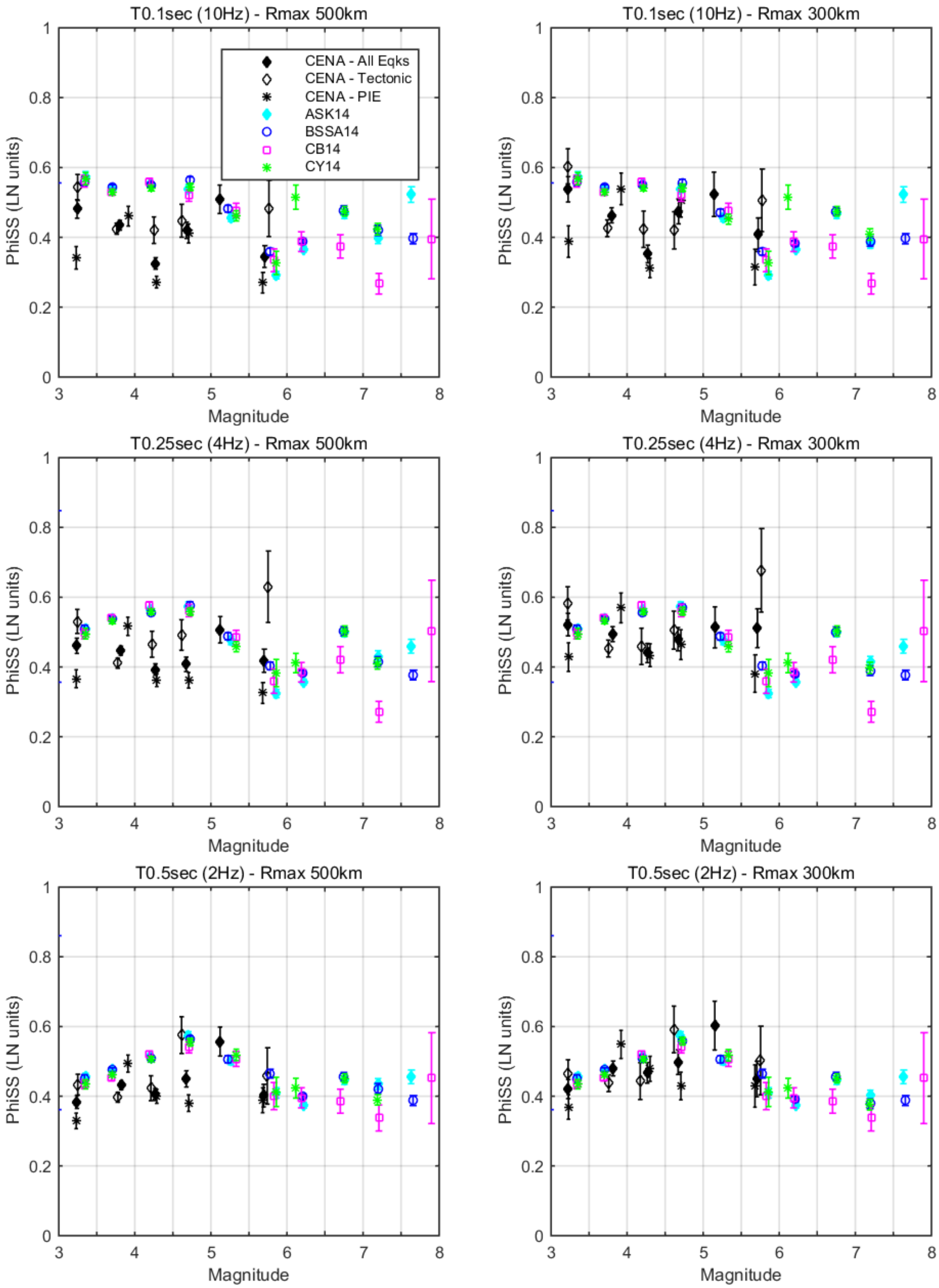

Figure 4.28 Comparison of CENA and WUS ϕ_{SS} versus magnitude for R_{RUP} distance up to 500 km (left) and 300 km (right) at F = 10, 4, and 2 Hz.

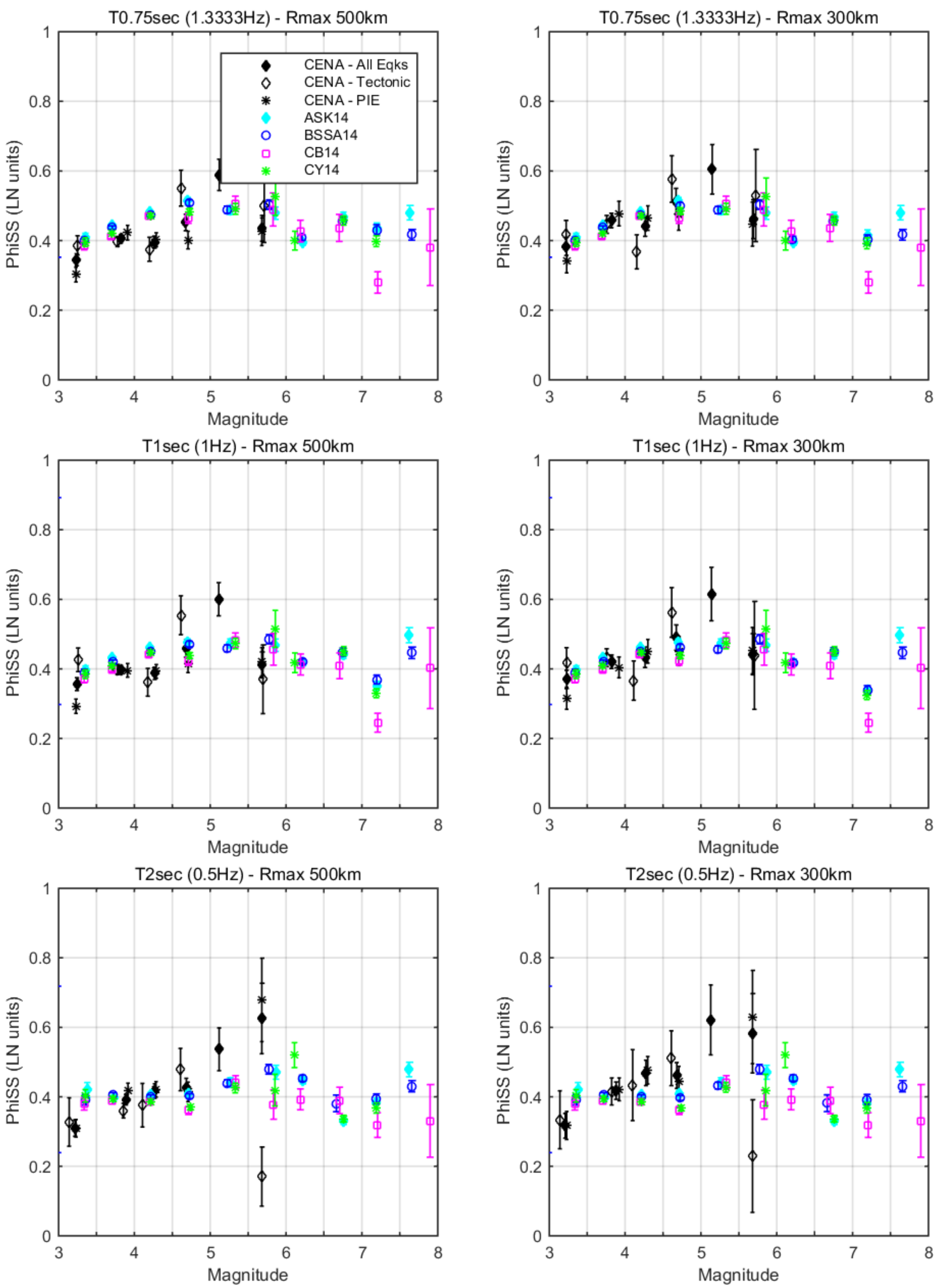

Figure 4.29 Comparison of CENA and WUS ϕ_{SS} versus magnitude for R_{RUP} distance up to 500 km (left) and 300 km (right) at F = 1.33, 1, and 0.5 Hz.

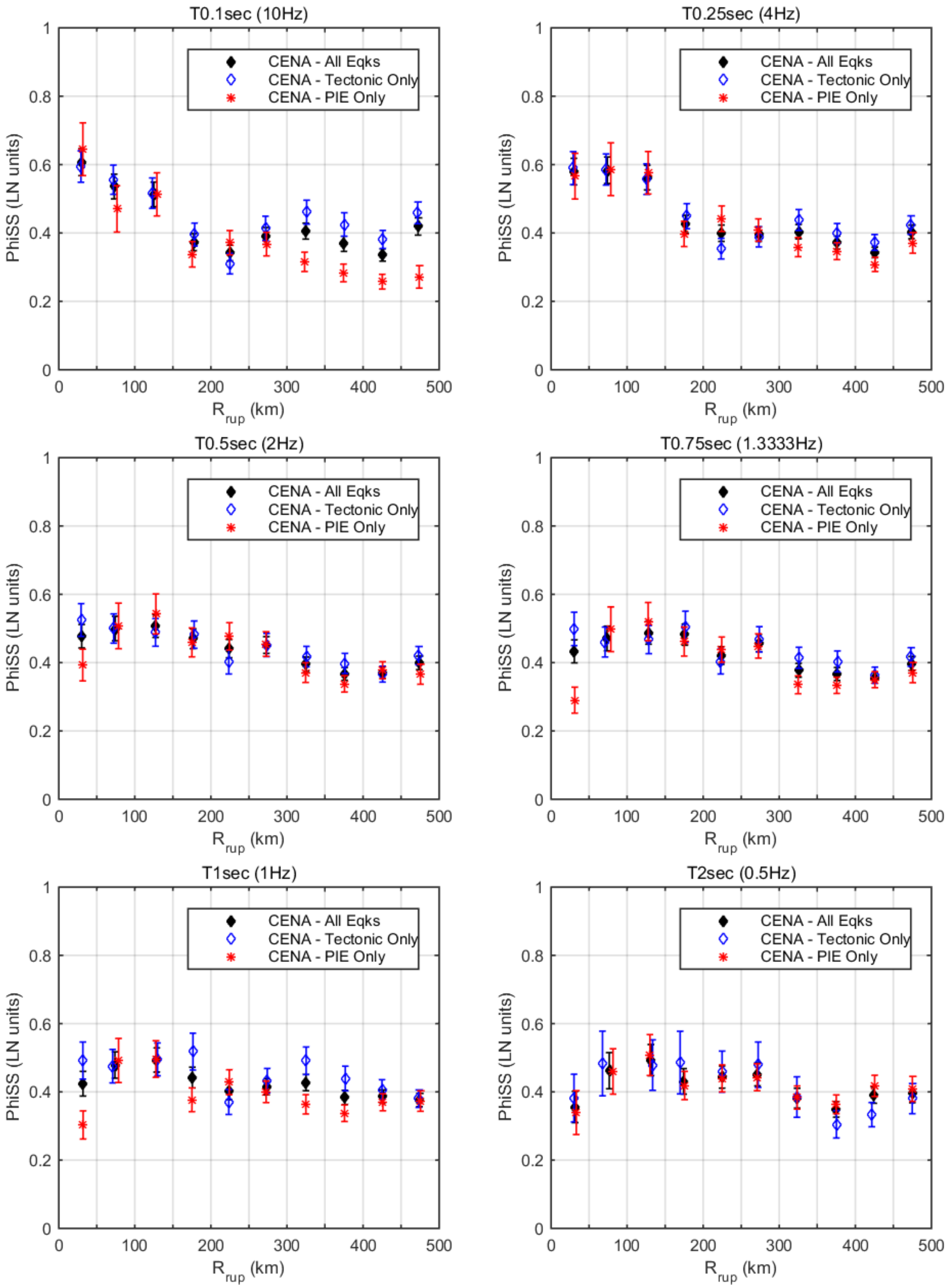

Figure 4.30 ϕ_{SS} versus R_{RUP} distance for CENA at F = 10, 4, 2, 1.33, 1, and 0.5 Hz.

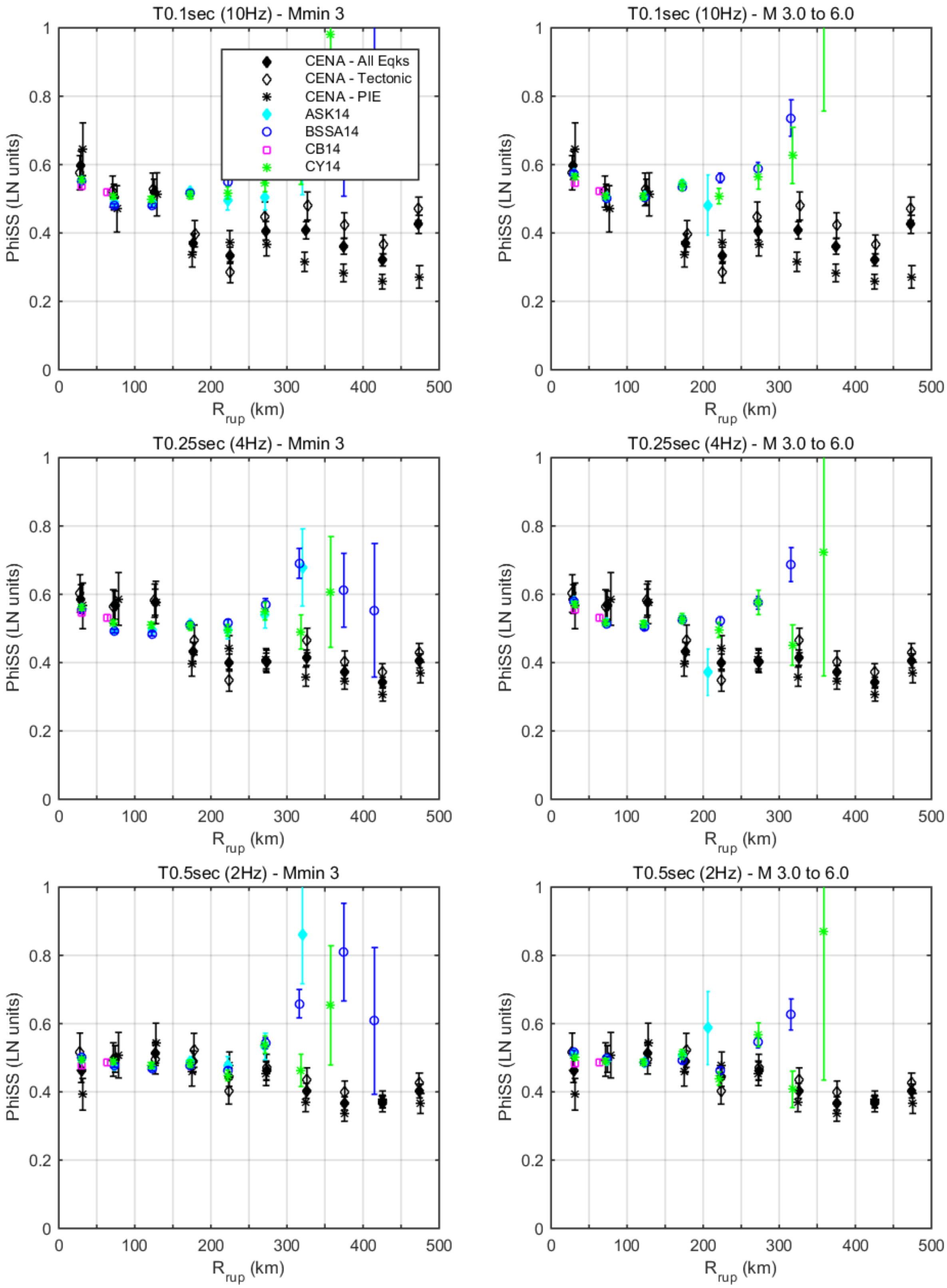

Figure 4.31 **Comparison of CENA and WUS ϕ_{SS} versus R_{rup} for M greater than 3.0 (left) and M between 3.0 and 6.0 (right) at F = 10, 4, and 2 Hz.**

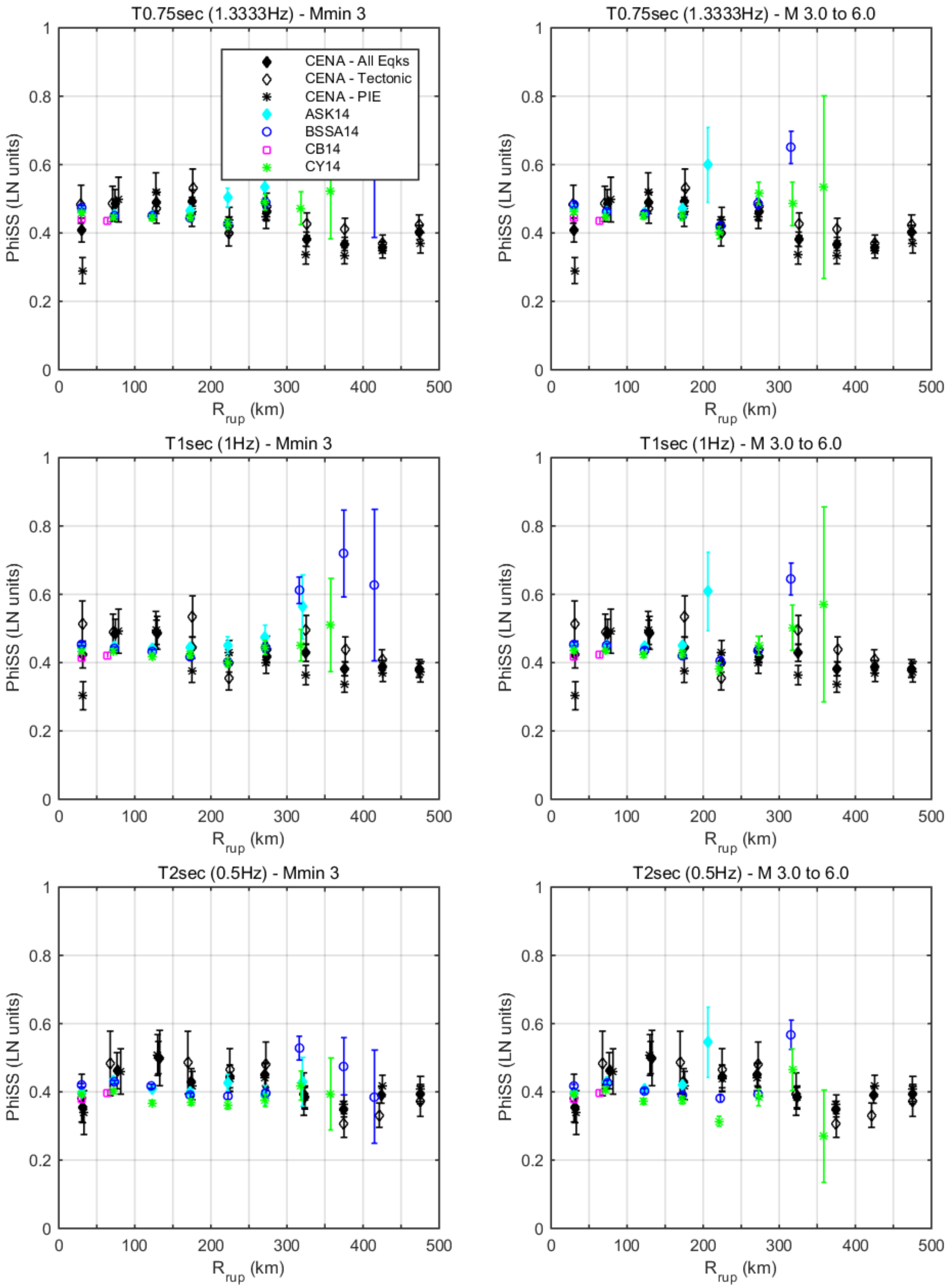

Figure 4.32 Comparison of CENA and WUS ϕ_{SS} versus R_{RUP} for M greater than 3.0 (left) and M between 3.0 and 6.0 (right) at F = 1.33, 1, and 0.5 Hz.

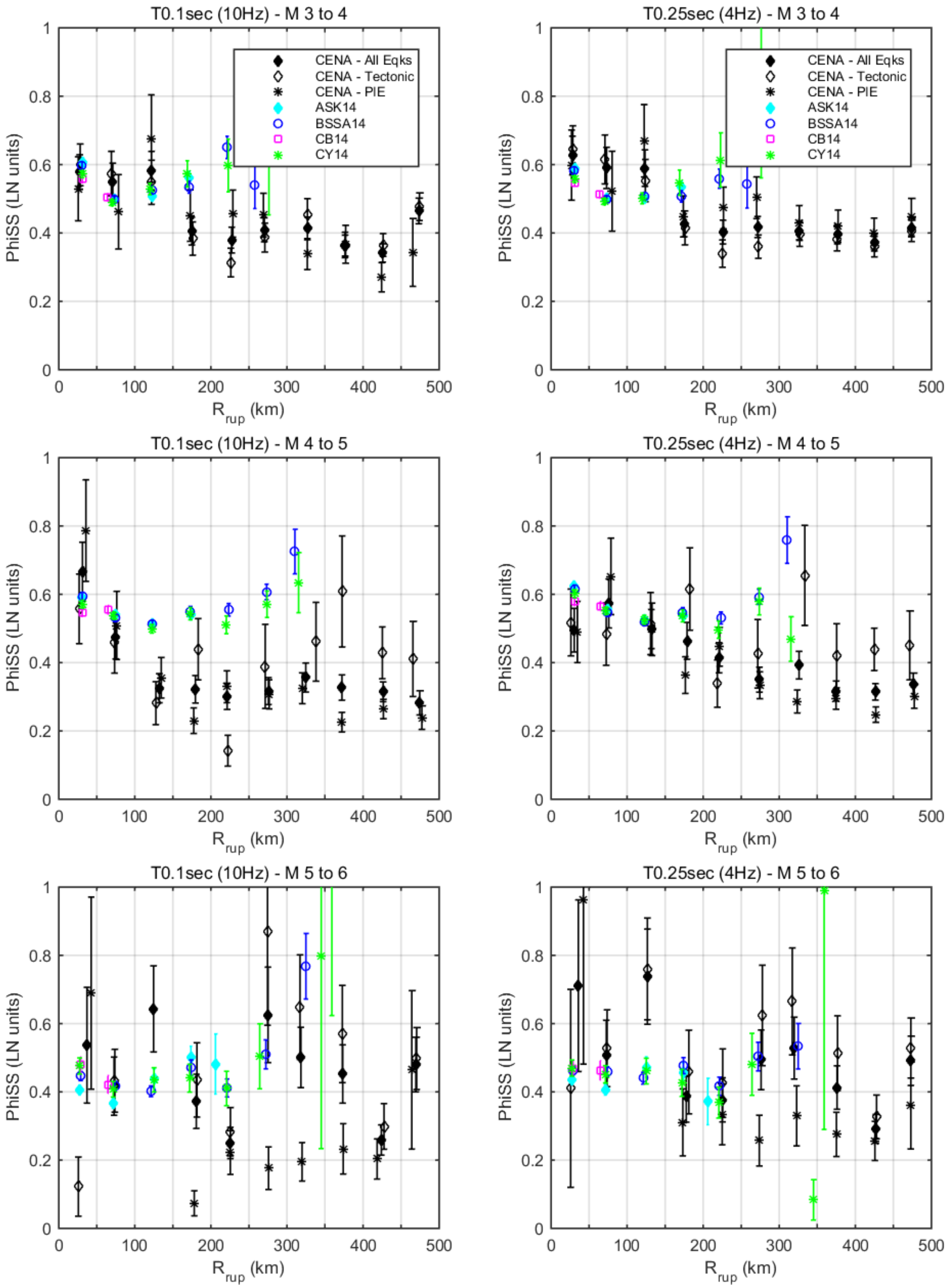

Figure 4.33 Comparison of CENA and WUS ϕ_{SS} versus distance in three magnitude bins at F = 10 and 4 Hz.

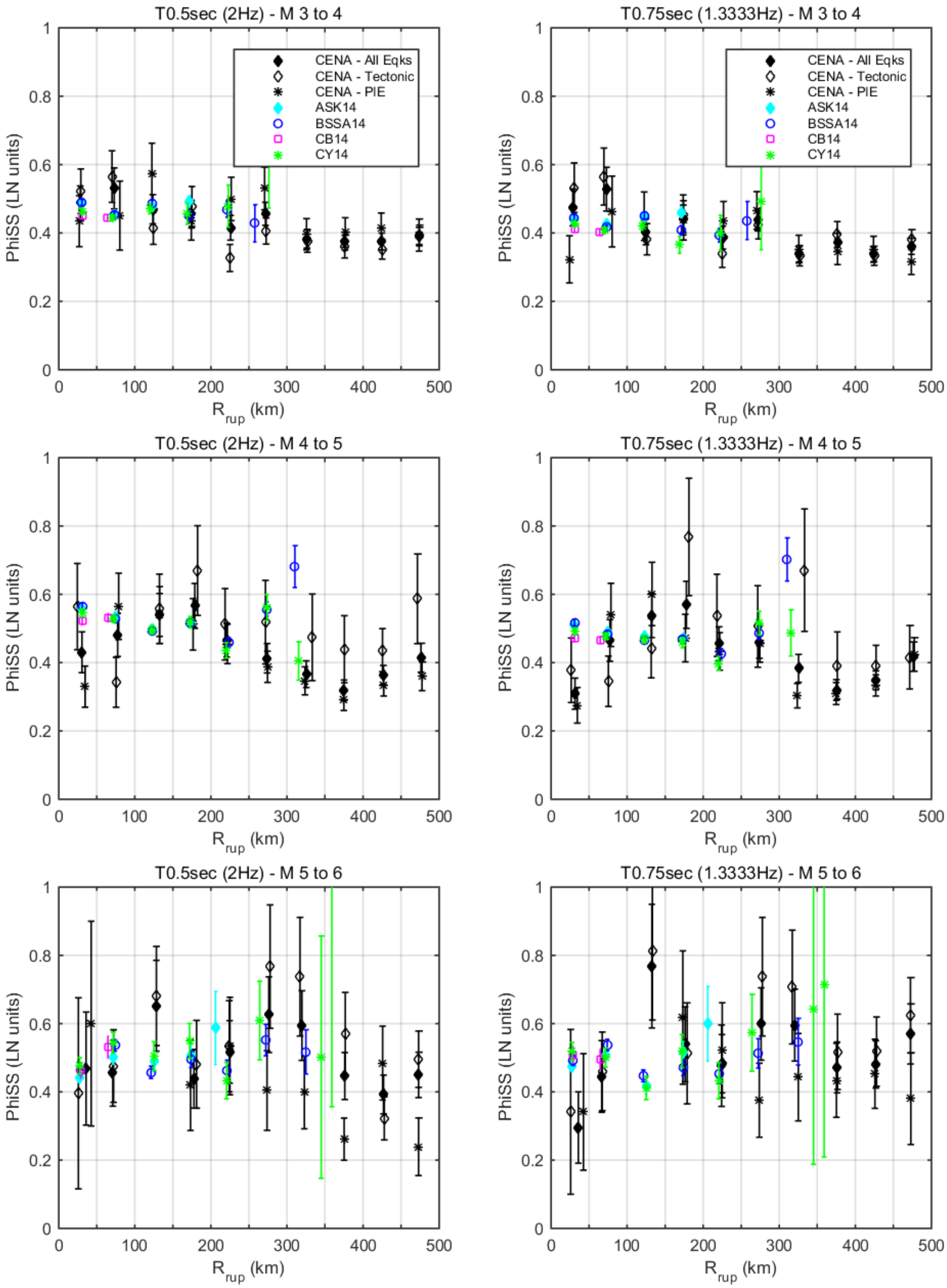

Figure 4.34 Comparison of CENA and WUS ϕ_{SS} versus distance in three magnitude bins at F = 2 and 1.33 Hz.

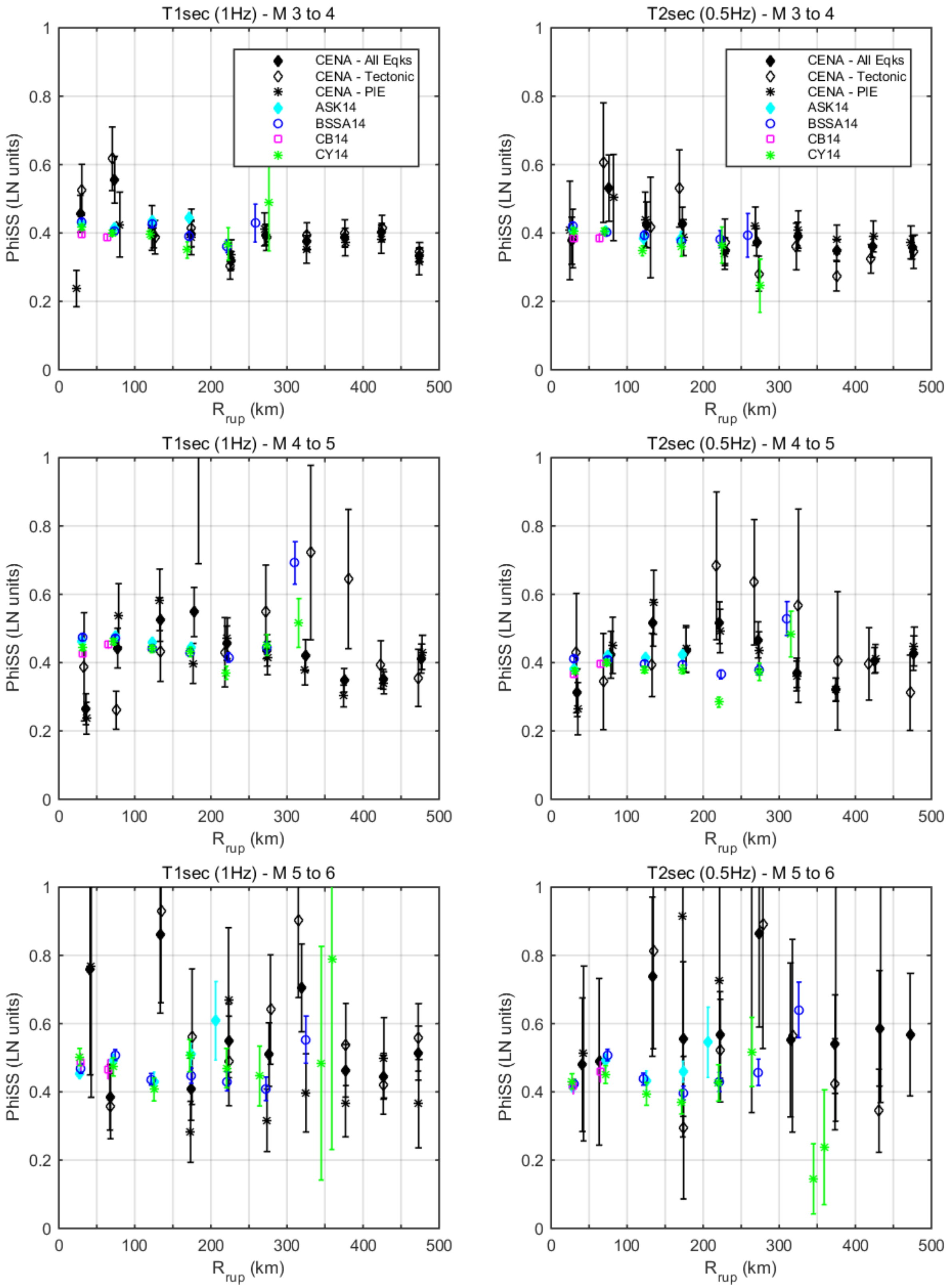

Figure 4.35 **Comparison of CENA and WUS ϕ_{SS} versus distance in three magnitude bins at F = 1 and 0.5 Hz.**

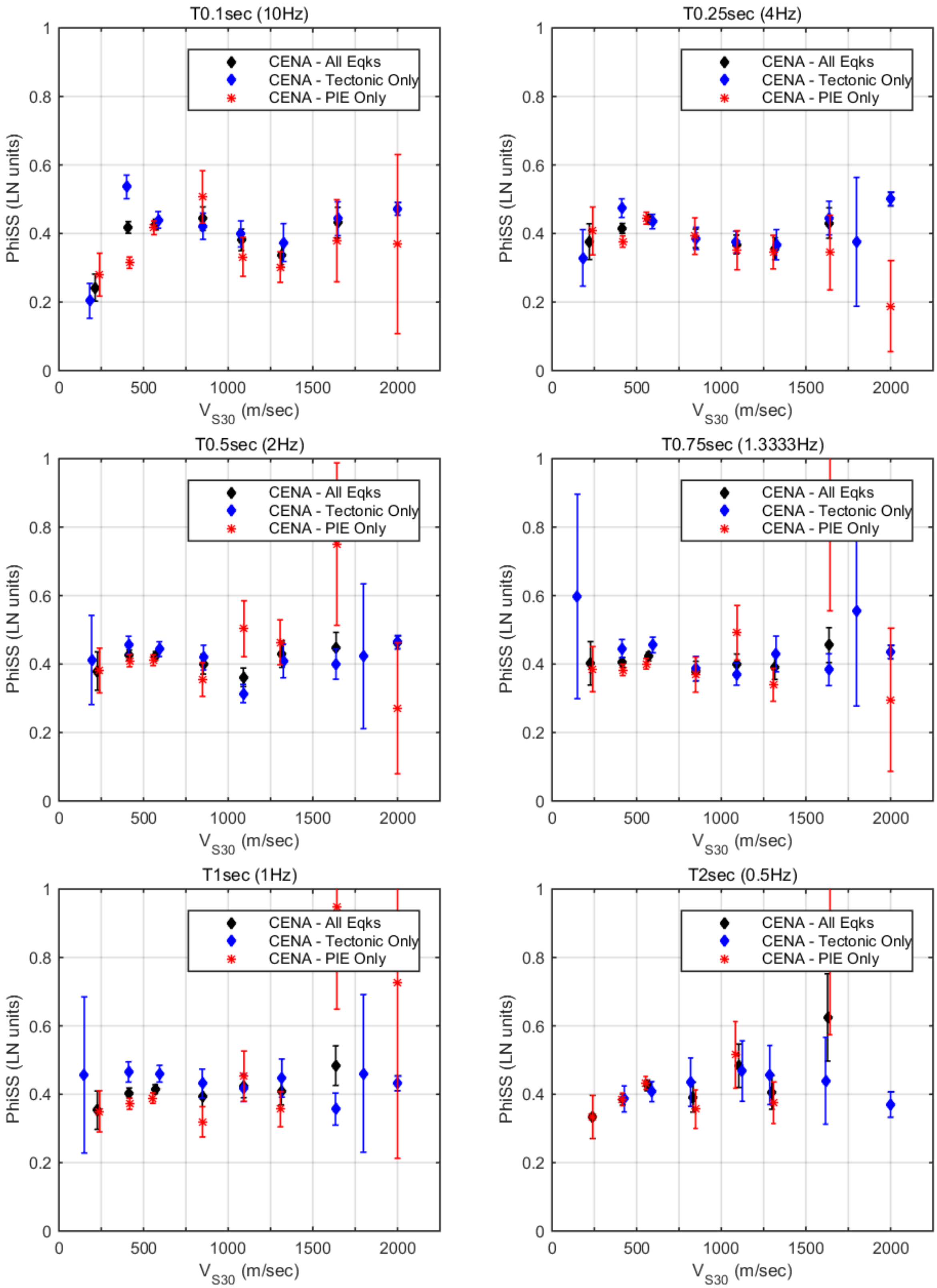

Figure 4.36 ϕ_{SS} **versus** V_{S30} **for CENA at** F **= 10, 4, 2, 1.33, 1, and 0.5 Hz.**

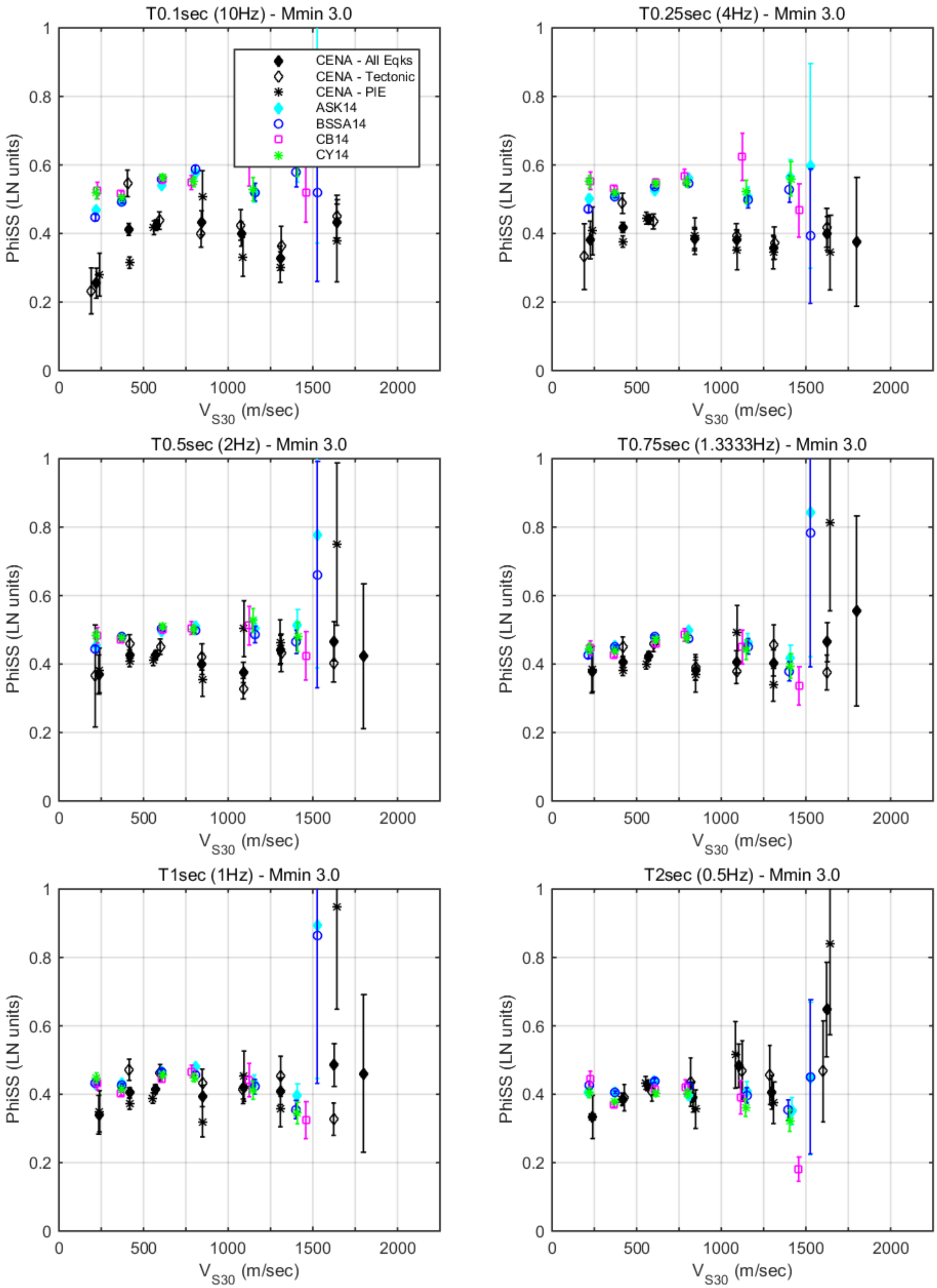

Figure 4.37 **Comparison of CENA and WUS ϕ_{SS} versus V_{S30} at F = 10, 4, 2, 1.33, 1, and 0.5 Hz.**

4.5 Φ_{S2S}

Figure 4.38 shows ϕ_{S2S} as a function of frequency for different minimum number of recordings per station (1, 3, 5, and 10) used in the mixed effects regression. The total number of stations used in the regression at F = 4 Hz is 447, 275, 167, and 22 for a minimum of 1, 3, 5, and 10 recordings per station, respectively. Figure 4.38 shows that ϕ_{S2S} values are comparable in the frequency range of 1 to 10 Hz when using a minimum of 1, 3, and 5 recordings per station in the regression. For a minimum of ten recordings per station, the number of stations used in the regression is small, and ϕ_{S2S} values are larger. For the rest of the analysis, site-to-site residuals obtained from the regression with a minimum of three recordings per station are used.

Figures 4.39 and 4.40 show the site-to-site residuals as a function of V_{S30}. The average of the site-to-site residuals in V_{S30} bins of 250 m/sec width are shown on the plots. Figures 4.39 and 4.40 generally show no trend of the site terms with V_{S30}. Next, site terms were binned by the V_{S30} code assigned to each stations, and ϕ_{S2S} was calculated in each bin to assess the impact of the errors in the V_{S30} estimates on the resulting ϕ_{S2S} values. Figure 4.41 shows ϕ_{S2S} as a function of frequency for the different V_{S30} codes (0 to 5). Note that for F = 4 Hz, there are 39 stations with V_{S30} code 0 (measured V_{S30}), 46 stations with V_{S30} code 1, eight stations with V_{S30} code 2, 23 stations with V_{S30} code 3, 11 stations with V_{S30} code 4, and 148 stations with V_{S30} code 5. Figure 4.42 compares ϕ_{S2S} for stations with measured versus inferred V_{S30}. Figures 4.41 and 4.42 indicate that ϕ_{S2S} values are generally comparable for stations with measured and inferred V_{S30} values. Therefore, errors in inferred V_{S30} estimates cannot explain the relatively large ϕ_{S2S} values for CENA.

The impact of the type of events (PIE versus tectonic) on the resulting ϕ_{S2S} was explored by running the mixed effects regression with PIE events only, tectonic events only, and all events. A minimum of three recordings per event was used in all three regressions. Figure 4.43 compares the resulting ϕ_{S2S} for PIE, tectonic, and all events, and indicates that ϕ_{S2S} for PIE is significantly smaller than that for tectonic events. Note that at F = 4 Hz, there are 275, 144, and 141 stations for the regressions with all events, tectonic only, and PIEs only, respectively. Next, the site terms for the three cases (PIE only, tectonic only, and all events) were binned in V_{S30} bins of 250 m/sec unit width, and ϕ_{S2S} was calculated for each bin for the purpose of evaluating the V_{S30} ranges covered in each of the three cases and its potential impact on the resulting ϕ_{S2S} values. Figure 4.44 compares ϕ_{S2S} as a function of V_{S30} for PIE and tectonic events, indicating that both PIE and tectonic events generally cover a comparable V_{S30} range, and that the difference in ϕ_{S2S} cannot be attributed to sampling different V_{S30} ranges. Next, the stations locations for the PIE and tectonic events are plotted on a map for the regression at F = 4 Hz, as shown in Figure 4.45. Figure 4.45 indicates that the stations that recorded PIE are located in a much narrower region than the ones that recorded tectonic events. Based on Figure 4.45, the reduced ϕ_{S2S} values for PIE compared to tectonic events could be due to the clustering of the stations that recorded PIE and the presence of more similar geologic conditions than for the stations that recorded tectonic events spanning a much larger area.

Figure 4.46 compares ϕ_{S2S} for CENA, WUS, and Japan. All earthquakes in the CENA dataset were used to calculate ϕ_{S2S}. The values of ϕ_{S2S} for Japan are based on a single-station sigma study by Dawood and Rodriguez-Marek [2015] using active crustal earthquakes recorded on the KiK-net stations. Their dataset consisted of 13,735 six-component (three at the surface and three at the borehole) ground-motion recordings from 679 active crustal earthquakes recorded at 643 stations. The V_{S30} values calculated for the KiK-net stations are based on seismic velocity profiles from downhole PS logging. Dawood and Rodriguez-Marek [2015] used a GMPE functional form adopted from ASK14 for the regression. Figure 4.47 shows the metadata distribution for the Japanese ground motion. Figure 4.46 indicates that CENA ϕ_{S2S} has a similar shape and amplitude around the peak at 10 Hz compared to ϕ_{S2S} for Japan. On the other hand, NGA-West2 ϕ_{S2S} has a flatter shape with frequency and lower amplitude in the 1 to 10 Hz frequency range compared to CENA. This plot indicates that the relatively large ϕ_{S2S} values observed for CENA are comparable to the Japanese ϕ_{S2S} values, where site conditions are broadly similar to CENA consisting of shallow soil cover over rock.

Site terms for CENA and NGA-West2 were binned in V_{S30} bins of 250 m/sec width and ϕ_{S2S} values were calculated in each bin. Figure 4.48 compares ϕ_{S2S} as a function of V_{S30} for CENA and NGA-West2 for spectral periods of 0.1, 0.25, 0.5, 0.75, 1, and 2 sec. Figure 4.48 shows that ϕ_{S2S} appears to increase with V_{S30} up to around 1000 m/sec and decreases for V_{S30} larger than 1000 m/sec for both CENA and WUS. These plots also show that CENA ϕ_{S2S} values are larger than those for WUS at high frequencies (greater than 4 Hz). At low frequencies, WUS ϕ_{S2S} values are larger than those for CENA.

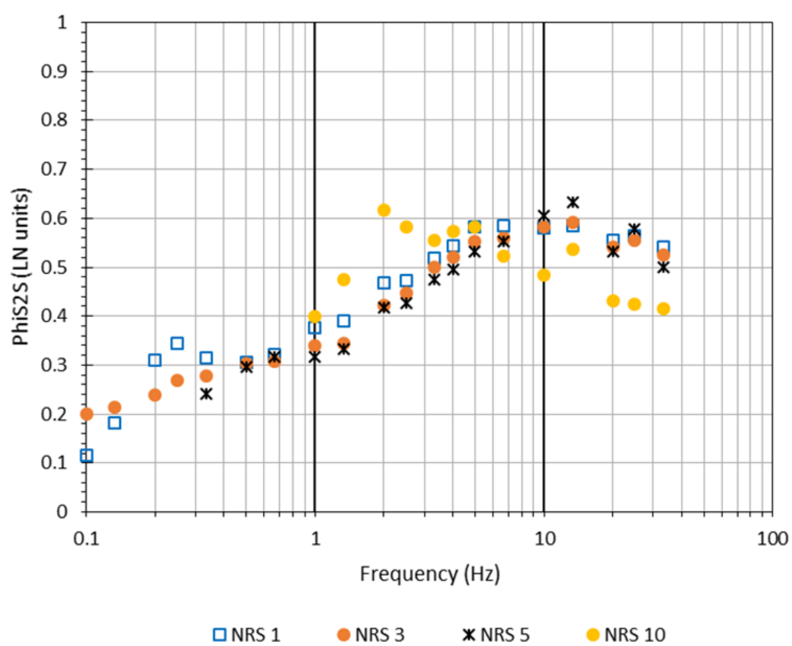

Figure 4.38 **CENA ϕ_{S2S} versus frequency for different minimum number of recordings per station (NRS) used in the regression.**

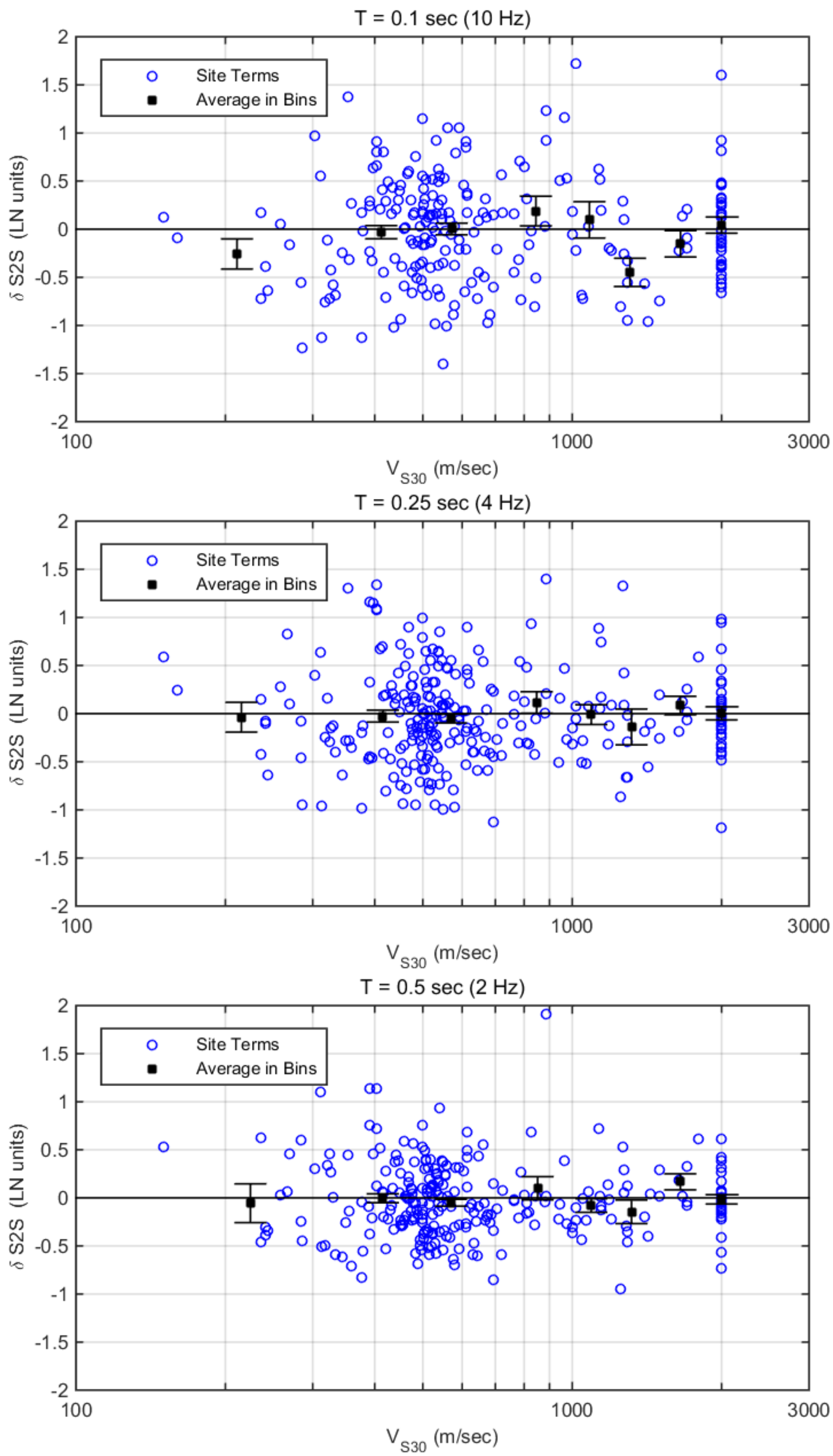

Figure 4.39 CENA site terms as a function of V_{S30} for F = 10, 4, and 2 Hz.

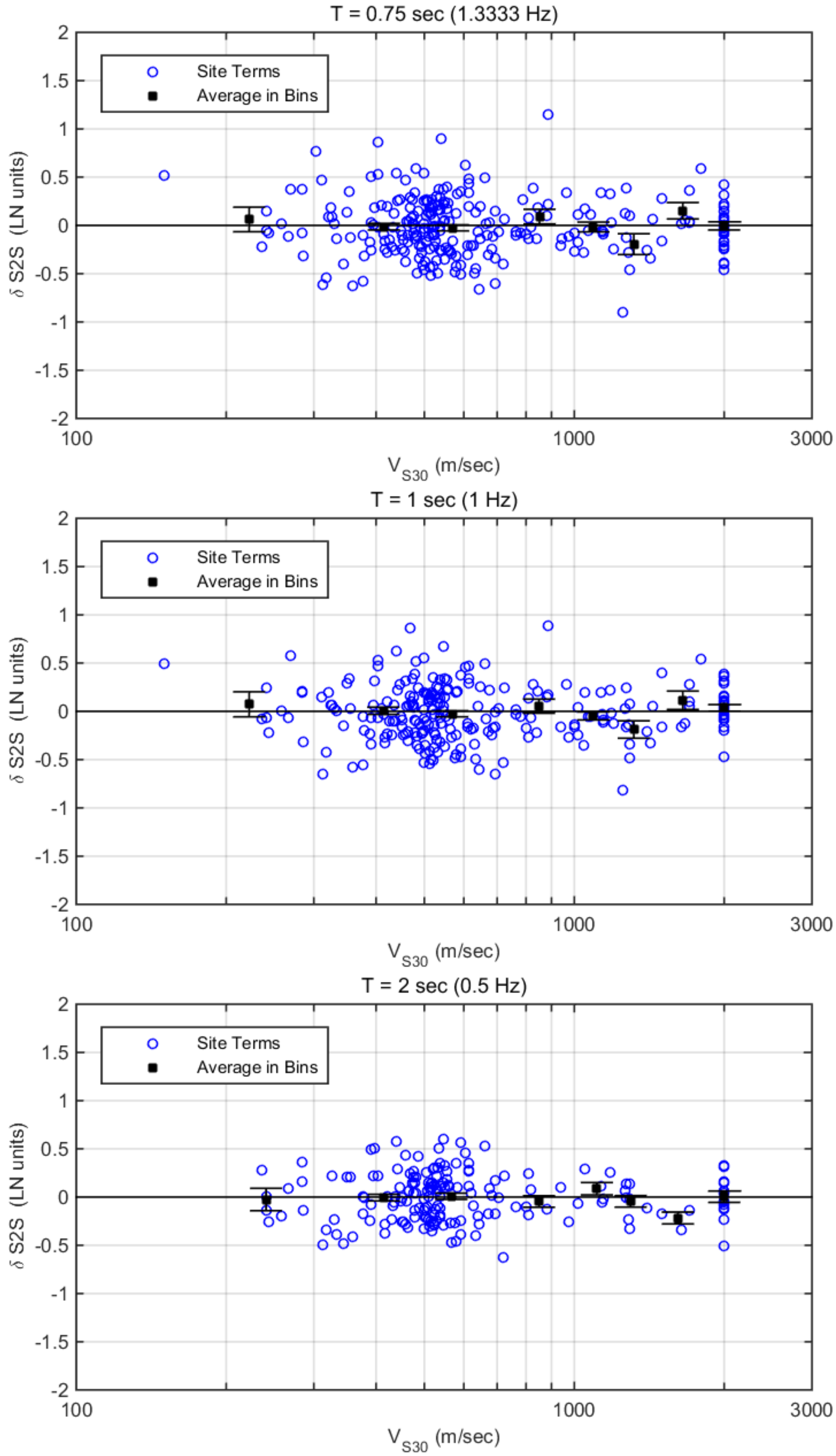

Figure 4.40 CENA site terms as a function of V_{S30} for F = 1.33, 1, and 0.5 Hz.

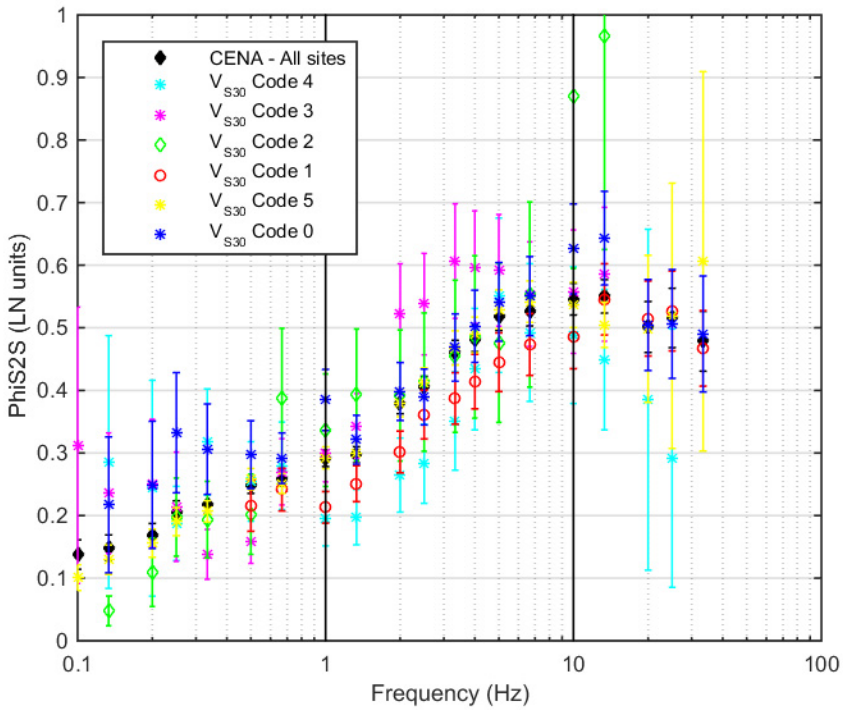

Figure 4.41 CENA ϕ_{S2S} versus frequency for the different V_{S30} codes.

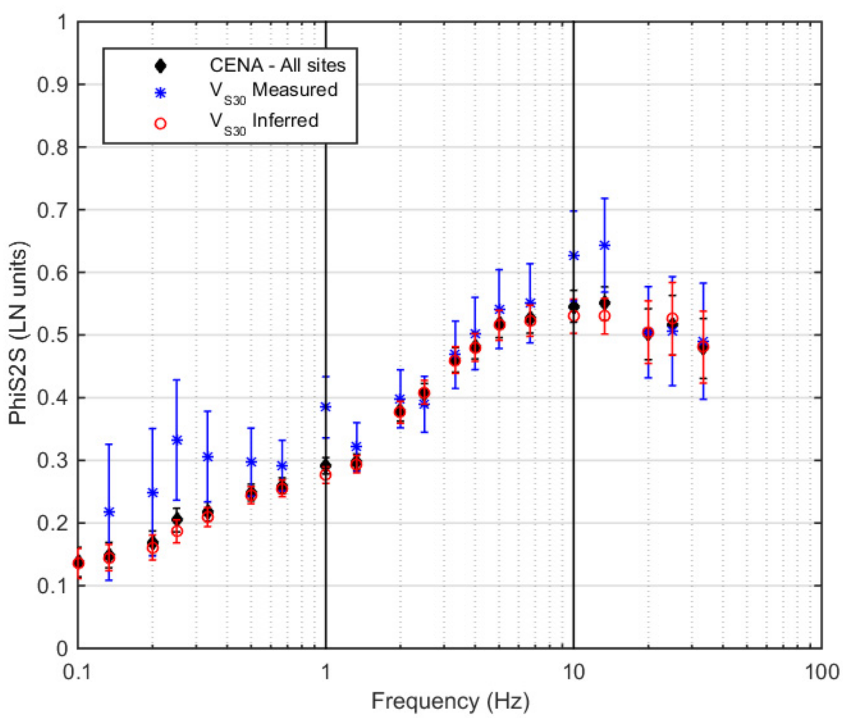

Figure 4.42 Comparison of ϕ_{S2S} for CENA stations with measured versus inferred V_{S30}.

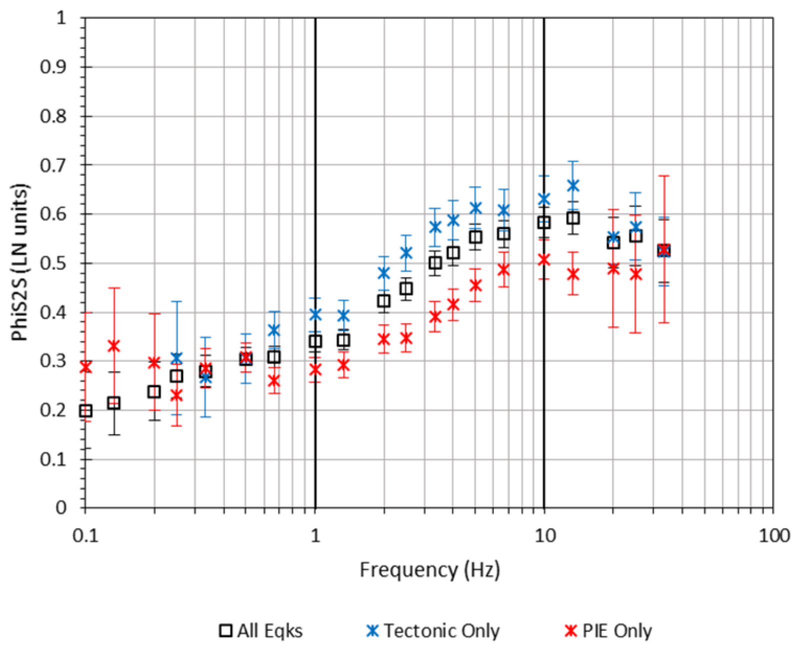

Figure 4.43 Comparison of CENA ϕ_{S2S} for PIE and tectonic events.

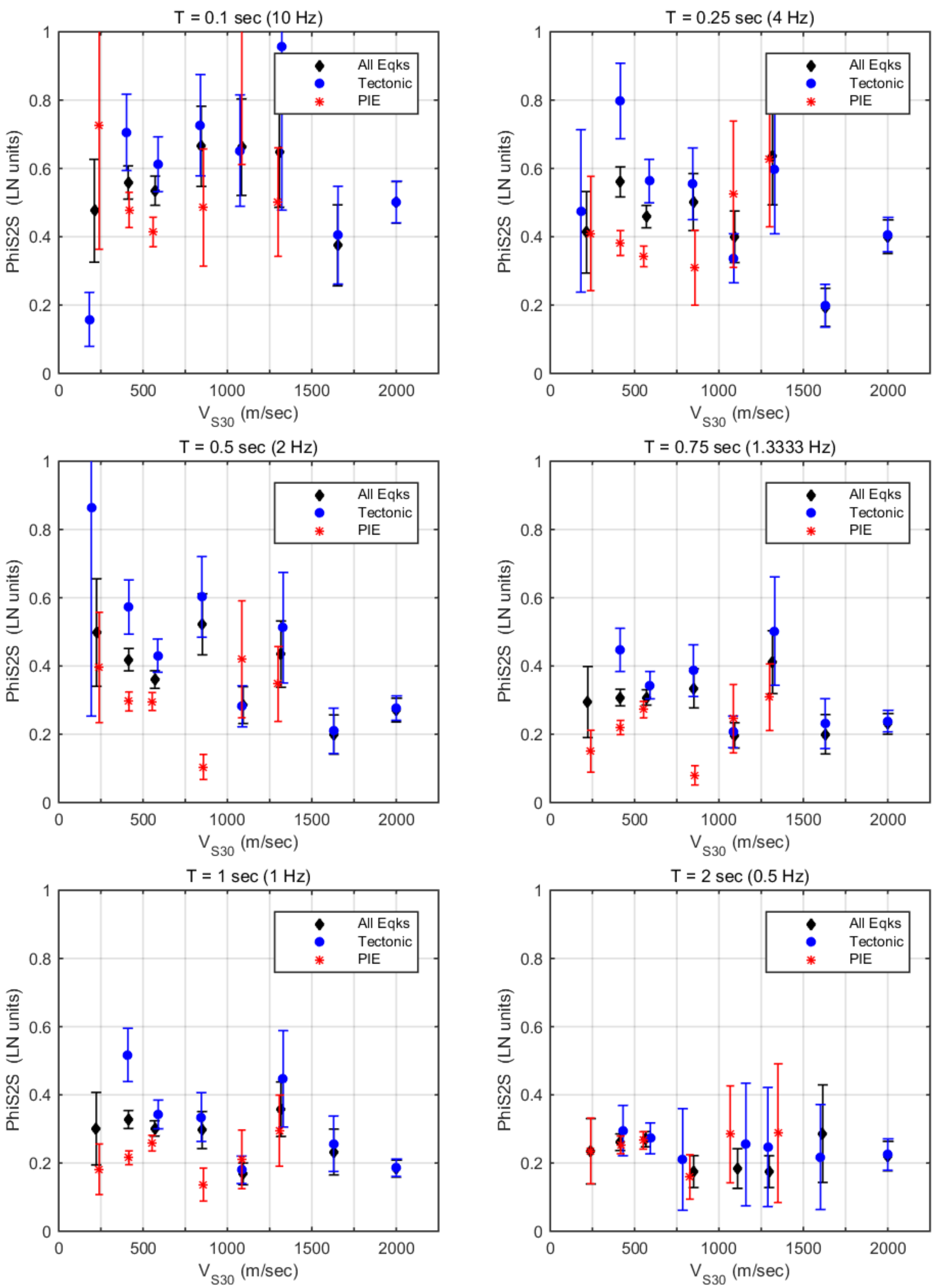

Figure 4.44 **Comparison of CENA ϕ_{S2S} versus V_{S30} for tectonic, PIE, and all earthquakes at F = 10, 4, 2, 1.33, 1, and 0.5 Hz.**

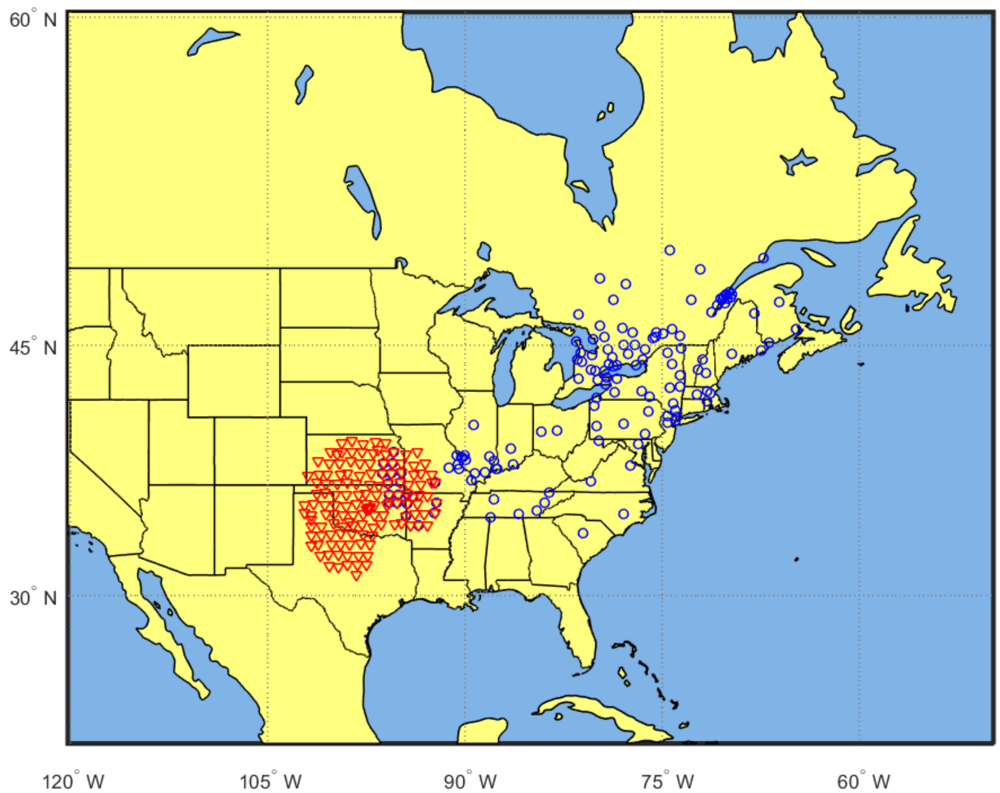

Figure 4.45 **Location of the stations that recorded PIEs (red) and tectonic events (blue) for *F* = 4 Hz.**

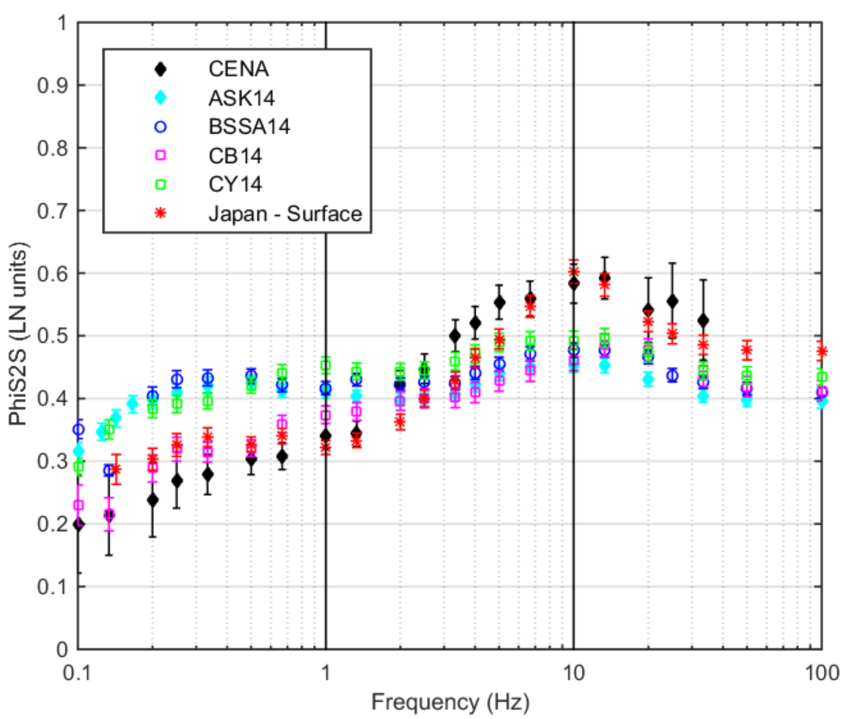

Figure 4.46 **Comparison of ϕ_{S2S} for CENA, NGA-West2, and Japan.**

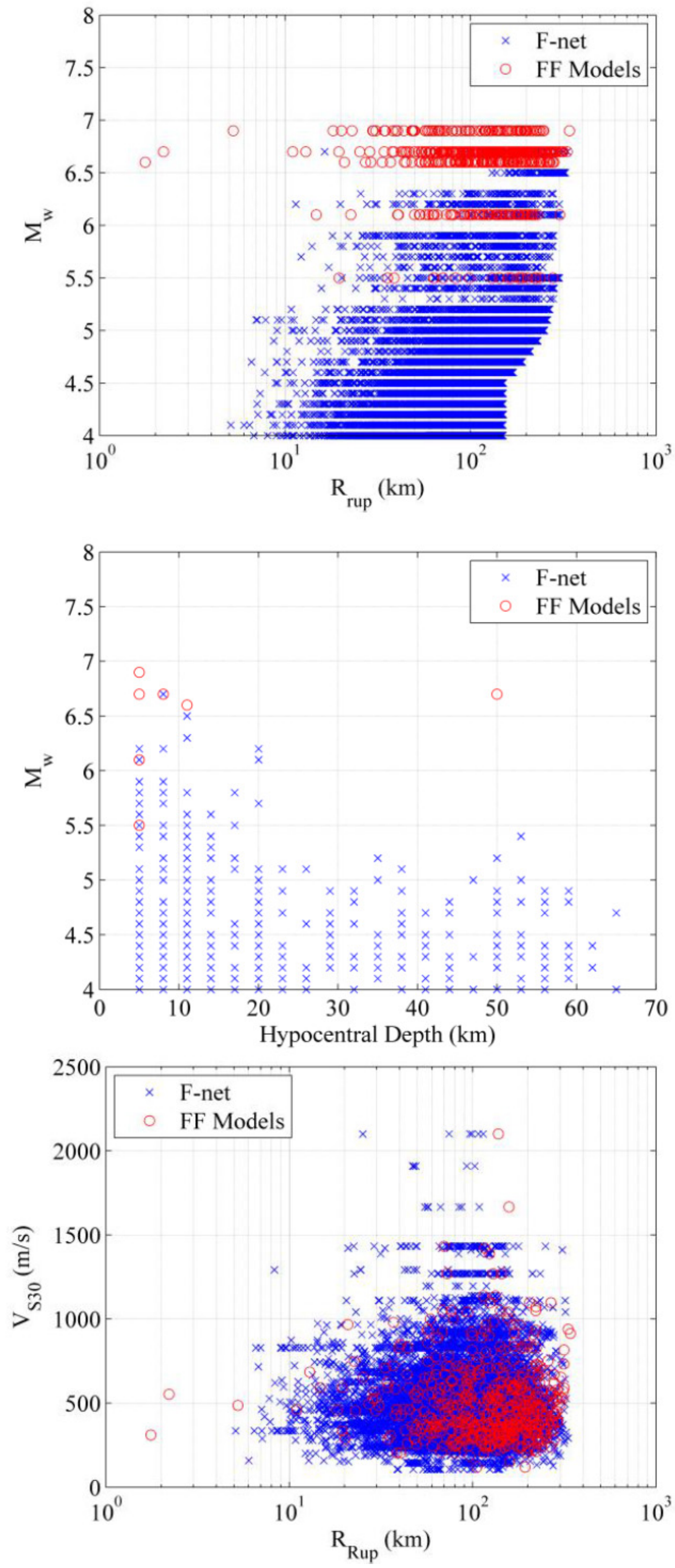

Figure 4.47 **Metadata for Japan single-station sigma study. M_w and R_{RUP} obtained from the *F*-net catalog (blue crosses) and previously published finite fault source models (red circles) (see Dawood and Rodriguez-Marek [2015]).**

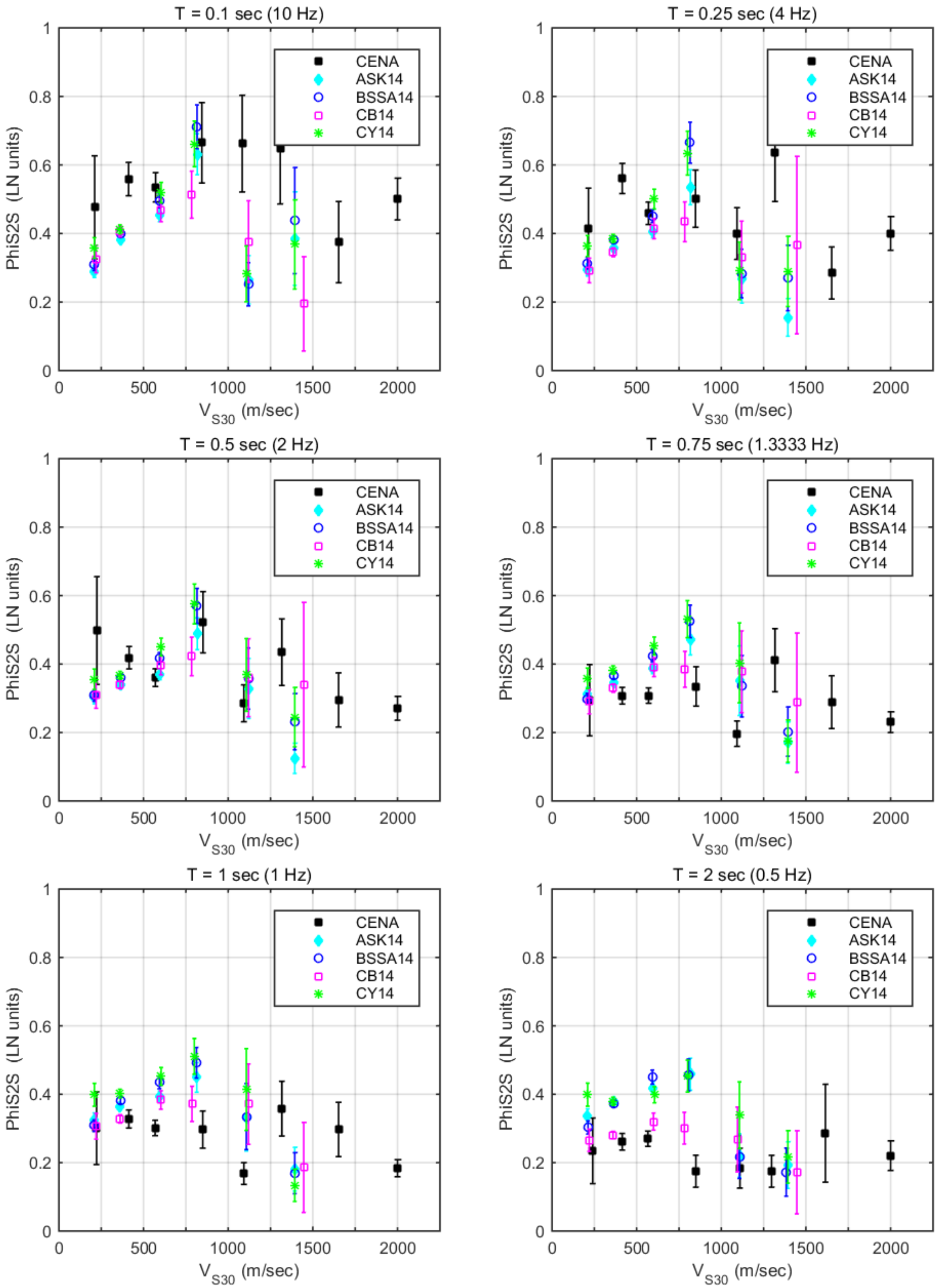

Figure 4.48 Comparison of CENA and WUS ϕ_{S2S} versus V_{S30} at F = 10, 4, 2, 1.33, 1, and 0.5 Hz.

4.6 OTHER EFFECTS

Figure 4.49 summarizes τ, ϕ, ϕ_{S2S}, and ϕ_{S2S} for CENA as obtained from the mixed effects regression with a minimum of three recordings per event for τ and ϕ and three recordings per station for ϕ_{SS} and ϕ_{S2S} using all available earthquakes in the CENA dataset. Figure 4.48 indicates that τ is relatively small compared to ϕ, and that ϕ_{S2S} is relatively large. Potential trade-offs between τ and ϕ were investigated, particularly the impact of the regression approach on the results as well as regional clustering and trade-offs between τ and ϕ_{S2S}.

4.6.1 Regression Approach

The results presented up to this point in this study are based on performing two mixed-effects regressions [Abrahamson and Youngs 1992] whereby the event terms, within-event residuals, ϕ, and τ are estimated in the first regression. The second regression uses the within-event residuals to estimate the site terms, single-station within-event residuals, ϕ_{SS}, and ϕ_{S2S}. Other regression approaches whereby site terms and event terms are estimated simultaneously were explored to evaluate potential trade-offs between ϕ and τ.

An iterative approach was used to estimate site terms and event terms and consists of the following steps:

1. Event terms and model coefficients are solved.
2. Site terms are computed from the within-event residuals.
3. Event terms and model coefficients are recomputed from ground-motion data after removing the site terms computed in the previous step.
4. Site terms are recomputed.
5. Steps 3 and 4 are repeated until the change in the likelihood of the fit falls below a set threshold.

To compare the ϕ and τ values estimated from the iterative approach to the two-regression approach, the model coefficients in the iterative approach were fixed to be equal to those derived in the two-regression approach. Figure 4.50 presents a comparison of the resulting ϕ and τ values.

A Bayesian mixed-effects regression was also used to simultaneously estimate site terms and event terms using the computer program "Stan" [PEER 2015b]. Due to computational demands, the full Bayesian regression was only run at $T = 0.2$ sec to estimate ϕ and τ; the results are shown in Figure 4.50, which indicates that the ϕ and τ values estimated using the Bayesian approach and the iterative approach are comparable. Moreover, while ϕ values estimated using a single-regression versus the iterative approach are comparable; τ values estimated using the iterative approach are slightly larger than those estimate using a single regression. The maximum difference in τ is on the order of 12%. Given the similarity in the ϕ and τ values estimated using the various approaches explored, we concluded that the regression approach does not have a significant impact on the obtained results, and that the two-regression approach can be used to estimate the components of the ground-motion variability.

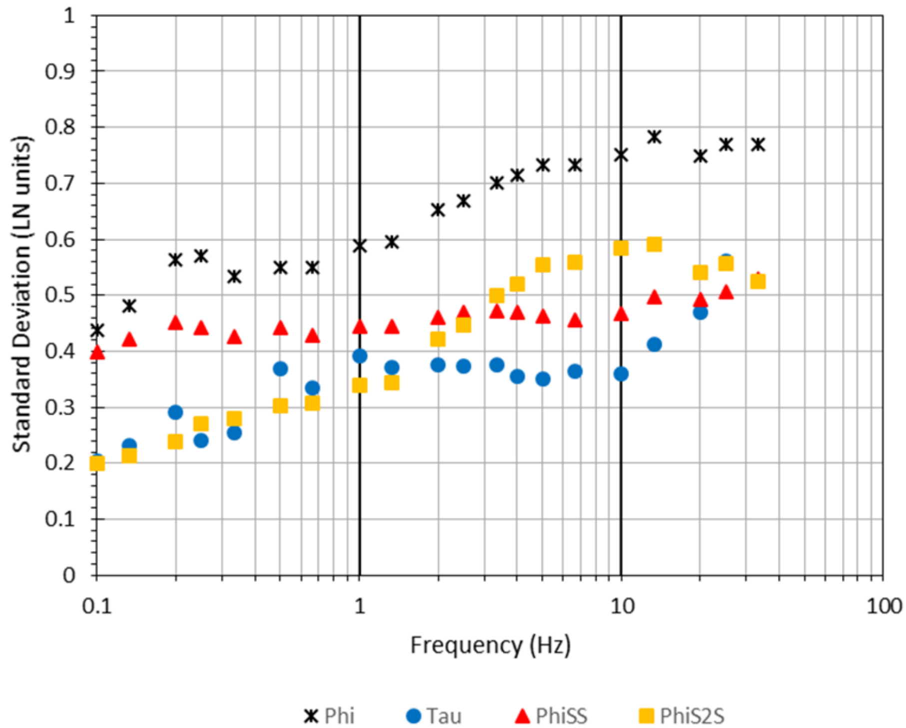

Figure 4.49 CENA τ, ϕ, ϕ_{SS}, and ϕ_{S2S} using three recordings per earthquake for τ and ϕ, and three recordings per station for ϕ_{SS} and ϕ_{S2S}.

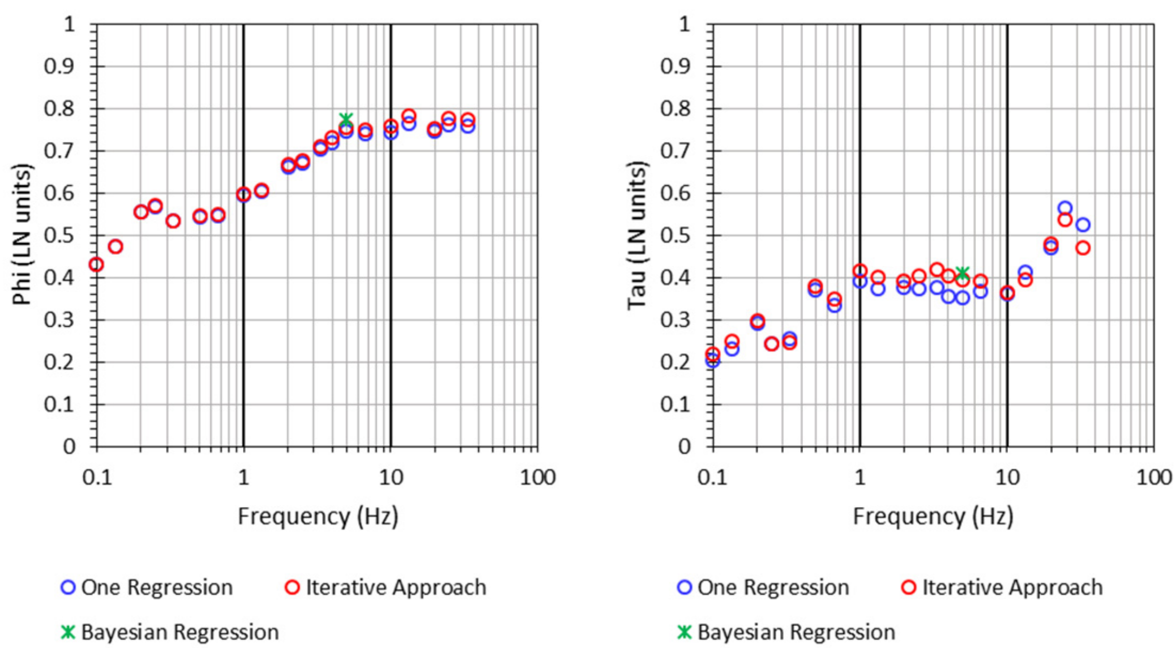

Figure 4.50 Comparison of CENA ϕ (left) and τ (right) using the two-regression, iterative, and Bayesian regression approaches.

4.6.2 Regional Effects

Figure 4.51 shows the geographical distribution of the event terms at F = 4 Hz, whereby event terms are binned based on their amplitudes in four groups and plotted at the earthquake locations on the map. Similarly, site terms at F = 4 Hz are binned in six groups based on their amplitudes and plotted at the stations locations on the map, as shown in Figure 4.52. Because Figures 4.51 and 4.52 show that both the event terms and the site terms are reasonably well distributed across the entire area covered by the earthquakes and the stations, there does not seem to be an obvious bias or trade-off in the event terms and the site terms.

Moreover, ϕ and τ were calculated for tectonic ground-motion data from two small geographical areas in CENA and compared to the values obtained from the entire CENA dataset (tectonic events only) to evaluate the impact of the distribution of the data over a large geographical area on the results. Figure 4.53 shows the distribution of the ground-motion data used in the analysis. A minimum of three recordings per event was used in the mixed effects regression, resulting in 692 recordings from 35 earthquakes recorded at 153 stations, and 246 recordings from 20 earthquakes recorded at 58 stations for areas 1 and 2, respectively. Figure 4.54 shows a comparison of ϕ and τ obtained for the small areas shown in Figure 4.53 to those obtained for the entire dataset. Figure 4.54 indicates that both ϕ and τ for area 1 are slightly larger than those for all tectonic data in the CENA dataset, with a maximum difference in τ on the order of 10%. For area 2, ϕ and τ are larger than those for area 1 and for all tectonic data, primarily due to the small subset of data used in the regression for area 2. Therefore, we concluded that the amplitudes of ϕ and τ for the CENA dataset are not primarily the result of trade-offs due to the CENA data covering a large geographical area.

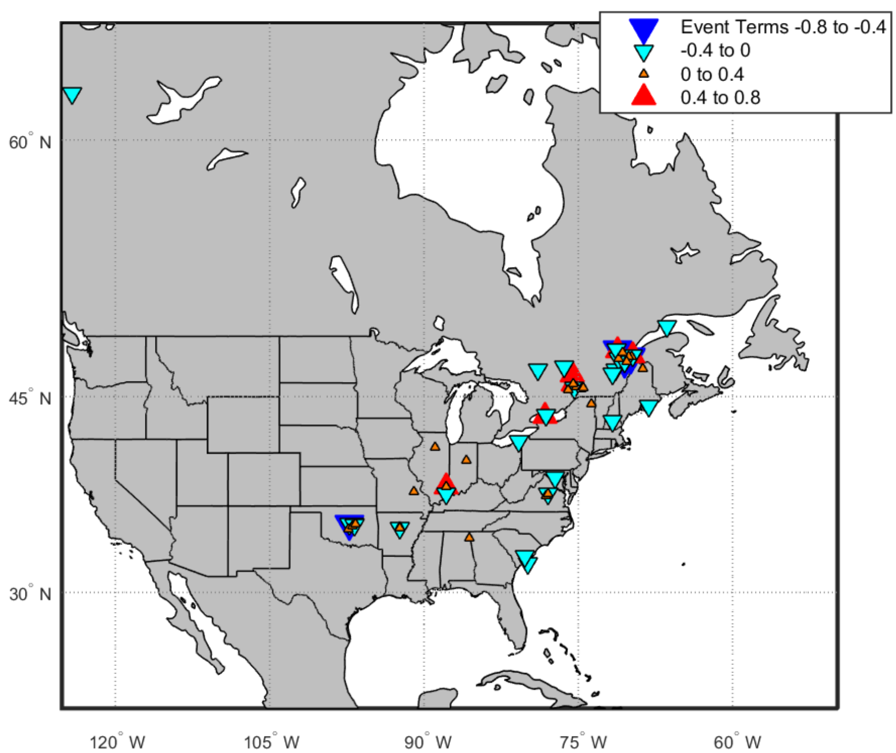

Figure 4.51 Geographical distribution of event terms at F = 4 Hz.

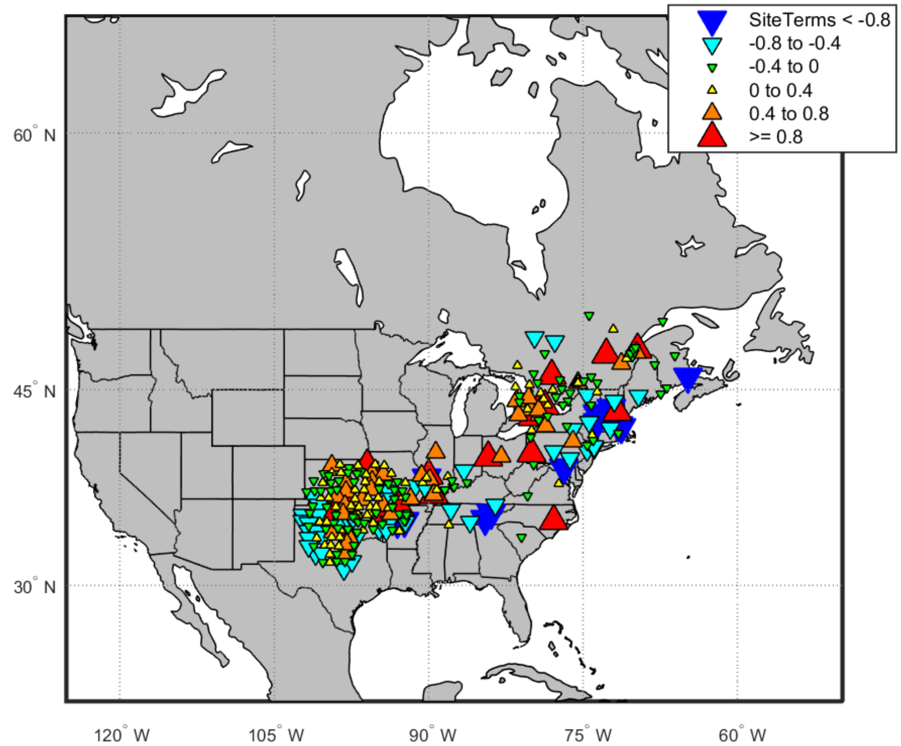

Figure 4.52 Geographical distribution of site terms at *F* = 4 Hz.

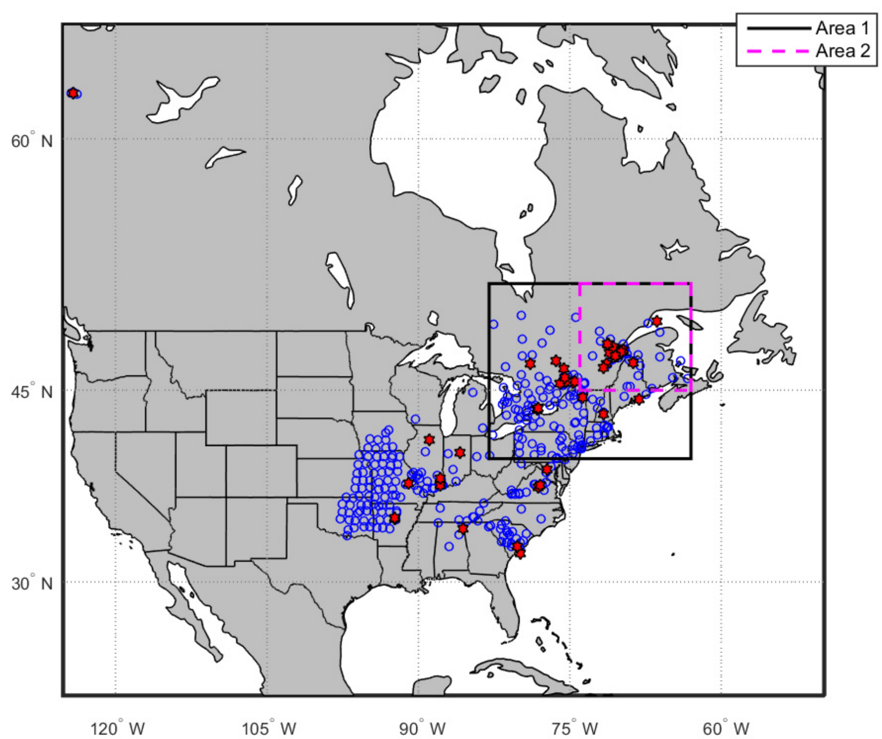

Figure 4.53 Geographical distribution of earthquakes and stations.

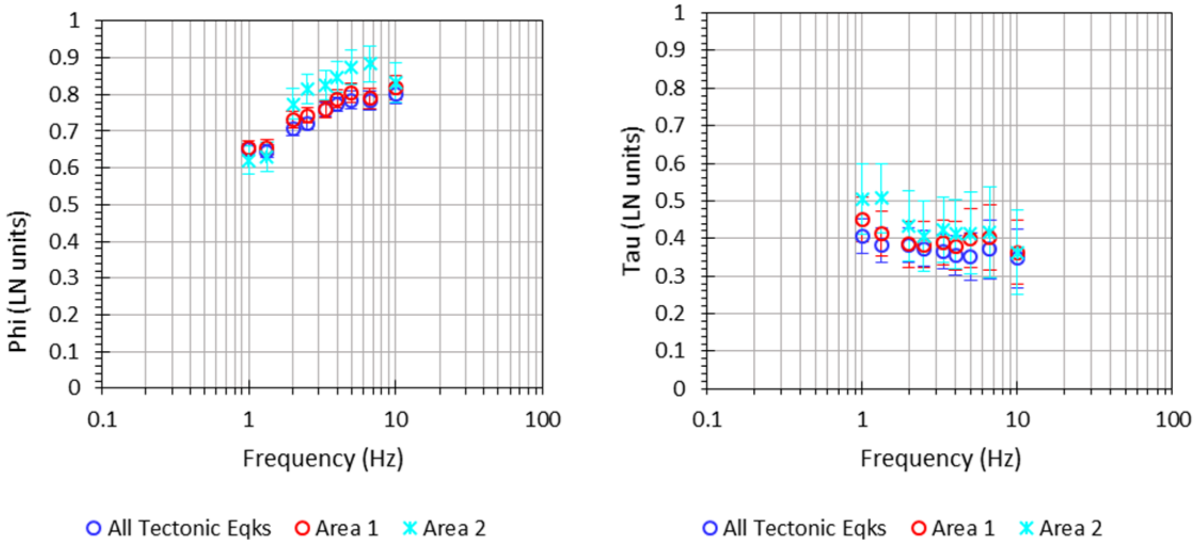

Figure 4.54 Comparison of ϕ (left) and τ (right) for all tectonic earthquakes and two subsets of tectonic earthquakes in the smaller regions.

5 CENA Standard Deviation Models

5.1 GENERAL FRAMEWORK

Two types of standard deviation models were developed for CENA: ergodic σ and partially non-ergodic (single-station) σ models. The single-station σ model provides a reduction in the aleatory variability of ground motion; however, it requires a careful characterization of the median site-specific response and its uncertainty. When site-response characterization is not performed, ergodic σ should be used.

In building the ergodic and the single-station σ models, the adopted approach consists of evaluating the individual components of ground-motion variability. Candidate models are evaluated for each of τ, ϕ_{SS}, and ϕ_{S2S} separately. For each candidate model, the best estimate (mean) and statistical variability are characterized. Candidate models for τ and ϕ_{SS} are combined to create candidate single-station σ models. Similarly, candidate τ, ϕ_{SS}, and ϕ_{S2S} models are combined to create candidate ergodic σ models for CENA.

This chapter describes the candidate models for τ, ϕ_{SS}, and ϕ_{S2S} developed for CENA. The single-station σ and ergodic σ models are also described, and comparisons of the different components of the CENA models to existing models are provided to ensure that the CENA models cover the range of existing models where appropriate.

5.1.1 χ-Square Distribution

The χ-square distribution describes the distribution of the sum of squares of independent normal random variables. As a result, the sample variance of a normal distribution follows a scaled χ-square distribution [Ang and Tang 2007]. The epistemic uncertainty of the ground-motion variability can therefore be represented by three discrete values at the 5th, 50th, and 95th percentiles of the continuous scaled χ-square distributions with weights of 0.185, 0.63, and 0.185, respectively [Keefer and Bodily 1983]. The derivation of the mean variance and standard deviation of the variance is described in the following sections for each component of the ground-motion variability.

For τ, the central estimate consists of the median of the scaled χ-square distribution with mean given by τ^2 and standard deviation given by $SD[\tau^2]$. The high and low estimates are obtained by first computing the 95th and 5th percentile of the scaled χ-square distribution and then taking the square root of these scaled values, respectively. This is expressed mathematically as follows:

$$\tau_{Central} = \sqrt{c\chi_{2,k}^{-1}(0.5)}, \tag{5.1}$$

$$\tau_{High} = \sqrt{c\chi_{2,k}^{-1}(0.95)}, \tag{5.2}$$

and

$$\tau_{Low} = \sqrt{c\chi_{2,k}^{-1}(0.05)}, \tag{5.3}$$

where $\chi_{2,k}^{-1}(x)$ is the inverse of the chi-square distribution with k degrees of freedom, and c is a scaling parameter; c and k are given by:

$$c = \frac{\left(SD(\tau^2)\right)^2}{2\tau^2} \tag{5.4}$$

$$k = \frac{2\tau^4}{\left(SD(\tau^2)\right)^2} \tag{5.5}$$

These central, high, and low values represent a three-point discrete approximation to a continuous distribution and have weights of 0.63 on the median model and 0.185 on the 5th and 95th percentile models [Keefer and Bodily 1983]. Similarly, the central, high, and low values of ϕ_{SS} and ϕ_{S2S} are obtained by assuming that the variance of the site-corrected within-event residuals (ϕ_{SS}^2), and the variance of the site-to-site residuals (ϕ_{SS}^2) follow scaled χ-square distributions with means and standard deviations, as described in the following sections.

5.2 τ

5.2.1 Candidate Models

As discussed in Chapter 4, the CENA dataset covers a limited magnitude range and does not allow a reliable extrapolation of τ for magnitudes greater than 5.0. Moreover, CENA τ values at frequencies outside of 1 to 10 Hz range are not reliable due to the frequency bandwidth limitations of the recordings. As a result, three candidate models for τ are developed:

- Global τ model based on the average of the four proposed NGA-West2 τ models (ASK14, BSSA14, CB14, and CY14);
- CENA constant model (magnitude-independent; homoscedastic), and
- CENA magnitude-dependent model.

The derivation of the three candidate τ models (mean and $SD[\tau^2]$) is described below.

5.2.1.1 Global τ Model

The global τ model is based on the average of the four NGA-West2 τ models (ASK14, BSSA14, CB14, and CY14). The NGA-West2 models were chosen because they are derived from a large and uniformly-processed global dataset, and are applicable to a large magnitude range (**M**3.0 to

8.0 or 8.5). All four NGA-West2 τ models are magnitude-dependent, and all models (except ASK14) are also period-dependent.

The global model is based on averaging τ^2 for the four NGA-West2 models. Because the individual models have different magnitude breaks, the resulting average has five magnitude breaks. Figures 5.1 and 5.2 show the four NGA-West2 τ models and their average at PGV and spectral periods of 0.01, 0.1, 0.2, 0.5, 1, 3, 5, 7.5, and 10 sec. The proposed global model is also shown in Figures 5.1 and 5.2. It follows closely the average NGA-West2 τ and has four magnitude breaks: 4.5, 5.0, 5.5, and 6.5. The global τ model has the following functional form:

$$\tau = \begin{cases} \tau_1 & for\ M \leq 4.5 \\ \tau_1 + (\tau_2 - \tau_1) * \frac{(M-4.5)}{0.5} & for\ M \leq 5.0 \\ \tau_2 + (\tau_3 - \tau_2) * \frac{(M-5.0)}{0.5} & for\ M \leq 5.5 \\ \tau_3 + (\tau_4 - \tau_3) * \frac{(M-5.5)}{1.0} & for\ M \leq 6.5 \\ \tau_4 & for\ M > 6.5 \end{cases} \tag{5.6}$$

where the model coefficients τ_1, τ_2, τ_3, and τ_4 are the τ values at the magnitude breaks of 4.5, 5.0, 5.5, and 6.5, respectively.

Figure 5.3 shows the derived model coefficients as a function of frequency, indicating that the average τ at the magnitude breaks is not constant with frequency but fluctuates around constant values. An upward bump can be observed in the average τ at a frequency of around 10 to 20 Hz. This bump can also be seen in some of the underlying models (BSSA14 and CB14), while the rest of the models smoothed through it (CY14 and ASK14). The origin of this bump has been investigated through point-source simulations as part of the Hanford Project [Coppersmith et al. 2014]. A first set of 250 point-source simulations were conducted with an average stress parameter of 50 bars and a logarithmic standard deviation of 0.5. Ground motions were computed at 50 sites per earthquake using a log-normal distribution of κ with median of 0.035 sec and a standard deviation of 0.3 (natural log units). WUS linear site amplification factors were used with a frequency-independent site factor that is log-normally distributed around zero with a standard deviation of 0.4 (natural log units). The resulting ϕ and τ values are shown in Figure 5.4, showing a bump in τ but not in ϕ. Other simulations with different distributions of κ and with frequency-dependent site factors were performed with similar results.

A second set of simulations was conducted allowing for correlation between earthquakes and κ values. This correlation would result if there are regional κ differences resulting in earthquakes sampling particular ranges of κ values. The uncertainty in κ was divided between a median value for each earthquake and a within-earthquake distribution, preserving the total variance of κ; all other parameters were kept the same. The resulting standard deviations are presented in Figure 5.5 and show that the correlation between earthquakes and κ values result in the bump occurring now in both ϕ and τ. Based on this analysis, we concluded that the bump observed in τ at around 10 to 20 Hz is likely to be an artifact of κ. We decided to smooth through it and adopt a constant τ versus frequency, as shown with the dashed lines in Figure 5.3.

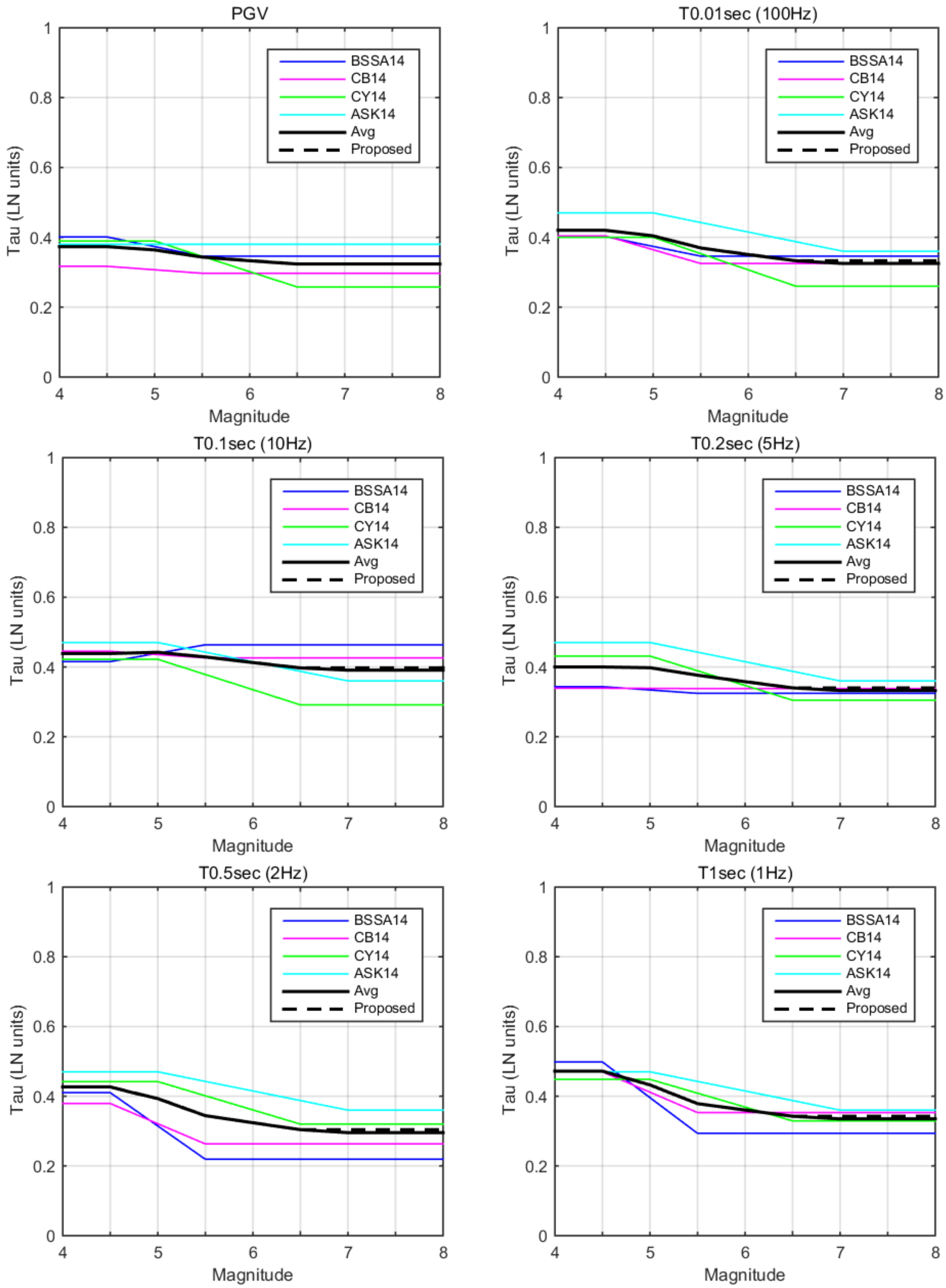

Figure 5.1 **Global τ model versus magnitude at PGV and F = 100, 10, 5, 2, and 1 Hz.**

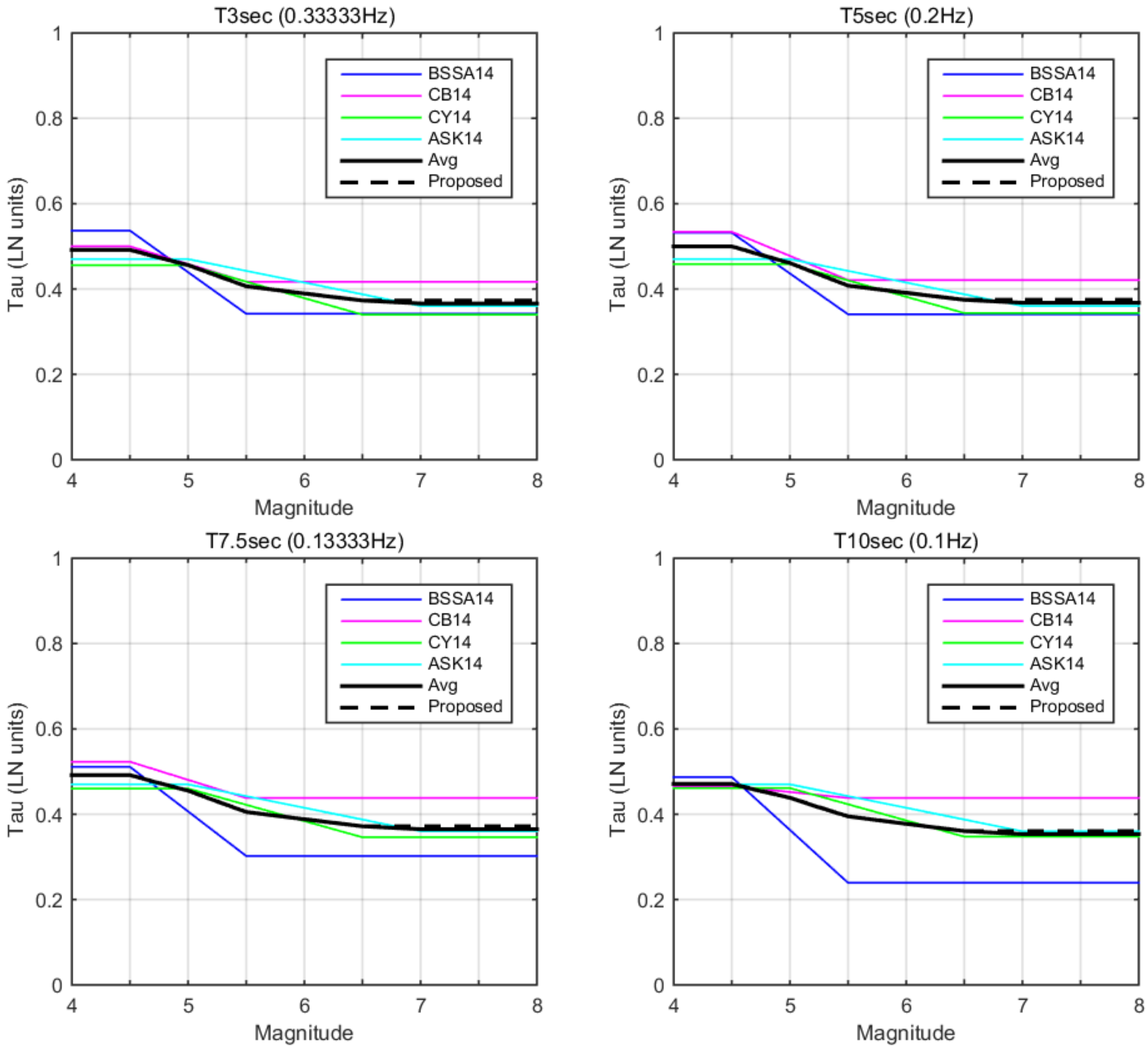

Figure 5.2 Global τ model versus magnitude at F = 0.33, 0.2, 0.13, and 0.1 Hz.

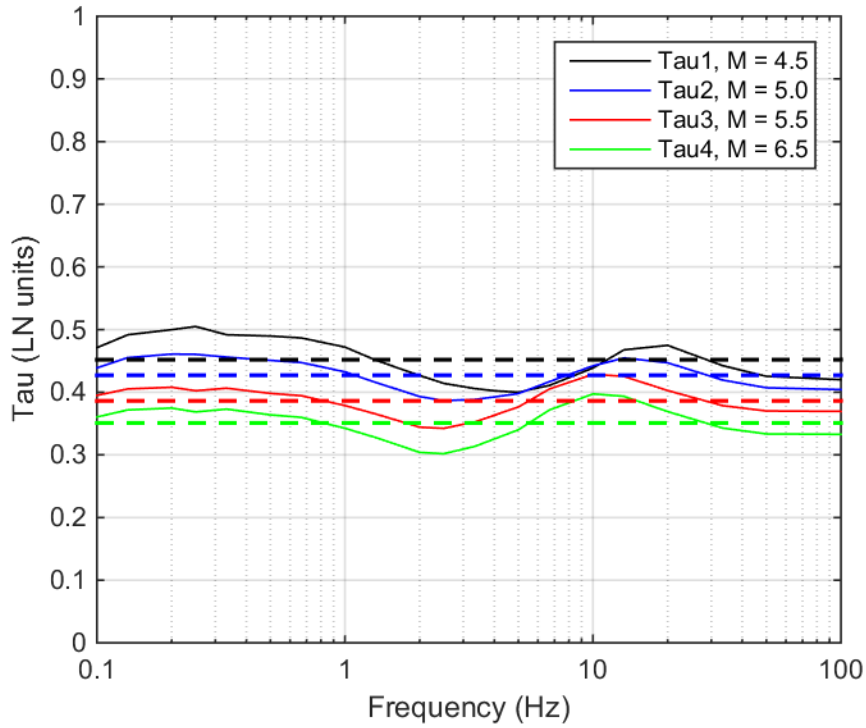

Figure 5.3 **Coefficients of the global τ model versus frequency as derived (solid lines) and smoothed (dashed lines).**

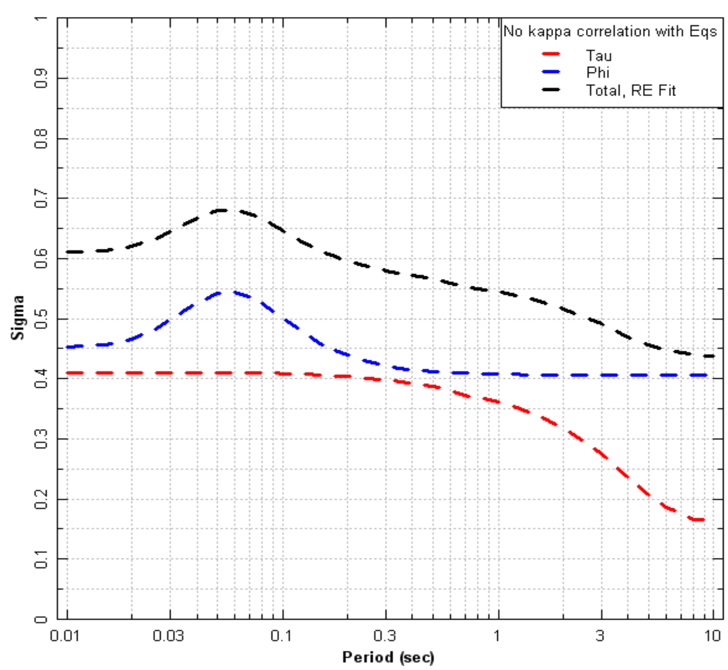

Figure 5.4 **Standard deviations computed using point-source stochastic simulations with random κ values [Coppersmith et al. 2014].**

The standard deviation of τ^2 $[SD(\tau^2)]$ consists of two components: within-model $[SD(\tau_W^2)]$ and between-model variability $[SD(\tau_B^2)]$ as shown below:

$$SD(\tau^2) = \sqrt{[SD(\tau_W^2)^2] + [SD(\tau_B^2)^2]} \tag{5.7}$$

The between-model variability is the standard deviation of τ^2 for the four underlying GMPEs and is shown in Figure 5.6. The within-model variability calculated as part of the regressions conducted for the CY14 model (R.R. Youngs, *personal communication*) was used here—see Figure 5.7—and represents the statistical variability in their τ^2 estimates. The total variability in τ^2 is shown in Figures 5.8 at the magnitude breaks of 4.5, 5.0, 5.5, and 6.5, respectively. The standard deviations were smoothed with a constant across period similar to the mean model. Figure 5.8 shows that the total variability in τ^2 is largest at **M**4.5 and 5.0 and decreases as **M** increases from **M**5.5 to **M**6.5. Table 5.1 presents the mean τ and $[SD(\tau^2)]$ at the four magnitude breaks for the derived global τ model.

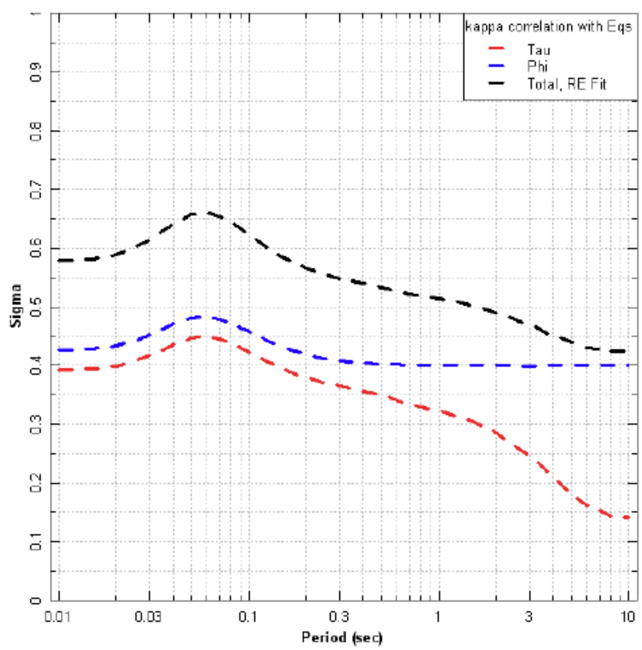

Figure 5.5 **Standard deviations computed using point-source stochastic simulations with correlated κ values [Coppersmith et al. 2014].**

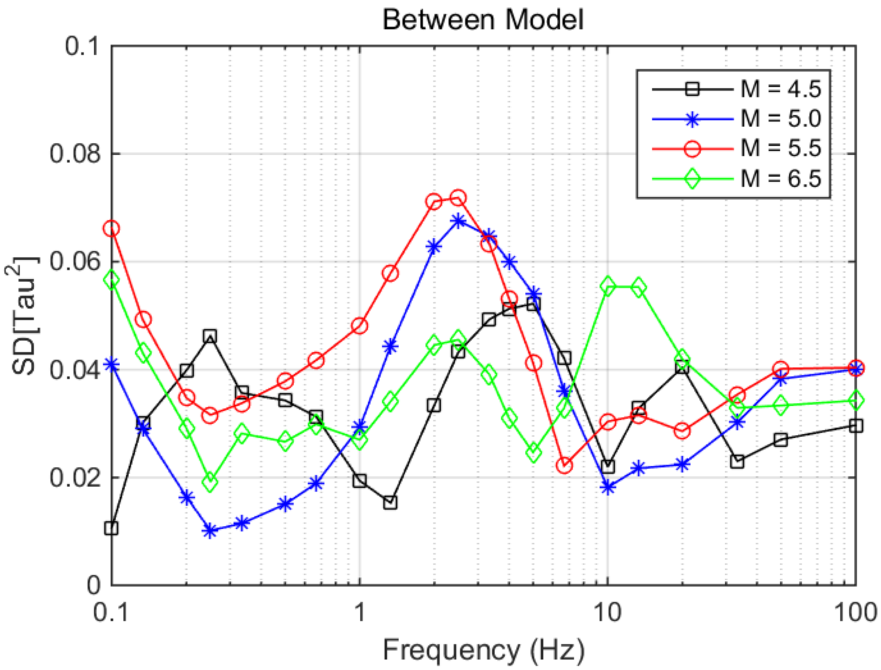

Figure 5.6 **Between-model variability of global τ^2.**

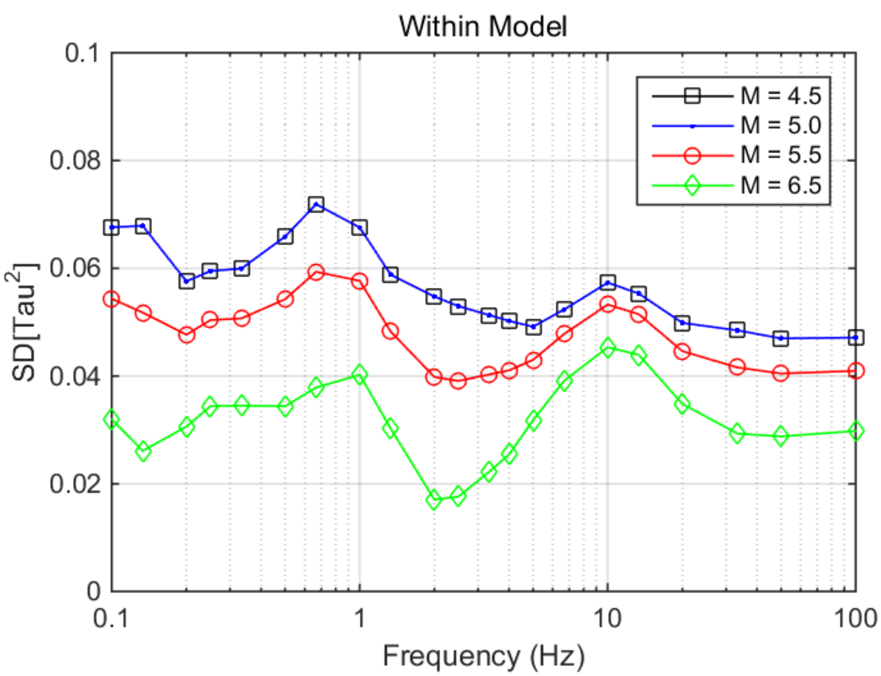

Figure 5.7 **Within-model variability of global τ^2.**

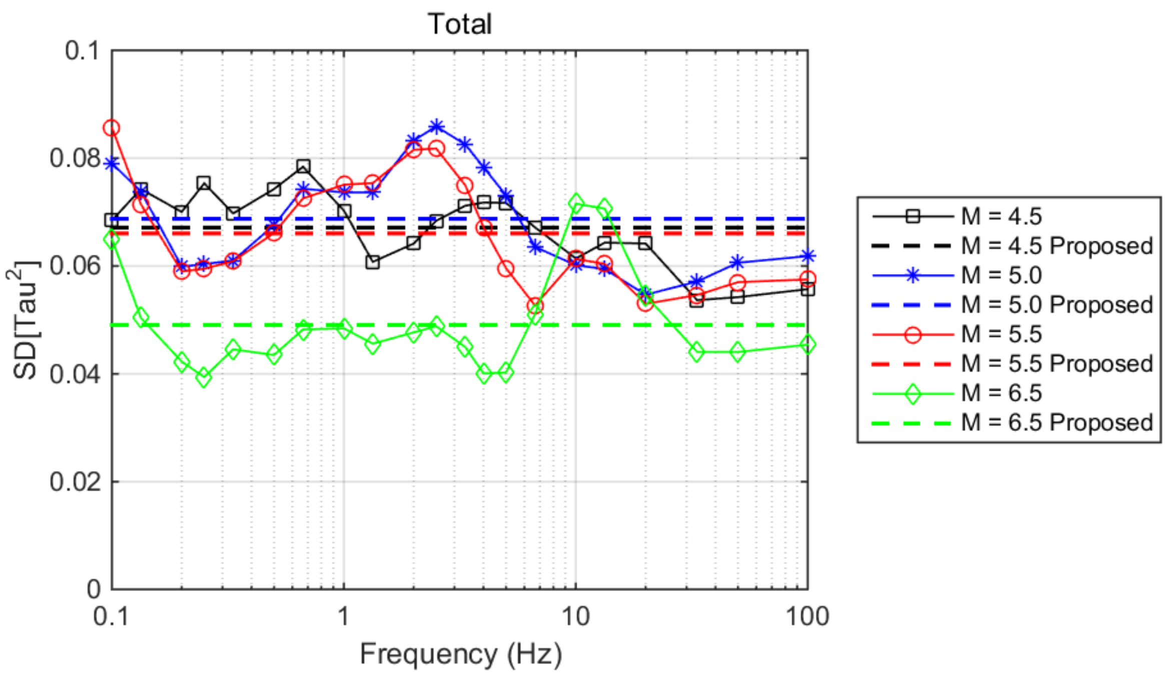

Figure 5.8 Total variability of global τ^2.

Table 5.1 Mean and standard deviation of the coefficients of the global τ model.

Period (sec)	Frequency (Hz)	Mean τ_1	$SD(\tau_1^2)$	Mean τ_2	$SD(\tau_2^2)$	Mean τ_3	$SD(\tau_3^2)$	Mean τ_4	$SD(\tau_4^2)$
0.01 to 10	0.1 to 100	0.4518	0.0671	0.4270	0.0688	0.3863	0.0661	0.3508	0.0491
PGV		0.3733	0.0558	0.3639	0.0554	0.3434	0.0477	0.3236	0.0449

5.2.1.2 CENA Constant τ Model

The CENA tectonic data with **M** larger than or equal to 3.0 were used to construct a τ model. Since CENA data are limited in magnitude range to a maximum **M** of about 5.5, two alternative models (constant and magnitude-dependent) were developed using the CENA data to address the uncertainty in the extrapolation of τ to magnitudes larger than about 5.0 to 5.5.

Figure 5.9 shows the constant CENA τ values as a function of frequency obtained by maximizing the likelihood function for the tectonic data with minimum **M** of 3.0. Because CENA data suffer from frequency bandwidth limitations, CENA τ values were averaged in the frequency range of 1 to 10 Hz to obtain the proposed CENA constant τ model (τ = 0.37 natural log units), which is magnitude-independent and period-independent. Figure 5.10 shows the standard deviation in τ^2 obtained from the regression and represents the statistical variability in τ^2. The standard deviation values were averaged between 1 and 10 Hz to obtain the proposed variability in τ^2, which is equal to 0.0377. We note that this variability in τ^2 is smaller than that observed for the global τ^2 model, which is based on a bigger dataset. As a result, we replace the variability in the constant CENA model with the variability in the global τ^2 model at **M** = 5.0 [$SD(\tau^2)$ = 0.0688]. Table 5.2 presents the mean τ and $SD(\tau^2)$ of the CENA constant τ model.

Table 5.2 Mean and standard deviation of the CENA constant τ model.

Period (sec)	Frequency (Hz)	Mean τ	$SD(\tau^2)$
0.01 to 10	0.1 to 100	0.3695	0.0688
PGV		0.3441	0.0554

5.2.1.3 CENA Magnitude-Dependent τ Model

Studies of between-event variability based on large datasets that cover a wide magnitude range generally note a magnitude-dependent trend of τ, whereby τ decreases as **M** increases and reaches a constant value at **M**6 to 7.5 (ex. NGA-West2 models). A CENA τ model was developed to incorporate the magnitude-dependence observed in the global τ models. This model is derived using CENA tectonic data with magnitude greater than or equal to 3.0. The model has the following form:

$$\tau = \begin{cases} \tau_1 & for\ M \leq 5.0 \\ \tau_1 + (\tau_2 - \tau_1) * \frac{(M-5.0)}{0.5} & for\ M \leq 5.5 \\ \tau_2 + (\tau_3 - \tau_2) * (M - 5.5) & for\ M \leq 6.5 \\ \tau_3 & for\ M > 6.5 \end{cases} \tag{5.8}$$

where the ratios τ_2/τ_1 and τ_3/τ_1 are obtained from the global model discussed above ($\tau_2/\tau_1 = 0.9047$ and $\tau_3/\tau_1 = 0.8215$); therefore, CENA data were used to solve for τ_1.

Figure 5.11 shows the values of τ_1 obtained from the regression as a function of frequency. The average of τ_1 values in the frequency range of 1 to 10 Hz was used to smooth τ_1 versus frequency. Figure 5.11 also shows the resulting τ_2 and τ_3 as function of frequency. Figure 5.12 shows the $SD(\tau_1^2)$ obtained from the regression. These values were again smoothed with a constant equal to the average of $SD(\tau_1^2)$ between frequencies of 1 and 10 Hz. Figure 5.12 also shows the $SD(\tau^2)$ for the global model at the magnitude breaks **M** 4.5, 5.0 5.5, and 6.5. Figure 5.12 indicates that the variability in the global τ^2 model at all magnitudes is larger than that for the CENA magnitude-dependent model, which is based on a smaller dataset. As a result, values of $SD(\tau^2)$ for CENA at **M**5.0, 5.5, and 6.5 were adopted from the global model.

Figure 5.13 compares the three candidate τ models as a function of magnitude for CENA: CENA constant model, CENA magnitude-dependent model, and global model. All three models are period-independent. The solid lines show the median values for each model, and the dashed lines show the 5th and 95th percentile values for each model calculated, assuming τ^2 follows a χ-square distribution with mean and standard deviations calculated as discussed in the preceding sections. Figure 5.13 shows that CENA constant and magnitude-dependent models agree for **M** less than 5.0. Both of the CENA τ models are smaller than the global model at **M** less than 5.0. At larger magnitudes, the CENA magnitude-dependent model follows the same magnitude-dependent trend as the global model. The CENA constant model agrees with the global model at **M** greater than 6.0. Table 5.3 presents the mean τ and $SD(\tau^2)$ at the three magnitude breaks for the CENA magnitude-dependent τ model.

Table 5.3 Mean and standard deviation of the coefficients of the CENA magnitude-dependent τ model.

Period (sec)	Frequency (Hz)	Mean τ_1	$SD(\tau_1^2)$	Mean τ_2	$SD(\tau_2^2)$	Mean τ_3	$SD(\tau_3^2)$
0.01 to 10	0.1 to 100	0.3730	0.0688	0.3375	0.0661	0.3064	0.0491
PGV		0.3477	0.0554	0.3281	0.0477	0.3092	0.0449

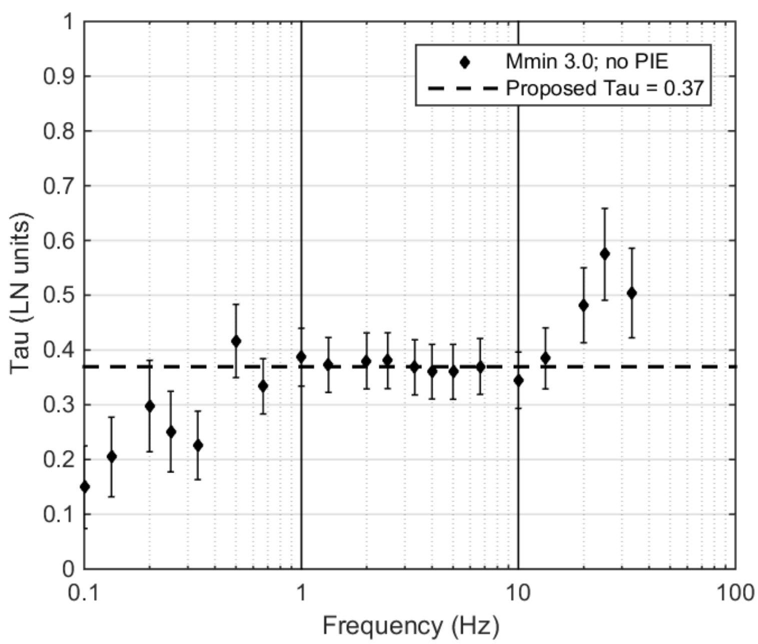

Figure 5.9 Constant CENA τ model.

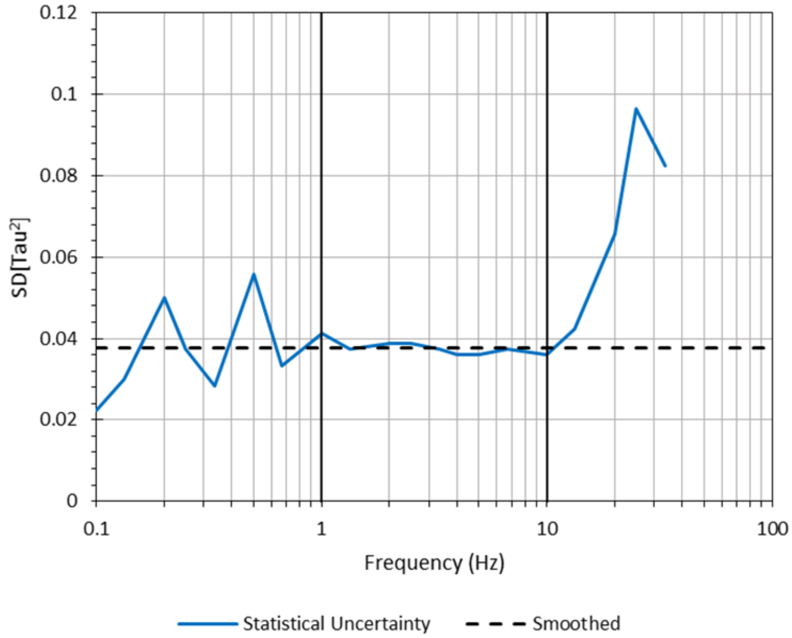

Figure 5.10 Variability in constant CENA τ^2 model.

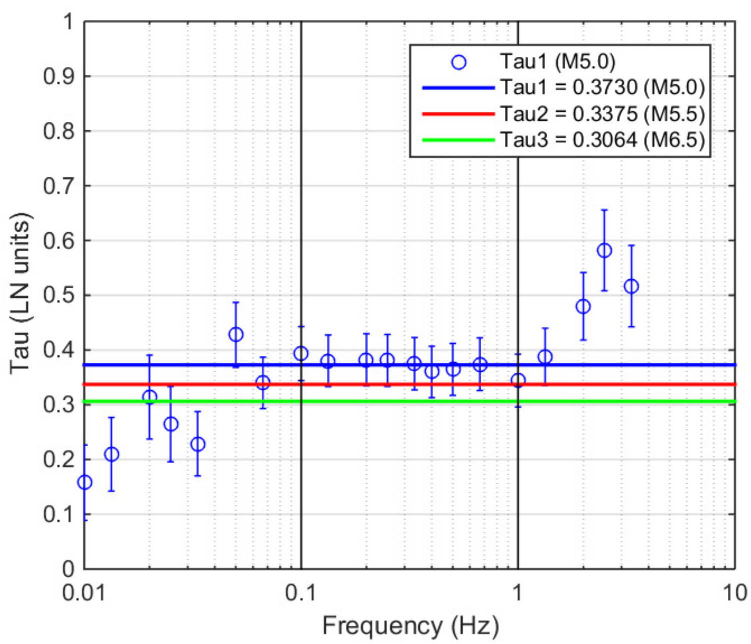

Figure 5.11 Coefficients of the CENA magnitude-dependent τ model.

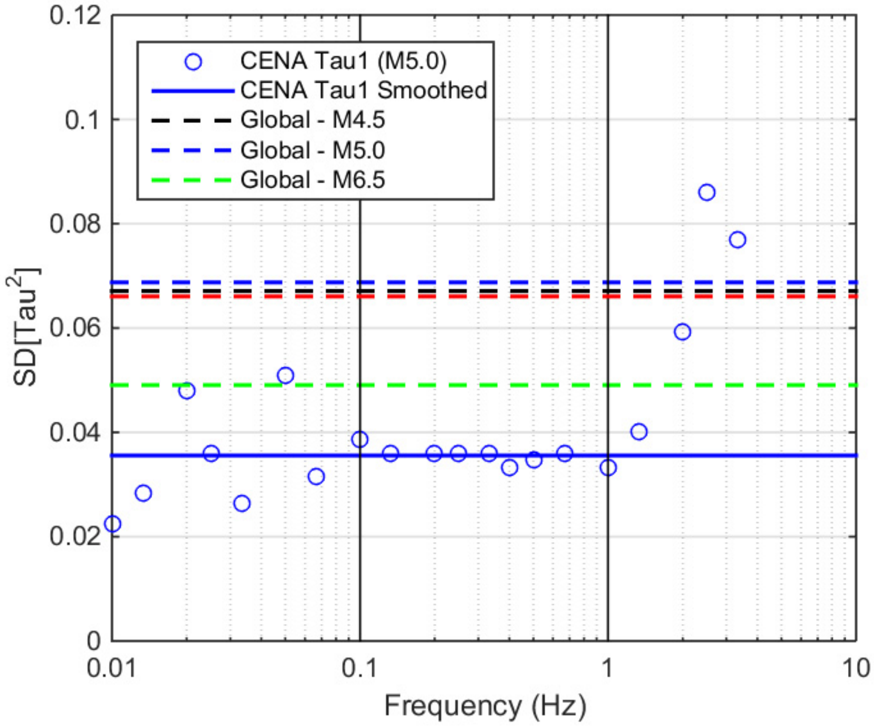

Figure 5.12 **Variability in CENA magnitude-dependent τ^2 model compared to the global model.**

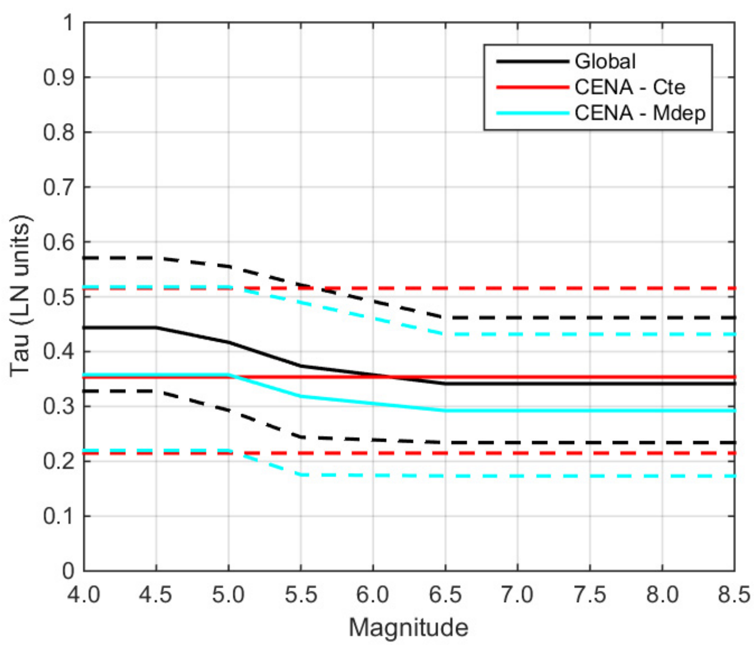

Figure 5.13 **Comparison of candidate τ models for CENA. Dashed lines represent the 5th and 95th percentiles of the models.**

5.2.2 Comparison to Existing Models

Tables 5.4 to 5.6 show the values of the coefficients of the global, CENA constant, and CENA magnitude-dependent τ models at PGV and spectral periods of 0.01 to 10 sec for the three candidate τ models for CENA. The low, central, and high τ estimates correspond to the 5th, 50th, and 95th percentile of the τ^2 distribution calculated, assuming τ^2 follows a χ-square distribution with mean and standard deviations calculated as discussed above. Figure 5.14 presents a comparison of the candidate τ models for CENA to the SWUS τ model (central, high and low branches). Because both the CENA and SWUS models are period-independent, they are shown versus magnitude. The SWUS τ model is based on the average of τ models for the four NGA-West2 GMPEs and for Zhao et al. [2006], which has a magnitude-independent τ. At small magnitudes (**M**4.0 to 5.0), the SWUS τ model is lower than the global τ model and has larger uncertainty due to the inclusion of the Zhao et al. [2006] τ model in SWUS, which is different than the four NGA-West2 models at small magnitudes. At larger magnitudes, the SWUS and the global τ models are similar.

Figure 5.15 shows a comparison of the candidate τ models for CENA to the Hanford τ model as a function of frequency for **M**5.0, 6.0, and 7.0. The Hanford τ model is based on the average of the four NGA-West2 τ models but adopted different magnitude breaks and smoothing with period (period-dependent) than the global τ model. Figure 5.15 shows that the Hanford and the global τ models are comparable in terms of their median values and uncertainty ranges.

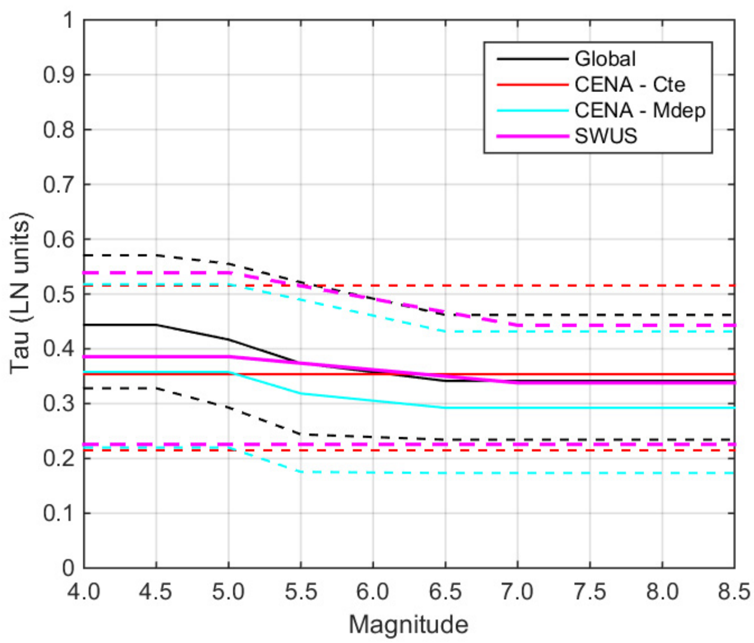

Figure 5.14 **Comparison of the candidate τ models for CENA to SWUS τ model. Dashed lines represent the 5th and 95th percentiles of the models.**

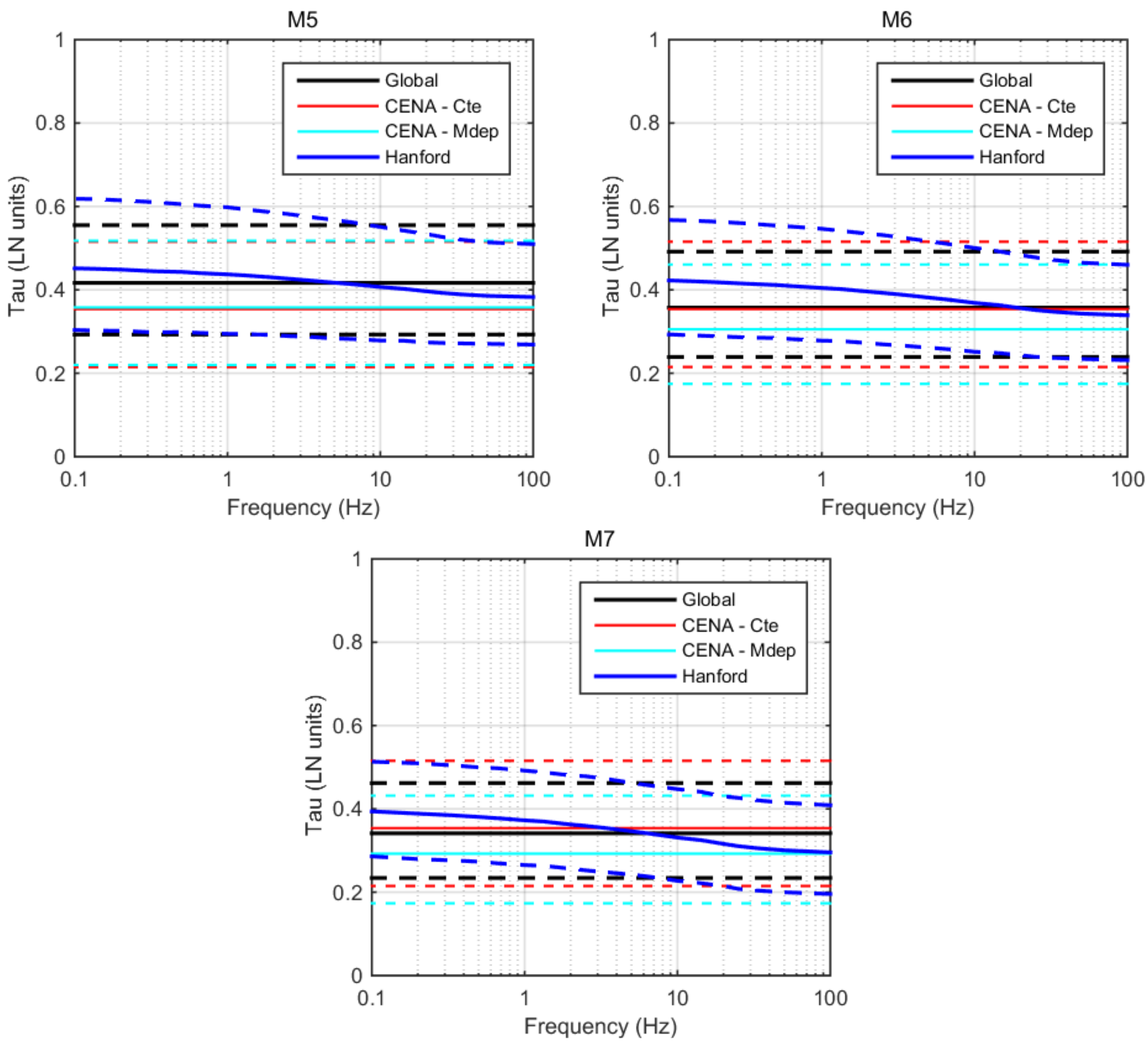

Figure 5.15 **Comparison of the candidate τ models for CENA to the Hanford τ model at M5.0, 6.0, and 7.0. Dashed lines represent the 5th and 95th percentiles of the models.**

Table 5.4 **Coefficients of the global τ model.**

		τ_1	τ_2	τ_3	τ_4
Central	*F* 0.1 to 100 Hz	0.4436	0.4169	0.3736	0.3415
	PGV	0.3633	0.3532	0.3340	0.3136
Low	*F* 0.1 to 100 Hz	0.3280	0.2928	0.2439	0.2343
	PGV	0.2488	0.2370	0.2278	0.2081
High	*F* 0.1 to 100 Hz	0.5706	0.5551	0.5214	0.4618
	PGV	0.4919	0.4845	0.4535	0.4333

Table 5.5 Coefficients of the CENA constant τ model.

Period (sec)	Frequency (Hz)	Central	High	Low
0.01 to 10	0.1 to 100	0.3538	0.5154	0.2149
PGV		0.3315	0.4710	0.2101

Table 5.6 Coefficients of the CENA magnitude-dependent τ model.

Period (sec)	Frequency (Hz)	Central			High			Low		
		τ_1	τ_2	τ_3	τ_1	τ_2	τ_3	τ_1	τ_2	τ_3
0.01 to 10	0.1 to 100	0.3577	0.3185	0.2924	0.5177	0.4895	0.4317	0.2198	0.1755	0.1734
PGV		0.3355	0.3174	0.2978	0.4734	0.4428	0.4235	0.2150	0.2072	0.1884

5.3 σ_{SS}

5.3.1 Candidate Models

The ϕ_{SS} analysis presented in Section 4.4 highlights the shortcomings of deriving ϕ_{SS} models using the CENA dataset. The main shortcoming is that the CENA dataset covers a limited magnitude range and does not allow a reliable extrapolation of ϕ_{SS} for magnitudes greater than about 5.0. Moreover, CENA ϕ_{SS} values at frequencies outside of 1 to 10 Hz range are not reliable due to the frequency bandwidth limitations of the recordings. As a result, we present three candidate models for ϕ_{SS}:

- Global ϕ_{SS} model based on the average of the four NGA-West2 ϕ_{SS} (ASK14, BSSA14, CB14, and CY14);
- CENA constant model (magnitude-independent; homoscedastic), and
- CENA magnitude-dependent model.

The derivation of the three candidate ϕ_{SS} models [mean and $SD(\tau\phi_{SS}^2)$] is described below.

5.3.1.1 Global ϕ_{SS} Model

Mean Model

The global ϕ_{SS} model is based on the average of the four NGA-West2 ϕ_{SS} (ASK14, BSSA14, CB14, and CY14). The datasets used to run the mixed-effects regression and estimate the site terms, and the single-station within-event residuals were discussed in Section 2.2 for the four NGA-West2 models. Single-station within-event residuals were binned by magnitude in bins of 0.5 magnitude unit width, and ϕ_{SS} was calculated in each bin as described in Chapter 4. Figures 5.16 and 5.17 show the resulting four NGA-West2 ϕ_{SS} values as a function of magnitude at PGV and spectral periods of 0.01, 0.1, 0.2, 0.5, 1, 3, 5, 10 sec. A clear trend of ϕ_{SS} with magnitude can be observed in these plots, particularly at short periods. At periods greater than 1 sec, the magnitude dependence becomes weaker, and ϕ_{SS} can be considered magnitude-independent.

Values of ϕ_{SS}^2 in each magnitude bin were averaged for the four NGA-West2 models (averaging variances) to obtain the average WUS ϕ_{SS}^2 as a function of magnitude. The variability in the average ϕ_{SS}^2 [$SD(\phi_{SS}^2)$] was also estimated in each bin based on the between-model variability (standard deviation of ϕ_{SS}^2 for the four NGA-west2 models) and the average within-model variability (standard error of the ϕ_{SS}^2 estimates in each magnitude bin per GMPE). A weighted linear fit was applied to the average ϕ_{SS} values as a function of magnitude, with the magnitude breaks selected at **M**5.0 and 6.5. Figures 5.16 and 5.17 show the average ϕ_{SS} values and the fit results at each period. The global ϕ_{SS} model has the following form:

$$\phi_{SS} = \begin{cases} a & for\ M \leq 5.0 \\ a + (M - 5.0) * \frac{(b-a)}{1.5} & for\ M \leq 6.5 \\ b & for\ M > 6.5 \end{cases} \tag{5.9}$$

where a and b are the ϕ_{SS} values at **M**5.0 and 6.5, respectively. Figure 5.18 shows the derived coefficients a and b versus frequency. These coefficients were smoothed while preserving their general trend as a function of frequency, as shown in Figure 5.18.

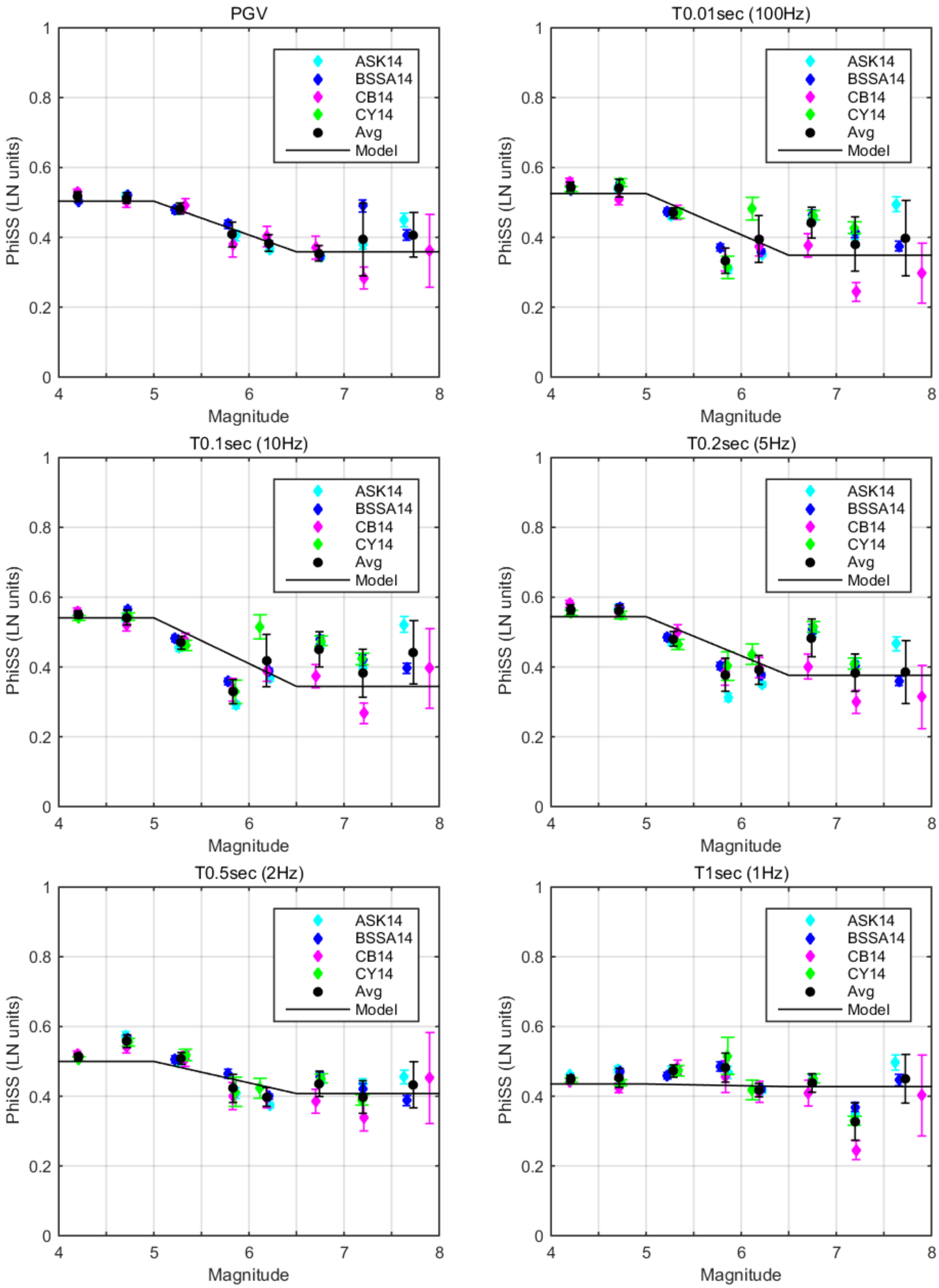

Figure 5.16 Global ϕ_{SS} model versus magnitude at PGV and F = 100, 10, 5, 2, and 1 Hz.

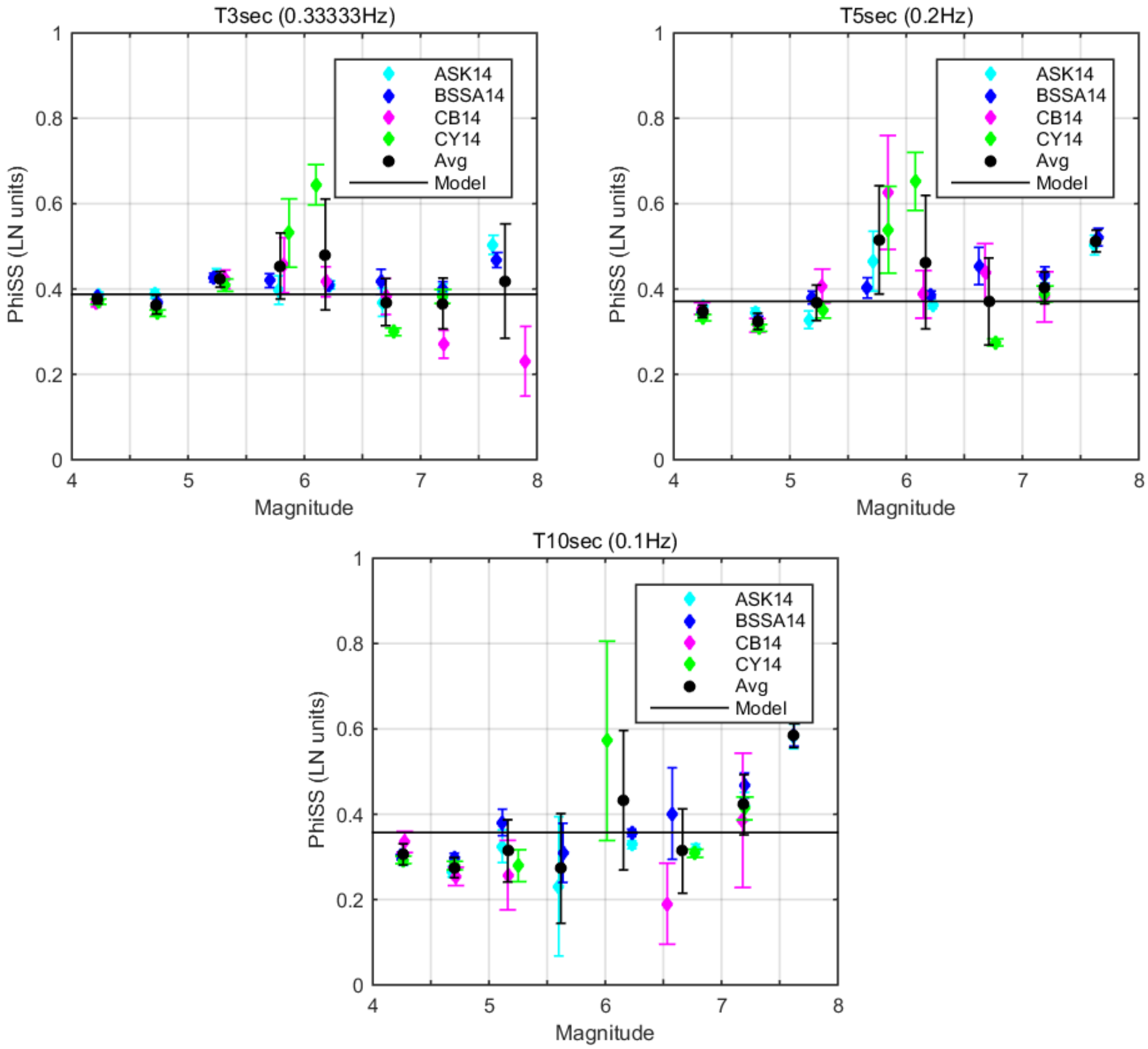

Figure 5.17 **Global ϕ_{SS} model versus magnitude at PGV and F = 0.33, 0.2, and 0.1 Hz.**

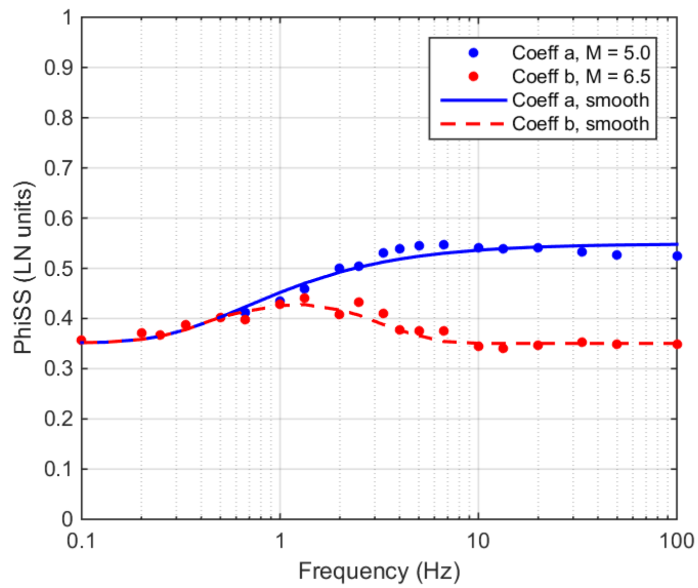

Figure 5.18 Coefficients of the global ϕ_{SS} model versus frequency.

Uncertainty

The uncertainty in the global ϕ_{SS} model has three components: (1) station-to-station variability in ϕ_{SS}; (2) statistical variability in ϕ_{SS} estimates; and (3) errors in the proposed model fit to the data. The station-to-station variability in ϕ_{SS} can be estimated across all sites in the dataset. It is a measure of variability in ϕ_{SS} from one site to another due to factors such as azimuthal dependency and topographic effects, as well as other unknown factors. As part of the SWUS project, the station-to-station variability in ϕ_{SS} was analyzed using the ASK14 dataset with **M** larger than or equal to 4.0. These results are adopted here, and their analysis is summarized below.

The estimate of ϕ_{SS} at an individual station is denoted as $\phi_{SS,S}$. The standard deviation of $\phi_{SS,S}$ [$SD(\phi_{SS,S})$] was estimated at all periods using the ASK14 dataset. The empirical estimates of $\phi_{SS,S}$ and their standard deviation are affected by a sampling error, however, that decreases as the number of recordings per site increases. Table 5.7 gives the $SD(\phi_{SS,S})$ for the ASK14 model at PGA and periods of 0.1 and 1 sec using a minimum of 5 through 25 recordings per station. As shown in Table 5.7, $SD(\phi_{SS,S})$ decreases as the minimum number of recordings per station increases due to the reduced sampling error.

To quantify the sampling error, a statistical exercise was undertaken, whereby a large set of single-station within-event residuals was simulated per station for the same number of stations as in the ASK14 dataset such that the coefficient of variation of $\phi_{SS,S}$ [CV = $SD(\phi_{SS,S})$/mean $\phi_{SS,S}$] is zero (all stations have the same $\phi_{SS,S}$ values), assuming a normal distribution. $\phi_{SS,S}$ values were then computed at each station using multiple realizations of the dataset (different number of recordings per station), and the corresponding CV of $\phi_{SS,S}$ was calculated for each realization. Figure 5.19 shows the CV values for the different number of realizations per site compared to the CV of $\phi_{SS,S}$ from the global dataset with different minimum numbers of recordings per station used in the regression for PGA and periods of 0.1 and 1.0 sec. The curve in Figure 5.19 represents the effect of pure sampling error on the estimates of the $SD(\phi_{SS,S})$, indicating that for large numbers of recordings per station, the sampling error decreases and approaches zero. The difference between the blue curve and the CV of $\phi_{SS,S}$ estimated using the empirical data represents the true $SD(\phi_{SS,S})$.

The statistical exercise was then repeated with different CV values (0.05, 0.10, 0.15) assigned for the simulations of the large dataset; the resulting CV for different realizations of the data are shown in Figure 5.20. Figure 5.20 shows that the CV of $\phi_{SS,S}$ for the empirical data fall between 0.10 and 0.15. A CV value of 0.12 was therefore adopted for calculating the station-to-station variability in ϕ_{SS}. It can be easily shown that for normally distributed residuals, the CV of the variance (ϕ_{SS}^2) is twice the CV of the standard deviation (ϕ_{SS}), hence, the standard deviation of ϕ_{SS}^2 can be computed as:

$$SD(\phi_{SS}^2) = 2\phi_{SS}^2 \tag{5.10}$$

Figures 5.21 and 5.22 show the components of the $SD(\phi_{SS}^2)$ for coefficients a and b of the global ϕ_{SS} model corresponding to ϕ_{SS} at **M**5.0 and 6.5, respectively. For each coefficient, the variability of the variance consists of the site-to-site variability of ϕ_{SS}^2 calculated as shown in Equation (5.10) as well as the standard error of the coefficient squared estimated from the weighted linear fit to the ϕ_{SS} values versus magnitude. The total $SD(\phi_{SS}^2)$ is also shown in the figures. For coefficient a, the standard error of a^2 is negligible compared to the site-to-site variability of ϕ_{SS}^2. For coefficient b, the standard deviation of b^2 is not negligible due to bigger differences among the NGA-West2 ϕ_{SS} values at large magnitudes, as well as smaller datasets with **M** larger than 6.5. Table 5.8 presents the mean ϕ_{SS} and $SD(\phi_{SS}^2)$ at the two magnitude breaks for the global ϕ_{SS} model.

Table 5.7 Standard deviation of $\phi_{SS,S}$ using the ASK14 residuals at PGA and periods of 0.1 and 1 sec for a minimum number of recordings per station (Nmin) of 5 to 25.

	$SD(\phi_{SS,S}^2)$		
	PGA	***T* = 0.1 sec**	***T* = 1.0 sec**
Nmin 5	0.149	0.153	0.126
Nmin 10	0.118	0.125	0.102
Nmin 15	0.110	0.117	0.095
Nmin 20	0.100	0.103	0.086
Nmin 25	0.073	0.079	0.075

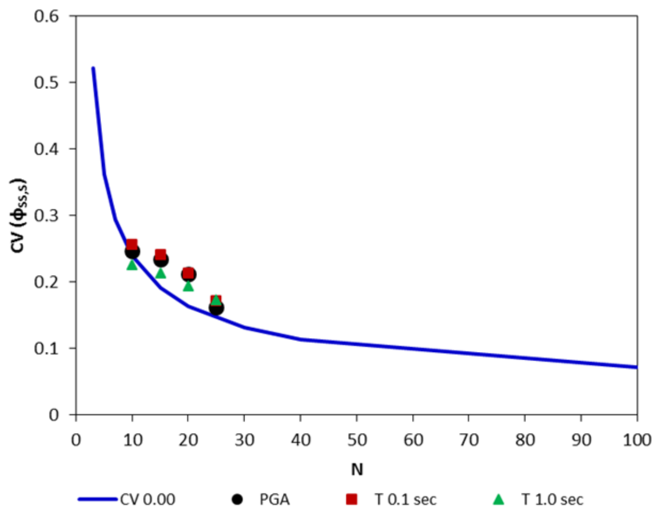

Figure 5.19 **Coefficient of variation (CV) of ϕ_{SS} at the stations in the ASK14 dataset for different number of recordings per station (N). The blue line represents the CV from a simulated ground-motion dataset where ϕ_{SS} at all stations are equal, hence the blue line represents pure sampling error.**

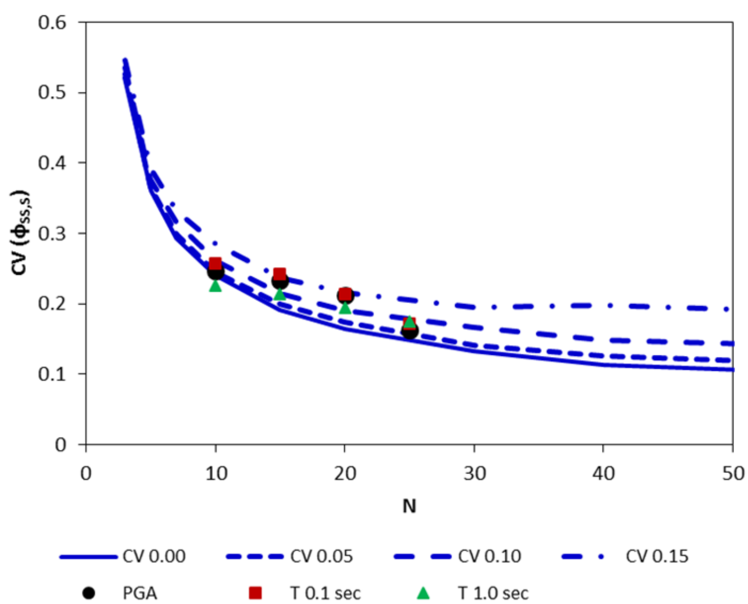

Figure 5.20 **Coefficient of variation (CV) for the ASK14 dataset for different number of recordings per station (N). The blue lines represent the CV of the realizations (N) of simulated datasets with different assigned CV.**

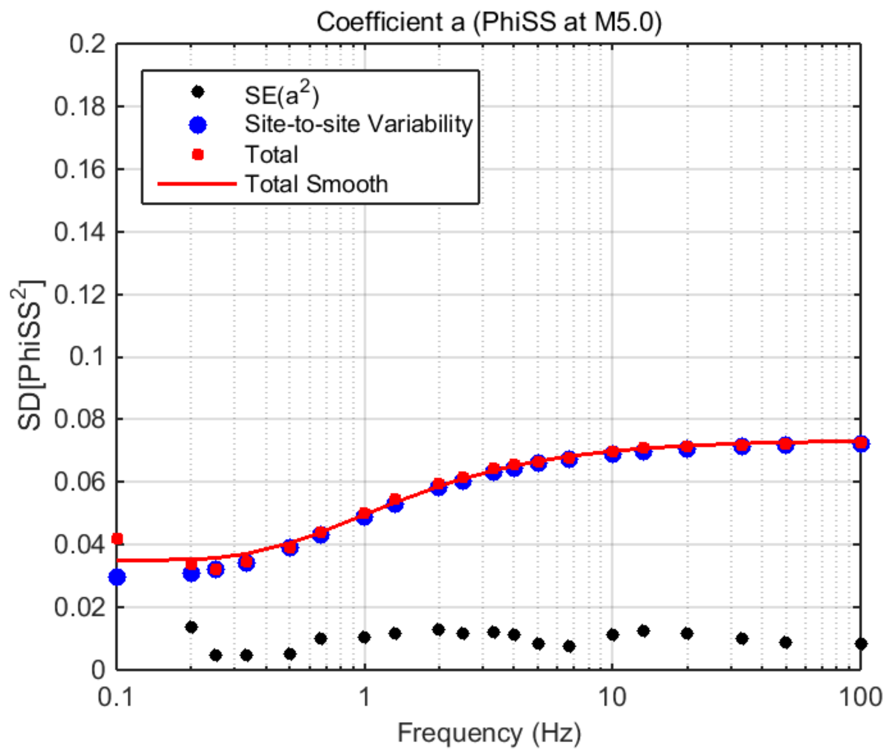

Figure 5.21 **Variability in the global ϕ_{SS}^2 model at M = 5.0 (coefficient *a*).**

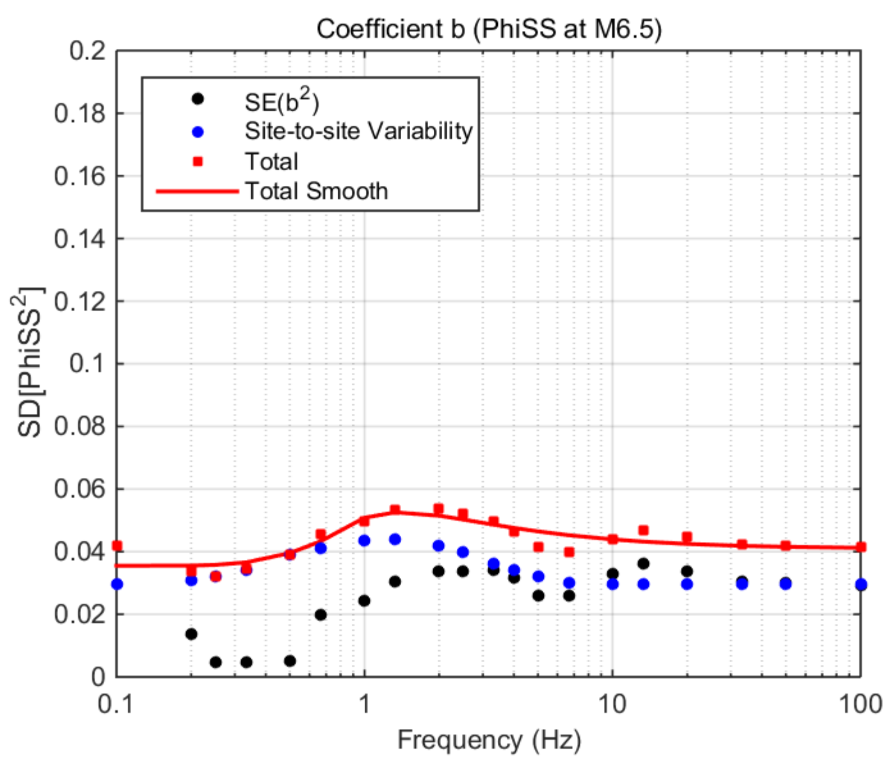

Figure 5.22 **Variability in the global ϕ_{SS}^2 model at M = 6.5 (coefficient *b*).**

Table 5.8 Mean and standard deviation of the coefficients of the global magnitude-dependent ϕ_{SS} model.

Period (sec)	Frequency (Hz)	Mean *a*	$SD(a^2)$	Mean b	$SD(b^2)$
0.01	100	0.5477	0.0731	0.3505	0.0412
0.02	50	0.5464	0.0727	0.3505	0.0416
0.03	33.33	0.5450	0.0723	0.3505	0.0419
0.04	25	0.5436	0.0720	0.3505	0.0422
0.05	20	0.5424	0.0716	0.3505	0.0425
0.075	13.33	0.5392	0.0707	0.3505	0.0432
0.1	10	0.5361	0.0699	0.3505	0.0439
0.15	6.67	0.5299	0.0682	0.3543	0.0453
0.2	5	0.5240	0.0666	0.3659	0.0465
0.25	4	0.5183	0.0651	0.3765	0.0476
0.3	3.33	0.5127	0.0637	0.3876	0.0486
0.4	2.5	0.5022	0.0611	0.4066	0.0503
0.5	2	0.4923	0.0586	0.4170	0.0515
0.75	1.33	0.4704	0.0535	0.4277	0.0526
1	1	0.4519	0.0495	0.4257	0.0508
1.5	0.67	0.4231	0.0439	0.4142	0.0433
2	0.5	0.4026	0.0405	0.4026	0.0396
3	0.33	0.3775	0.0371	0.3775	0.0366
4	0.25	0.3648	0.0358	0.3648	0.0358
5	0.2	0.3583	0.0353	0.3583	0.0356
7.5	0.13	0.3529	0.0350	0.3529	0.0355
10	0.1	0.3519	0.0350	0.3519	0.0355
PGV		0.5034	0.0609	0.3585	0.0316

5.3.1.2 CENA Constant ϕ_{SS} Model

The CENA tectonic data with minimum **M** of 3.0 and maximum R_{RUP} distance of 300 km were used to construct ϕ_{SS} models. The distance limit of 300 km was used in order to limit the slightly smaller ϕ_{SS} values at large distances from biasing the average ϕ_{SS} at the different periods. Since the usable CENA data for these computations are limited in magnitude range to a maximum **M** of about 5.5, two alternative models (constant and magnitude-dependent) were developed using the CENA data to address the uncertainty in the extrapolation of ϕ_{SS} to magnitudes larger than about 5.5.

Figure 5.23 shows the constant CENA ϕ_{SS} values as a function of frequency obtained by maximizing the likelihood function for the tectonic data with minimum **M** of 3.0 and maximum R_{RUP} distance of 300 km. Because CENA data suffer from frequency bandwidth limitations, CENA ϕ_{SS} values were averaged in the frequency range of 1 to 10 Hz to obtain the proposed CENA constant ϕ_{SS} model (ϕ_{SS} = 0.51 natural log units), which is magnitude-independent and period-independent.

Figure 5.24 shows the standard deviation in ϕ_{SS}^2 consisting of the site-to-site variability obtained using CV (ϕ_{SS}^2) =2*0.12 and the statistical variability in the ϕ_{SS}^2 estimates obtained from the regression. The standard deviation values were averaged between 1 and 10 Hz to obtain the proposed variability in ϕ_{SS}^2, which is equal to 0.06755. Table 5.9 presents the mean ϕ_{SS} and $SD(\phi_{SS}^2)$ for the CENA constant ϕ_{SS} model.

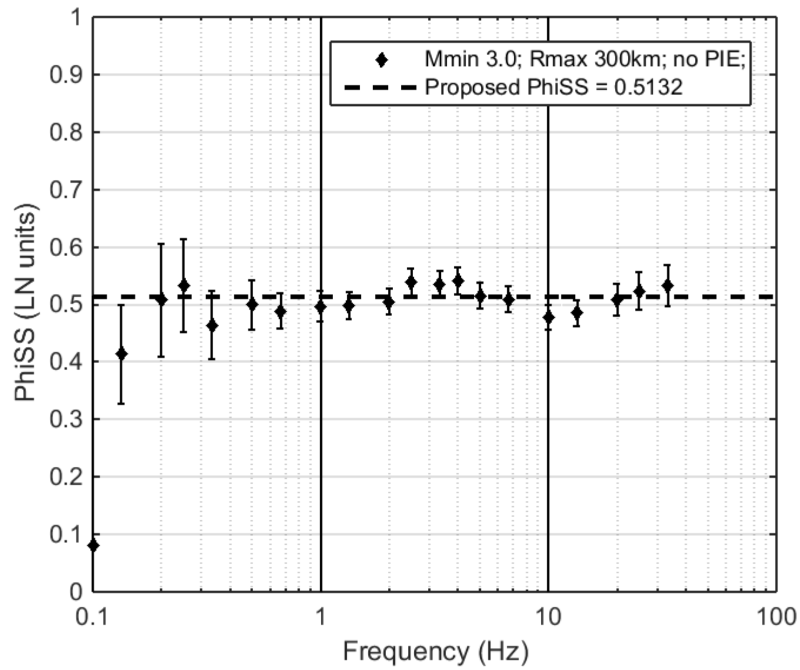

Figure 5.23 Constant CENA ϕ_{SS} model.

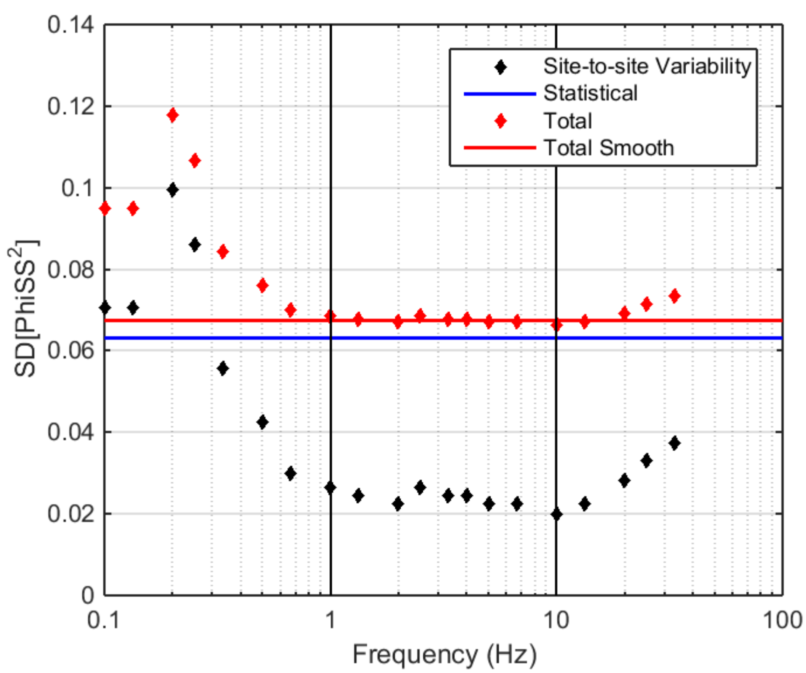

Figure 5.24 Variability in constant CENA ϕ_{SS}^2 model.

Table 5.9 Mean and standard deviation of the CENA constant ϕ_{SS} model.

Period (sec)	Frequency (Hz)	Mean ϕ_{SS}	$SD(\phi_{SS}^2)$
0.01 to 10	0.1 to 100	0.5132	0.0675
PGV		0.5507	0.0678

5.3.1.3 CENA Magnitude-Dependent ϕ_{SS} Model

Previous single-station within-event standard deviation studies based on large global datasets that cover a wide magnitude range observed a magnitude-dependent trend of ϕ_{SS} whereby ϕ_{SS} decreases as **M** increases and reaches a constant value at **M**6 to 7.5 (ex. PRP, TNSP, Hanford, and SWUS Projects). As a result, a CENA ϕ_{SS} model was developed to incorporate the magnitude-dependence observed in the global ϕ_{SS} model. This model is derived using CENA tectonic data with magnitude greater than or equal to 3.0 and R_{RUP} distance less than or equal to 300 km. The model has the following form:

$$\phi_{SS} = \begin{cases} a & for\ M \le 5.0 \\ a + (M - 5.0) * \frac{(b-a)}{1.5} & for\ M \le 6.5 \\ b & for\ M > 6.5 \end{cases} \tag{5.11}$$

where the ratios of b/a at all frequencies are constrained to those from the global ϕ_{SS} model; therefore, CENA data were used to solve for coefficient a. Figure 5.25 shows the a values obtained from the regression as a function of frequency. The average of a values in the frequency range of 1 to 10 Hz was used to smooth a versus frequency. Figure 5.25 also shows the resulting coefficient b as function of frequency.

Figure 5.26 shows the statistical variability obtained from the regression and the site-to-site variability of ϕ_{SS}^2 at **M**5.0 (a^2). These values of the statistical variability were again smoothed using the average of the values between frequencies of 1 and 10 Hz. The total $SD(a^2)$ is also shown on the plot. Similarly, Figure 5.27 shows the components of the total variability in ϕ_{SS}^2 at **M**6.5 (b^2). The statistical variability in a^2 obtained from the regression is assumed to apply to b^2.

Figures 5.28 and 5.29 compare the three candidate ϕ_{SS} models for CENA as a function of magnitude: CENA constant model, CENA magnitude-dependent model, and global model at PGV and spectral periods of 0.01, 0.1, 0.2, 0.5, 1, 3, 5, 10 sec. The solid lines show the median branches for each model and the dashed lines show the 5^{th} and 95^{th} percentile branches for each model calculated assuming ϕ_{SS}^2 follows a χ-square distribution with mean and standard deviations calculated as discussed in the preceding sections. Both the global and the CENA magnitude-dependent ϕ_{SS} models are period-dependent, while the constant CENA model is period-independent. Figure 5.30 presents a comparison of the three candidate models as a function of frequency at **M**5.0, 6.0, and 7.0. Figures 5.28 and 5.29 show that for periods less than 1 sec, both CENA ϕ_{SS} models agree for magnitude less than or equal to 5.0. For longer periods, all three candidate models become magnitude-independent with the two CENA ϕ_{SS} models having comparable values. Moreover, the CENA magnitude-dependent and the global ϕ_{SS} model are comparable at periods less than 1 sec. At longer periods, the CENA magnitude dependent ϕ_{SS}

model becomes larger than the global ϕ_{SS} model because the CENA magnitude-dependent coefficient at **M**5.0 is constant while the global coefficient at **M**5.0 decreases as the period increases. Figure 5.30 shows that for **M**5.0, all three models have comparable ϕ_{SS} values at high frequencies. As magnitude increases, the two magnitude-dependent models stay comparable at high frequencies, while the constant CENA model overestimate the ϕ_{SS} values predicted by the magnitude-dependent models. Table 5.10 presents the mean ϕ_{SS} and $SD(\phi_{SS}^2)$ at the two magnitude breaks for the CENA magnitude-dependent ϕ_{SS} model.

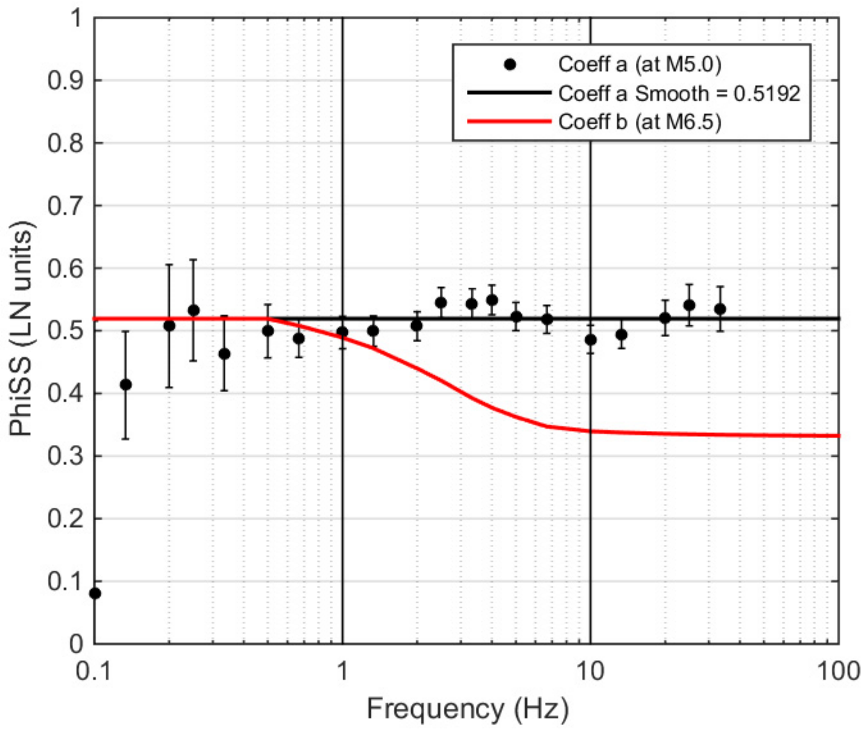

Figure 5.25 Coefficients of magnitude-dependent CENA ϕ_{SS} model.

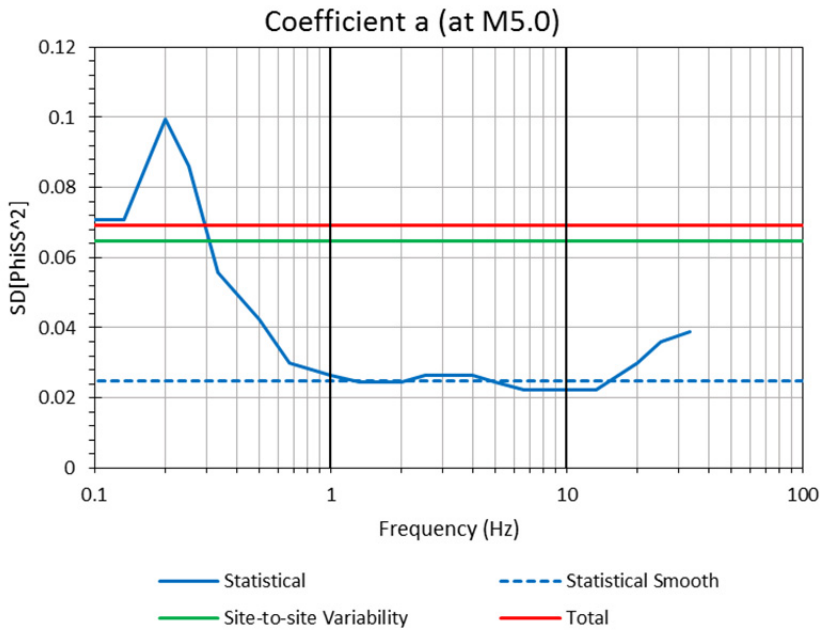

Figure 5.26 Variability in the magnitude-dependent CENA ϕ_{SS}^2 at M = 5.0 (coefficient *a*).

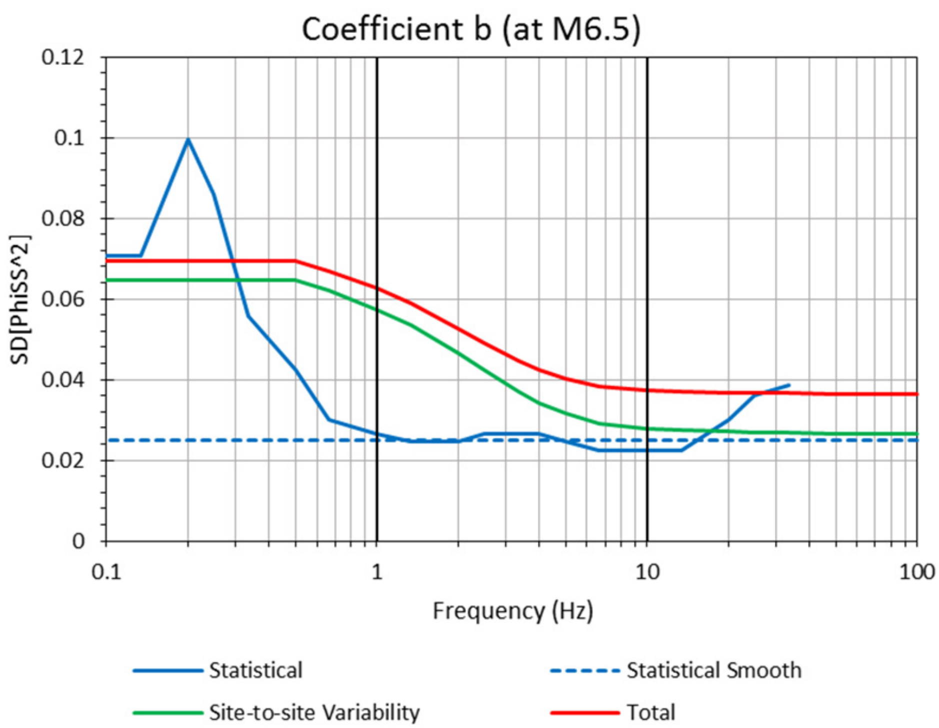

Figure 5.27 Variability in the magnitude-dependent CENA ϕ_{SS}^2 model at M = 6.5 (coefficient *b*).

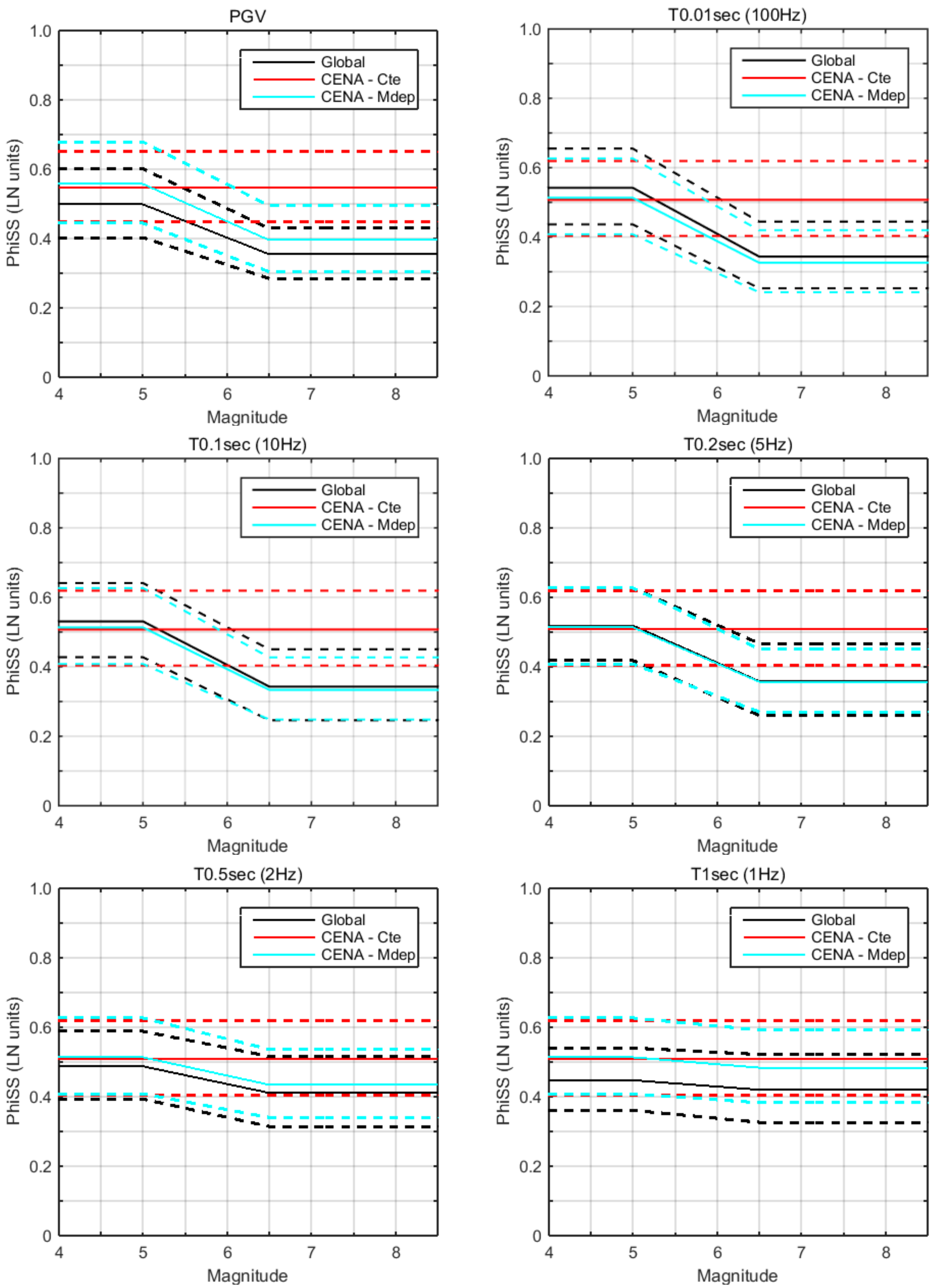

Figure 5.28 Comparison of candidate ϕ_{SS} models for CENA versus magnitude at PGV and F = 100, 10, 5, 1, and 1 Hz. Dashed lines represent the 5th and 95th percentiles of the models.

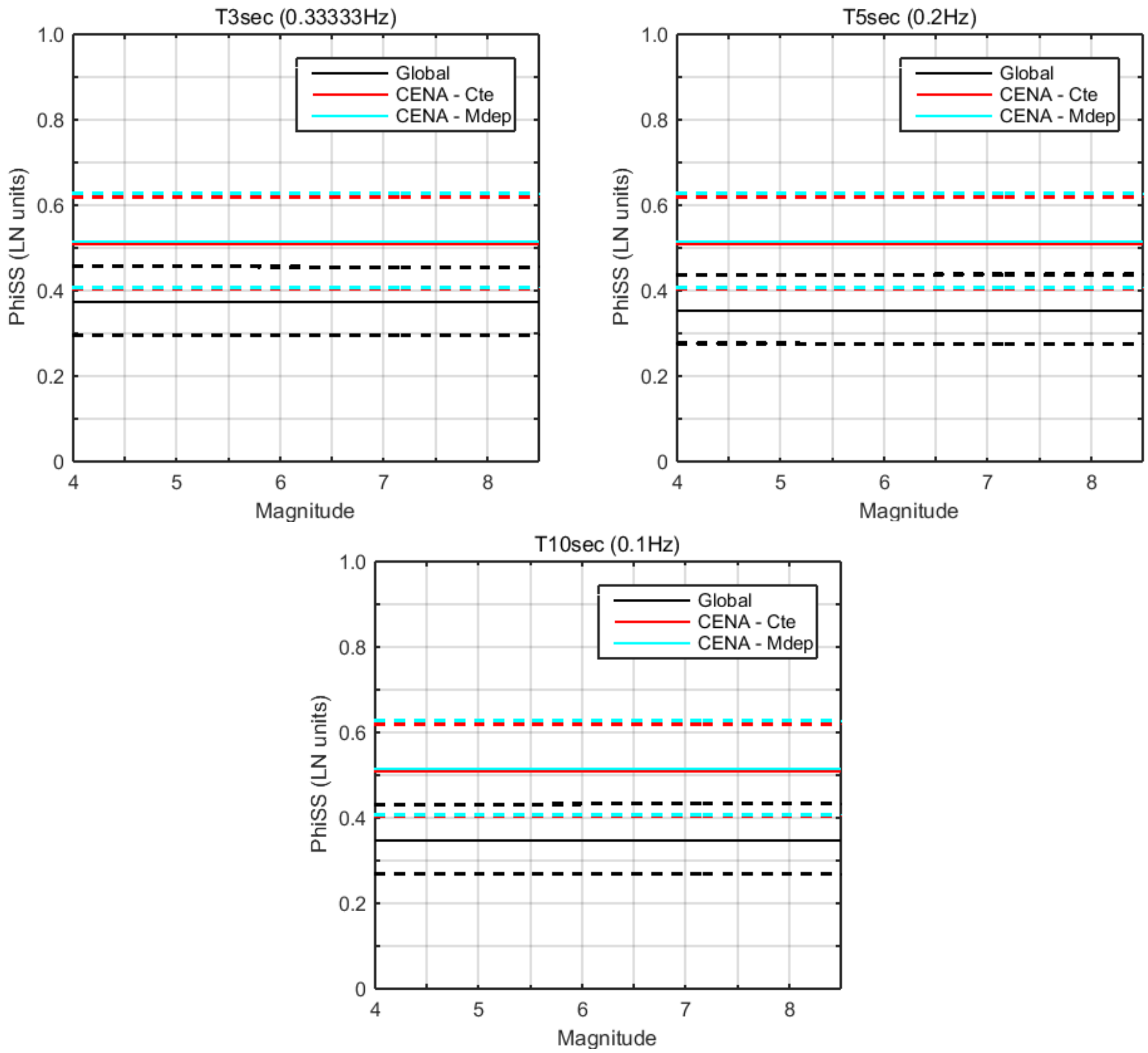

Figure 5.29 **Comparison of candidate ϕ_{SS} models for CENA versus magnitude at F = 0.33, 0.2, and 0.1 Hz. Dashed lines represent the 5th and 95th percentiles of the models.**

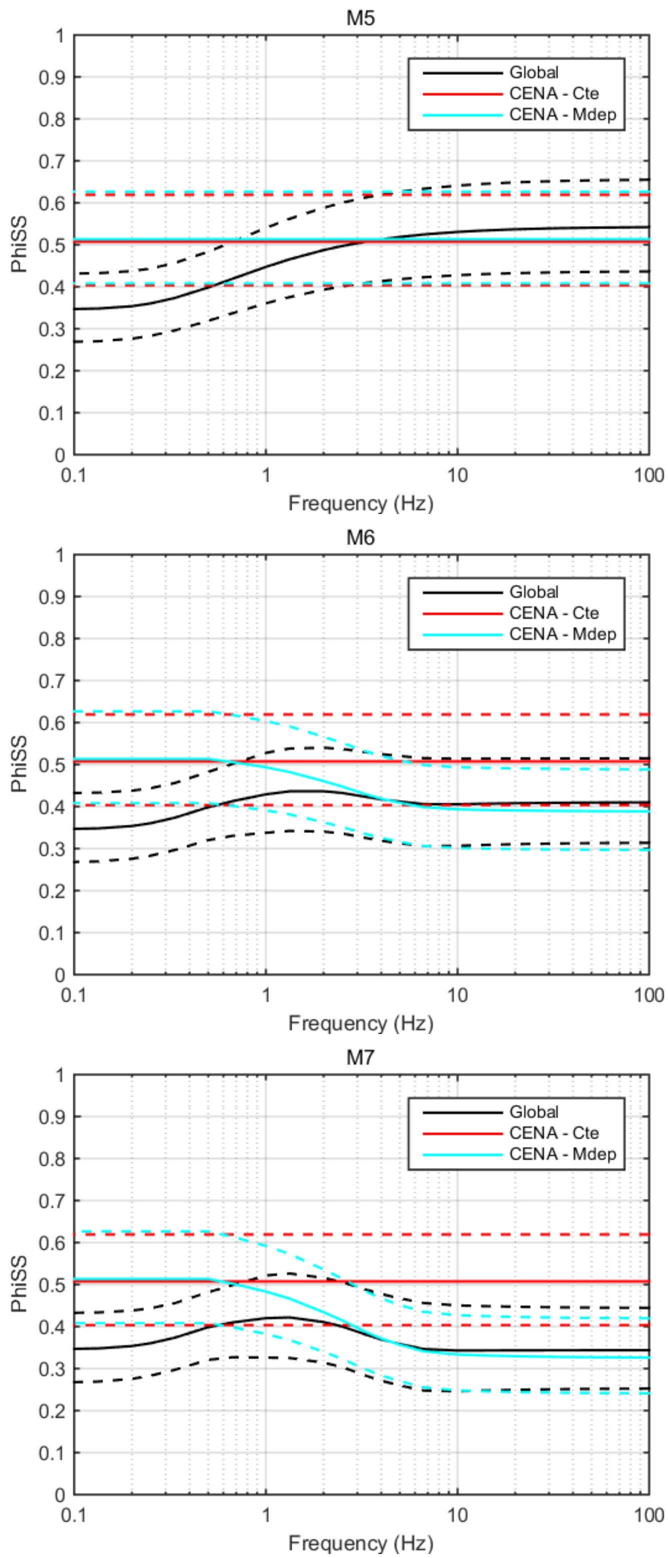

Figure 5.30 Comparison of candidate ϕ_{SS} models for CENA versus frequency for M = 5.0, 6.0, and 7.0. Dashed lines represent the 5th and 95th percentiles of the models.

Table 5.10 Mean and standard deviation of the coefficients of the CENA magnitude-dependent ϕ_{SS} model.

Period (sec)	Frequency (Hz)	Mean *a*	$SD(a^2)$	Mean b	$SD(b^2)$
0.01	100	0.5192	0.0693	0.3323	0.0364
0.02	50	0.5192	0.0693	0.3331	0.0365
0.03	33.33	0.5192	0.0693	0.3339	0.0365
0.04	25	0.5192	0.0693	0.3348	0.0367
0.05	20	0.5192	0.0693	0.3355	0.0367
0.075	13.33	0.5192	0.0693	0.3375	0.0370
0.1	10	0.5192	0.0693	0.3395	0.0372
0.15	6.67	0.5192	0.0693	0.3471	0.0382
0.2	5	0.5192	0.0693	0.3625	0.0402
0.25	4	0.5192	0.0693	0.3772	0.0423
0.3	3.33	0.5192	0.0693	0.3925	0.0446
0.4	2.5	0.5192	0.0693	0.4204	0.0492
0.5	2	0.5192	0.0693	0.4398	0.0527
0.75	1.33	0.5192	0.0693	0.4721	0.0590
1	1	0.5192	0.0693	0.4892	0.0626
1.5	0.67	0.5192	0.0693	0.5082	0.0668
2	0.5	0.5192	0.0693	0.5192	0.0693
3	0.33	0.5192	0.0693	0.5192	0.0693
4	0.25	0.5192	0.0693	0.5192	0.0693
5	0.2	0.5192	0.0693	0.5192	0.0693
7.5	0.13	0.5192	0.0693	0.5192	0.0693
10	0.1	0.5192	0.0693	0.5192	0.0693
PGV		0.5636	0.0807	0.4013	0.0468

5.3.2 Comparison to Existing Models

Tables 5.11, 5.12, and 5.13 show the values of the coefficients of the three candidate ϕ_{SS} models at PGV and spectral periods of 0.01 to 10 sec. The low, central, and high ϕ_{SS} estimates correspond to the 5th, 50th, and 95th percentile of the ϕ_{SS}^2 distribution calculated, assuming ϕ_{SS}^2 follows a χ-square distribution with mean and standard deviations calculated as discussed above.

Figure 5.31 compares the three candidate ϕ_{SS} models for CENA to the Hanford ϕ_{SS} model (central, high and low branches) at spectral periods of 0.01 and 1 sec. Recall that the Hanford model is based on the PRP data and is magnitude-dependent. Figure 5.31 shows that the Hanford ϕ_{SS} model (central, high, and low branches) is captured by the global ϕ_{SS} model. The uncertainty range of the Hanford model is smaller than that of the CENA models because the Hanford model used a coefficient of variation of ϕ_{SS} equal to 0.1 in calculating the site-to-site variability.

Figure 5.32 compares the three candidate ϕ_{SS} models for CENA to one of the SWUS ϕ_{SS} models at spectral periods of 0.01 and 1 sec. As discussed in Section 1.4.2, the SWUS project developed several ϕ_{SS} models based on the controlling sources (magnitude and distance) in their hazard results. The model presented in Figure 5.32 is magnitude-dependent with magnitude breaks at **M**5.0 and 7.0 and is derived based on the California NGA-West2 data with magnitude greater than or equal to 5.0 and distance up to 50 km. Figure 5.32 shows that all three branches of the SWUS ϕ_{SS} model are captured by the global model. The uncertainty in the SWUS model is smaller than that of the global model because the SWUS model did not include the uncertainty in the magnitude-dependent model fit to the data. This uncertainty was negligible for SWUS because the ϕ_{SS} values versus magnitude were similar for the four NGA-West2 models in the magnitude and distance range used to build their model.

Table 5.11 Coefficients of the global ϕ_{SS} model.

Period (sec)	Frequency (Hz)	Central		High		Low	
		a	*b*	*a*	*b*	*a*	*b*
0.01	100	0.5423	0.3439	0.6553	0.4446	0.4367	0.2525
0.02	50	0.5410	0.3438	0.6537	0.4452	0.4357	0.2518
0.03	33.33	0.5397	0.3437	0.6521	0.4459	0.4347	0.2510
0.04	25	0.5382	0.3436	0.6503	0.4466	0.4334	0.2503
0.05	20	0.5371	0.3435	0.6489	0.4473	0.4326	0.2496
0.075	13.33	0.5339	0.3433	0.6450	0.4489	0.4301	0.2478
0.1	10	0.5308	0.3431	0.6412	0.4505	0.4277	0.2461
0.15	6.67	0.5247	0.3466	0.6338	0.4561	0.4229	0.2478
0.2	5	0.5189	0.3585	0.6266	0.4673	0.4182	0.2600
0.25	4	0.5132	0.3694	0.6196	0.4776	0.4137	0.2712
0.3	3.33	0.5077	0.3808	0.6129	0.4879	0.4093	0.2831
0.4	2.5	0.4973	0.4004	0.6002	0.5057	0.4010	0.3037
0.5	2	0.4875	0.4109	0.5884	0.5161	0.3932	0.3142
0.75	1.33	0.4658	0.4218	0.5622	0.5264	0.3757	0.3253
1	1	0.4475	0.4201	0.5403	0.5217	0.3607	0.3263
1.5	0.67	0.4188	0.4097	0.5068	0.4985	0.3367	0.3271
2	0.5	0.3984	0.3986	0.4836	0.4818	0.3189	0.3208
3	0.33	0.3733	0.3734	0.4565	0.4556	0.2958	0.2969
4	0.25	0.3604	0.3604	0.4436	0.4437	0.2832	0.2831
5	0.2	0.3538	0.3537	0.4374	0.4381	0.2764	0.2757
7.5	0.13	0.3482	0.3481	0.4325	0.4337	0.2703	0.2691
10	0.1	0.3472	0.3471	0.4317	0.4329	0.2692	0.2679
PGV		0.4985	0.3548	0.6010	0.4296	0.4027	0.2850

Table 5.12 Coefficients of the CENA constant ϕ_{SS} model.

Period (sec)	Frequency (Hz)	Central	High	Low
0.01 to 10	0.1 to 100	0.5076	0.6192	0.4037
PGV		0.5461	0.6502	0.4483

Table 5.13 Coefficients of the CENA magnitude-dependent ϕ_{SS} model.

Period (sec)	Frequency (Hz)	Central		High		Low	
		a	***b***	***a***	***b***	***a***	***b***
0.01	100	0.5135	0.3263	0.6267	0.4198	0.4081	0.2412
0.02	50	0.5135	0.3271	0.6267	0.4206	0.4081	0.2420
0.03	33.33	0.5135	0.3279	0.6267	0.4215	0.4081	0.2427
0.04	25	0.5135	0.3288	0.6267	0.4224	0.4081	0.2436
0.05	20	0.5135	0.3296	0.6267	0.4231	0.4081	0.2443
0.075	13.33	0.5135	0.3316	0.6267	0.4252	0.4081	0.2463
0.1	10	0.5135	0.3336	0.6267	0.4272	0.4081	0.2482
0.15	6.67	0.5135	0.3413	0.6267	0.4351	0.4081	0.2555
0.2	5	0.5135	0.3569	0.6267	0.4514	0.4081	0.2702
0.25	4	0.5135	0.3717	0.6267	0.4671	0.4081	0.2839
0.3	3.33	0.5135	0.3870	0.6267	0.4837	0.4081	0.2979
0.4	2.5	0.5135	0.4150	0.6267	0.5145	0.4081	0.3230
0.5	2	0.5135	0.4344	0.6267	0.5362	0.4081	0.3401
0.75	1.33	0.5135	0.4665	0.6267	0.5726	0.4081	0.3680
1	1	0.5135	0.4836	0.6267	0.5922	0.4081	0.3827
1.5	0.67	0.5135	0.5026	0.6267	0.6141	0.4081	0.3988
2	0.5	0.5135	0.5135	0.6267	0.6267	0.4081	0.4081
3	0.33	0.5135	0.5135	0.6267	0.6267	0.4081	0.4081
4	0.25	0.5135	0.5135	0.6267	0.6267	0.4081	0.4081
5	0.2	0.5135	0.5135	0.6267	0.6267	0.4081	0.4081
7.5	0.13	0.5135	0.5135	0.6267	0.6267	0.4081	0.4081
10	0.1	0.5135	0.5135	0.6267	0.6267	0.4081	0.4081
PGV		0.5575	0.3957	0.6789	0.4950	0.4445	0.3041

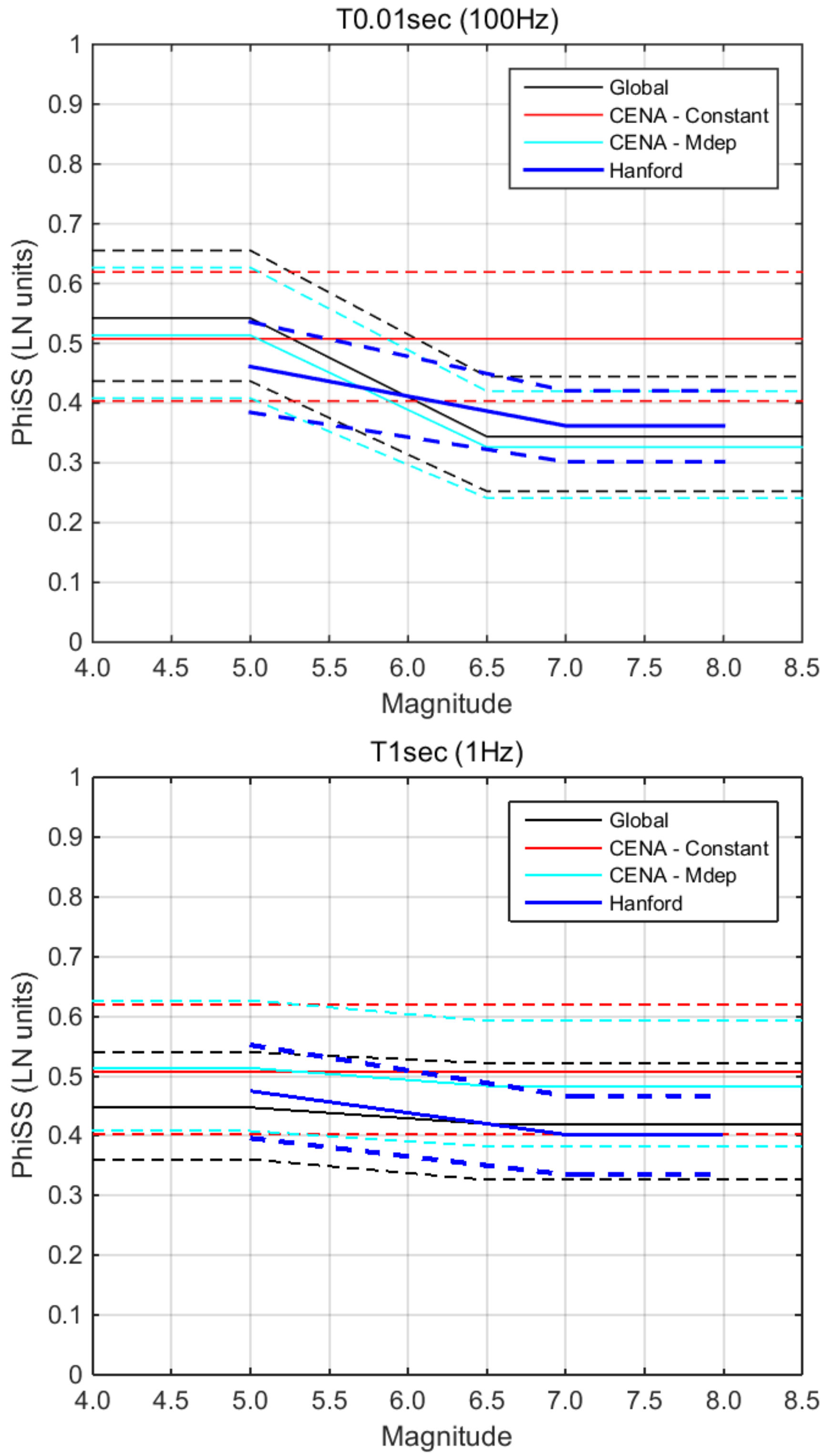

Figure 5.31 Comparison of the CENA ϕ_{SS} models to the Hanford model at *F* = 100 and 1 Hz. Dashed lines represent the 5th and 95th percentiles of the models.

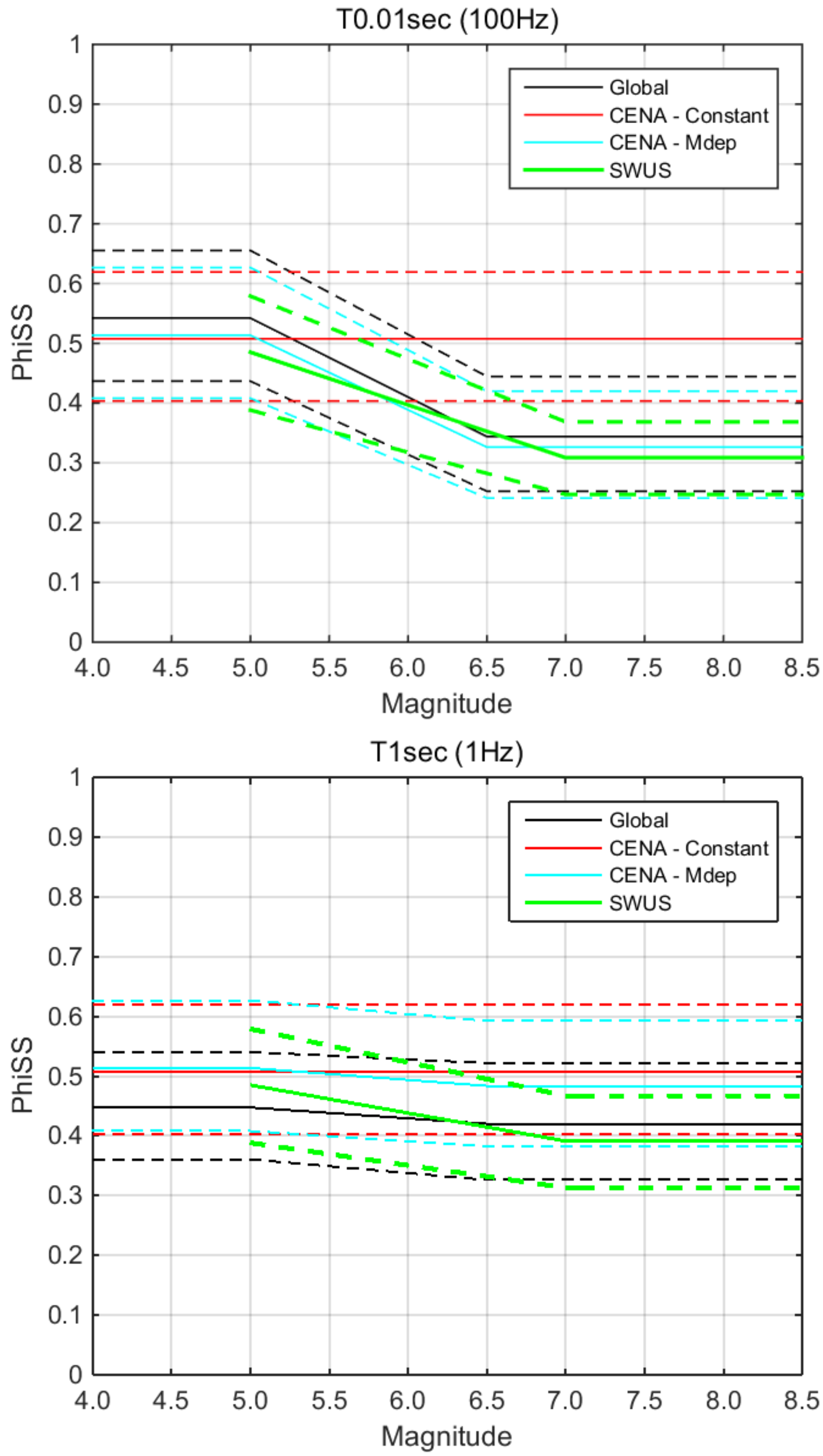

Figure 5.32 **Comparison of the CENA ϕ_{SS} models to one the SWUS magnitude-dependent ϕ_{SS} models derived from California data at F = 100 and 1 Hz. Dashed lines represent the 5th and 95th percentiles of the models.**

5.4 Φ_{S2S}

The ϕ_{S2S} values obtained from the analysis of the CENA data are relatively large compared to the corresponding values for WUS. Section 4.5 compared the CENA ϕ_{S2S} values to those for the NGA-West2 GMPEs as well as for Japanese data [Dawood and Rodriguez-Marek 2015]. These comparisons indicated that CENA ϕ_{S2S} values are comparable to Japanese $\phi_{S2S,}$ both in terms of amplitude as well as general spectral shape. Recall that Sections 4.5 and 4.6 discussed the analyses performed to investigate factors such as regression approach, PIE/tectonic events, and regional impact that could have influenced the ϕ_{S2S} results for CENA. These analyses indicated that the investigated issues are unlikely to have controlled the CENA ϕ_{S2S} results. Based on the similarity of ϕ_{S2S} for CENA and Japan, it appears that for site conditions with relatively shallow soil cover over hard rock, V_{S30} may not a good parameter for capturing the site response. This is reflected in the relatively large ϕ_{S2S} values for CENA and Japan.

Based on these factors, we propose a ϕ_{S2S} model derived from the CENA data. Models of from other regions are not adopted because the variability in the site terms is not constant across regions. Values of ϕ_{S2S} obtained from the regression analysis of all the CENA data (PIE and tectonic events) with a minimum of three recordings per station were used to derive a CENA ϕ_{S2S} model at PGV and for frequencies between 1 and 10 Hz. For frequencies less than 1 Hz, the CENA ϕ_{S2S} values were replaced by those obtained from assuming that the ratios of ϕ_{S2S} at frequencies less than 1 Hz to ϕ_{S2S} at 1 Hz observed for the Japanese data apply to CENA. Similarly, the ratios of Japanese ϕ_{S2S} at frequencies greater than 10 Hz to that at 10 Hz are used to scale the CENA ϕ_{S2S} values for frequencies greater than 10 Hz. Figure 5.33 shows the CENA ϕ_{S2S} values versus frequency between 1 and 10 Hz, the extrapolated values outside of this frequency range, as well as the smoothed ϕ_{S2S} model.

Figure 5.34 shows the variability of $\phi^2_{S2S,}$ $SD(\phi^2_{S2S})$, obtained from the regression for CENA and compared to the corresponding values for Japan. Similar to the mean ϕ_{S2S} values, the CENA $SD(\phi^2_{S2S})$, were used at PGV and for frequencies between 1 and 10 Hz. Outside of this frequency range, the $SD(\phi^2_{S2S})$ were extrapolated based on the shape of $SD(\phi^2_{S2S})$ values for Japan. Table 5.14 presents the mean ϕ_{S2S} and $SD(\phi^2_{S2S})$ for the CENA ϕ_{S2S} model. Table 5.15 presents the values of the proposed ϕ_{S2S} model for CENA whereby the central, high, and low branches are obtained by assuming that ϕ^2_{S2S} follows a scaled χ-square distribution with mean and standard deviation values shown in Figures 5.33 and 5.34.

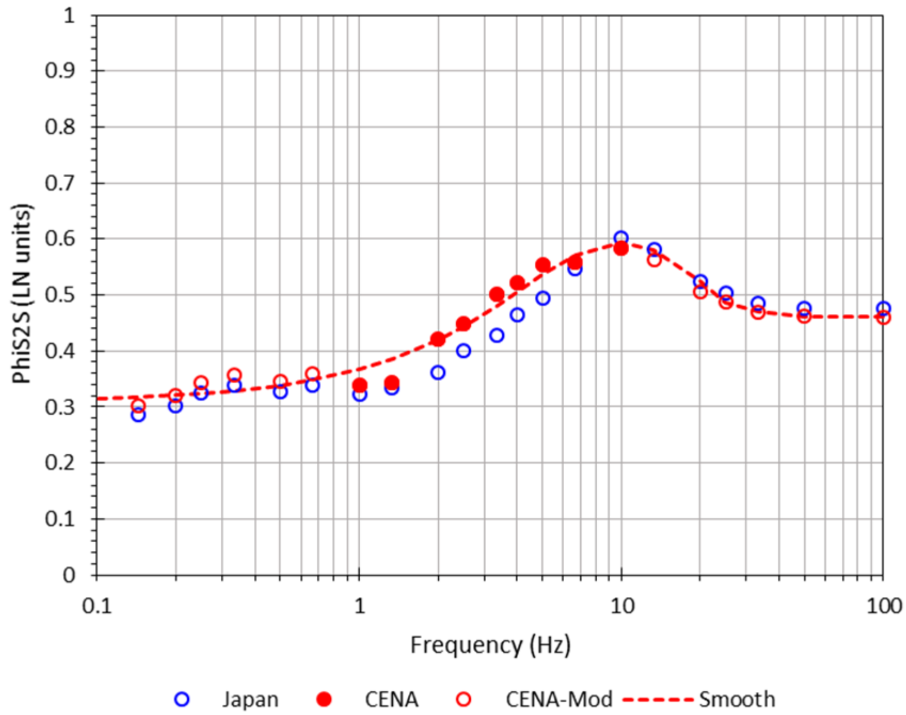

Figure 5.33 ϕ_{S2S} **mean model for CENA.**

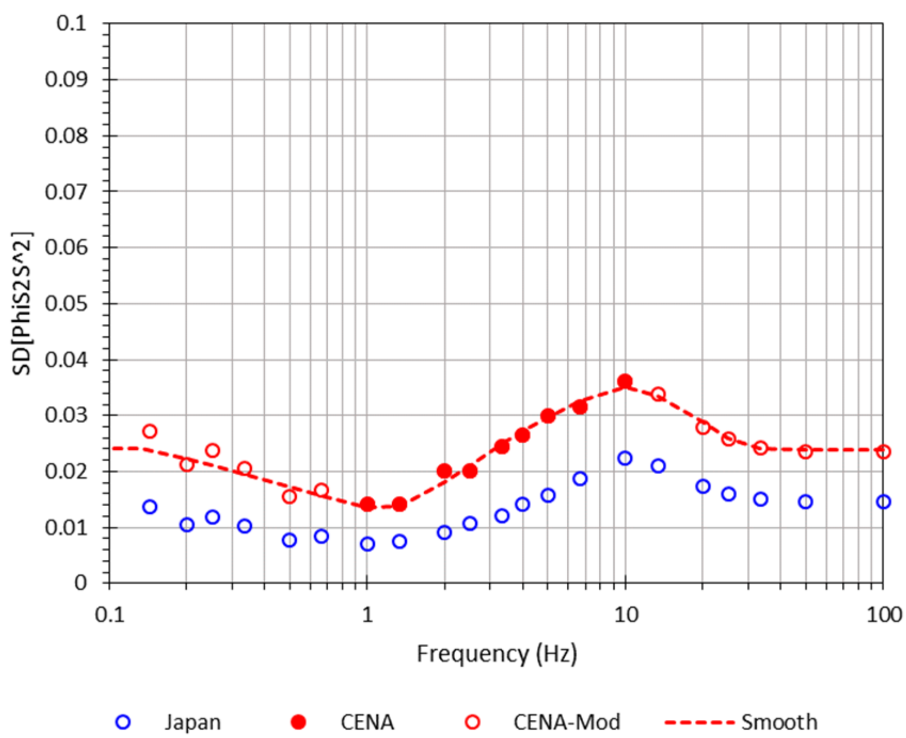

Figure 5.34 **Variability of CENA** ϕ_{S2S}^2**.**

Table 5.14 Mean and standard deviation of the CENA ϕ_{S2S} model.

Period (sec)	Frequency (Hz)	Mean	$SD(\phi_{S2S}^{2})$
0.01	100	0.4608	0.0238
0.02	50	0.4617	0.0238
0.03	33.33	0.4700	0.0240
0.04	25	0.4871	0.0260
0.05	20	0.5250	0.0290
0.075	13.33	0.5800	0.0335
0.1	10	0.5930	0.0350
0.15	6.67	0.5714	0.0325
0.2	5	0.5368	0.0296
0.25	4	0.5058	0.0272
0.3	3.33	0.4805	0.0250
0.4	2.5	0.4440	0.0212
0.5	2	0.4197	0.0182
0.75	1.33	0.3849	0.0139
1	1	0.3667	0.0135
1.5	0.67	0.3481	0.0157
2	0.5	0.3387	0.0173
3	0.33	0.3292	0.0195
4	0.25	0.3245	0.0211
5	0.2	0.3216	0.0224
7.5	0.13	0.3178	0.0240
10	0.1	0.3159	0.0240
PGV		0.4344	0.0200

Table 5.15 Central, high, and low values of the CENA ϕ_{S2S} model.

Period (sec)	Frequency (Hz)	Central	High	Low
0.01	100	0.4598	0.5030	0.4180
0.02	50	0.4607	0.5038	0.4190
0.03	33.33	0.4691	0.5117	0.4278
0.04	25	0.4861	0.5306	0.4429
0.05	20	0.5240	0.5701	0.4793
0.075	13.33	0.5790	0.6272	0.5322
0.1	10	0.5920	0.6412	0.5441
0.15	6.67	0.5705	0.6178	0.5244
0.2	5	0.5359	0.5818	0.4913
0.25	4	0.5048	0.5497	0.4613
0.3	3.33	0.4796	0.5230	0.4375
0.4	2.5	0.4431	0.4830	0.4045
0.5	2	0.4189	0.4550	0.3839
0.75	1.33	0.3843	0.4143	0.3551
1	1	0.3661	0.3968	0.3363
1.5	0.67	0.3471	0.3849	0.3107
2	0.5	0.3374	0.3803	0.2963
3	0.33	0.3275	0.3774	0.2800
4	0.25	0.3223	0.3772	0.2704
5	0.2	0.3191	0.3778	0.2638
7.5	0.13	0.3148	0.3787	0.2550
10	0.1	0.3128	0.3772	0.2527
PGV		0.4336	0.4720	0.3963

5.5 ϕ

The candidate models for CENA ϕ are derived by combining the models for ϕ_{SS} and ϕ_{S2S}. Since the computed covariance of ϕ_{SS}^2 and $\phi_{S2S}^2$is close to zero at all frequencies, ϕ^2 and $SD(\phi^2)$ can be derived as follows:

$$\phi^2 = \phi_{SS}^2 + \phi_{S2S}^2, \tag{5.12}$$

$$SD[\phi^2] = \sqrt{(SD[\phi_{SS}^2])^2 + (SD[\phi_{S2S}^2])^2} \tag{5.13}$$

where the mean and standard deviations of the ϕ_{SS}^2 and ϕ_{S2S}^2 are discussed in Sections 5.3 and 5.4, respectively.

Three candidate ϕ models are developed for CENA: (1) a global ϕ model derived by combining the CENA ϕ_{S2S} model and the global ϕ_{SS} model; (2) a CENA constant ϕ model derived by combining the CENA ϕ_{S2S} model and the CENA constant ϕ_{SS} model; and (3) a CENA magnitude-dependent ϕ model derived by combining the CENA ϕ_{S2S} model and the CENA magnitude-dependent ϕ_{SS} model. The magnitude-dependent global and CENA ϕ models have the following form:

$$\phi = \begin{cases} a & for\ M \leq 5.0 \\ a + (M - 5.0) * \frac{(b-a)}{1.5} & for\ M \leq 6.5 \\ b & for\ M > 6.5 \end{cases} \tag{5.14}$$

where coefficients a and b for the central, high, and low branches of the global model, and the CENA magnitude-dependent models are given in Tables 5.16 and 5.17, respectively. The values of the CENA constant ϕ model are given in Table 5.18.

Figures 5.35 and 5.36 show the three candidate ϕ models for CENA as a function of magnitude: CENA constant model, CENA magnitude-dependent model, and global model at PGV and spectral periods of 0.01, 0.1, 0.2, 0.5, 1, 3, 5, 10 sec. The solid lines show the median branches for each model, and the dashed lines show the 5th and 95th percentile branches for each model calculated, assuming ϕ^2 follows a χ-square distribution with mean and standard deviations calculated as discussed above. Similar to the observations made for the ϕ_{SS} models, Figures 5.35 and 5.36 show that the CENA constant and magnitude-dependent models are similar for **M** < 5.0. For larger magnitudes, the CENA constant model is larger than the two magnitude-dependent models. For periods longer than 1 sec, all models are magnitude-independent. Figure 5.37 shows the three candidate ϕ models for CENA versus frequency for **M**5.0, 6.0, and 7.0. For **M**5.0, the two CENA models are comparable. For **M** > 5.0, the two CENA models are similar at low frequencies, while the two magnitude-dependent models are comparable at high frequencies. Figure 5.38 compares the three candidate ϕ models for CENA as a function of frequency to the NGA-West2 ϕ models for **M**5.0, 6.0, and 7.0. For the global ϕ model and the NGA-West2 ϕ models, the main difference lies in the difference in ϕ_{S2S} between CENA and WUS. Therefore, Figure 5.38 shows that NGA-West2 ϕ values are larger than the global CENA ϕ values at low frequencies because WUS ϕ_{S2S} is larger than CENA ϕ_{S2S} at low frequencies, as shown in Figure 4.46. At high frequencies, the opposite trend is observed.

Table 5.16 Coefficients of the global ϕ model.

Period (sec)	Frequency (Hz)	Central		High		Low	
		a	***b***	***a***	***b***	***a***	***b***
0.01	100	0.7131	0.5770	0.8031	0.6459	0.6267	0.5108
0.02	50	0.7126	0.5777	0.8023	0.6469	0.6266	0.5112
0.03	33.33	0.7171	0.5844	0.8059	0.6533	0.6320	0.5181
0.04	25	0.7274	0.5982	0.8152	0.6673	0.6430	0.5317
0.05	20	0.7526	0.6295	0.8382	0.6976	0.6701	0.5638
0.075	13.33	0.7899	0.6761	0.8725	0.7435	0.7101	0.6109
0.1	10	0.7974	0.6872	0.8791	0.7553	0.7184	0.6213
0.15	6.67	0.7773	0.6706	0.8583	0.7399	0.6990	0.6037
0.2	5	0.7481	0.6478	0.8294	0.7187	0.6697	0.5794
0.25	4	0.7220	0.6286	0.8036	0.7013	0.6434	0.5585
0.3	3.33	0.7005	0.6152	0.7820	0.6894	0.6220	0.5440
0.4	2.5	0.6680	0.5998	0.7488	0.6758	0.5904	0.5269
0.5	2	0.6446	0.5893	0.7241	0.6666	0.5682	0.5151
0.75	1.33	0.6055	0.5728	0.6818	0.6521	0.5324	0.4970
1	1	0.5797	0.5593	0.6537	0.6379	0.5088	0.4842
1.5	0.67	0.5457	0.5388	0.6171	0.6103	0.4773	0.4703
2	0.5	0.5239	0.5240	0.5941	0.5928	0.4567	0.4580
3	0.33	0.4986	0.4986	0.5688	0.5682	0.4315	0.4322
4	0.25	0.4857	0.4857	0.5572	0.5573	0.4176	0.4176
5	0.2	0.4789	0.4789	0.5518	0.5523	0.4095	0.4091
7.5	0.13	0.4721	0.4720	0.5473	0.5480	0.4007	0.3999
10	0.1	0.4700	0.4700	0.5455	0.5463	0.3984	0.3976
PGV		0.6626	0.5619	0.7434	0.6174	0.5850	0.5082

Table 5.17 Coefficients of the CENA magnitude-dependent ϕ model.

Period (sec)	Frequency (Hz)	Central		High		Low	
		a	***b***	***a***	***b***	***a***	***a***
0.01	100	0.6915	0.5664	0.7800	0.6304	0.6066	0.5047
0.02	50	0.6921	0.5676	0.7806	0.6316	0.6073	0.5059
0.03	33.33	0.6978	0.5749	0.7856	0.6383	0.6135	0.5138
0.04	25	0.7094	0.5894	0.7965	0.6530	0.6257	0.5281
0.05	20	0.7360	0.6216	0.8212	0.6843	0.6540	0.5609
0.075	13.33	0.7764	0.6697	0.8590	0.7317	0.6965	0.6095
0.1	10	0.7861	0.6819	0.8684	0.7443	0.7066	0.6214
0.15	6.67	0.7699	0.6672	0.8529	0.7297	0.6899	0.6065
0.2	5	0.7446	0.6463	0.8290	0.7106	0.6632	0.5840
0.25	4	0.7224	0.6293	0.8085	0.6959	0.6397	0.5650
0.3	3.33	0.7049	0.6186	0.7922	0.6875	0.6211	0.5522
0.4	2.5	0.6804	0.6094	0.7694	0.6828	0.5952	0.5389
0.5	2	0.6647	0.6056	0.7548	0.6825	0.5786	0.5319
0.75	1.33	0.6432	0.6064	0.7351	0.6899	0.5556	0.5266
1	1	0.6324	0.6084	0.7258	0.6964	0.5434	0.5244
1.5	0.67	0.6217	0.6127	0.7173	0.7064	0.5307	0.5235
2	0.5	0.6164	0.6164	0.7134	0.7134	0.5242	0.5242
3	0.33	0.6111	0.6111	0.7097	0.7097	0.5175	0.5175
4	0.25	0.6084	0.6084	0.7082	0.7082	0.5140	0.5139
5	0.2	0.6069	0.6069	0.7074	0.7074	0.5117	0.5117
7.5	0.13	0.6048	0.6048	0.7063	0.7063	0.5086	0.5086
10	0.1	0.6037	0.6037	0.7055	0.7055	0.5075	0.5075
PGV		0.7084	0.5893	0.8065	0.6615	0.6146	0.5200

Table 5.18 Coefficients of the CENA constant ϕ model.

Period (sec)	Frequency (Hz)	Central	High	Low
0.01	100	0.6871	0.7742	0.6036
0.02	50	0.6877	0.7747	0.6043
0.03	33.33	0.6934	0.7797	0.6105
0.04	25	0.7051	0.7908	0.6227
0.05	20	0.7319	0.8157	0.6512
0.075	13.33	0.7724	0.8538	0.6938
0.1	10	0.7822	0.8633	0.7039
0.15	6.67	0.7660	0.8476	0.6872
0.2	5	0.7405	0.8235	0.6604
0.25	4	0.7182	0.8028	0.6368
0.3	3.33	0.7006	0.7864	0.6181
0.4	2.5	0.6759	0.7634	0.5921
0.5	2	0.6601	0.7487	0.5754
0.75	1.33	0.6385	0.7288	0.5523
1	1	0.6276	0.7194	0.5401
1.5	0.67	0.6168	0.7108	0.5273
2	0.5	0.6114	0.7068	0.5207
3	0.33	0.6061	0.7032	0.5140
4	0.25	0.6034	0.7016	0.5104
5	0.2	0.6018	0.7008	0.5081
7.5	0.13	0.5997	0.6998	0.5050
10	0.1	0.5987	0.6990	0.5038
PGV		0.6990	0.7834	0.6179

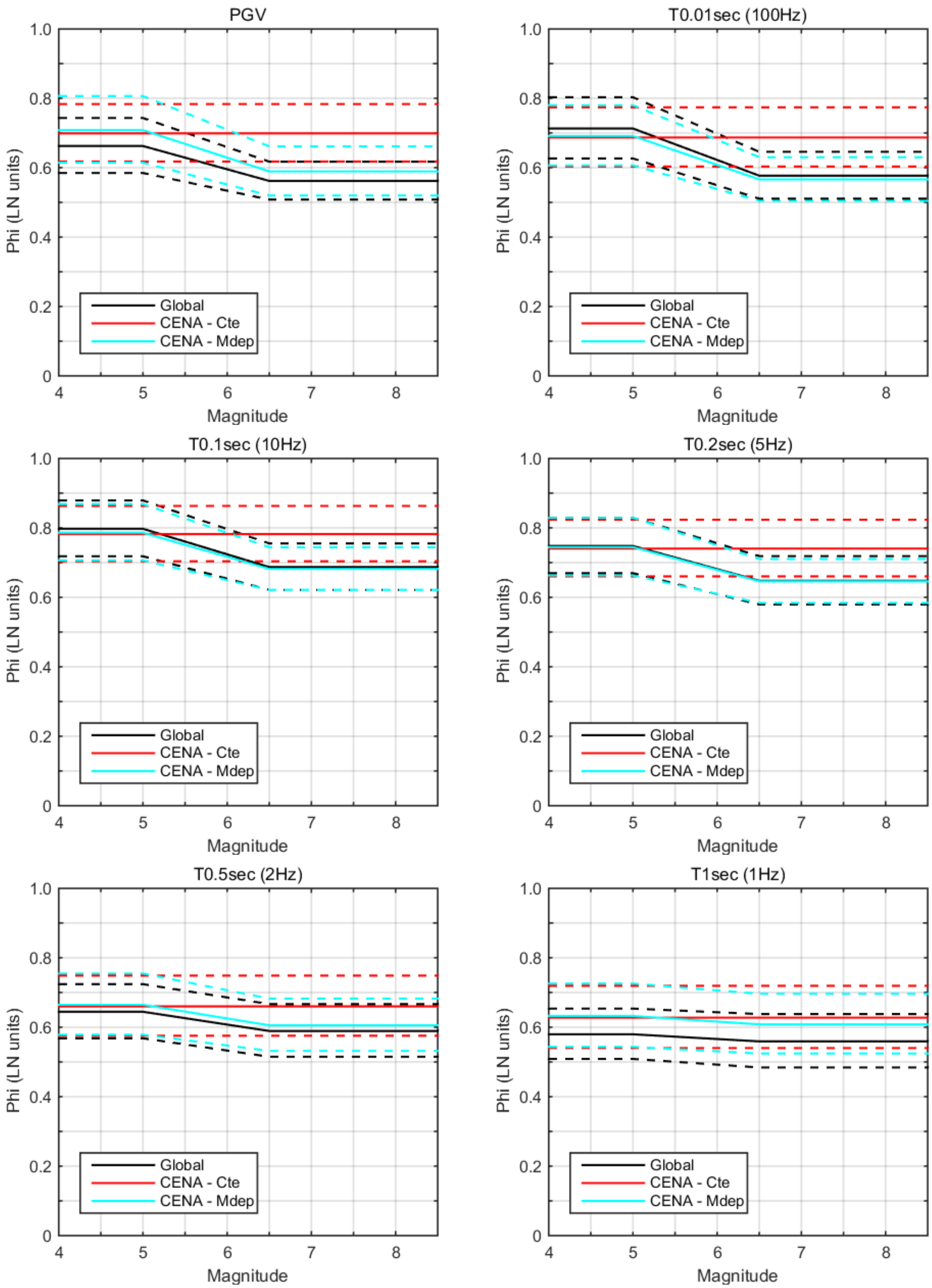

Figure 5.35 Comparison of ϕ models for CENA versus magnitude at PGV and F = 100, 10, 5, 2, and 1 Hz. Dashed lines represent the 5th and 95th percentiles of the models.

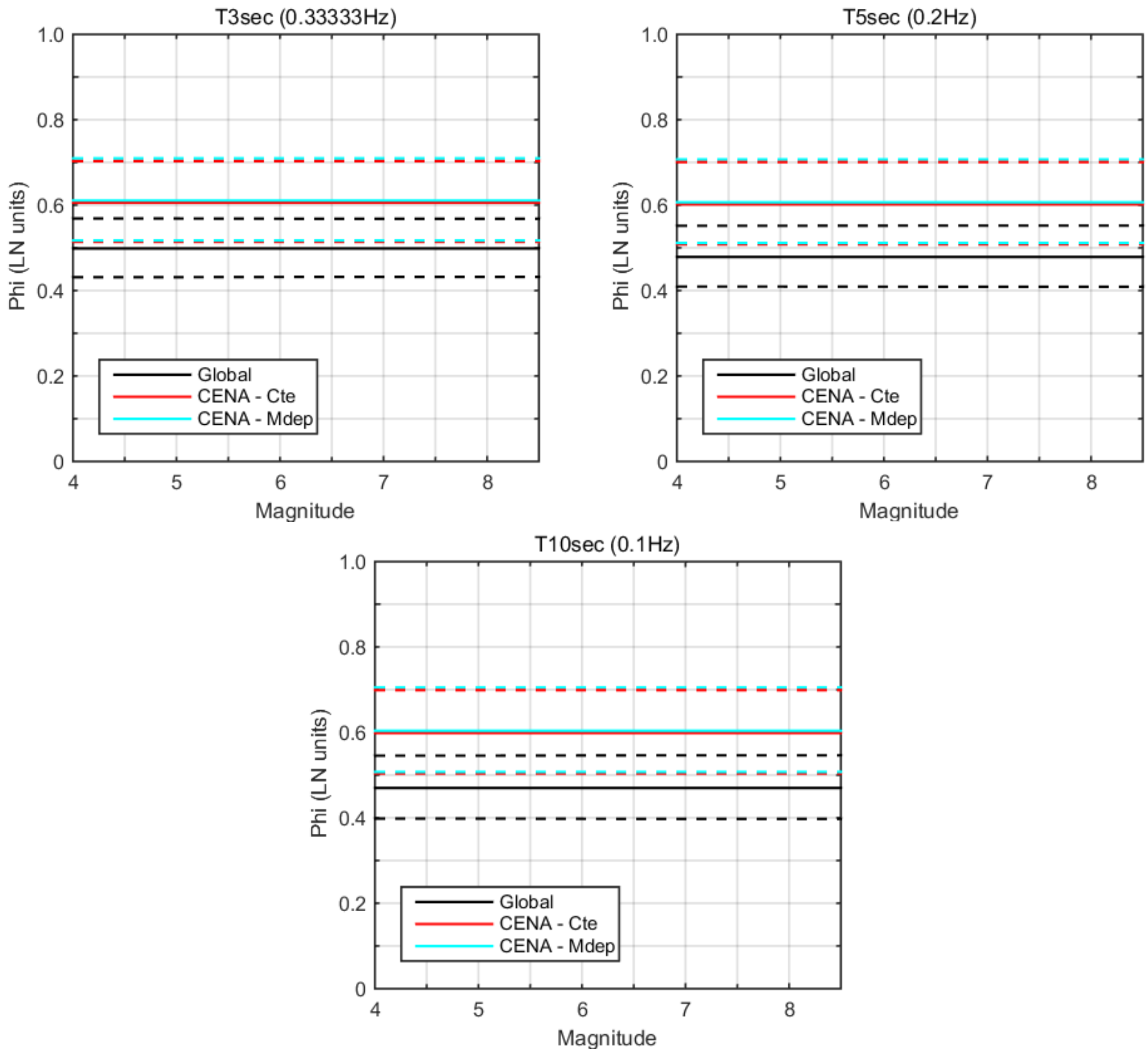

Figure 5.36 Comparison of ϕ models for CENA versus magnitude at F = 0.33, 0.2, and 0.1 Hz. Dashed lines represent the 5th and 95th percentiles of the models.

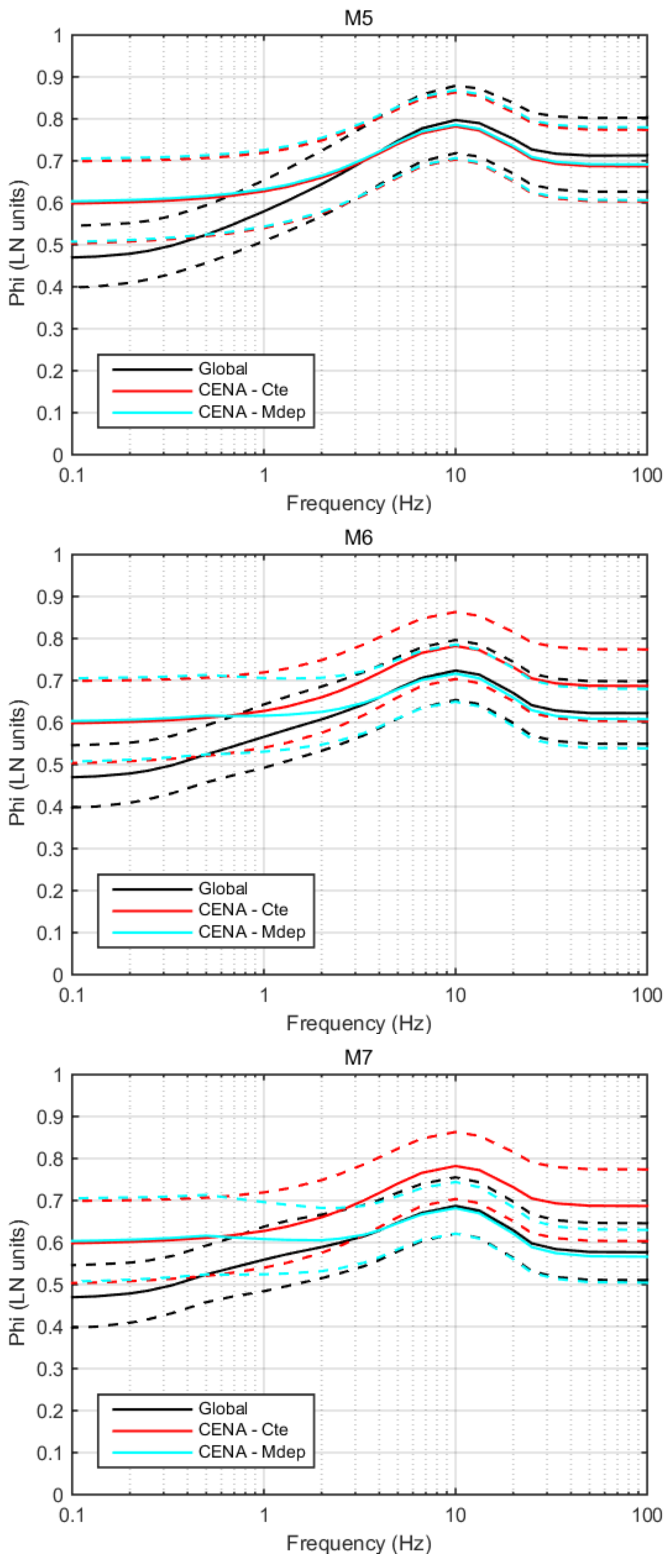

Figure 5.37 **Comparison of ϕ models for CENA versus frequency for M = 5.0, 6.0, and 7.0. Dashed lines represent the 5th and 95th percentiles of the models.**

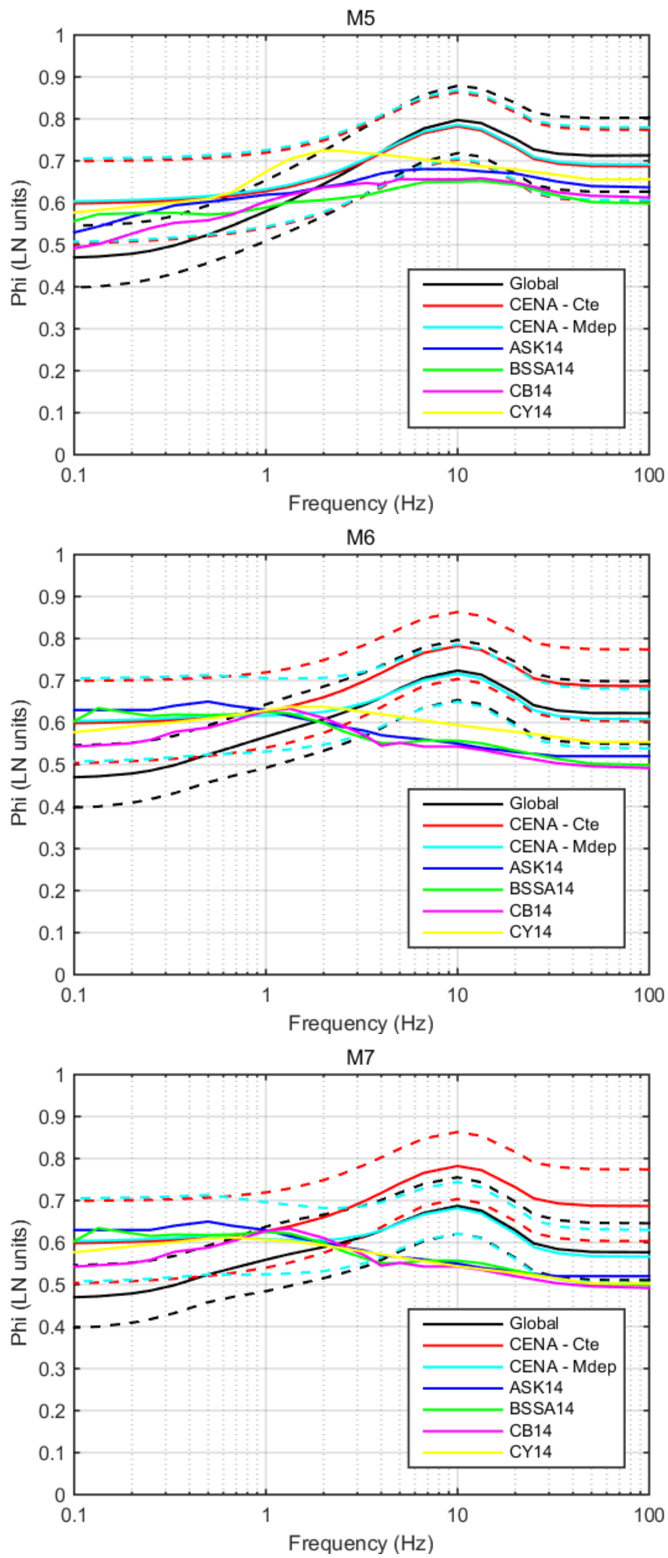

Figure 5.38 Comparison of ϕ models for CENA and NGA-West2 versus frequency for M = 5.0, 6.0, and 7.0. Dashed lines represent the 5th and 95th percentiles of the CENA models.

5.6 SINGLE-STATION σ

The models for CENA σ_{SS} are derived by combining the models for ϕ_{SS} and τ, whereby the mean σ_{SS}^2 and $SD(\sigma_{SS}^2)$ are derived as follows:

$$\sigma_{SS}^2 = \phi_{SS}^2 + \tau^2, \tag{5.15}$$

$$SD[\sigma_{SS}^2] = \sqrt{(SD[\phi_{SS}^2])^2 + (SD[\tau^2])^2} \tag{5.16}$$

The equations above are based on the assumption that ϕ_{SS} and τ are statistically independent, which is justified based on the regression results that show very weak to no correlation between ϕ and τ and between ϕ_{SS} and ϕ_{S2S}. The mean and standard deviations of the ϕ_{SS}^2 and τ^2 are discussed in Sections 5.3 and 5.2, respectively.

Combining the three candidate τ and ϕ_{SS} models results in nine candidate σ_{SS} models. One of the candidate σ_{SS} models is magnitude-independent resulting from combining the CENA constant τ model with the CENA constant ϕ_{SS} model, while the rest of the models are magnitude-dependent with two to four magnitude breaks. Values of all nine candidate σ_{SS} models are not presented here but can be easily obtained by the reader. The mean and standard deviation values of the nine candidate σ_{SS} models can be obtained using Equations (5.15) and (5.16) along with the mean and standard deviations of ϕ_{SS}^2 and τ^2 given in the tables in Sections 5.3 and 5.2. Moreover, the central, high and low estimates of the nine candidate σ_{SS} models can be obtained by assuming that σ_{SS}^2 follows a scaled χ-square distribution, as described in Section 5.1.1.

Three candidate σ_{SS} models are presented here as an example: (1) global σ_{SS} model derived by combining the global ϕ_{SS} model and the global τ model; (2) CENA σ_{SS} model-1 derived by combining the CENA constant ϕ_{SS} model and the global τ model; and (3) CENA σ_{SS} model-2 resulting from combining the CENA magnitude-dependent ϕ_{SS} model and the global τ model. Because the global τ model is magnitude-dependent with four magnitude breaks, all three σ_{SS} models are also magnitude-dependent and have the following form:

$$\sigma_{SS} = \begin{cases} \sigma_{SS_1} & for\ M \leq 4.5 \\ \sigma_{SS_1} + \left(\sigma_{SS_2} - \sigma_{SS_1}\right) * \frac{(M-4.5)}{0.5} & for\ M \leq 5.0 \\ \sigma_{SS_2} + \left(\sigma_{SS_3} - \sigma_{SS_2}\right) * \frac{(M-5.0)}{0.5} & for\ M \leq 5.5 \\ \sigma_{SS_3} + \left(\sigma_{SS_4} - \sigma_{SS_3}\right) * \frac{(M-5.5)}{1.0} & for\ M \leq 6.5 \\ \sigma_{SS_4} & for\ M > 6.5 \end{cases} \tag{5.17}$$

The four coefficients for the central, high, and low branches of these three candidate σ_{SS} models are given in Tables 5.19, 5.20, and 5.21 for the global model, CENA model-1and CENA model-2, respectively. Figures 5.39 and 5.40 show the three candidate σ_{SS} models for CENA as a function of magnitude at PGV and spectral periods of 0.01, 0.1, 0.2, 0.5, 1, 3, 5, 10 sec. The solid lines show the median branches for each model, and the dashed lines show the 5th and 95th percentile branches for each model calculated, assuming σ_{SS}^2 follows a χ-square distribution with mean and standard deviations calculated, as discussed above. Figure 5.41 shows the three σ_{SS} models for CENA as a function of frequency for **M**5.0, 6.0, and 7.0.

Figures 5.39 through 5.41 indicate that at **M**5.0, the two CENA models are comparable. At larger magnitudes, the two CENA models are only comparable at low frequencies. At high frequencies, the CENA model-2 σ_{SS} agrees with the global σ_{SS} and smaller than σ_{SS} for the CENA model-1. Figure 5.42 compares the three σ_{SS} models for CENA to the Hanford σ_{SS} model (central, high, and low branches) versus frequency for **M**5.0, 6.0, and 7.0. Figure 5.42 shows that the Hanford model falls within the range of the three candidate σ_{SS} models for CENA.

Table 5.19 Coefficients of the global single-station σ model resulting from combining the global ϕ_{SS} model and the global τ model.

Period (sec)	Frequency (Hz)	Central				High				Low			
		σ_{SS1}	σ_{SS2}	σ_{SS3}	σ_{SS4}	σ_{SS1}	σ_{SS2}	σ_{SS3}	σ_{SS4}	σ_{SS1}	σ_{SS2}	σ_{SS3}	σ_{SS4}
0.01	100	0.7054	0.6895	0.6122	0.4903	0.8232	0.8114	0.7322	0.6000	0.5939	0.5744	0.4998	0.3884
0.02	50	0.7044	0.6884	0.6115	0.4903	0.8220	0.8102	0.7315	0.6003	0.5930	0.5735	0.4990	0.3880
0.03	33.33	0.7034	0.6874	0.6109	0.4902	0.8208	0.8090	0.7309	0.6006	0.5922	0.5726	0.4983	0.3877
0.04	25	0.7023	0.6862	0.6101	0.4902	0.8196	0.8077	0.7301	0.6009	0.5912	0.5716	0.4975	0.3873
0.05	20	0.7014	0.6853	0.6095	0.4902	0.8185	0.8067	0.7296	0.6013	0.5905	0.5708	0.4969	0.3870
0.075	13.33	0.6989	0.6828	0.6078	0.4901	0.8157	0.8039	0.7280	0.6020	0.5884	0.5687	0.4951	0.3862
0.1	10	0.6965	0.6804	0.6061	0.4900	0.8130	0.8011	0.7265	0.6028	0.5863	0.5665	0.4934	0.3854
0.15	6.67	0.6919	0.6756	0.6039	0.4926	0.8077	0.7957	0.7244	0.6063	0.5822	0.5623	0.4911	0.3871
0.2	5	0.6874	0.6710	0.6038	0.5010	0.8026	0.7906	0.7243	0.6142	0.5783	0.5582	0.4910	0.3959
0.25	4	0.6831	0.6666	0.6036	0.5089	0.7977	0.7856	0.7241	0.6216	0.5745	0.5543	0.4908	0.4041
0.3	3.33	0.6789	0.6623	0.6036	0.5172	0.7930	0.7809	0.7241	0.6292	0.5709	0.5505	0.4908	0.4128
0.4	2.5	0.6710	0.6542	0.6031	0.5317	0.7843	0.7720	0.7236	0.6425	0.5639	0.5432	0.4902	0.4282
0.5	2	0.6638	0.6468	0.6006	0.5398	0.7762	0.7638	0.7213	0.6503	0.5574	0.5364	0.4877	0.4364
0.75	1.33	0.6478	0.6304	0.5920	0.5480	0.7588	0.7462	0.7133	0.6581	0.5429	0.5213	0.4787	0.4450
1	1	0.6346	0.6167	0.5820	0.5467	0.7447	0.7319	0.7040	0.6551	0.5305	0.5084	0.4682	0.4451
1.5	0.67	0.6145	0.5960	0.5646	0.5383	0.7238	0.7108	0.6878	0.6402	0.5113	0.4883	0.4498	0.4425
2	0.5	0.6005	0.5816	0.5515	0.5296	0.7099	0.6966	0.6758	0.6294	0.4975	0.4738	0.4361	0.4358
3	0.33	0.5840	0.5645	0.5334	0.5108	0.6940	0.6805	0.6592	0.6112	0.4805	0.4560	0.4169	0.4166
4	0.25	0.5758	0.5559	0.5244	0.5013	0.6865	0.6729	0.6510	0.6029	0.4718	0.4468	0.4074	0.4063
5	0.2	0.5716	0.5517	0.5198	0.4966	0.6828	0.6692	0.6469	0.5989	0.4673	0.4421	0.4026	0.4009
7.5	0.13	0.5682	0.5481	0.5161	0.4926	0.6799	0.6662	0.6435	0.5957	0.4635	0.4381	0.3986	0.3963
10	0.1	0.5676	0.5474	0.5154	0.4919	0.6794	0.6656	0.6428	0.5952	0.4628	0.4373	0.3978	0.3955
PGV		0.6221	0.6164	0.5654	0.4785	0.7333	0.7284	0.6725	0.5747	0.5171	0.5109	0.4648	0.3883

Table 5.20 Coefficients of the CENA single-station σ model-1 resulting from combining the CENA constant ϕ_{SS} model and the global τ model.

Period (sec)	Frequency (Hz)	Central				High				Low			
		σ_{SS1}	σ_{SS2}	σ_{SS3}	σ_{SS4}	σ_{SS1}	σ_{SS2}	σ_{SS3}	σ_{SS4}	σ_{SS1}	σ_{SS2}	σ_{SS3}	σ_{SS4}
0.01 to 10	0.1 to 100	0.6790	0.6624	0.6367	0.6168	0.7965	0.7843	0.7611	0.7302	0.5680	0.5476	0.5200	0.5100
PGV		0.6609	0.6556	0.6448	0.6345	0.7722	0.7675	0.7524	0.7418	0.5556	0.5498	0.5429	0.5330

Table 5.21 **Coefficients of the CENA single-station σ model-2 resulting from combining the CENA magnitude-dependent ϕ_{SS} model and the global τ model.**

Period (sec)	Frequency (Hz)	Central				High				Low			
		σ_{SS1}	σ_{SS2}	σ_{SS3}	σ_{SS4}	σ_{SS1}	σ_{SS2}	σ_{SS3}	σ_{SS4}	σ_{SS1}	σ_{SS2}	σ_{SS3}	σ_{SS4}
0.01	100	0.6835	0.6670	0.5922	0.4777	0.8017	0.7897	0.7182	0.5850	0.5718	0.5515	0.4746	0.3780
0.02	50	0.6835	0.6670	0.5924	0.4783	0.8017	0.7897	0.7184	0.5855	0.5718	0.5515	0.4748	0.3786
0.03	33.33	0.6835	0.6670	0.5926	0.4788	0.8017	0.7897	0.7186	0.5860	0.5718	0.5515	0.4750	0.3792
0.04	25	0.6835	0.6670	0.5928	0.4795	0.8017	0.7897	0.7188	0.5866	0.5718	0.5515	0.4753	0.3798
0.05	20	0.6835	0.6670	0.5930	0.4799	0.8017	0.7897	0.7190	0.5871	0.5718	0.5515	0.4755	0.3803
0.075	13.33	0.6835	0.6670	0.5935	0.4813	0.8017	0.7897	0.7195	0.5884	0.5718	0.5515	0.4760	0.3818
0.1	10	0.6835	0.6670	0.5940	0.4827	0.8017	0.7897	0.7199	0.5898	0.5718	0.5515	0.4765	0.3832
0.15	6.67	0.6835	0.6670	0.5960	0.4881	0.8017	0.7897	0.7218	0.5950	0.5718	0.5515	0.4786	0.3887
0.2	5	0.6835	0.6670	0.6000	0.4992	0.8017	0.7897	0.7256	0.6058	0.5718	0.5515	0.4827	0.3999
0.25	4	0.6835	0.6670	0.6038	0.5100	0.8017	0.7897	0.7292	0.6165	0.5718	0.5515	0.4867	0.4105
0.3	3.33	0.6835	0.6670	0.6078	0.5214	0.8017	0.7897	0.7330	0.6280	0.5718	0.5515	0.4908	0.4217
0.4	2.5	0.6835	0.6670	0.6152	0.5427	0.8017	0.7897	0.7400	0.6500	0.5718	0.5515	0.4984	0.4420
0.5	2	0.6835	0.6670	0.6204	0.5577	0.8017	0.7897	0.7449	0.6660	0.5718	0.5515	0.5037	0.4562
0.75	1.33	0.6835	0.6670	0.6289	0.5833	0.8017	0.7897	0.7531	0.6936	0.5718	0.5515	0.5125	0.4797
1	1	0.6835	0.6670	0.6335	0.5971	0.8017	0.7897	0.7575	0.7087	0.5718	0.5515	0.5173	0.4921
1.5	0.67	0.6835	0.6670	0.6387	0.6127	0.8017	0.7897	0.7624	0.7261	0.5718	0.5515	0.5226	0.5060
2	0.5	0.6835	0.6670	0.6416	0.6217	0.8017	0.7897	0.7652	0.7362	0.5718	0.5515	0.5256	0.5139
3	0.33	0.6835	0.6670	0.6416	0.6217	0.8017	0.7897	0.7652	0.7362	0.5718	0.5515	0.5256	0.5139
4	0.25	0.6835	0.6670	0.6416	0.6217	0.8017	0.7897	0.7652	0.7362	0.5718	0.5515	0.5256	0.5139
5	0.2	0.6835	0.6670	0.6416	0.6217	0.8017	0.7897	0.7652	0.7362	0.5718	0.5515	0.5256	0.5139
7.5	0.13	0.6835	0.6670	0.6416	0.6217	0.8017	0.7897	0.7652	0.7362	0.5718	0.5515	0.5256	0.5139
10	0.1	0.6835	0.6670	0.6416	0.6217	0.8017	0.7897	0.7652	0.7362	0.5718	0.5515	0.5256	0.5139
PGV		0.6708	0.6656	0.6096	0.5104	0.7934	0.7888	0.7220	0.6170	0.5554	0.5496	0.5038	0.4109

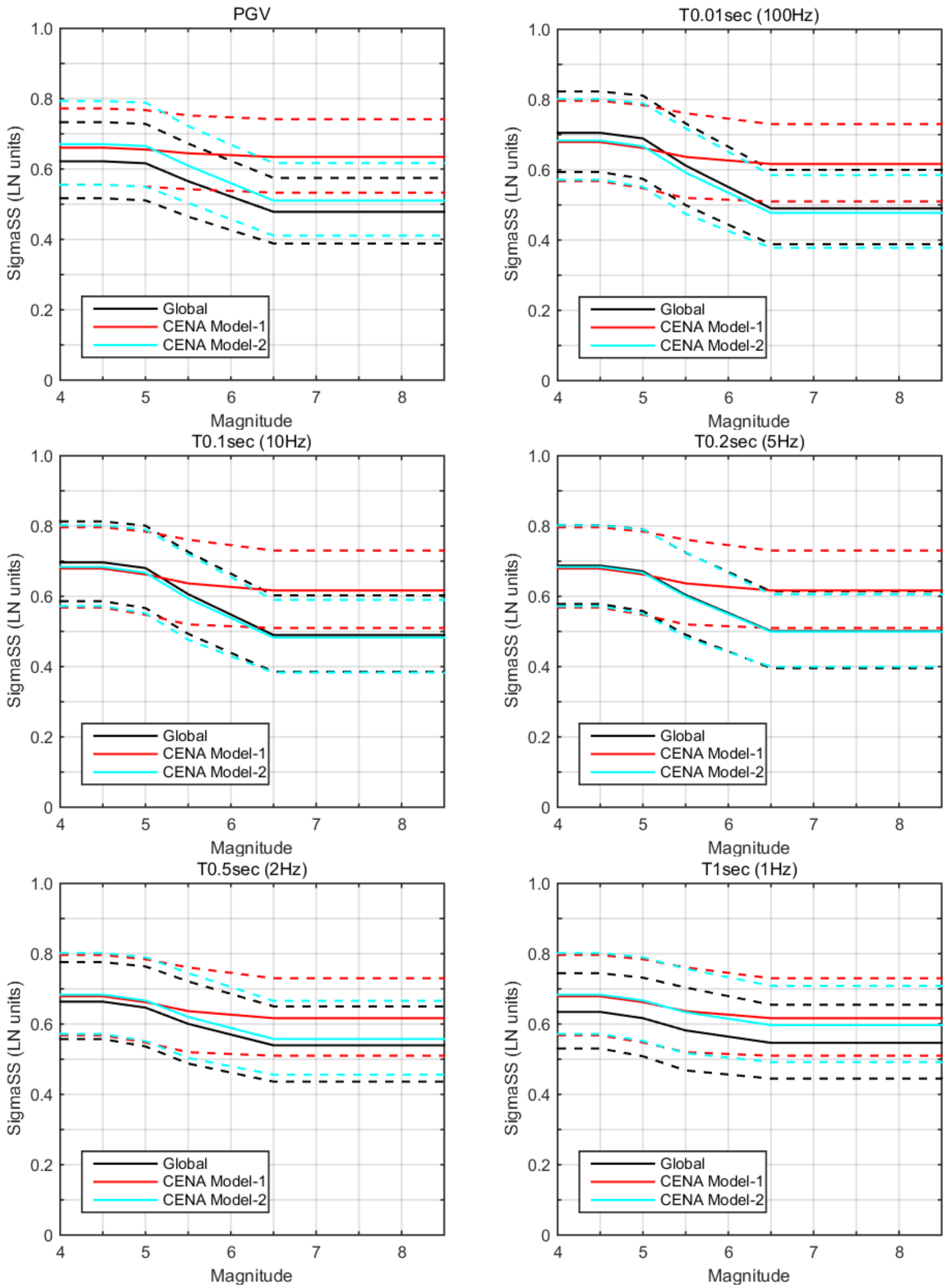

Figure 5.39 **Comparison of three candidate single-station σ models for CENA versus magnitude at PGV and F = 100, 10, 5, 2, and 1 Hz. Dashed lines represent the 5th and 95th percentiles of the models.**

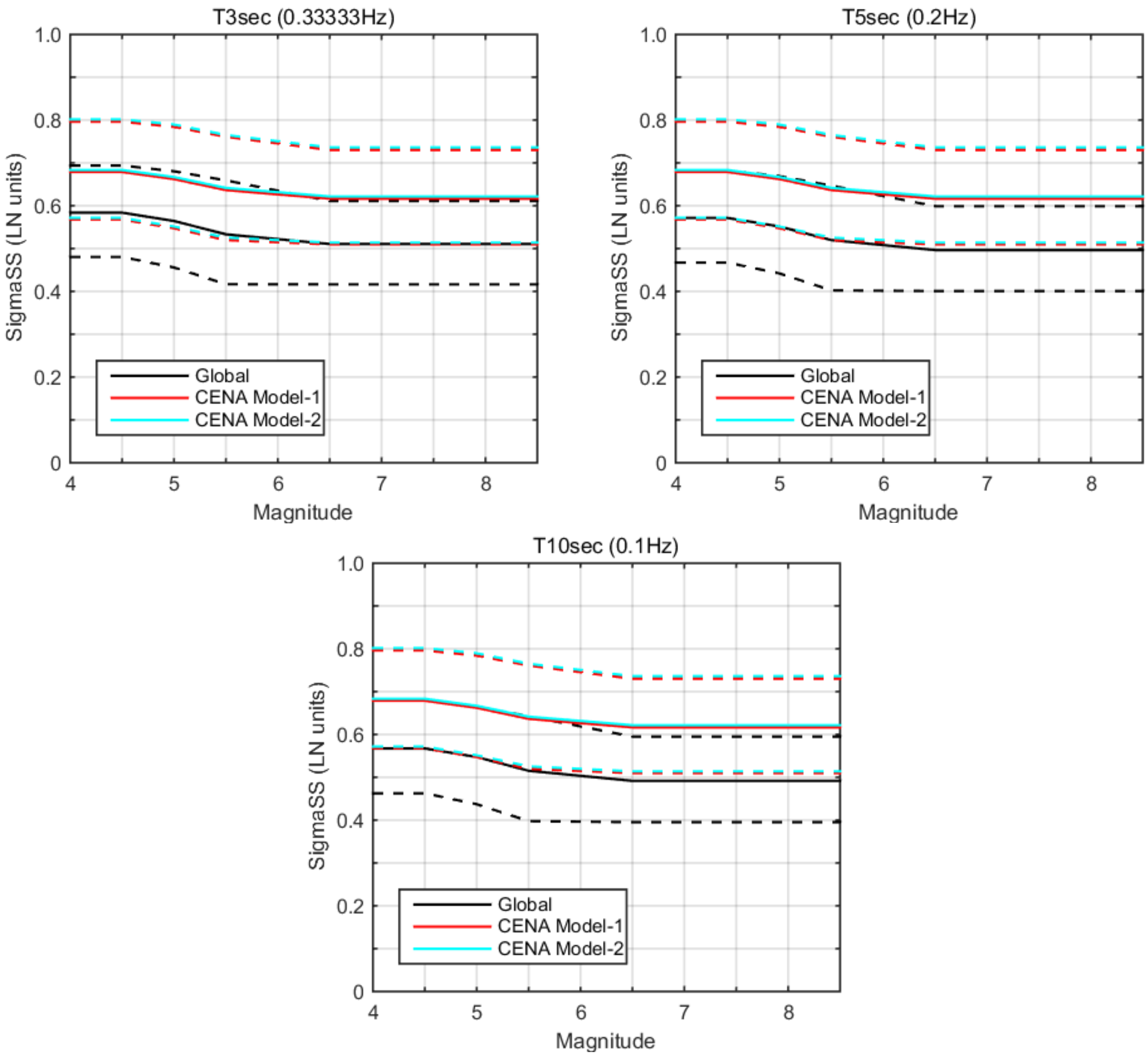

Figure 5.40 Comparison of three candidate single-station σ models for CENA versus magnitude at PGV and F = 0.33, 0.2, and 0.1 Hz. Dashed lines represent the 5th and 95th percentiles of the models.

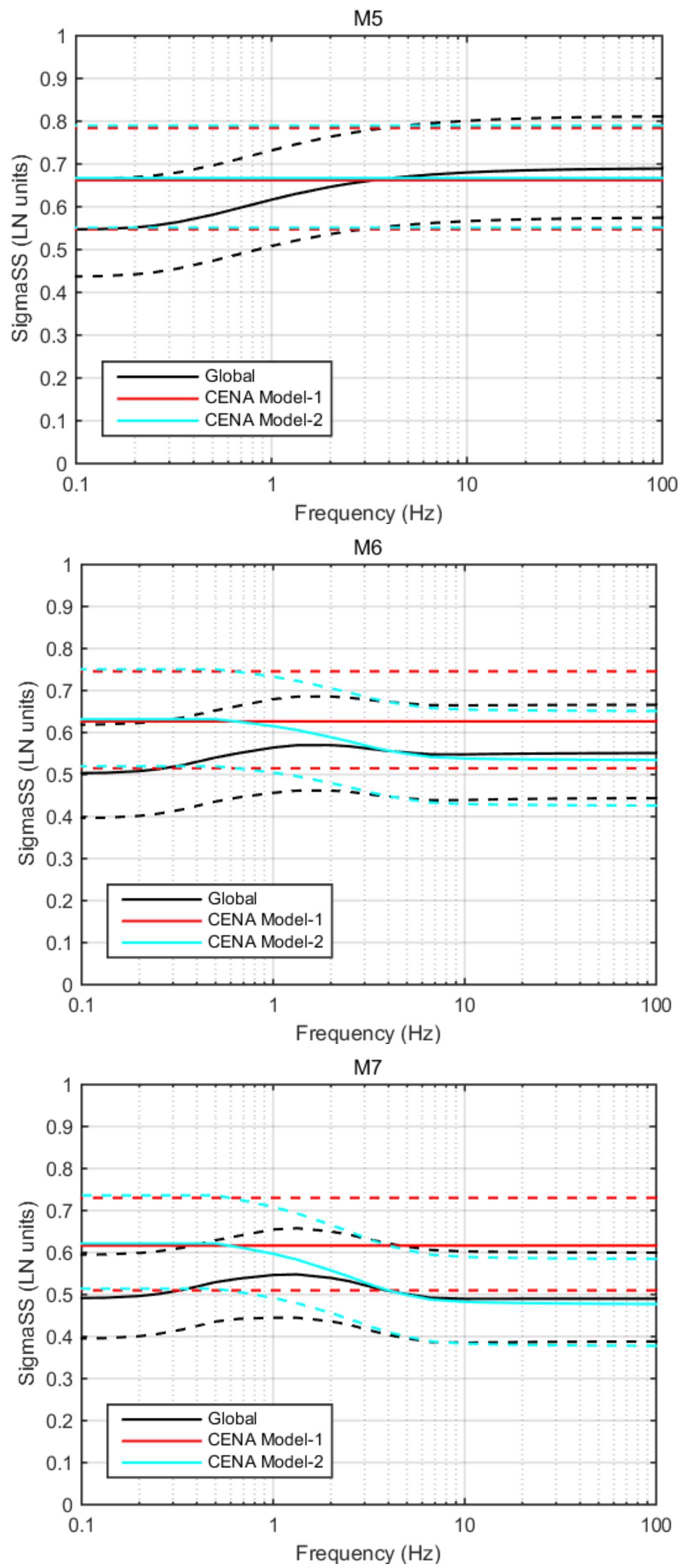

Figure 5.41 Comparison of three candidate single-station σ models for CENA versus frequency for M = 5.0, 6.0, and 7.0. Dashed lines represent the 5th and 95th percentiles of the models.

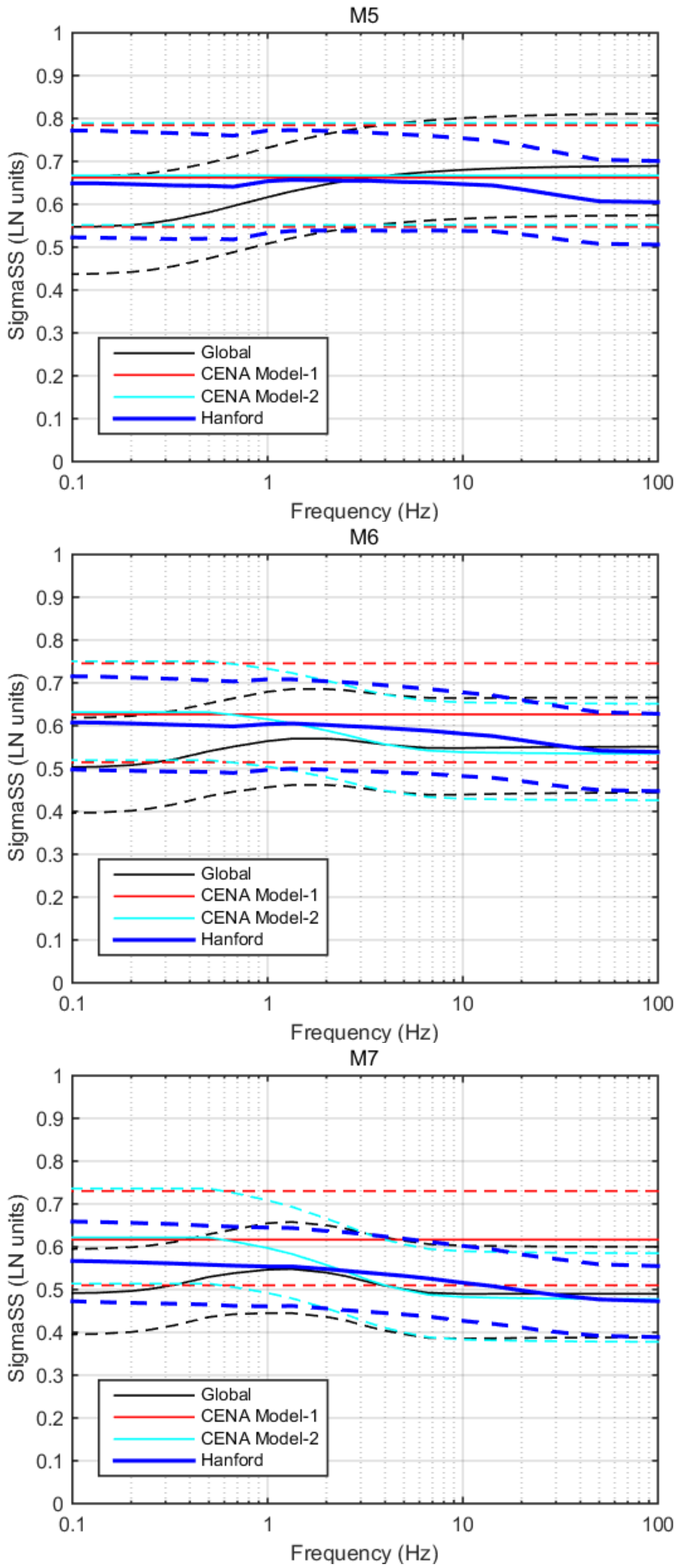

Figure 5.42 **Comparison of three candidate single-station σ models for CENA and Hanford versus frequency for M = 5.0, 6.0, and 7.0. Dashed lines represent the 5th and 95th percentiles of the models.**

5.7 ERGODIC σ

The models for ergodic σ for CENA are derived by combining the models for ϕ_{SS}, ϕ_{S2S}, and τ, whereby the mean σ^2 and $SD(\sigma^2)$ are derived as follows:

$$\sigma^2 = \phi_{SS}^2 + \phi_{S2S}^2 + \tau^2 \tag{5.18}$$

$$SD[\sigma^2] = \sqrt{(SD[\phi_{SS}^2])^2 + (SD[\phi_{S2S}^2])^2 + (SD[\tau^2])^2} \tag{5.19}$$

The equation for $SD(\sigma^2)$ is based on the assumption that ϕ_{SS}, ϕ_{S2S}, and τ are statistically independent, which is justified based on the regression results that show very weak to no correlation between ϕ and τ and between ϕ_{SS} and ϕ_{S2S}. The mean and standard deviations of ϕ_{SS}^2, ϕ_{S2S}^2, and τ^2 are discussed in Sections 5.3, 5.4, and 5.2, respectively.

Combining all candidate τ, ϕ_{SS}, and ϕ_{S2S} models results in nine candidate σ models for CENA. One of the candidate σ models is magnitude-independent resulting from combining the CENA constant τ model with the CENA constant ϕ_{SS} model and the CENA ϕ_{S2S} model, while the rest of the models are magnitude-dependent with two to four magnitude breaks. Values of all nine candidate σ models are not presented here but can be easily obtained by the reader by using Equations (5.18) and (5.19), along with the values of the variability components (mean and standard deviations) given in the tables in Sections 5.2, 5.3, and 5.4.

Three candidate σ models are presented here as an example: (1) global σ model derived by combining the global ϕ_{SS} and τ models with the CENA ϕ_{S2S} model; (2) CENA σ model-1 derived by combining the CENA constant ϕ_{SS} model with the CENA ϕ_{S2S} model and the global τ model; and (3) CENA σ model-2 resulting from combining the CENA magnitude-dependent ϕ_{SS} model with the CENA ϕ_{S2S} model and the global τ model. Because the global τ model is magnitude-dependent with four magnitude breaks, the three candidate σ models are also magnitude-dependent and have the following form:

$$\sigma = \begin{cases} \sigma_1 & for\ M \le 4.5 \\ \sigma_1 + (\sigma_2 - \sigma_1) * \frac{(M-4.5)}{0.5} & for\ M \le 5.0 \\ \sigma_2 + (\sigma_3 - \sigma_2) * \frac{(M-5.0)}{0.5} & for\ M \le 5.5 \\ \sigma_3 + (\sigma_4 - \sigma_3) * \frac{(M-5.5)}{1.0} & for\ M \le 6.5 \\ \sigma_4 & for\ M > 6.5 \end{cases} \tag{5.20}$$

The four coefficients for the central, high, and low branches are given in Tables 5.22, 5.23, and 5.24 for the global model, CENA model-1and CENA model-2, respectively. Figures 5.43 and 5.44 show the three candidate σ models for CENA as a function of magnitude at PGV and spectral periods of 0.01, 0.1, 0.2, 0.5, 1, 3, 5, 10 sec. The solid lines show the median branches for each model and the dashed lines show the 5th and 95th percentile branches for each model calculated assuming σ^2 follows a χ-square distribution with mean and standard deviations calculated as discussed above. Figure 5.45 shows the three σ models for CENA as a function of frequency for **M**5.0, 6.0, and 7.0. Figures 5.43 through 5.45 indicate that for **M**5.0, the two CENA models are similar. At frequencies greater than 2 Hz, the three σ models are similar for **M**

5.0 with the global model resulting in lower σ values at low frequencies. At **M**6.0 and 7.0, the two CENA models are only similar at low frequencies. At high frequencies, the CENA model-2 σ is comparable to the global σ.

Figures 5.46 to 5.48 compare the three candidate ergodic σ models for CENA to the NGA-West2 σ models versus frequency for **M**5.0, 6.0, and 7.0. The main difference between the global and NGAWest2 σ models is the ϕ_{S2S} component. Figure 5.46 shows that the global σ model is lower at low frequencies than the NGA-West2 σ models and vice-versa at high frequencies, mirroring the difference between the CENA and WUS ϕ_{S2S} values. The NGA-West2 σ values are contained within the range of the CENA σ models at low frequencies but are generally below the CENA models at high frequencies. Figure 5.49 presents a comparison of the three candidate ergodic σ models for CENA to the EPRI [2013] σ model for CEUS and the Atkinson et al. [2012] σ model used in the seismic hazard maps for Canada for **M**5.0, 6.0, and 7.0. Figure 5.49 shows that the CENA σ models are larger than the EPRI 2013 and the Atkinson et al. [2012] models, particularly at frequencies greater than 1 to 2 Hz.

Table 5.22 **Coefficients of the global ergodic σ model resulting from combining the global ϕ_{SS} model, the global τ model, and the CENA ϕ_{S2S} model.**

Period (sec)	Frequency (Hz)	Central				High				Low			
		σ_1	σ_2	σ_3	σ_4	σ_1	σ_2	σ_3	σ_4	σ_1	σ_2	σ_3	σ_4
0.01	100	0.8435	0.8304	0.7676	0.6744	0.9445	0.9341	0.8664	0.7591	0.7465	0.7308	0.6729	0.5932
0.02	50	0.8432	0.8300	0.7676	0.6751	0.9439	0.9335	0.8663	0.7599	0.7463	0.7307	0.6730	0.5937
0.03	33.33	0.8470	0.8339	0.7722	0.6808	0.9470	0.9366	0.8702	0.7652	0.7507	0.7352	0.6781	0.5998
0.04	25	0.8557	0.8427	0.7821	0.6927	0.9549	0.9446	0.8794	0.7767	0.7601	0.7448	0.6887	0.6120
0.05	20	0.8772	0.8646	0.8059	0.7200	0.9745	0.9644	0.9012	0.8023	0.7834	0.7685	0.7143	0.6406
0.075	13.33	0.9094	0.8972	0.8417	0.7611	1.0039	0.9940	0.9342	0.8416	0.8181	0.8038	0.7525	0.6834
0.1	10	0.9159	0.9039	0.8495	0.7710	1.0097	0.9999	0.9416	0.8516	0.8253	0.8111	0.7607	0.6931
0.15	6.67	0.8985	0.8862	0.8330	0.7562	0.9922	0.9823	0.9257	0.8381	0.8079	0.7934	0.7436	0.6772
0.2	5	0.8733	0.8606	0.8095	0.7361	0.9679	0.9577	0.9040	0.8197	0.7820	0.7670	0.7186	0.6555
0.25	4	0.8510	0.8380	0.7890	0.7192	0.9465	0.9361	0.8852	0.8046	0.7590	0.7435	0.6966	0.6371
0.3	3.33	0.8328	0.8194	0.7730	0.7076	0.9288	0.9183	0.8705	0.7942	0.7403	0.7245	0.6794	0.6243
0.4	2.5	0.8056	0.7918	0.7503	0.6942	0.9021	0.8913	0.8496	0.7824	0.7128	0.6963	0.6551	0.6095
0.5	2	0.7863	0.7721	0.7341	0.6851	0.8828	0.8718	0.8346	0.7746	0.6935	0.6765	0.6380	0.5993
0.75	1.33	0.7544	0.7396	0.7075	0.6710	0.8507	0.8393	0.8099	0.7622	0.6621	0.6443	0.6097	0.5837
1	1	0.7338	0.7186	0.6892	0.6594	0.8300	0.8184	0.7932	0.7506	0.6416	0.6232	0.5903	0.5723
1.5	0.67	0.7070	0.6912	0.6645	0.6420	0.8037	0.7917	0.7708	0.7296	0.6147	0.5954	0.5637	0.5582
2	0.5	0.6903	0.6740	0.6485	0.6295	0.7875	0.7753	0.7563	0.7163	0.5974	0.5776	0.5464	0.5466
3	0.33	0.6712	0.6544	0.6281	0.6085	0.7697	0.7574	0.7379	0.6968	0.5772	0.5566	0.5245	0.5243
4	0.25	0.6617	0.6447	0.6179	0.5980	0.7614	0.7490	0.7289	0.6880	0.5667	0.5458	0.5133	0.5124
5	0.2	0.6567	0.6395	0.6126	0.5924	0.7574	0.7448	0.7244	0.6837	0.5609	0.5397	0.5072	0.5057
7.5	0.13	0.6517	0.6344	0.6073	0.5870	0.7537	0.7411	0.7203	0.6799	0.5549	0.5335	0.5009	0.4988
10	0.1	0.6502	0.6329	0.6057	0.5853	0.7524	0.7398	0.7190	0.6785	0.5532	0.5318	0.4991	0.4969
PGV		0.7598	0.7552	0.7142	0.6475	0.8532	0.8489	0.8018	0.7228	0.6701	0.6653	0.6300	0.5750

Table 5.23 Coefficients of the CENA ergodic σ model-1 resulting from combining the CENA constant ϕ_{SS} model, the global τ model, and the CENA ϕ_{S2S} model.

Period (sec)	Frequency (Hz)	Central				High				Low			
		σ_1	σ_2	σ_3	σ_4	σ_1	σ_2	σ_3	σ_4	σ_1	σ_2	σ_3	σ_4
0.01	100	0.8216	0.8081	0.7873	0.7711	0.9214	0.9107	0.8907	0.8651	0.7258	0.7097	0.6883	0.6808
0.02	50	0.8222	0.8086	0.7879	0.7716	0.9218	0.9112	0.8912	0.8656	0.7264	0.7103	0.6889	0.6814
0.03	33.33	0.8269	0.8135	0.7928	0.7767	0.9260	0.9154	0.8955	0.8700	0.7316	0.7156	0.6944	0.6869
0.04	25	0.8367	0.8235	0.8031	0.7871	0.9352	0.9247	0.9050	0.8798	0.7420	0.7263	0.7053	0.6980
0.05	20	0.8595	0.8466	0.8267	0.8113	0.9561	0.9458	0.9265	0.9021	0.7664	0.7511	0.7308	0.7237
0.075	13.33	0.8942	0.8819	0.8629	0.8480	0.9883	0.9783	0.9598	0.9364	0.8034	0.7888	0.7695	0.7626
0.1	10	0.9027	0.8905	0.8717	0.8569	0.9964	0.9865	0.9681	0.9450	0.8122	0.7978	0.7787	0.7718
0.15	6.67	0.8887	0.8762	0.8571	0.8421	0.9831	0.9730	0.9543	0.9308	0.7975	0.7829	0.7634	0.7565
0.2	5	0.8668	0.8540	0.8344	0.8190	0.9627	0.9525	0.9334	0.9092	0.7743	0.7592	0.7391	0.7320
0.25	4	0.8478	0.8347	0.8146	0.7989	0.9453	0.9349	0.9154	0.8906	0.7540	0.7385	0.7179	0.7106
0.3	3.33	0.8329	0.8196	0.7991	0.7831	0.9316	0.9210	0.9013	0.8760	0.7381	0.7222	0.7012	0.6938
0.4	2.5	0.8123	0.7986	0.7776	0.7611	0.9126	0.9018	0.8816	0.8556	0.7160	0.6997	0.6780	0.6704
0.5	2	0.7992	0.7853	0.7639	0.7472	0.9005	0.8896	0.8691	0.8427	0.7021	0.6854	0.6633	0.6556
0.75	1.33	0.7814	0.7672	0.7452	0.7281	0.8843	0.8732	0.8524	0.8252	0.6829	0.6658	0.6430	0.6351
1	1	0.7726	0.7581	0.7359	0.7186	0.8766	0.8654	0.8444	0.8169	0.6730	0.6557	0.6325	0.6245
1.5	0.67	0.7638	0.7492	0.7267	0.7092	0.8694	0.8582	0.8370	0.8093	0.6629	0.6453	0.6218	0.6135
2	0.5	0.7595	0.7448	0.7222	0.7045	0.8660	0.8548	0.8334	0.8057	0.6578	0.6400	0.6164	0.6080
3	0.33	0.7553	0.7405	0.7177	0.6999	0.8629	0.8516	0.8302	0.8024	0.6526	0.6347	0.6108	0.6023
4	0.25	0.7532	0.7383	0.7154	0.6976	0.8614	0.8501	0.8287	0.8009	0.6499	0.6319	0.6079	0.5993
5	0.2	0.7519	0.7370	0.7141	0.6963	0.8607	0.8493	0.8279	0.8001	0.6482	0.6302	0.6061	0.5974
7.5	0.13	0.7502	0.7353	0.7123	0.6945	0.8597	0.8483	0.8269	0.7991	0.6459	0.6279	0.6037	0.5949
10	0.1	0.7494	0.7345	0.7115	0.6936	0.8590	0.8476	0.8262	0.7984	0.6450	0.6269	0.6027	0.5939
PGV		0.7919	0.7875	0.7784	0.7699	0.8868	0.8827	0.8698	0.8607	0.7006	0.6960	0.6905	0.6826

Table 5.24 Coefficients of the CENA ergodic σ model-2 resulting from combining the CENA magnitude-dependent ϕ_{SS} model, the global τ model, and the CENA ϕ_{S2S} model.

Period (sec)	Frequency (Hz)	Central				High				Low			
		σ_1	σ_2	σ_3	σ_4	σ_1	σ_2	σ_3	σ_4	σ_1	σ_2	σ_3	σ_4
0.01	100	0.8254	0.8119	0.7519	0.6653	0.9259	0.9153	0.8543	0.7476	0.7288	0.7127	0.6540	0.5863
0.02	50	0.8259	0.8124	0.7526	0.6663	0.9263	0.9157	0.8549	0.7485	0.7294	0.7133	0.6548	0.5874
0.03	33.33	0.8306	0.8172	0.7580	0.6726	0.9305	0.9200	0.8596	0.7541	0.7346	0.7186	0.6607	0.5942
0.04	25	0.8404	0.8272	0.7689	0.6851	0.9396	0.9292	0.8697	0.7661	0.7449	0.7292	0.6724	0.6071
0.05	20	0.8630	0.8502	0.7937	0.7129	0.9604	0.9501	0.8923	0.7923	0.7692	0.7540	0.6991	0.6365
0.075	13.33	0.8977	0.8853	0.8317	0.7553	0.9925	0.9826	0.9272	0.8325	0.8061	0.7916	0.7397	0.6807
0.1	10	0.9061	0.8939	0.8411	0.7662	1.0005	0.9907	0.9361	0.8433	0.8149	0.8005	0.7496	0.6917
0.15	6.67	0.8921	0.8797	0.8274	0.7531	0.9873	0.9773	0.9234	0.8307	0.8003	0.7856	0.7351	0.6781
0.2	5	0.8703	0.8576	0.8068	0.7346	0.9670	0.9568	0.9047	0.8141	0.7771	0.7620	0.7128	0.6580
0.25	4	0.8514	0.8384	0.7893	0.7197	0.9497	0.9393	0.8891	0.8011	0.7569	0.7414	0.6936	0.6413
0.3	3.33	0.8366	0.8233	0.7764	0.7104	0.9360	0.9255	0.8777	0.7937	0.7410	0.7252	0.6794	0.6304
0.4	2.5	0.8161	0.8024	0.7601	0.7024	0.9171	0.9064	0.8635	0.7888	0.7190	0.7028	0.6613	0.6195
0.5	2	0.8030	0.7892	0.7503	0.6992	0.9051	0.8943	0.8550	0.7879	0.7051	0.6885	0.6504	0.6142
0.75	1.33	0.7853	0.7711	0.7386	0.7000	0.8890	0.8780	0.8452	0.7930	0.6861	0.6690	0.6369	0.6109
1	1	0.7765	0.7622	0.7331	0.7017	0.8814	0.8703	0.8411	0.7978	0.6762	0.6590	0.6303	0.6099
1.5	0.67	0.7678	0.7533	0.7284	0.7056	0.8742	0.8631	0.8381	0.8055	0.6661	0.6486	0.6239	0.6102
2	0.5	0.7635	0.7489	0.7265	0.7088	0.8709	0.8596	0.8372	0.8111	0.6611	0.6434	0.6211	0.6113
3	0.33	0.7593	0.7446	0.7220	0.7043	0.8677	0.8565	0.8340	0.8078	0.6559	0.6381	0.6156	0.6056
4	0.25	0.7572	0.7425	0.7198	0.7020	0.8663	0.8550	0.8325	0.8063	0.6532	0.6354	0.6128	0.6027
5	0.2	0.7560	0.7412	0.7185	0.7006	0.8655	0.8542	0.8317	0.8055	0.6515	0.6336	0.6110	0.6008
7.5	0.13	0.7543	0.7395	0.7167	0.6988	0.8645	0.8532	0.8307	0.8045	0.6492	0.6313	0.6085	0.5983
10	0.1	0.7535	0.7386	0.7159	0.6980	0.8638	0.8525	0.8300	0.8037	0.6483	0.6304	0.6076	0.5973
PGV		0.8003	0.7960	0.7497	0.6717	0.9048	0.9008	0.8435	0.7561	0.7002	0.6955	0.6597	0.5907

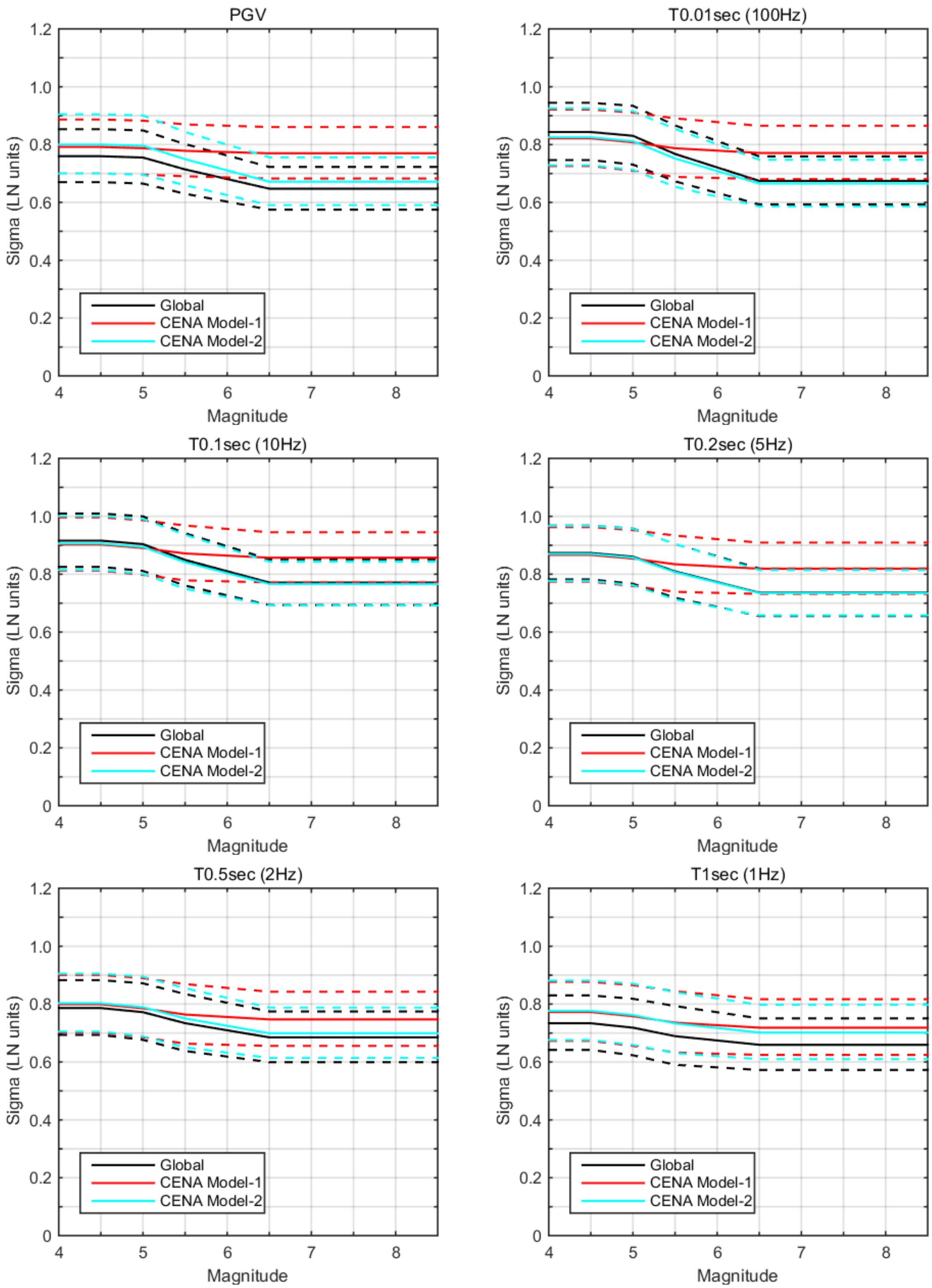

Figure 5.43 **Comparison of three candidate ergodic σ models for CENA versus magnitude at PGV and F = 100, 10, 5, 2, and 1 Hz. Dashed lines represent the 5th and 95th percentiles of the models.**

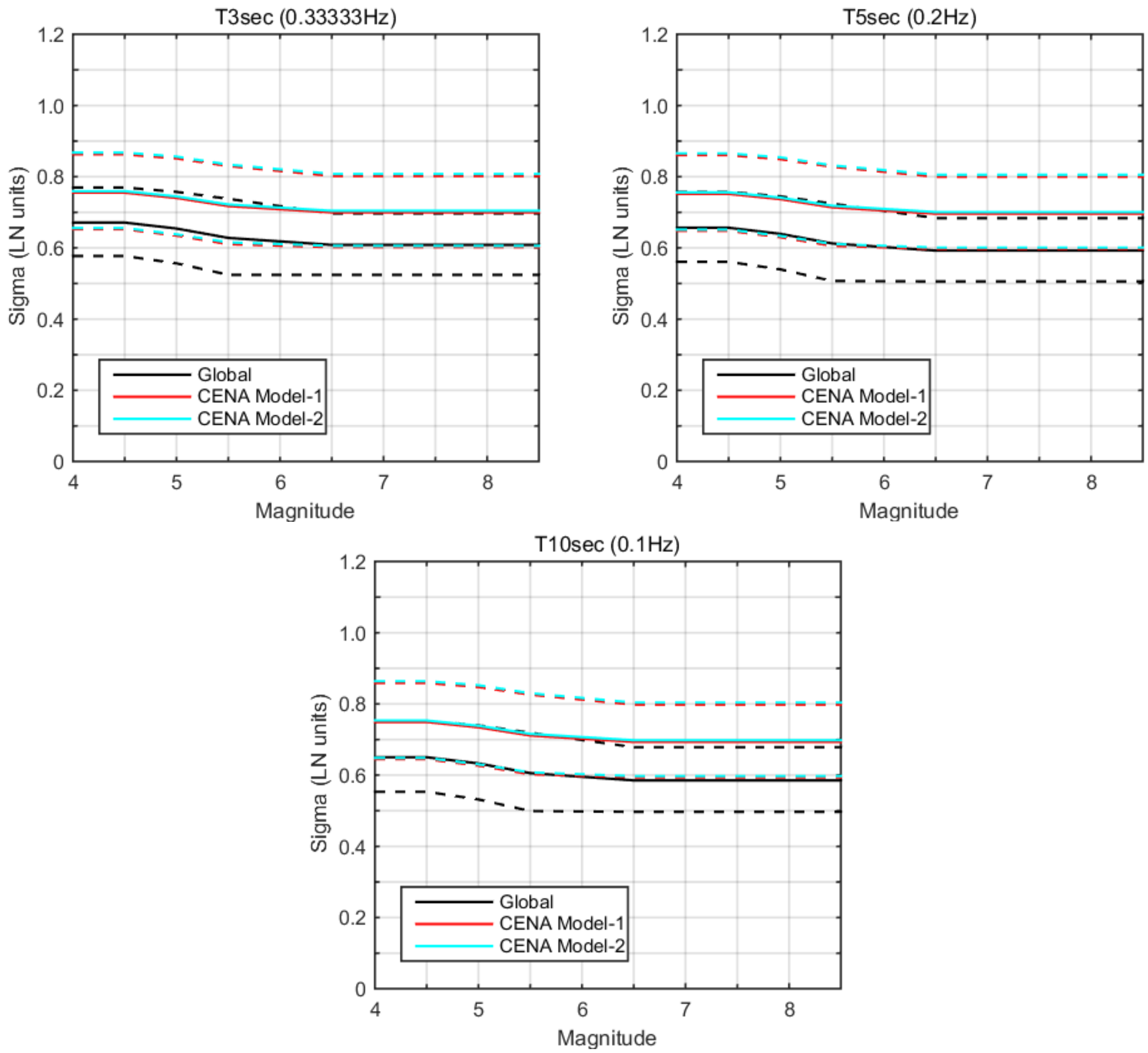

Figure 5.44 **Comparison of three candidate ergodic σ models for CENA versus magnitude at PGV and F = 0.33, 0.2, and 0.1 Hz. Dashed lines represent the 5th and 95th percentiles of the models.**

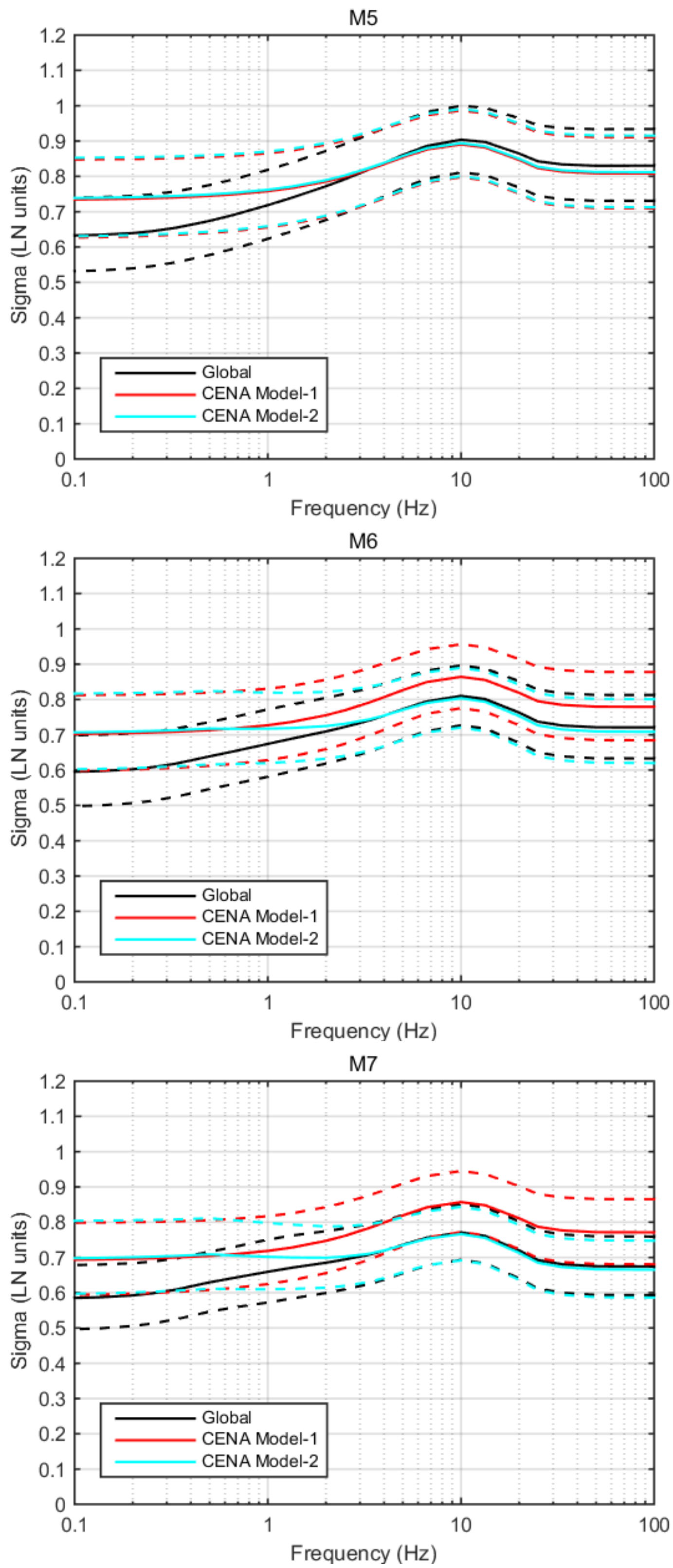

Figure 5.45 **Comparison of three candidate ergodic σ models for CENA versus frequency for M = 5.0, 6.0, and 7.0. Dashed lines represent the 5th and 95th percentiles of the models.**

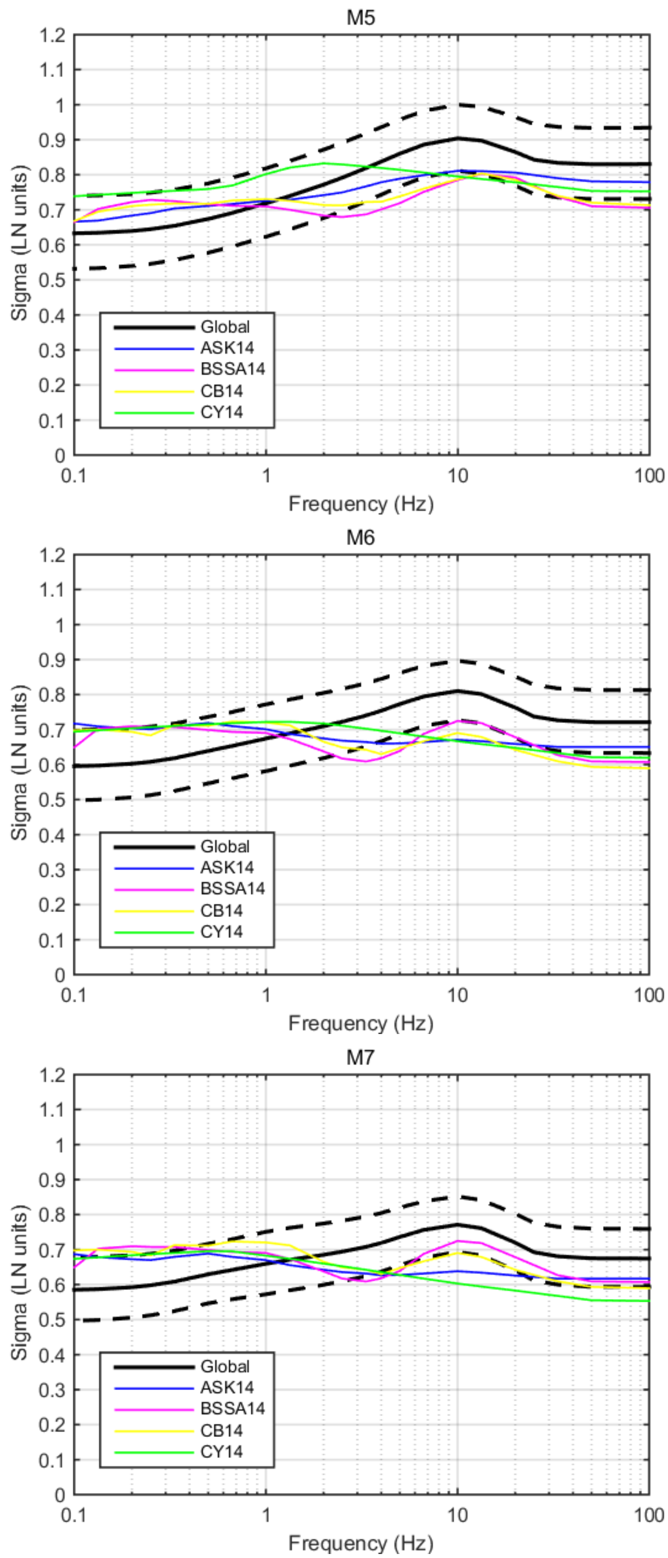

Figure 5.46 **Comparison of three candidate ergodic global σ models for CENA and NGA-West2 models versus frequency for M = 5.0, 6.0, and 7.0. Dashed lines represent the 5th and 95th percentiles of the CENA global model.**

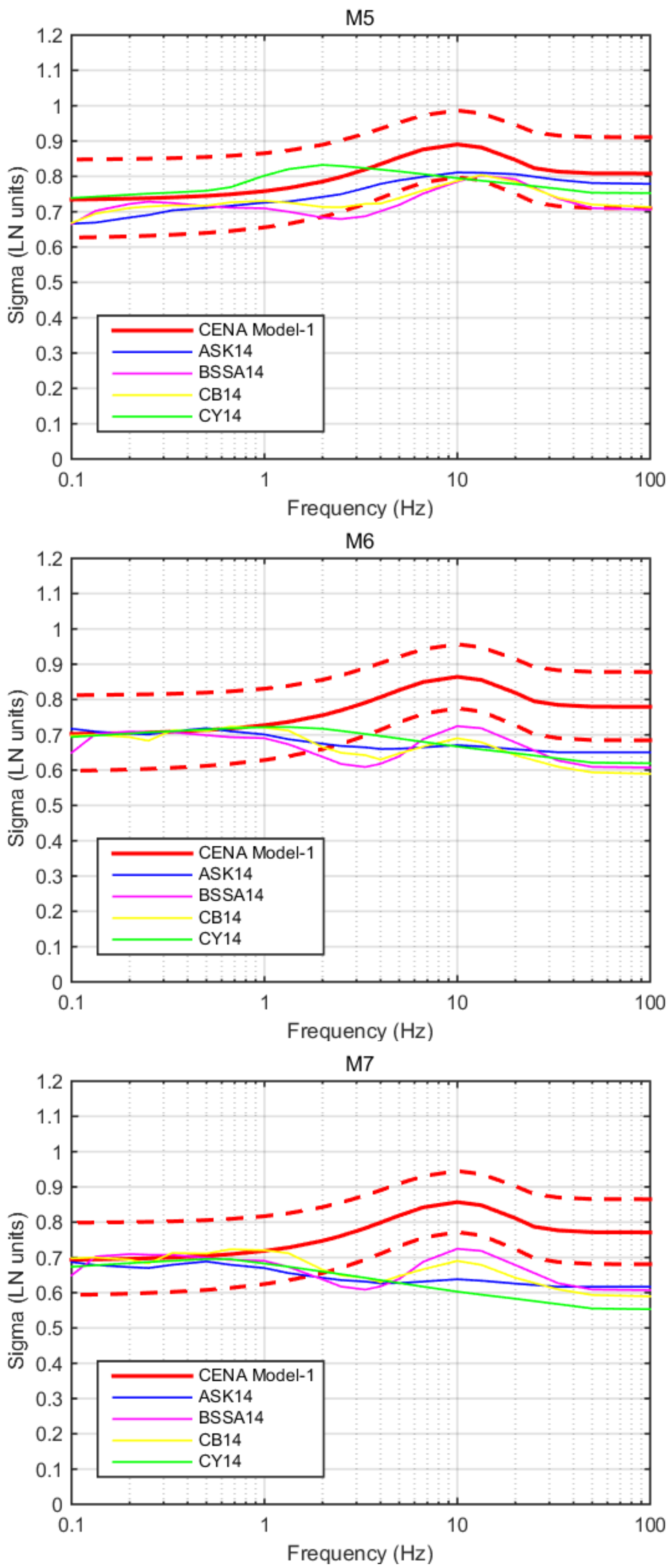

Figure 5.47 **Comparison of three candidate ergodic CENA σ model-1 and NGA-West2 models versus frequency for M = 5.0, 6.0, and 7.0. Dashed lines represent the 5th and 95th percentiles of CENA model-1.**

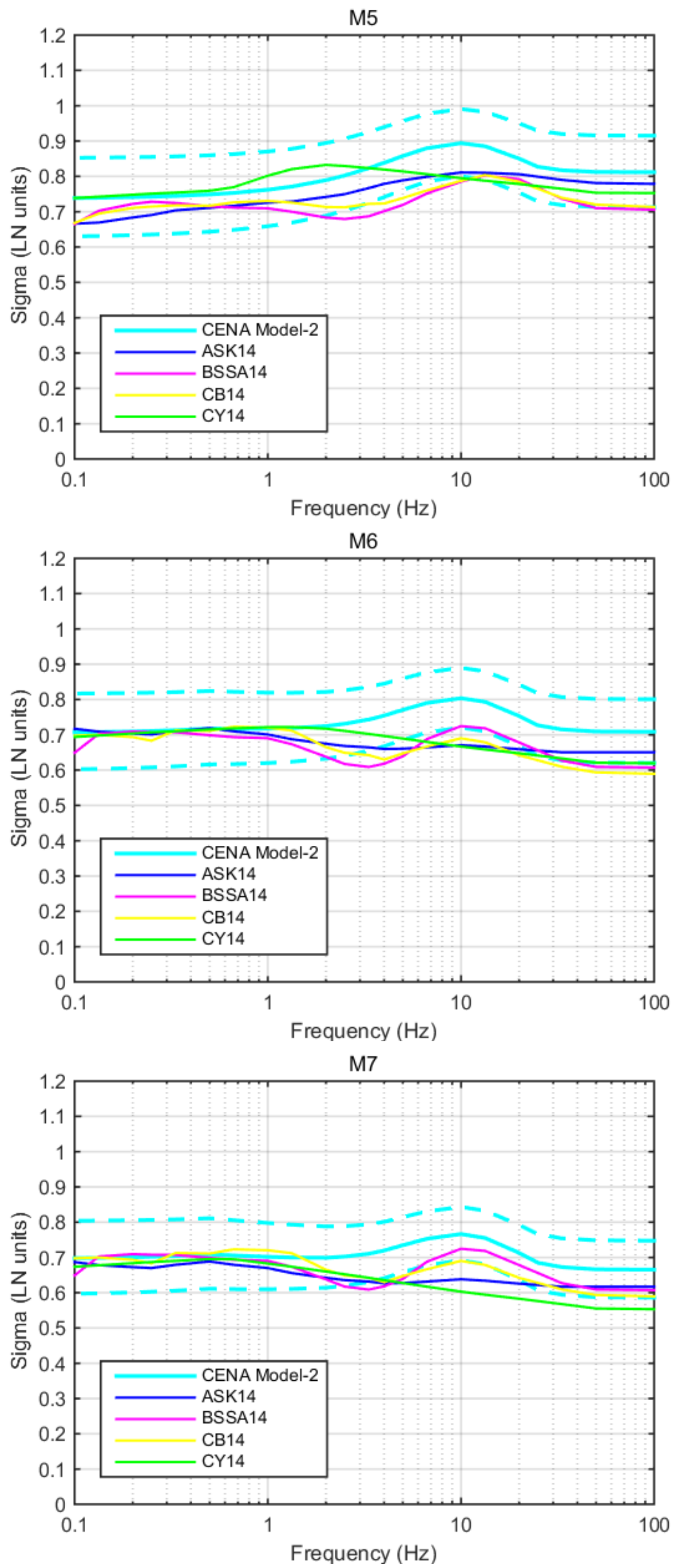

Figure 5.48 **Comparison of three candidate ergodic CENA σ model-2 and NGA-West2 models versus frequency for M = 5.0, 6.0, and 7.0. Dashed lines represent the 5th and 95th percentiles of CENA model-2.**

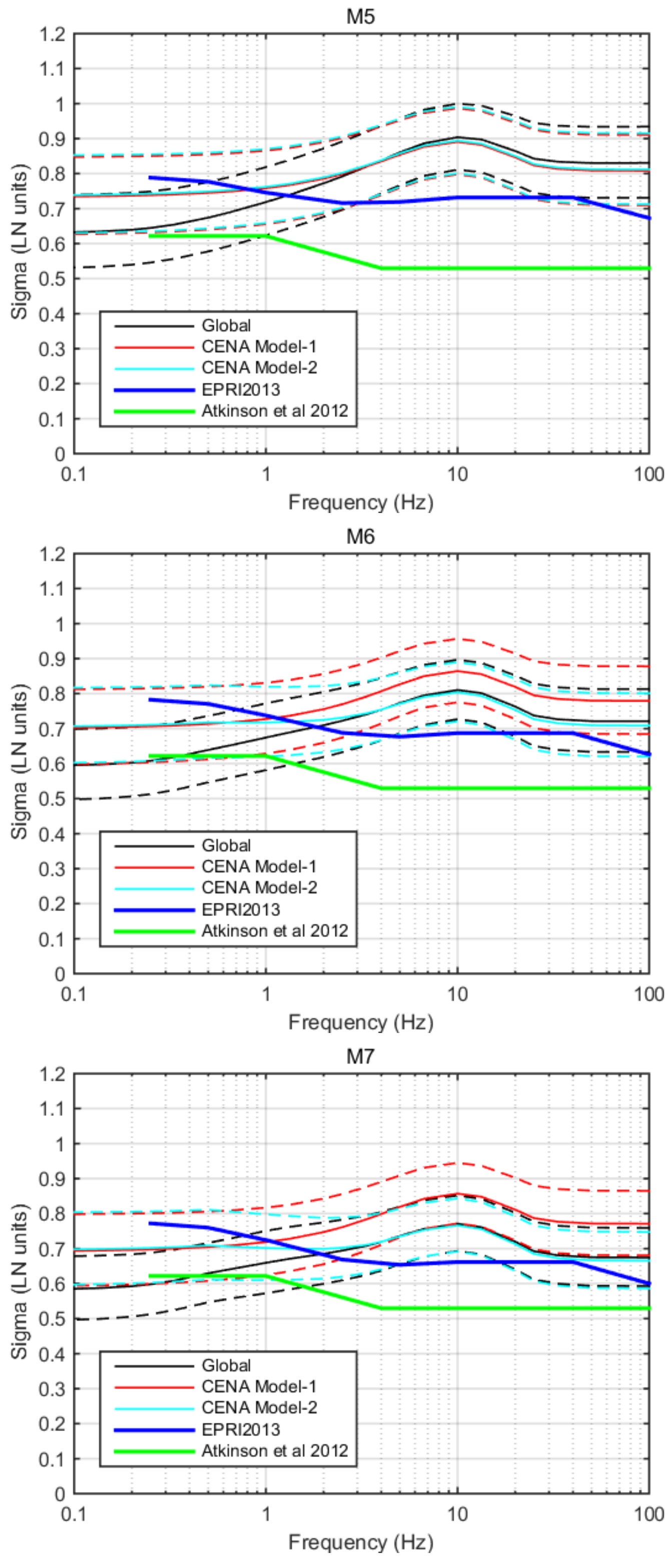

Figure 5.49 **Comparison of three candidate ergodic σ models for CENA to the EPRI 2013 and Atkinson et al. [2012] σ models versus frequency for M = 5.0, 6.0, and 7.0. Dashed lines represent the 5th and 95th percentiles of the CENA models.**

5.8 OTHER CONSIDERATIONS

5.8.1 Application to Potentially Induced Earthquakes

The candidate models for τ and ϕ_{SS} developed using the CENA data are based on CENA ground-motion residuals from tectonic events; see Sections 5.2 and 5.3. The CENA dataset includes a large number of recordings from PIE, as shown in Section 2.1. All of the PIE data have magnitudes greater than 3.0. This section investigates the application of the candidate CENA standard deviation models shown in the preceding sections to ground motion from PIE in CENA.

Figure 5.50 shows a comparison of the τ values obtained from the mixed effects regressions using all earthquakes in the CENA dataset with minimum **M**3.0 (54 earthquakes at F = 4 Hz) as well as PIE-only (a total of nine events at F = 4 Hz) and tectonic-only events with minimum **M**3.0 (45 earthquakes at F = 4 Hz). Figure 5.50 shows that τ for PIE is smaller than that for tectonic earthquakes in the frequency range of 1 to 10 Hz. The statistical significance of the difference between PIE and tectonic τ for magnitudes greater than or equal to 3.0 was evaluated. Specifically, an F-test of equality of variance was conducted to test against the null hypothesis of equal variance of event terms for PIE and tectonic events. Table 5.25 shows the p-values of the F-test at frequencies of 1 to 10 Hz and shows relatively large p-values, indicating that the equality of τ^2 for PIE and tectonic events with **M** larger than or equal to 3.0 cannot be rejected at 5% significance level. As a result, we concluded that the candidate τ models developed for tectonic events in CENA are applicable to PIE in CENA.

Figure 5.51 compares ϕ_{SS} obtained from the mixed effects regressions using all earthquakes in the CENA dataset with a minimum **M**3.0 and maximum R_{RUP} of 300 km (708 recordings at F = 4 Hz) as well as PIE-only (315 recordings at F = 4 Hz) and tectonic-only events with minimum **M**3.0 and maximum R_{RUP} of 300 km (393 recordings at F = 4 Hz). Stations with a minimum of three recordings within the magnitude and distance range of interest are used in the regression. Figure 5.51 indicates that ϕ_{SS} values are comparable between tectonic events and PIE in the frequency range of 1 to 10 Hz. Table 5.26 shows the p-values of the F-test of equality of variances of the single-station within-event residuals for PIE and tectonic events. Table 5.26 indicates that the equality of ϕ_{SS}^2 for PIE and tectonic events with **M** larger than or equal to 3.0 and R_{RUP} distance of less than or equal to 300 km cannot be rejected at 5% significance level. As a result, we concluded that the candidate ϕ_{SS} models developed for tectonic events in CENA and discussed in Section 5.3 are applicable to PIE in CENA.

Figure 5.52 presents a comparison of ϕ_{S2S} obtained from the mixed effects regressions off CENA data (275 stations at F = 4 Hz), tectonic events only (144 stations at F = 4 Hz), and PIE only (141 stations at F = 4 Hz). Figure 5.52 shows a significant difference in ϕ_{S2S} between PIE and tectonic events. Note that all CENA data (PIE and tectonic events) were used in deriving the ϕ_{S2S} model for CENA, as discussed in Section 5.4. All data were used in order to maximize the dataset used in the regression. Section 4.5 discussed the difference in ϕ_{S2S} between PIE and tectonic events, and concluded that the reduced ϕ_{S2S} values for PIE compared to tectonic events are likely due to the clustering of the stations that recorded PIE and the presence of more similar geologic conditions as opposed to stations that recorded tectonic events spanning a much larger area. Therefore, we consider the ϕ_{S2S} model derived for CENA to be applicable to PIE events in CENA.

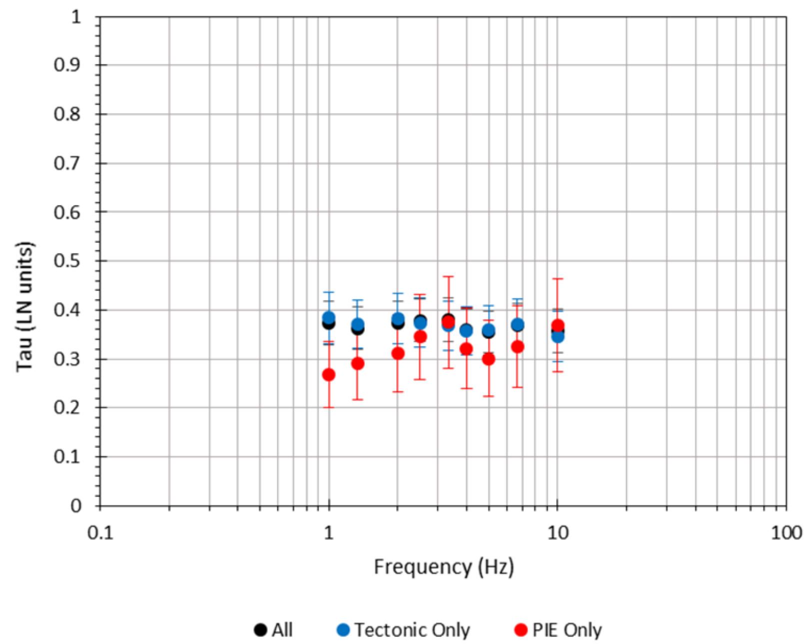

Figure 5.50 **Comparison of τ values obtained from mixed effects regressions using all CENA earthquakes, PIE-only and tectonic-only events. Only earthquakes with minimum M of 3.0 were used.**

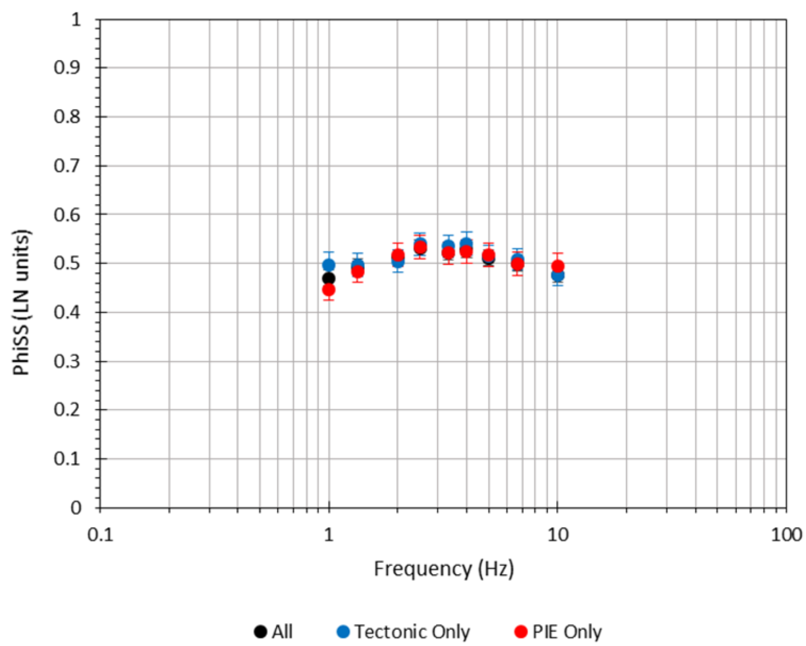

Figure 5.51 **Comparison of ϕ_{SS} values obtained from mixed effects regressions using all CENA earthquakes, PIE-only and tectonic-only events. Only earthquakes with minimum M of 3.0 were used.**

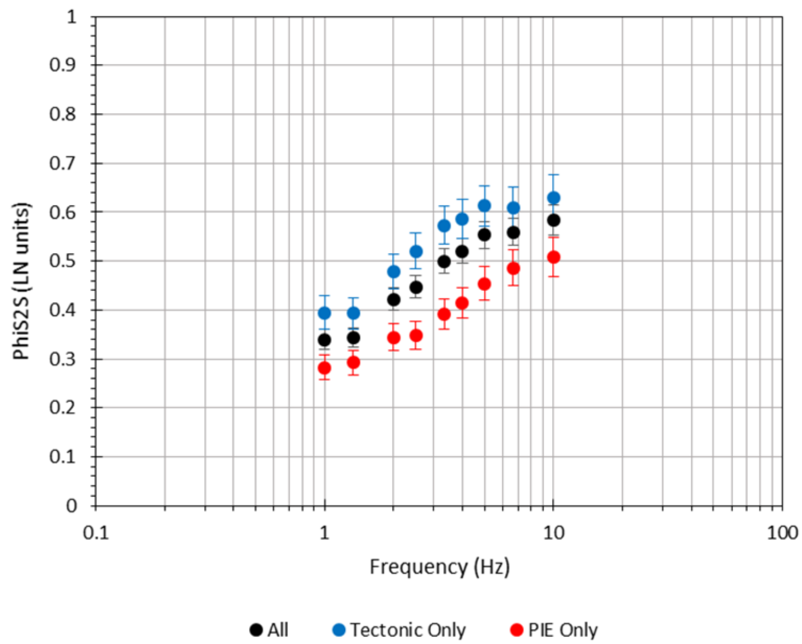

Figure 5.52 Comparison of ϕ_{S2S} values obtained from mixed effects regressions using all CENA earthquakes, PIE-only and tectonic-only events. Earthquakes with M greater than 2.0 were used.

Table 5.25 *P*-values from the *F*-test of equality of τ^2 for PIE and the tectonic events for CENA.

	T0.100	T0.150	T0.200	T0.250	T0.300	T0.400	T0.500	T0.750	T1.00
	F10.00	F6.67	F5.00	F4.00	F3.33	F2.50	F2.00	F1.33	F1.00
Tectonic versus PIE	0.72	0.73	0.63	0.80	0.85	0.87	0.56	0.48	0.28

Table 5.26 *P*-values from the *F*-test of equality of ϕ_{SS}^2 for PIE and the tectonic events for CENA.

	T0.100	T0.150	T0.200	T0.250	T0.300	T0.400	T0.500	T0.750	T1.00
	F10.00	F6.67	F5.00	F4.00	F3.33	F2.50	F2.00	F1.33	F1.00
Tectonic versus PIE	0.54	0.71	0.94	0.61	0.62	0.83	0.64	0.61	0.06

5.8.2 Application to Gulf Region

Ground-motion data from the Gulf Coast and Mississippi Embayment region (hereafter referred to as "Gulf" region) were not used in the derivation of the empirical ground-motion model presented in Chapter 3. Residuals from the Gulf region were not used in developing the standard deviation models for CENA presented in Section 5.2 to 5.7. The Gulf region is treated separately in the NGA-East project, and adjustment factors to the NGA-East median ground-motion models (GMMs) were developed to make the median models applicable to the Gulf region. This section presents the analysis of the standard deviations of the residuals of the Gulf data with respect to the two PEER-developed models for the Gulf region and the evaluation of the applicability of the developed standard deviation models for CENA to the Gulf region. The median GMMs for the Gulf region (referred to here as GULF_Model1 and GULF_Model2) are described in Chapter 4 of *PEER Report No. 2014/08* [PEER 2015b].

The Gulf data used to develop the median GMMs consist of eight tectonic events and one PIE with **M** between 3.4 and 4.7. The magnitude and distance distribution of the data is presented in Figure 5.53 at $F = 4$ Hz. We note that the PIE event with **M**4.7 has a large negative event term at short periods compared to the tectonic events. Figure 5.54 compares the global τ model for **M**5.0 to the τ values for the tectonic events in the Gulf region. The CENA constant τ model is also included in the plot. The CENA magnitude-dependent τ model is not shown in the plot because its values agree with the CENA model at **M**5.0. Figure 5.54 indicates that the τ values for the Gulf are within the range of the CENA constant model except for frequencies of 3 to 4 Hz. The uncertainty in the estimates of τ for the gulf region is large because of the small number of events available for the analysis. Table 5.27 presents the p-values from the F-test of equality of variance of the event terms for the Gulf and non-Gulf tectonic data with **M**3.0 to 5.0. Values in red indicate cases where the equality of τ^2 is rejected at a 5% significance level. Table 5.27 indicates that the equality of τ^2 for the Gulf and the rest of CENA cannot be rejected for most of the frequencies between 1 and 10 Hz for a 5% significance level. Based on these p-values and since the available data from the Gulf region is insufficient to develop a τ model, we recommend the application of the global τ model to the Gulf region.

Figure 5.55 compares the global and CENA constant ϕ_{SS} models for **M** less than or equal to 5.0 to the ϕ_{SS} values for the Gulf region obtained using tectonic data and consisting of 132 recordings at $F = 4$ Hz. The CENA magnitude-dependent ϕ_{SS} model is not shown in Figure 5.55 because it leads to similar values as the CENA constant model for **M** less than or equal to 5.0. We note that the single-station analysis of the Gulf region within-event residuals was performed using stations with a minimum of three recordings. As a result of this criterion, only recordings from tectonic events remained in the dataset for the single-station sigma analysis. Figure 5.55 shows that the ϕ_{SS} values for the Gulf region are generally within the range of the ϕ_{SS} models developed for CENA. Table 5.28 shows the p-values of the F-test of equality of ϕ_{SS}^2 for the Gulf region and the rest of CENA using tectonic data with **M**3.0 to 5.0 and maximum R_{RUP} distance of 400 km (comparable **M** and R_{RUP} ranges for the Gulf region and the rest of CENA). Table 5.28 indicates that the equality of ϕ_{SS}^2 cannot be rejected at a 5% significance level. As a result, we recommend the application of the CENA ϕ_{SS} models to the Gulf region.

Figure 5.56 presents a comparison of the CENA ϕ_{S2S} model to the ϕ_{S2S} values obtained for the Gulf region, indicating that the ϕ_{S2S} values for the Gulf region are lower than those for the rest of CENA and have large error bars. Table 5.29 presents the p-values of the F-test of equality of ϕ_{S2S}^2 for Gulf region and the rest of CENA. Values in red indicate cases where the equality of

$\phi_{S2S}{}^2$ is rejected at a 5% significance level at frequencies of 6.67 and 10 Hz. For the rest of the frequencies between 1 and 10 Hz, the equality of variances is not rejected at 5% significance level. Moreover, the small dataset for the Gulf region does not allow the development of a Gulf-specific ϕ_{S2S} model. We, therefore, recommend the application of the CENA ϕ_{S2S} model to the Gulf region. Finally, the CENA single-station sigma models and total ergodic sigma models are considered applicable to the Gulf region.

Table 5.27 *P*-values from the *F*-test of equality of τ^2 for tectonic events in the Gulf region and the rest of CENA. Values in red indicate cases where the equality of τ^2 is rejected at 5% significance level.

	T0.10	T0.15	T0.20	T0.25	T0.30	T0.40	T0.50	T0.75	T1.00
	F10.00	F6.67	F5.00	F4.00	F3.33	F2.50	F2.00	F1.33	F1.00
CENA vs GULF_Model1	0.54	0.26	0.08	0.00	0.01	0.58	0.63	0.79	0.89
CENA vs GULF_Model2	0.48	0.61	0.63	0.09	0.25	0.58	0.88	0.92	0.77

Table 5.28 *P*-values from the *F*-test of equality of ϕ_{SS}^2 for tectonic events in the Gulf region and the rest of CENA.

	T0.10	T0.15	T0.20	T0.25	T0.30	T0.40	T0.50	T0.75	T1.00
	F10.00	F6.67	F5.00	F4.00	F3.33	F2.50	F2.00	F1.33	F1.00
CENA vs GULF_Model1	0.25	0.47	0.30	0.10	0.56	0.17	0.13	0.13	0.13
CENA vs GULF_Model2	0.43	0.26	0.21	0.06	0.48	0.12	0.09	0.05	0.09

Table 5.29 *P*-values from the *F*-test of equality of ϕ_{S2S}^2 for tectonic events in the Gulf region and the rest of CENA. Values in red indicate cases where the equality of ϕ_{S2S}^2 is rejected at 5% significance level.

	T0.10	T0.15	T0.20	T0.25	T0.30	T0.40	T0.50	T0.75	T1.00
	F10.00	F6.67	F5.00	F4.00	F3.33	F2.50	F2.00	F1.33	F1.00
CENA vs GULF_Model1	0.00	0.00	0.09	0.51	0.28	0.21	0.35	0.38	0.16
CENA vs GULF_Model2	0.00	0.01	0.14	0.68	0.40	0.28	0.60	0.97	0.41

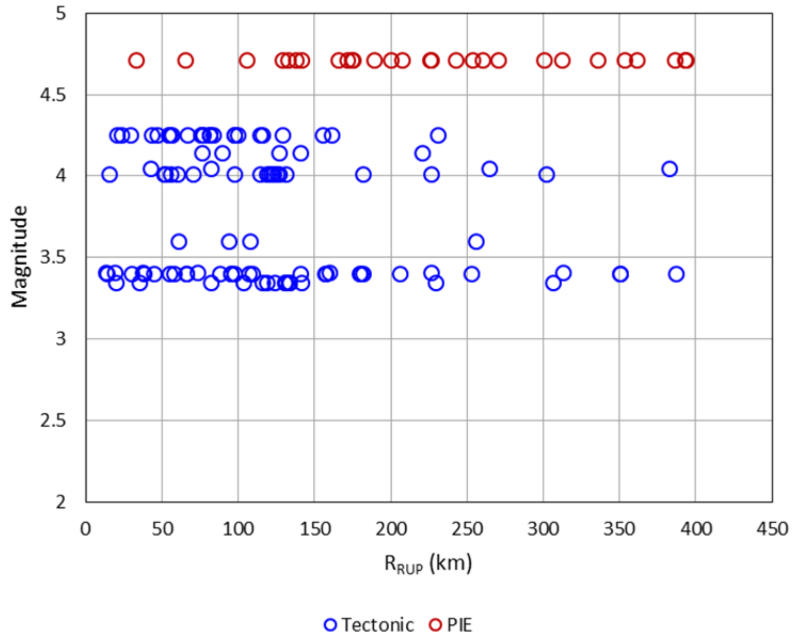

Figure 5.53 **Magnitude and distance distribution of the Gulf region data at *F* = 4 Hz.**

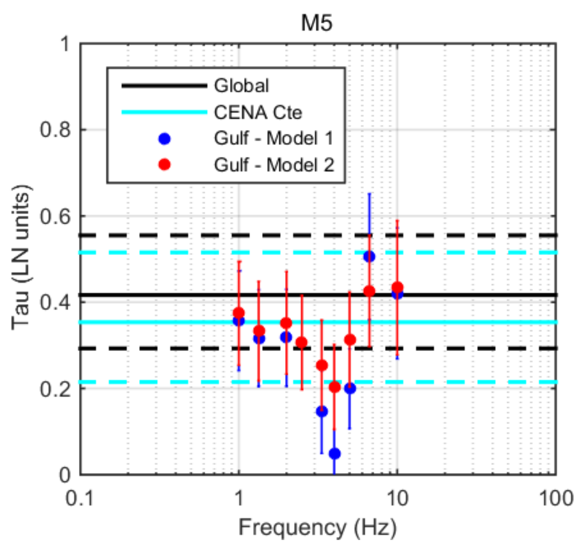

Figure 5.54 **Comparison of CENA τ models at M5.0 to τ values for the Gulf region. Dashed lines represent the 5th and 95th percentiles of the CENA models.**

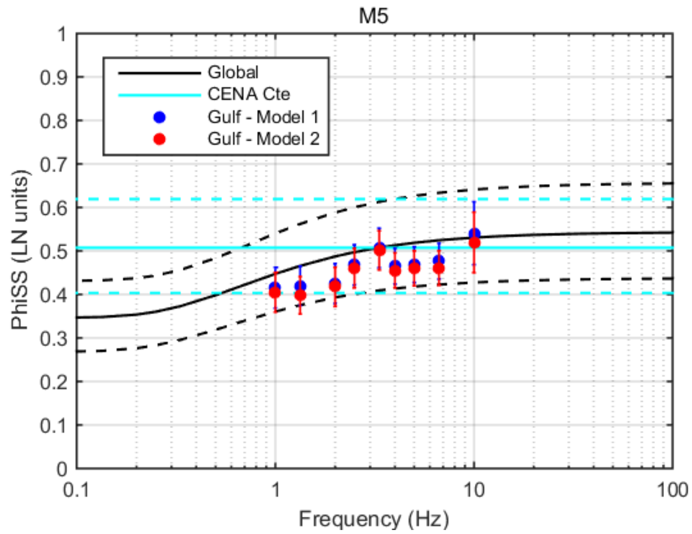

Figure 5.55 Comparison of CENA ϕ_{SS} models at M5.0 to ϕ_{SS} values for the Gulf region. Dashed lines represent the 5th and 95th percentiles of the CENA models.

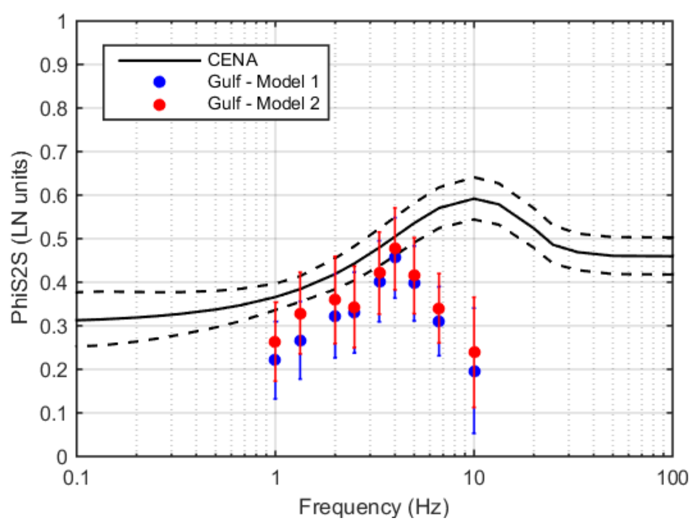

Figure 5.56 Comparison of CENA ϕ_{S2S} model to ϕ_{S2S} values for the Gulf region. Dashed lines represent the 5th and 95th percentiles of the CENA ϕ_{S2S} model.

6 Conclusions

Analysis of the components of the ground-motion variability (τ, ϕ, ϕ_{SS}, and ϕ_{S2S}) using the NGA-East CENA dataset was presented, and results were compared to those obtained for other regions particularly the NGA-West2 dataset. Ground-motion data from CENA are limited to small-to-moderate magnitudes and are limited in the frequency range to 1 to 10 Hz. As a result, CENA data cannot be reliably used to extrapolate standard deviation models to large magnitudes and to frequencies outside of 1 to 10 Hz. To address these limitations of the CENA data, standard deviation models and trends based on a global dataset were evaluated for applicability to CENA.

Candidate standard deviation models were developed for CENA for each of the components of the ground-motion variability. Three models were presented for τ to address the uncertainty in the large magnitude extrapolation: CENA constant model, CENA magnitude-dependent model, and global model. Similarly, three models were presented for ϕ_{SS}: CENA constant model, CENA magnitude-dependent model, and global model. Data from CENA were used to derive a CENA ϕ_{S2S} extrapolated to frequencies outside of 1 to 10 Hz using results from analysis of Japanese data. Mean and standard deviations of each of the candidate models were quantified. Finally, standard deviation models for single-station σ and ergodic σ were presented.

REFERENCES

Abrahamson N.A., Youngs, R. R. (1992). A stable algorithm for regression analyses using the random effects model, *Bull. Seismol. Soc. Am.,* 82(1): 505–510.

Abrahamson N.A., Silva W.J., Kamai R. (2014a). Summary of the ASK14 ground-motion relation for active crustal regions, *Earthq. Spectra*, 30(3): 1025–1055.

Abrahamson N.A., Gregor, N., and Addo, K. (2014b). BCHydro ground motion prediction equations for subduction earthquakes. *Submitted for publication to Earthquake Spectra*.

Abrahamson N.A., Silva, W.J. (2008). Summary of the Abrahamson & Silva NGA ground-motion relations, *Earthq. Spectra*, 24(1), 67-97.

Akkar S., Çağnan Z., Yenier E., Erdoğan Ö., Sandikkaya A., Gülkan P. (2010). The recently compiled Turkish strong motion database: preliminary investigation for seismological parameters, *J. Seismol*.,14: 457–479.

Akkar S., Sandikkaya M.A., Bommer J.J. (2014). Empirical ground-motion models for point- and extended-source crustal earthquake scenarios in Europe and the Middle East, *Bull. Earthq. Eng.,* 12(1): 359–387, DOI 10.1007/s10518-013-9461-4.

Al Atik L., Abrahamson N.A., Bommer J.J., Scherbaum F., Cotton F., Kuehn N. (2010). The variability of ground-motion prediction models and its components, *Seismol. Res. Lett.,* 81(5): 794−801.

Ancheta T.D., Darragh R.B., Stewart J.P., Seyhan E, Silva W.J., Chiou B.S.-J., Wooddell K.E., Graves R.W., Kottke A.R., Boore D.M., Kishida T., Donahue J.L. (2014). NGA-West2 database, Earthq. Spectra, 30: 989-1005.

Anderson J.G., Brune J.N. (1999). Probabilistic seismic hazard assessment without the ergodic assumption, *Seismol. Res. Lett.,* 70: 19−28.

Ang A.H-S., Tang W.H. (2007). *Probability Concepts in Engineering: Emphasis on Applications to Civil and Environmental Engineering*, Chichester, U.K.: John Wiley and Sons.

Atkinson G.M. (2006). Single-station sigma. *Bull. Seismol. Soc. Am.,* 96(2): 446–455.

Atkinson G.M. (2013). Empirical evaluation of aleatory and epistemic uncertainty in Eastern ground motions. *Seismol. Res. Lett.,* 84: 130−138.

Atkinson G.M., Boore, D. (1995). New ground motion relations for Eastern North America, *Bull. Seismol. Soc. Am.,* 85, 17–30.

Atkinson G.M., Adams J., Rogers G., Onur T., Assatourians, K. (2012). White paper on proposed ground-motion prediction equations (GMPEs) for 2015 National Seismic Hazard Maps. Final Version, November; available at *http://www.seismotoolbox .ca/GMPEtables2012/ri 2_GMPEs9b.pdf*.

Atkinson G.M., Boore D.M. (2006). Earthquake ground-motion prediction equations for Eastern North America, *Bull. Seismol. Soc. Am.,* 96: 2181–2205.

Atkinson G.M., Boore D.M. (2011). Modifications to existing ground-motion prediction equations in light of new data. *Bull. Seismol. Soc. Am.,* 101(3): 1121–1135.

Bommer J.J., Coppersmith K.J., Coppersmith R.T., Hanson K.L., Mangongolo A., Neveling J., Rathje E.M., Rodriguez-Marek A., Scherbaum F., Shelembe R., Stafford P.J., Strasser F.O. (2013). A SSHAC level 3 PSHA for a new-build nuclear site in South Africa, *Earthq. Spectra* (in press), DOI: 10.1193/060913EQS145M.

BC Hydro (2011). Probabilistic Seismic Hazard Assessment. Volume 3: Ground Motion Report. *Report No. E658 –* Vol. 3. February.

Boore D.M. (2005). SMSIM---Fortran programs for simulating ground motions from earthquakes: Version 2.3---A *Revision of OFR 96-80-A, U.S. Geological Survey OpenFile Report, U. S. Geological Survey Open-File Report 00-509*, revised 15 August 2005, 55 pgs. Available from the online publications link on *http://quake.usgs.gov/~boore*.

Boore D.M., Stewart J.P., Seyhan E., Atkinson, G.M. (2014). NGA-West2 equations for predicting response spectral accelerations for shallow crustal earthquakes, *Earthq. Spectra*, 30(3): 1057−1085.

Campbell K.W. (2003). Prediction of strong ground motion using the hybrid empirical method and its use in the development of ground motion (attenuation) relations in Eastern North America, *Bull. Seismol. Soc. Am.,* 93: 1012–1033.

Campbell K.W., Bozorgnia Y. (2014). NGA-West2 Campbell-Bozorgnia ground-motion model for the horizontal components of PGA, PGV, and 5%-damped elastic pseudo-acceleration response spectra for periods ranging from 0.01 to 10 sec. *Earthq. Spectra*, 30(3): 1087−1115.

Chen Y-H., Tsai, C-C.P. (2002). A new method for estimation of the attenuation relationship with variance components, *Bull. Seismol. Soc. Am.,* 92(5): 1984−1991.

Chen L., Faccioli E. (2013). Single-station standard deviation analysis of 2010–2012 strong-motion data from the Canterbury region, New Zealand, *Bull. Earthq. Eng.,* 11: 1617−1632.

Chiou B.S.-J., Youngs R., Abrahamson N.A., Addo K. (2010). Ground-motion attenuation model for small-to-moderate shallow crustal earthquakes in California and its implications on regionalization of ground-motion prediction models, *Earthq. Spectra*, 26: 907−926.

Chiou B.S.-J., Youngs, R.R. (2014). Update of the Chiou and Youngs NGA ground-motion model for average horizontal component of peak ground motion and response spectra, *Earthq. Spectra*, 30(3): 1117−1153.

Coppersmith K.J., Bommer J., Hanson K., Coppersmith R., Unruh J.R., Wolf L., Youngs R., Al Atik L., Rodriguez-Marek A., Toro G., Montaldo-Falero,V. (2014). Hanford sitewide probabilistic seismic hazard analysis, *PNNL-23361*, Pacific Northwest National Laboratory, Richland, WA.

Dawood H.M., Rodriguez-Marek A. (2015). Empirical ground motion prediction equations for active crustal earthquakes using the Japanese KiK-net database: Ergodic and site-specific formulations. Submitted for publication.

Edwards B., Fäh, D. (2013). A stochastic ground-motion model for Switzerland, *Bull. Seismol. Soc. Am.,* 103(1):78−98, doi: 10.1785/0120110331.

EPRI) (2004). CEUS ground motion project, Electrical Power Research Institute, *Final Report, EPRI Rept. TR-1009684*, Palo Alto, CA.

EPRI (2006). Program on Technology Innovation: Truncation of the lognormal distribution and value of the standard deviation for ground-motion models in the Central and Eastern United States, Electrical Power Research Institute, *EPRI Rept. 1013105*, Technical Update, Palo Alto, CA.

EPRI (2013). Ground-motion model (GMM) review project. Electrical Power Research Institute, *EPRI Rept. 3002000717*, Palo Alto, CA.

GeoPentech (2015). Southwestern United States ground motion characterization SSHAC Level 3. Technical Report Rev.2, March 2015.

Goulet C.A., Kishida T. Ancheta T D., Cramer C.H., Darragh R.B., Silva W.J., Hashash Y.M.A., Harmon J., Stewart J.P., Wooddell K.E., Youngs R.R. (2014). PEER NGA-East database, *PEER Report 2014/17,* Pacific Earthquake Engineering Research Center, University of California, Berkeley, CA.

Idriss I.M. (2014). An NGA-West2 empirical model for estimating the horizontal spectral values generated by shallow crustal earthquakes, *Earthq. Spectra,* 30(3): 1155−1177.

Keefer D.L., Bodily S.E. (1983). Three-point approximations for continuous random variables, *Management Sci.*, 29: 595–609.

Kim B., Hashash Y.M.A., Rathje E.M., Stewart J.P., Ni S., Somerville P.G., Kottke A.R., Silva W.J., Campbell K.W. (2014). Subsurface shear-wave velocity characterization using *P*-wave seismograms in Central and Eastern North America, *Earthq. Spectra*, *doi: http://dx.doi.org/10.1193/123013EQS299M.*

Lin P.-S., Chiou B., Abrahamson N.A., Walling M., Lee C.-T., Cheng, C.-T. (2011). Repeatable source, site, and path effects on the standard deviation for empirical ground-motion prediction models, *Bull. Seismol. Soc. Am.*, 101(5): 2281–2295.

Luzi L., Bindi D., Puglia R., Pacor F., Oth A. (2014). Single-station sigma for Italian strong-motion stations, *Bull. Seismol. Soc. Am.*, 104(1): 467–483.

Morikawa N., Kanno T., Narita A., Fujiwara H., Okumura T., Fukushima Y., Guerpinar A. (2008). Strong motion uncertainty determined from observed records by dense network in Japan, *J. Seismol.*, 12(4): 529–546.

PEER (2015a). NGA-East: Median Ground-Motion Models for the Central and Eastern North America Region, *PEER Report No. 2015/04*, Pacific Earthquake Engineering Research Center, University of California, Berkeley, CA.

PEER (2015b). NGA-East: Adjustments to Median Ground-Motion Models for Central and Eastern North America, *PEER Report No. 2015/08*, Pacific Earthquake Engineering Research Center, University of California, Berkeley, CA. *(in prep.)*

Pezeshk S., Zandieh A., Tavakoli B. (2011). Hybrid empirical ground-motion prediction equations for Eastern North America using NGA models and updated seismological parameters, *Bull. Seismol. Soc. Am.,* 101: 1859–1870.

Renault P., Heuberger S., Abrahamson, N.A. (2010). PEGASOS Refinement Project: An improved PSHA for Swiss nuclear power plants, *Proceedings, 14th European Conference of Earthquake Engineering*, Ohrid, Republic of Macedonia, Paper ID 991.

Rodriguez-Marek A., Montalva G.A., Cotton F., Bonilla F. (2011). Analysis of single-station standard deviation using the KiK-net data, *Bull. Seismol. Soc. Am.*, 101: 1242–1258.

Rodriguez-Marek A., Cotton F., Abrahamson N.A., Akkar S., Al Atik L., Edwards B., Montalva G.A., Dawood H.M. (2013). A model for single-station standard deviation using data from various tectonic regions, *Bull. Seismol. Soc. Am.*, 103: 3149–3163.

Rodriguez-Marek A., Rathje, E.M., Bommer, J.J., Scherbaum, F., and Stafford, P.J. (2014). Application of single-station sigma and site-response characterization in a probabilistic seismic-hazard analysis for a new nuclear site. *Bull. Seismol. Soc. Am.,* 104:1601-1619, DOI: 10.1785/0120130196.

Tavakoli, B., Pezeshk, S. (2005). Empirical-stochastic ground-motion prediction for Eastern North America. *Bull. Seismol. Soc. Am.*, 95(6): 2283–2296.

Silva W.J., Gregor N., Darragh R. (2002). Development of regional hard rock attenuation relations for Central and Eastern North America, *Technical Report*, Pacific Engineering and Analysis, El Cerrito, CA.

Thompson E., Silva W.J. (2013) Empirical assessment of site amplification and development of NEHRP factors for CEUS: collaborative research with Pacific Engineering and Tufts University, *Report to USGS*, *http://earthquake.usgs.gov/research/external/reports/G12AP20003.pdf*.

Toro G.R., Abrahamson N.A., Schneider J.F. (1997). Model of strong ground motions from earthquakes in Central and Eastern North America: Best estimates and uncertainties, *Seismol. Res. Lett.,* 68: 41–57.

Zhao J.X., Zhang J., Asano A., Ohno Y., Oouchi T., Takahashi T., Ogawa H., Irikura K., Thio H.K., Somerville P.G., Fukushima Y., Fukushima Y. (2006). Attenuation relations of strong ground motion in Japan using site classification based on predominant period, *Bull. Seismol. Soc. Am*., 96(3): 898–913.

PEER REPORTS

PEER reports are available as a free PDF download from http://peer.berkeley.edu/publications/peer_reports_complete.html. Printed hard copies of PEER reports can be ordered directly from our printer by following the instructions at http://peer.berkeley.edu/publications/peer_reports.html. For other related questions about the PEER Report Series, contact the Pacific Earthquake Engineering Research Center, 325 Davis Hall mail code 1792, Berkeley, CA 94720. Tel.: (510) 642-3437; Fax: (510) 665-1655; Email: peer_editor@berkeley.edu

PEER 2015/07 *NGA-East: Ground-Motion Standard-Deviation Models for Central and Eastern North America.* Linda Al Atik. June 2015.

PEER 2015/06 *Adjusting Ground-Motion Intensity Measures to a Reference Site for which V_{S30} = 3000 m/sec.* David M. Boore. May 2015.

PEER 2015/05 *Hybrid Simulation of Seismic Isolation Systems Applied to an APR-1400 Nuclear Power Plant.* Andreas H. Schellenberg, Alireza Sarebanha, Matthew J. Schoettler, Gilberto Mosqueda, Gianmario Benzoni, and Stephen A. Mahin. April 2015.

PEER 2015/04 *NGA-East: Median Ground-Motion Models for the Central and Eastern North America Region.* April 2015.

PEER 2015/03 *Single Series Solution for the Rectangular Fiber-Reinforced Elastomeric Isolator Compression Modulus.* James M. Kelly and Niel C. Van Engelen. March 2015.

PEER 2015/02 *A Full-Scale, Single-Column Bridge Bent Tested by Shake-Table Excitation.* Matthew J. Schoettler, José I. Restrepo, Gabriele Guerrini, David E. Duck, and Francesco Carrea. March 2015.

PEER 2015/01 *Concrete Column Blind Prediction Contest 2010: Outcomes and Observations.* Vesna Terzic, Matthew J. Schoettler, José I. Restrepo, and Stephen A Mahin. March 2015.

PEER 2014/20 *Stochastic Modeling and Simulation of Near-Fault Ground Motions for Performance-Based Earthquake Engineering.* Mayssa Dabaghi and Armen Der Kiureghian. December 2014.

PEER 2014/19 *Seismic Response of a Hybrid Fiber-Reinforced Concrete Bridge Column Detailed for Accelerated Bridge Construction.* Wilson Nguyen, William Trono, Marios Panagiotou, and Claudia P. Ostertag. December 2014.

PEER 2014/18 *Three-Dimensional Beam-Truss Model for Reinforced Concrete Walls and Slabs Subjected to Cyclic Static or Dynamic Loading.* Yuan Lu, Marios Panagiotou, and Ioannis Koutromanos. December 2014.

PEER 2014/17 *PEER NGA-East Database.* Christine A. Goulet, Tadahiro Kishida, Timothy D. Ancheta, Chris H. Cramer, Robert B. Darragh, Walter J. Silva, Youssef M.A. Hashash, Joseph Harmon, Jonathan P. Stewart, Katie E. Wooddell, and Robert R. Youngs. October 2014.

PEER 2014/16 *Guidelines for Performing Hazard-Consistent One-Dimensional Ground Response Analysis for Ground Motion Prediction.* Jonathan P. Stewart, Kioumars Afshari, and Youssef M.A. Hashash. October 2014.

PEER 2014/15 *NGA-East Regionalization Report: Comparison of Four Crustal Regions within Central and Eastern North America using Waveform Modeling and 5%-Damped Pseudo-Spectral Acceleration Response*. Jennifer Dreiling, Marius P. Isken, Walter D. Mooney, Martin C. Chapman, and Richard W. Godbee. October 2014.

PEER 2014/14 *Scaling Relations between Seismic Moment and Rupture Area of Earthquakes in Stable Continental Regions*. Paul Somerville. August 2014.

PEER 2014/13 *PEER Preliminary Notes and Observations on the August 24, 2014, South Napa Earthquake*. Grace S. Kang (Editor), Stephen A. Mahin (Editors). September 2014.

PEER 2014/12 *Reference-Rock Site Conditions for Central and Eastern North America: Part II – Attenuation (Kappa) Definition*. Kenneth W. Campbell, Youssef M.A. Hashash, Byungmin Kim, Albert R. Kottke, Ellen M. Rathje, Walter J. Silva, and Jonathan P. Stewart. August 2014.

PEER 2014/11 *Reference-Rock Site Conditions for Central and Eastern North America: Part I - Velocity Definition*. Youssef M.A. Hashash, Albert R. Kottke, Jonathan P. Stewart, Kenneth W. Campbell, Byungmin Kim, Ellen M. Rathje, Walter J. Silva, Sissy Nikolaou, and Cheryl Moss. August 2014.

PEER 2014/10 *Evaluation of Collapse and Non-Collapse of Parallel Bridges Affected by Liquefaction and Lateral Spreading*. Benjamin Turner, Scott J. Brandenberg, and Jonathan P. Stewart. August 2014.

PEER 2014/09 *PEER Arizona Strong-Motion Database and GMPEs Evaluation*. Tadahiro Kishida, Robert E. Kayen, Olga-Joan Ktenidou, Walter J. Silva, Robert B. Darragh, and Jennie Watson-Lamprey. June 2014.

PEER 2014/08 *Unbonded Pretensioned Bridge Columns with Rocking Detail*. Jeffrey A. Schaefer, Bryan Kennedy, Marc O. Eberhard, John F. Stanton. June 2014.

PEER 2014/07 *Northridge 20 Symposium Summary Report: Impacts, Outcomes, and Next Steps*. May 2014.

PEER 2014/06 *Report of the Tenth Planning Meeting of NEES/E-Defense Collaborative Research on Earthquake Engineering*. December 2013.

PEER 2014/05 *Seismic Velocity Site Characterization of Thirty-One Chilean Seismometer Stations by Spectral Analysis of Surface Wave Dispersion.* Robert Kayen, Brad D. Carkin, Skye Corbet, Camilo Pinilla, Allan Ng, Edward Gorbis, and Christine Truong. April 2014.

PEER 2014/04 *Effect of Vertical Acceleration on Shear Strength of Reinforced Concrete Columns.* Hyerin Lee and Khalid M. Mosalam. April 2014.

PEER 2014/03 *Retest of Thirty-Year-Old Neoprene Isolation Bearings.* James M. Kelly and Niel C. Van Engelen. March 2014.

PEER 2014/02 *Theoretical Development of Hybrid Simulation Applied to Plate Structures.* Ahmed A. Bakhaty, Khalid M. Mosalam, and Sanjay Govindjee. January 2014.

PEER 2014/01 *Performance-Based Seismic Assessment of Skewed Bridges.* Peyman Kaviani, Farzin Zareian, and Ertugrul Taciroglu. January 2014.

PEER 2013/26 *Urban Earthquake Engineering. Proceedings of the U.S.-Iran Seismic Workshop.* December 2013.

PEER 2013/25 *Earthquake Engineering for Resilient Communities: 2013 PEER Internship Program Research Report Collection.* Heidi Tremayne (Editor), Stephen A. Mahin (Editor), Jorge Archbold Monterossa, Matt Brosman, Shelly Dean, Katherine deLaveaga, Curtis Fong, Donovan Holder, Rakeeb Khan, Elizabeth Jachens, David Lam, Daniela Martinez Lopez, Mara Minner, Geffen Oren, Julia Pavicic, Melissa Quinonez, Lorena Rodriguez, Sean Salazar, Kelli Slaven, Vivian Steyert, Jenny Taing, and Salvador Tena. December 2013.

PEER 2013/24 *NGA-West2 Ground Motion Prediction Equations for Vertical Ground Motions.* September 2013.

PEER 2013/23 *Coordinated Planning and Preparedness for Fire Following Major Earthquakes.* Charles Scawthorn. November 2013.

PEER 2013/22 *GEM-PEER Task 3 Project: Selection of a Global Set of Ground Motion Prediction Equations.* Jonathan P. Stewart, John Douglas, Mohammad B. Javanbarg, Carola Di Alessandro, Yousef Bozorgnia, Norman A. Abrahamson, David M. Boore, Kenneth W. Campbell, Elise Delavaud, Mustafa Erdik and Peter J. Stafford. December 2013.

PEER 2013/21 *Seismic Design and Performance of Bridges with Columns on Rocking Foundations.* Grigorios Antonellis and Marios Panagiotou. September 2013.

PEER 2013/20 *Experimental and Analytical Studies on the Seismic Behavior of Conventional and Hybrid Braced Frames.* Jiun-Wei Lai and Stephen A. Mahin. September 2013.

PEER 2013/19 *Toward Resilient Communities: A Performance-Based Engineering Framework for Design and Evaluation of the Built Environment.* Michael William Mieler, Bozidar Stojadinovic, Robert J. Budnitz, Stephen A. Mahin and Mary C. Comerio. September 2013.

PEER 2013/18 *Identification of Site Parameters that Improve Predictions of Site Amplification.* Ellen M. Rathje and Sara Navidi. July 2013.

PEER 2013/17 *Response Spectrum Analysis of Concrete Gravity Dams Including Dam-Water-Foundation Interaction.* Arnkjell Løkke and Anil K. Chopra. July 2013.

PEER 2013/16 *Effect of hoop reinforcement spacing on the cyclic response of large reinforced concrete special moment frame beams.* Marios Panagiotou, Tea Visnjic, Grigorios Antonellis, Panagiotis Galanis, and Jack P. Moehle. June 2013.

PEER 2013/15 *A Probabilistic Framework to Include the Effects of Near-Fault Directivity in Seismic Hazard Assessment.* Shrey Kumar Shahi, Jack W. Baker. October 2013.

PEER 2013/14 *Hanging-Wall Scaling using Finite-Fault Simulations.* Jennifer L. Donahue and Norman A. Abrahamson. September 2013.

PEER 2013/13 *Semi-Empirical Nonlinear Site Amplification and its Application in NEHRP Site Factors.* Jonathan P. Stewart and Emel Seyhan. November 2013.

PEER 2013/12 *Nonlinear Horizontal Site Response for the NGA-West2 Project.* Ronnie Kamai, Norman A. Abramson, Walter J. Silva. May 2013.

PEER 2013/11 *Epistemic Uncertainty for NGA-West2 Models.* Linda Al Atik and Robert R. Youngs. May 2013.

PEER 2013/10 *NGA-West 2 Models for Ground-Motion Directionality.* Shrey K. Shahi and Jack W. Baker. May 2013.

PEER 2013/09 *Final Report of the NGA-West2 Directivity Working Group.* Paul Spudich, Jeffrey R. Bayless, Jack W. Baker, Brian S.J. Chiou, Badie Rowshandel, Shrey Shahi, and Paul Somerville. May 2013.

PEER 2013/08 *NGA-West2 Model for Estimating Average Horizontal Values of Pseudo-Absolute Spectral Accelerations Generated by Crustal Earthquakes.* I. M. Idriss. May 2013.

PEER 2013/07 *Update of the Chiou and Youngs NGA Ground Motion Model for Average Horizontal Component of Peak Ground Motion and Response Spectra.* Brian Chiou and Robert Youngs. May 2013.

PEER 2013/06 *NGA-West2 Campbell-Bozorgnia Ground Motion Model for the Horizontal Components of PGA, PGV, and 5%-Damped Elastic Pseudo-Acceleration Response Spectra for Periods Ranging from 0.01 to 10 sec.* Kenneth W. Campbell and Yousef Bozorgnia. May 2013.

PEER 2013/05 *NGA-West 2 Equations for Predicting Response Spectral Accelerations for Shallow Crustal Earthquakes.* David M. Boore, Jonathan P. Stewart, Emel Seyhan, Gail M. Atkinson. May 2013.

PEER 2013/04 *Update of the AS08 Ground-Motion Prediction Equations Based on the NGA-West2 Data Set.* Norman Abrahamson, Walter Silva, and Ronnie Kamai. May 2013.

PEER 2013/03 *PEER NGA-West2 Database.* Timothy D. Ancheta, Robert B. Darragh, Jonathan P. Stewart, Emel Seyhan, Walter J. Silva, Brian S.J. Chiou, Katie E. Wooddell, Robert W. Graves, Albert R. Kottke, David M. Boore, Tadahiro Kishida, and Jennifer L. Donahue. May 2013.

PEER 2013/02 *Hybrid Simulation of the Seismic Response of Squat Reinforced Concrete Shear Walls.* Catherine A. Whyte and Bozidar Stojadinovic. May 2013.

PEER 2013/01 *Housing Recovery in Chile: A Qualitative Mid-program Review.* Mary C. Comerio. February 2013.

PEER 2012/08 *Guidelines for Estimation of Shear Wave Velocity.* Bernard R. Wair, Jason T. DeJong, and Thomas Shantz. December 2012.

PEER 2012/07 *Earthquake Engineering for Resilient Communities: 2012 PEER Internship Program Research Report Collection.* Heidi Tremayne (Editor), Stephen A. Mahin (Editor), Collin Anderson, Dustin Cook, Michael Erceg, Carlos Esparza, Jose Jimenez, Dorian Krausz, Andrew Lo, Stephanie Lopez, Nicole McCurdy, Paul Shipman, Alexander Strum, Eduardo Vega. December 2012.

PEER 2012/06 *Fragilities for Precarious Rocks at Yucca Mountain.* Matthew D. Purvance, Rasool Anooshehpoor, and James N. Brune. December 2012.

PEER 2012/05 *Development of Simplified Analysis Procedure for Piles in Laterally Spreading Layered Soils.* Christopher R. McGann, Pedro Arduino, and Peter Mackenzie–Helnwein. December 2012.

PEER 2012/04 *Unbonded Pre-Tensioned Columns for Bridges in Seismic Regions.* Phillip M. Davis, Todd M. Janes, Marc O. Eberhard, and John F. Stanton. December 2012.

PEER 2012/03 *Experimental and Analytical Studies on Reinforced Concrete Buildings with Seismically Vulnerable Beam-Column Joints.* Sangjoon Park and Khalid M. Mosalam. October 2012.

PEER 2012/02 *Seismic Performance of Reinforced Concrete Bridges Allowed to Uplift during Multi-Directional Excitation.* Andres Oscar Espinoza and Stephen A. Mahin. July 2012.

PEER 2012/01 *Spectral Damping Scaling Factors for Shallow Crustal Earthquakes in Active Tectonic Regions.* Sanaz Rezaeian, Yousef Bozorgnia, I. M. Idriss, Kenneth Campbell, Norman Abrahamson, and Walter Silva. July 2012.

PEER 2011/10 *Earthquake Engineering for Resilient Communities: 2011 PEER Internship Program Research Report Collection.* Eds. Heidi Faison and Stephen A. Mahin. December 2011.

PEER 2011/09 *Calibration of Semi-Stochastic Procedure for Simulating High-Frequency Ground Motions.* Jonathan P. Stewart, Emel Seyhan, and Robert W. Graves. December 2011.

PEER 2011/08 *Water Supply in regard to Fire Following Earthquake.* Charles Scawthorn. November 2011.

PEER 2011/07 *Seismic Risk Management in Urban Areas. Proceedings of a U.S.-Iran-Turkey Seismic Workshop.* September 2011.

PEER 2011/06 *The Use of Base Isolation Systems to Achieve Complex Seismic Performance Objectives.* Troy A. Morgan and Stephen A. Mahin. July 2011.

PEER 2011/05 *Case Studies of the Seismic Performance of Tall Buildings Designed by Alternative Means.* Task 12 Report for the Tall Buildings Initiative. Jack Moehle, Yousef Bozorgnia, Nirmal Jayaram, Pierson Jones, Mohsen Rahnama, Nilesh Shome, Zeynep Tuna, John Wallace, Tony Yang, and Farzin Zareian. July 2011.

PEER 2011/04 *Recommended Design Practice for Pile Foundations in Laterally Spreading Ground.* Scott A. Ashford, Ross W. Boulanger, and Scott J. Brandenberg. June 2011.

PEER 2011/03 *New Ground Motion Selection Procedures and Selected Motions for the PEER Transportation Research Program.* Jack W. Baker, Ting Lin, Shrey K. Shahi, and Nirmal Jayaram. March 2011.

PEER 2011/02 *A Bayesian Network Methodology for Infrastructure Seismic Risk Assessment and Decision Support.* Michelle T. Bensi, Armen Der Kiureghian, and Daniel Straub. March 2011.

PEER 2011/01 *Demand Fragility Surfaces for Bridges in Liquefied and Laterally Spreading Ground.* Scott J. Brandenberg, Jian Zhang, Pirooz Kashighandi, Yili Huo, and Minxing Zhao. March 2011.

PEER 2010/05 *Guidelines for Performance-Based Seismic Design of Tall Buildings.* Developed by the Tall Buildings Initiative. November 2010.

PEER 2010/04 *Application Guide for the Design of Flexible and Rigid Bus Connections between Substation Equipment Subjected to Earthquakes.* Jean-Bernard Dastous and Armen Der Kiureghian. September 2010.

PEER 2010/03 *Shear Wave Velocity as a Statistical Function of Standard Penetration Test Resistance and Vertical Effective Stress at Caltrans Bridge Sites.* Scott J. Brandenberg, Naresh Bellana, and Thomas Shantz. June 2010.

PEER 2010/02 *Stochastic Modeling and Simulation of Ground Motions for Performance-Based Earthquake Engineering.* Sanaz Rezaeian and Armen Der Kiureghian. June 2010.

PEER 2010/01 *Structural Response and Cost Characterization of Bridge Construction Using Seismic Performance Enhancement Strategies.* Ady Aviram, Božidar Stojadinović, Gustavo J. Parra-Montesinos, and Kevin R. Mackie. March 2010.

PEER 2009/03 *The Integration of Experimental and Simulation Data in the Study of Reinforced Concrete Bridge Systems Including Soil-Foundation-Structure Interaction.* Matthew Dryden and Gregory L. Fenves. November 2009.

PEER 2009/02 *Improving Earthquake Mitigation through Innovations and Applications in Seismic Science, Engineering, Communication, and Response. Proceedings of a U.S.-Iran Seismic Workshop.* October 2009.

PEER 2009/01 *Evaluation of Ground Motion Selection and Modification Methods: Predicting Median Interstory Drift Response of Buildings.* Curt B. Haselton, Ed. June 2009.

PEER 2008/10 *Technical Manual for Strata.* Albert R. Kottke and Ellen M. Rathje. February 2009.

PEER 2008/09 *NGA Model for Average Horizontal Component of Peak Ground Motion and Response Spectra.* Brian S.-J. Chiou and Robert R. Youngs. November 2008.

PEER 2008/08 *Toward Earthquake-Resistant Design of Concentrically Braced Steel Structures.* Patxi Uriz and Stephen A. Mahin. November 2008.

PEER 2008/07 *Using OpenSees for Performance-Based Evaluation of Bridges on Liquefiable Soils.* Stephen L. Kramer, Pedro Arduino, and HyungSuk Shin. November 2008.

PEER 2008/06 *Shaking Table Tests and Numerical Investigation of Self-Centering Reinforced Concrete Bridge Columns.* Hyung IL Jeong, Junichi Sakai, and Stephen A. Mahin. September 2008.

PEER 2008/05 *Performance-Based Earthquake Engineering Design Evaluation Procedure for Bridge Foundations Undergoing Liquefaction-Induced Lateral Ground Displacement.* Christian A. Ledezma and Jonathan D. Bray. August 2008.

PEER 2008/04 *Benchmarking of Nonlinear Geotechnical Ground Response Analysis Procedures.* Jonathan P. Stewart, Annie On-Lei Kwok, Yousseff M. A. Hashash, Neven Matasovic, Robert Pyke, Zhiliang Wang, and Zhaohui Yang. August 2008.

PEER 2008/03 *Guidelines for Nonlinear Analysis of Bridge Structures in California.* Ady Aviram, Kevin R. Mackie, and Božidar Stojadinović. August 2008.

PEER 2008/02 *Treatment of Uncertainties in Seismic-Risk Analysis of Transportation Systems.* Evangelos Stergiou and Anne S. Kiremidjian. July 2008.

PEER 2008/01 *Seismic Performance Objectives for Tall Buildings.* William T. Holmes, Charles Kircher, William Petak, and Nabih Youssef. August 2008.

PEER 2007/12 *An Assessment to Benchmark the Seismic Performance of a Code-Conforming Reinforced Concrete Moment-Frame Building.* Curt Haselton, Christine A. Goulet, Judith Mitrani-Reiser, James L. Beck, Gregory G. Deierlein, Keith A. Porter, Jonathan P. Stewart, and Ertugrul Taciroglu. August 2008.

PEER 2007/11 *Bar Buckling in Reinforced Concrete Bridge Columns.* Wayne A. Brown, Dawn E. Lehman, and John F. Stanton. February 2008.

PEER 2007/10 *Computational Modeling of Progressive Collapse in Reinforced Concrete Frame Structures.* Mohamed M. Talaat and Khalid M. Mosalam. May 2008.

PEER 2007/09 *Integrated Probabilistic Performance-Based Evaluation of Benchmark Reinforced Concrete Bridges.* Kevin R. Mackie, John-Michael Wong, and Božidar Stojadinović. January 2008.

PEER 2007/08 *Assessing Seismic Collapse Safety of Modern Reinforced Concrete Moment-Frame Buildings.* Curt B. Haselton and Gregory G. Deierlein. February 2008.

PEER 2007/07 *Performance Modeling Strategies for Modern Reinforced Concrete Bridge Columns.* Michael P. Berry and Marc O. Eberhard. April 2008.

PEER 2007/06 *Development of Improved Procedures for Seismic Design of Buried and Partially Buried Structures.* Linda Al Atik and Nicholas Sitar. June 2007.

PEER 2007/05 *Uncertainty and Correlation in Seismic Risk Assessment of Transportation Systems.* Renee G. Lee and Anne S. Kiremidjian. July 2007.

PEER 2007/04 *Numerical Models for Analysis and Performance-Based Design of Shallow Foundations Subjected to Seismic Loading.* Sivapalan Gajan, Tara C. Hutchinson, Bruce L. Kutter, Prishati Raychowdhury, José A. Ugalde, and Jonathan P. Stewart. May 2008.

PEER 2007/03 *Beam-Column Element Model Calibrated for Predicting Flexural Response Leading to Global Collapse of RC Frame Buildings.* Curt B. Haselton, Abbie B. Liel, Sarah Taylor Lange, and Gregory G. Deierlein. May 2008.

PEER 2007/02 *Campbell-Bozorgnia NGA Ground Motion Relations for the Geometric Mean Horizontal Component of Peak and Spectral Ground Motion Parameters.* Kenneth W. Campbell and Yousef Bozorgnia. May 2007.

PEER 2007/01 *Boore-Atkinson NGA Ground Motion Relations for the Geometric Mean Horizontal Component of Peak and Spectral Ground Motion Parameters.* David M. Boore and Gail M. Atkinson. May. May 2007.

PEER 2006/12 *Societal Implications of Performance-Based Earthquake Engineering.* Peter J. May. May 2007.

PEER 2006/11 *Probabilistic Seismic Demand Analysis Using Advanced Ground Motion Intensity Measures, Attenuation Relationships, and Near-Fault Effects.* Polsak Tothong and C. Allin Cornell. March 2007.

PEER 2006/10 *Application of the PEER PBEE Methodology to the I-880 Viaduct.* Sashi Kunnath. February 2007.

PEER 2006/09 *Quantifying Economic Losses from Travel Forgone Following a Large Metropolitan Earthquake.* James Moore, Sungbin Cho, Yue Yue Fan, and Stuart Werner. November 2006.

PEER 2006/08 *Vector-Valued Ground Motion Intensity Measures for Probabilistic Seismic Demand Analysis*. Jack W. Baker and C. Allin Cornell. October 2006.

PEER 2006/07 *Analytical Modeling of Reinforced Concrete Walls for Predicting Flexural and Coupled–Shear-Flexural Responses*. Kutay Orakcal, Leonardo M. Massone, and John W. Wallace. October 2006.

PEER 2006/06 *Nonlinear Analysis of a Soil-Drilled Pier System under Static and Dynamic Axial Loading.* Gang Wang and Nicholas Sitar. November 2006.

PEER 2006/05 *Advanced Seismic Assessment Guidelines.* Paolo Bazzurro, C. Allin Cornell, Charles Menun, Maziar Motahari, and Nicolas Luco. September 2006.

PEER 2006/04 *Probabilistic Seismic Evaluation of Reinforced Concrete Structural Components and Systems.* Tae Hyung Lee and Khalid M. Mosalam. August 2006.

PEER 2006/03 *Performance of Lifelines Subjected to Lateral Spreading.* Scott A. Ashford and Teerawut Juirnarongrit. July 2006.

PEER 2006/02 *Pacific Earthquake Engineering Research Center Highway Demonstration Project.* Anne Kiremidjian, James Moore, Yue Yue Fan, Nesrin Basoz, Ozgur Yazali, and Meredith Williams. April 2006.

PEER 2006/01 *Bracing Berkeley. A Guide to Seismic Safety on the UC Berkeley Campus.* Mary C. Comerio, Stephen Tobriner, and Ariane Fehrenkamp. January 2006.

PEER 2005/16 *Seismic Response and Reliability of Electrical Substation Equipment and Systems.* Junho Song, Armen Der Kiureghian, and Jerome L. Sackman. April 2006.

PEER 2005/15 *CPT-Based Probabilistic Assessment of Seismic Soil Liquefaction Initiation.* R. E. S. Moss, R. B. Seed, R. E. Kayen, J. P. Stewart, and A. Der Kiureghian. April 2006.

PEER 2005/14 *Workshop on Modeling of Nonlinear Cyclic Load-Deformation Behavior of Shallow Foundations.* Bruce L. Kutter, Geoffrey Martin, Tara Hutchinson, Chad Harden, Sivapalan Gajan, and Justin Phalen. March 2006.

PEER 2005/13 *Stochastic Characterization and Decision Bases under Time-Dependent Aftershock Risk in Performance-Based Earthquake Engineering.* Gee Liek Yeo and C. Allin Cornell. July 2005.

PEER 2005/12 *PEER Testbed Study on a Laboratory Building: Exercising Seismic Performance Assessment.* Mary C. Comerio, editor. November 2005.

PEER 2005/11 *Van Nuys Hotel Building Testbed Report: Exercising Seismic Performance Assessment.* Helmut Krawinkler, editor. October 2005.

PEER 2005/10 *First NEES/E-Defense Workshop on Collapse Simulation of Reinforced Concrete Building Structures.* September 2005.

PEER 2005/09 *Test Applications of Advanced Seismic Assessment Guidelines.* Joe Maffei, Karl Telleen, Danya Mohr, William Holmes, and Yuki Nakayama. August 2006.

PEER 2005/08 *Damage Accumulation in Lightly Confined Reinforced Concrete Bridge Columns.* R. Tyler Ranf, Jared M. Nelson, Zach Price, Marc O. Eberhard, and John F. Stanton. April 2006.

PEER 2005/07 *Experimental and Analytical Studies on the Seismic Response of Freestanding and Anchored Laboratory Equipment.* Dimitrios Konstantinidis and Nicos Makris. January 2005.

PEER 2005/06 *Global Collapse of Frame Structures under Seismic Excitations*. Luis F. Ibarra and Helmut Krawinkler. September 2005.

PEER 2005//05 *Performance Characterization of Bench- and Shelf-Mounted Equipment.* Samit Ray Chaudhuri and Tara C. Hutchinson. May 2006.

PEER 2005/04 *Numerical Modeling of the Nonlinear Cyclic Response of Shallow Foundations.* Chad Harden, Tara Hutchinson, Geoffrey R. Martin, and Bruce L. Kutter. August 2005.

PEER 2005/03 *A Taxonomy of Building Components for Performance-Based Earthquake Engineering.* Keith A. Porter. September 2005.

PEER 2005/02 *Fragility Basis for California Highway Overpass Bridge Seismic Decision Making*. Kevin R. Mackie and Božidar Stojadinović. June 2005.

PEER 2005/01 *Empirical Characterization of Site Conditions on Strong Ground Motion.* Jonathan P. Stewart, Yoojoong Choi, and Robert W. Graves. June 2005.

PEER 2004/09 *Electrical Substation Equipment Interaction: Experimental Rigid Conductor Studies.* Christopher Stearns and André Filiatrault. February 2005.

PEER 2004/08 *Seismic Qualification and Fragility Testing of Line Break 550-kV Disconnect Switches.* Shakhzod M. Takhirov, Gregory L. Fenves, and Eric Fujisaki. January 2005.

PEER 2004/07 *Ground Motions for Earthquake Simulator Qualification of Electrical Substation Equipment.* Shakhzod M. Takhirov, Gregory L. Fenves, Eric Fujisaki, and Don Clyde. January 2005.

PEER 2004/06 *Performance-Based Regulation and Regulatory Regimes.* Peter J. May and Chris Koski. September 2004.

PEER 2004/05 *Performance-Based Seismic Design Concepts and Implementation: Proceedings of an International Workshop.* Peter Fajfar and Helmut Krawinkler, editors. September 2004.

PEER 2004/04 *Seismic Performance of an Instrumented Tilt-up Wall Building.* James C. Anderson and Vitelmo V. Bertero. July 2004.

PEER 2004/03 *Evaluation and Application of Concrete Tilt-up Assessment Methodologies.* Timothy Graf and James O. Malley. October 2004.

PEER 2004/02 *Analytical Investigations of New Methods for Reducing Residual Displacements of Reinforced Concrete Bridge Columns.* Junichi Sakai and Stephen A. Mahin. August 2004.

PEER 2004/01 *Seismic Performance of Masonry Buildings and Design Implications.* Kerri Anne Taeko Tokoro, James C. Anderson, and Vitelmo V. Bertero. February 2004.

PEER 2003/18 *Performance Models for Flexural Damage in Reinforced Concrete Columns.* Michael Berry and Marc Eberhard. August 2003.

PEER 2003/17 *Predicting Earthquake Damage in Older Reinforced Concrete Beam-Column Joints.* Catherine Pagni and Laura Lowes. October 2004.

PEER 2003/16 *Seismic Demands for Performance-Based Design of Bridges.* Kevin Mackie and Božidar Stojadinović. August 2003.

PEER 2003/15 *Seismic Demands for Nondeteriorating Frame Structures and Their Dependence on Ground Motions.* Ricardo Antonio Medina and Helmut Krawinkler. May 2004.

PEER 2003/14 *Finite Element Reliability and Sensitivity Methods for Performance-Based Earthquake Engineering.* Terje Haukaas and Armen Der Kiureghian. April 2004.

PEER 2003/13 *Effects of Connection Hysteretic Degradation on the Seismic Behavior of Steel Moment-Resisting Frames.* Janise E. Rodgers and Stephen A. Mahin. March 2004.

PEER 2003/12 *Implementation Manual for the Seismic Protection of Laboratory Contents: Format and Case Studies.* William T. Holmes and Mary C. Comerio. October 2003.

PEER 2003/11 *Fifth U.S.-Japan Workshop on Performance-Based Earthquake Engineering Methodology for Reinforced Concrete Building Structures.* February 2004.

PEER 2003/10 *A Beam-Column Joint Model for Simulating the Earthquake Response of Reinforced Concrete Frames.* Laura N. Lowes, Nilanjan Mitra, and Arash Altoontash. February 2004.

PEER 2003/09 *Sequencing Repairs after an Earthquake: An Economic Approach.* Marco Casari and Simon J. Wilkie. April 2004.

PEER 2003/08 *A Technical Framework for Probability-Based Demand and Capacity Factor Design (DCFD) Seismic Formats*. Fatemeh Jalayer and C. Allin Cornell. November 2003.

PEER 2003/07 *Uncertainty Specification and Propagation for Loss Estimation Using FOSM Methods.* Jack W. Baker and C. Allin Cornell. September 2003.

PEER 2003/06 *Performance of Circular Reinforced Concrete Bridge Columns under Bidirectional Earthquake Loading*. Mahmoud M. Hachem, Stephen A. Mahin, and Jack P. Moehle. February 2003.

PEER 2003/05 *Response Assessment for Building-Specific Loss Estimation.* Eduardo Miranda and Shahram Taghavi. September 2003.

PEER 2003/04 *Experimental Assessment of Columns with Short Lap Splices Subjected to Cyclic Loads*. Murat Melek, John W. Wallace, and Joel Conte. April 2003.

PEER 2003/03 *Probabilistic Response Assessment for Building-Specific Loss Estimation.* Eduardo Miranda and Hesameddin Aslani. September 2003.

PEER 2003/02 *Software Framework for Collaborative Development of Nonlinear Dynamic Analysis Program.* Jun Peng and Kincho H. Law. September 2003.

PEER 2003/01 *Shake Table Tests and Analytical Studies on the Gravity Load Collapse of Reinforced Concrete Frames.* Kenneth John Elwood and Jack P. Moehle. November 2003.

PEER 2002/24 *Performance of Beam to Column Bridge Joints Subjected to a Large Velocity Pulse.* Natalie Gibson, André Filiatrault, and Scott A. Ashford. April 2002.

PEER 2002/23 *Effects of Large Velocity Pulses on Reinforced Concrete Bridge Columns.* Greg L. Orozco and Scott A. Ashford. April 2002.

PEER 2002/22 *Characterization of Large Velocity Pulses for Laboratory Testing.* Kenneth E. Cox and Scott A. Ashford. April 2002.

PEER 2002/21 *Fourth U.S.-Japan Workshop on Performance-Based Earthquake Engineering Methodology for Reinforced Concrete Building Structures*. December 2002.

PEER 2002/20 *Barriers to Adoption and Implementation of PBEE Innovations.* Peter J. May. August 2002.

PEER 2002/19 *Economic-Engineered Integrated Models for Earthquakes: Socioeconomic Impacts.* Peter Gordon, James E. Moore II, and Harry W. Richardson. July 2002.

PEER 2002/18 *Assessment of Reinforced Concrete Building Exterior Joints with Substandard Details.* Chris P. Pantelides, Jon Hansen, Justin Nadauld, and Lawrence D. Reaveley. May 2002.

PEER 2002/17 *Structural Characterization and Seismic Response Analysis of a Highway Overcrossing Equipped with Elastomeric Bearings and Fluid Dampers: A Case Study.* Nicos Makris and Jian Zhang. November 2002.

PEER 2002/16 *Estimation of Uncertainty in Geotechnical Properties for Performance-Based Earthquake Engineering.* Allen L. Jones, Steven L. Kramer, and Pedro Arduino. December 2002.

PEER 2002/15 *Seismic Behavior of Bridge Columns Subjected to Various Loading Patterns.* Asadollah Esmaeily-Gh. and Yan Xiao. December 2002.

PEER 2002/14 *Inelastic Seismic Response of Extended Pile Shaft Supported Bridge Structures.* T.C. Hutchinson, R.W. Boulanger, Y.H. Chai, and I.M. Idriss. December 2002.

PEER 2002/13 *Probabilistic Models and Fragility Estimates for Bridge Components and Systems.* Paolo Gardoni, Armen Der Kiureghian, and Khalid M. Mosalam. June 2002.

PEER 2002/12 *Effects of Fault Dip and Slip Rake on Near-Source Ground Motions: Why Chi-Chi Was a Relatively Mild M7.6 Earthquake.* Brad T. Aagaard, John F. Hall, and Thomas H. Heaton. December 2002.

PEER 2002/11 *Analytical and Experimental Study of Fiber-Reinforced Strip Isolators*. James M. Kelly and Shakhzod M. Takhirov. September 2002.

PEER 2002/10 *Centrifuge Modeling of Settlement and Lateral Spreading with Comparisons to Numerical Analyses***.** Sivapalan Gajan and Bruce L. Kutter. January 2003.

PEER 2002/09 *Documentation and Analysis of Field Case Histories of Seismic Compression during the 1994 Northridge, California, Earthquake.* Jonathan P. Stewart, Patrick M. Smith, Daniel H. Whang, and Jonathan D. Bray. October 2002.

PEER 2002/08 *Component Testing, Stability Analysis and Characterization of Buckling-Restrained Unbonded Braces™.* Cameron Black, Nicos Makris, and Ian Aiken. September 2002.

PEER 2002/07 *Seismic Performance of Pile-Wharf Connections.* Charles W. Roeder, Robert Graff, Jennifer Soderstrom, and Jun Han Yoo. December 2001.

PEER 2002/06 *The Use of Benefit-Cost Analysis for Evaluation of Performance-Based Earthquake Engineering Decisions*. Richard O. Zerbe and Anthony Falit-Baiamonte. September 2001.

PEER 2002/05 *Guidelines, Specifications, and Seismic Performance Characterization of Nonstructural Building Components and Equipment*. André Filiatrault, Constantin Christopoulos, and Christopher Stearns. September 2001.

PEER 2002/04 *Consortium of Organizations for Strong-Motion Observation Systems and the Pacific Earthquake Engineering Research Center Lifelines Program: Invited Workshop on Archiving and Web Dissemination of Geotechnical Data, 4–5 October 2001*. September 2002.

PEER 2002/03 *Investigation of Sensitivity of Building Loss Estimates to Major Uncertain Variables for the Van Nuys Testbed.* Keith A. Porter, James L. Beck, and Rustem V. Shaikhutdinov. August 2002.

PEER 2002/02 *The Third U.S.-Japan Workshop on Performance-Based Earthquake Engineering Methodology for Reinforced Concrete Building Structures*. July 2002.

PEER 2002/01 *Nonstructural Loss Estimation: The UC Berkeley Case Study.* Mary C. Comerio and John C. Stallmeyer. December 2001.

PEER 2001/16 *Statistics of SDF-System Estimate of Roof Displacement for Pushover Analysis of Buildings.* Anil K. Chopra, Rakesh K. Goel, and Chatpan Chintanapakdee. December 2001.

PEER 2001/15 *Damage to Bridges during the 2001 Nisqually Earthquake.* R. Tyler Ranf, Marc O. Eberhard, and Michael P. Berry. November 2001.

PEER 2001/14 *Rocking Response of Equipment Anchored to a Base Foundation.* Nicos Makris and Cameron J. Black. September 2001.

PEER 2001/13 *Modeling Soil Liquefaction Hazards for Performance-Based Earthquake Engineering.* Steven L. Kramer and Ahmed-W. Elgamal. February 2001.

PEER 2001/12 *Development of Geotechnical Capabilities in OpenSees.* Boris Jeremić. September 2001.

PEER 2001/11 *Analytical and Experimental Study of Fiber-Reinforced Elastomeric Isolators*. James M. Kelly and Shakhzod M. Takhirov. September 2001.

PEER 2001/10 *Amplification Factors for Spectral Acceleration in Active Regions.* Jonathan P. Stewart, Andrew H. Liu, Yoojoong Choi, and Mehmet B. Baturay. December 2001.

PEER 2001/09 *Ground Motion Evaluation Procedures for Performance-Based Design.* Jonathan P. Stewart, Shyh-Jeng Chiou, Jonathan D. Bray, Robert W. Graves, Paul G. Somerville, and Norman A. Abrahamson. September 2001.

PEER 2001/08 *Experimental and Computational Evaluation of Reinforced Concrete Bridge Beam-Column Connections for Seismic Performance*. Clay J. Naito, Jack P. Moehle, and Khalid M. Mosalam. November 2001.

PEER 2001/07 *The Rocking Spectrum and the Shortcomings of Design Guidelines.* Nicos Makris and Dimitrios Konstantinidis. August 2001.

PEER 2001/06 *Development of an Electrical Substation Equipment Performance Database for Evaluation of Equipment Fragilities*. Thalia Agnanos. April 1999.

PEER 2001/05 *Stiffness Analysis of Fiber-Reinforced Elastomeric Isolators.* Hsiang-Chuan Tsai and James M. Kelly. May 2001.

PEER 2001/04 *Organizational and Societal Considerations for Performance-Based Earthquake Engineering.* Peter J. May. April 2001.

PEER 2001/03 *A Modal Pushover Analysis Procedure to Estimate Seismic Demands for Buildings: Theory and Preliminary Evaluation.* Anil K. Chopra and Rakesh K. Goel. January 2001.

PEER 2001/02 *Seismic Response Analysis of Highway Overcrossings Including Soil-Structure Interaction.* Jian Zhang and Nicos Makris. March 2001.

PEER 2001/01 *Experimental Study of Large Seismic Steel Beam-to-Column Connections.* Egor P. Popov and Shakhzod M. Takhirov. November 2000.

PEER 2000/10 *The Second U.S.-Japan Workshop on Performance-Based Earthquake Engineering Methodology for Reinforced Concrete Building Structures.* March 2000.

PEER 2000/09 *Structural Engineering Reconnaissance of the August 17, 1999 Earthquake: Kocaeli (Izmit), Turkey.* Halil Sezen, Kenneth J. Elwood, Andrew S. Whittaker, Khalid Mosalam, John J. Wallace, and John F. Stanton. December 2000.

PEER 2000/08 *Behavior of Reinforced Concrete Bridge Columns Having Varying Aspect Ratios and Varying Lengths of Confinement.* Anthony J. Calderone, Dawn E. Lehman, and Jack P. Moehle. January 2001.

PEER 2000/07 *Cover-Plate and Flange-Plate Reinforced Steel Moment-Resisting Connections.* Taejin Kim, Andrew S. Whittaker, Amir S. Gilani, Vitelmo V. Bertero, and Shakhzod M. Takhirov. September 2000.

PEER 2000/06 *Seismic Evaluation and Analysis of 230-kV Disconnect Switches.* Amir S. J. Gilani, Andrew S. Whittaker, Gregory L. Fenves, Chun-Hao Chen, Henry Ho, and Eric Fujisaki. July 2000.

PEER 2000/05 *Performance-Based Evaluation of Exterior Reinforced Concrete Building Joints for Seismic Excitation.* Chandra Clyde, Chris P. Pantelides, and Lawrence D. Reaveley. July 2000.

PEER 2000/04 *An Evaluation of Seismic Energy Demand: An Attenuation Approach.* Chung-Che Chou and Chia-Ming Uang. July 1999.

PEER 2000/03 *Framing Earthquake Retrofitting Decisions: The Case of Hillside Homes in Los Angeles.* Detlof von Winterfeldt, Nels Roselund, and Alicia Kitsuse. March 2000.

PEER 2000/02 *U.S.-Japan Workshop on the Effects of Near-Field Earthquake Shaking.* Andrew Whittaker, ed. July 2000.

PEER 2000/01 *Further Studies on Seismic Interaction in Interconnected Electrical Substation Equipment.* Armen Der Kiureghian, Kee-Jeung Hong, and Jerome L. Sackman. November 1999.

PEER 1999/14 *Seismic Evaluation and Retrofit of 230-kV Porcelain Transformer Bushings*. Amir S. Gilani, Andrew S. Whittaker, Gregory L. Fenves, and Eric Fujisaki. December 1999.

PEER 1999/13 *Building Vulnerability Studies: Modeling and Evaluation of Tilt-up and Steel Reinforced Concrete Buildings.* John W. Wallace, Jonathan P. Stewart, and Andrew S. Whittaker, editors. December 1999.

PEER 1999/12 *Rehabilitation of Nonductile RC Frame Building Using Encasement Plates and Energy-Dissipating Devices.* Mehrdad Sasani, Vitelmo V. Bertero, James C. Anderson. December 1999.

PEER 1999/11 *Performance Evaluation Database for Concrete Bridge Components and Systems under Simulated Seismic Loads.* Yael D. Hose and Frieder Seible. November 1999.

PEER 1999/10 *U.S.-Japan Workshop on Performance-Based Earthquake Engineering Methodology for Reinforced Concrete Building Structures.* December 1999.

PEER 1999/09 *Performance Improvement of Long Period Building Structures Subjected to Severe Pulse-Type Ground Motions*. James C. Anderson, Vitelmo V. Bertero, and Raul Bertero. October 1999.

PEER 1999/08 *Envelopes for Seismic Response Vectors.* Charles Menun and Armen Der Kiureghian. July 1999.

PEER 1999/07 *Documentation of Strengths and Weaknesses of Current Computer Analysis Methods for Seismic Performance of Reinforced Concrete Members.* William F. Cofer. November 1999.

PEER 1999/06 *Rocking Response and Overturning of Anchored Equipment under Seismic Excitations.* Nicos Makris and Jian Zhang. November 1999.

PEER 1999/05 *Seismic Evaluation of 550 kV Porcelain Transformer Bushings.* Amir S. Gilani, Andrew S. Whittaker, Gregory L. Fenves, and Eric Fujisaki. October 1999.

PEER 1999/04 *Adoption and Enforcement of Earthquake Risk-Reduction Measures.* Peter J. May, Raymond J. Burby, T. Jens Feeley, and Robert Wood.

PEER 1999/03 *Task 3 Characterization of Site Response General Site Categories*. Adrian Rodriguez-Marek, Jonathan D. Bray, and Norman Abrahamson. February 1999.

PEER 1999/02 *Capacity-Demand-Diagram Methods for Estimating Seismic Deformation of Inelastic Structures: SDF Systems*. Anil K. Chopra and Rakesh Goel. April 1999.

PEER 1999/01 *Interaction in Interconnected Electrical Substation Equipment Subjected to Earthquake Ground Motions.* Armen Der Kiureghian, Jerome L. Sackman, and Kee-Jeung Hong. February 1999.

PEER 1998/08 *Behavior and Failure Analysis of a Multiple-Frame Highway Bridge in the 1994 Northridge Earthquake.* Gregory L. Fenves and Michael Ellery. December 1998.

PEER 1998/07 *Empirical Evaluation of Inertial Soil-Structure Interaction Effects.* Jonathan P. Stewart, Raymond B. Seed, and Gregory L. Fenves. November 1998.

PEER 1998/06 *Effect of Damping Mechanisms on the Response of Seismic Isolated Structures.* Nicos Makris and Shih-Po Chang. November 1998.

PEER 1998/05 *Rocking Response and Overturning of Equipment under Horizontal Pulse-Type Motions.* Nicos Makris and Yiannis Roussos. October 1998.

PEER 1998/04 *Pacific Earthquake Engineering Research Invitational Workshop Proceedings, May 14–15, 1998: Defining the Links between Planning, Policy Analysis, Economics and Earthquake Engineering.* Mary Comerio and Peter Gordon. September 1998.

PEER 1998/03 *Repair/Upgrade Procedures for Welded Beam to Column Connections.* James C. Anderson and Xiaojing Duan. May 1998.

PEER 1998/02 *Seismic Evaluation of 196 kV Porcelain Transformer Bushings.* Amir S. Gilani, Juan W. Chavez, Gregory L. Fenves, and Andrew S. Whittaker. May 1998.

PEER 1998/01 *Seismic Performance of Well-Confined Concrete Bridge Columns.* Dawn E. Lehman and Jack P. Moehle. December 2000.

ONLINE PEER REPORTS

The following PEER reports are available by Internet only at http://peer.berkeley.edu/publications/peer_reports_complete.html.

PEER 2012/103 *Performance-Based Seismic Demand Assessment of Concentrically Braced Steel Frame Buildings.* Chui-Hsin Chen and Stephen A. Mahin. December 2012.

PEER 2012/102 *Procedure to Restart an Interrupted Hybrid Simulation: Addendum to PEER Report 2010/103.* Vesna Terzic and Bozidar Stojadinovic. October 2012.

PEER 2012/101 *Mechanics of Fiber Reinforced Bearings.* James M. Kelly and Andrea Calabrese. February 2012.

PEER 2011/107 *Nonlinear Site Response and Seismic Compression at Vertical Array Strongly Shaken by 2007 Niigata-ken Chuetsu-oki Earthquake.* Eric Yee, Jonathan P. Stewart, and Kohji Tokimatsu. December 2011.

PEER 2011/106 *Self Compacting Hybrid Fiber Reinforced Concrete Composites for Bridge Columns.* Pardeep Kumar, Gabriel Jen, William Trono, Marios Panagiotou, and Claudia Ostertag. September 2011.

PEER 2011/105 *Stochastic Dynamic Analysis of Bridges Subjected to Spacially Varying Ground Motions.* Katerina Konakli and Armen Der Kiureghian. August 2011.

PEER 2011/104 *Design and Instrumentation of the 2010 E-Defense Four-Story Reinforced Concrete and Post-Tensioned Concrete Buildings.* Takuya Nagae, Kenichi Tahara, Taizo Matsumori, Hitoshi Shiohara, Toshimi Kabeyasawa, Susumu Kono, Minehiro Nishiyama (Japanese Research Team) and John Wallace, Wassim Ghannoum, Jack Moehle, Richard Sause, Wesley Keller, Zeynep Tuna (U.S. Research Team). June 2011.

PEER 2011/103 *In-Situ Monitoring of the Force Output of Fluid Dampers: Experimental Investigation.* Dimitrios Konstantinidis, James M. Kelly, and Nicos Makris. April 2011.

PEER 2011/102 *Ground-motion prediction equations 1964 - 2010.* John Douglas. April 2011.

PEER 2011/101 *Report of the Eighth Planning Meeting of NEES/E-Defense Collaborative Research on Earthquake Engineering.* Convened by the Hyogo Earthquake Engineering Research Center (NIED), NEES Consortium, Inc. February 2011.

PEER 2010/111 *Modeling and Acceptance Criteria for Seismic Design and Analysis of Tall Buildings.* Task 7 Report for the Tall Buildings Initiative - Published jointly by the Applied Technology Council. October 2010.

PEER 2010/110 *Seismic Performance Assessment and Probabilistic Repair Cost Analysis of Precast Concrete Cladding Systems for Multistory Buildlings.* Jeffrey P. Hunt and Božidar Stojadinovic. November 2010.

PEER 2010/109 *Report of the Seventh Joint Planning Meeting of NEES/E-Defense Collaboration on Earthquake Engineering. Held at the E-Defense, Miki, and Shin-Kobe, Japan, September 18–19, 2009.* August 2010.

PEER 2010/108 *Probabilistic Tsunami Hazard in California.* Hong Kie Thio, Paul Somerville, and Jascha Polet, preparers. October 2010.

PEER 2010/107 *Performance and Reliability of Exposed Column Base Plate Connections for Steel Moment-Resisting Frames.* Ady Aviram, Božidar Stojadinovic, and Armen Der Kiureghian. August 2010.

PEER 2010/106 *Verification of Probabilistic Seismic Hazard Analysis Computer Programs.* Patricia Thomas, Ivan Wong, and Norman Abrahamson. May 2010.

PEER 2010/105 *Structural Engineering Reconnaissance of the April 6, 2009, Abruzzo, Italy, Earthquake, and Lessons Learned.* M. Selim Günay and Khalid M. Mosalam. April 2010.

PEER 2010/104 *Simulating the Inelastic Seismic Behavior of Steel Braced Frames, Including the Effects of Low-Cycle Fatigue.* Yuli Huang and Stephen A. Mahin. April 2010.

PEER 2010/103 *Post-Earthquake Traffic Capacity of Modern Bridges in California.* Vesna Terzic and Božidar Stojadinović. March 2010.

PEER 2010/102 *Analysis of Cumulative Absolute Velocity (CAV) and JMA Instrumental Seismic Intensity (I_{JMA}) Using the PEER–NGA Strong Motion Database.* Kenneth W. Campbell and Yousef Bozorgnia. February 2010.

PEER 2010/101 *Rocking Response of Bridges on Shallow Foundations.* Jose A. Ugalde, Bruce L. Kutter, and Boris Jeremic. April 2010.

PEER 2009/109 *Simulation and Performance-Based Earthquake Engineering Assessment of Self-Centering Post-Tensioned Concrete Bridge Systems.* Won K. Lee and Sarah L. Billington. December 2009.

PEER 2009/108 *PEER Lifelines Geotechnical Virtual Data Center.* J. Carl Stepp, Daniel J. Ponti, Loren L. Turner, Jennifer N. Swift, Sean Devlin, Yang Zhu, Jean Benoit, and John Bobbitt. September 2009.

PEER 2009/107 *Experimental and Computational Evaluation of Current and Innovative In-Span Hinge Details in Reinforced Concrete Box-Girder Bridges: Part 2: Post-Test Analysis and Design Recommendations.* Matias A. Hube and Khalid M. Mosalam. December 2009.

PEER 2009/106 *Shear Strength Models of Exterior Beam-Column Joints without Transverse Reinforcement.* Sangjoon Park and Khalid M. Mosalam. November 2009.

PEER 2009/105 *Reduced Uncertainty of Ground Motion Prediction Equations through Bayesian Variance Analysis.* Robb Eric S. Moss. November 2009.

PEER 2009/104 *Advanced Implementation of Hybrid Simulation.* Andreas H. Schellenberg, Stephen A. Mahin, Gregory L. Fenves. November 2009.

PEER 2009/103 *Performance Evaluation of Innovative Steel Braced Frames.* T. Y. Yang, Jack P. Moehle, and Božidar Stojadinovic. August 2009.

PEER 2009/102 *Reinvestigation of Liquefaction and Nonliquefaction Case Histories from the 1976 Tangshan Earthquake.* Robb Eric Moss, Robert E. Kayen, Liyuan Tong, Songyu Liu, Guojun Cai, and Jiaer Wu. August 2009.

PEER 2009/101 *Report of the First Joint Planning Meeting for the Second Phase of NEES/E-Defense Collaborative Research on Earthquake Engineering.* Stephen A. Mahin et al. July 2009.

PEER 2008/104 *Experimental and Analytical Study of the Seismic Performance of Retaining Structures.* Linda Al Atik and Nicholas Sitar. January 2009.

PEER 2008/103 *Experimental and Computational Evaluation of Current and Innovative In-Span Hinge Details in Reinforced Concrete Box-Girder Bridges. Part 1: Experimental Findings and Pre-Test Analysis.* Matias A. Hube and Khalid M. Mosalam. January 2009.

PEER 2008/102 *Modeling of Unreinforced Masonry Infill Walls Considering In-Plane and Out-of-Plane Interaction.* Stephen Kadysiewski and Khalid M. Mosalam. January 2009.

PEER 2008/101 *Seismic Performance Objectives for Tall Buildings.* William T. Holmes, Charles Kircher, William Petak, and Nabih Youssef. August 2008.

PEER 2007/101 *Generalized Hybrid Simulation Framework for Structural Systems Subjected to Seismic Loading.* Tarek Elkhoraibi and Khalid M. Mosalam. July 2007.

PEER 2007/100 *Seismic Evaluation of Reinforced Concrete Buildings Including Effects of Masonry Infill Walls.* Alidad Hashemi and Khalid M. Mosalam. July 2007.

The Pacific Earthquake Engineering Research Center (PEER) is a multi-institutional research and education center with headquarters at the University of California, Berkeley. Investigators from over 20 universities, several consulting companies, and researchers at various state and federal government agencies contribute to research programs focused on performance-based earthquake engineering.

These research programs aim to identify and reduce the risks from major earthquakes to life safety and to the economy by including research in a wide variety of disciplines including structural and geotechnical engineering, geology/seismology, lifelines, transportation, architecture, economics, risk management, and public policy.

PEER is supported by federal, state, local, and regional agencies, together with industry partners.

PEER Core Institutions:
University of California, Berkeley (Lead Institution)
California Institute of Technology
Oregon State University
Stanford University
University of California, Davis
University of California, Irvine
University of California, Los Angeles
University of California, San Diego
University of Southern California
University of Washington

PEER reports can be ordered at http://peer.berkeley.edu/publications/peer_reports.html or by contacting

Pacific Earthquake Engineering Research Center
University of California, Berkeley
325 Davis Hall, mail code 1792
Berkeley, CA 94720-1792
Tel: 510-642-3437
Fax: 510-642-1655
Email: peer_editor@berkeley.edu

ISSN 1547-0587X